TENSILE STRENGTH OF UNSATURATED SOILS

PENGHAI YIN

B.Sc., Wuhan University, China
M.Sc., Wuhan University, China

Thesis submitted to University of Ottawa
in partial fulfillment of the requirements for the
Doctorate in Philosophy degree in Civil Engineering

Department of Civil Engineering
Faculty of Engineering
University of Ottawa

The Doctor of Philosophy in Civil Engineering is a joint program between
Carleton University and University of Ottawa, which is administered by
the Ottawa-Carleton Institute for Civil Engineering

Abstract

Desiccation-induced soil cracking is of significant interest in several engineering disciplines, which include geotechnical and geoenvironmental engineering, mining engineering, and agriculture engineering. The hydraulic, mechanical, thermal and other physico-chemical properties of unsaturated soils can be predominantly influenced due to cracks. Reliable information of these properties is required for the rational design and maintenance of earth structures taking account of the influence the soil-atmosphere interactions (e.g., for expansive soil slopes, earth dams, and embankments). In spite of significant research studies published in the literature on the desiccation-induced cracks during the past century, the fundamental mechanism of crack initiation and propagation of soils induced by drying and shrinkage is still elusive. For this reason, the focus of this thesis is directed towards understanding the tensile strength of unsaturated soils which is associated with soil crack initiation criterion (i.e. maximum tensile stress criterion).

Tensile strength is the key property of soils for interpreting the initiation of soil cracking from a macroscopic point of view. A semi-empirical model is proposed for predicting the tensile strength of unsaturated cohesionless soils taking into account the effect of both the negative pore-water pressure in saturated pores and the air-water interfacial surface tension in unsaturated pores. The proposed model is calibrated and validated by providing comparisons between the model predictions and the experimental measurements on 10 cohesionless soils (i.e. five sandy soils and five silty soils) published in the literature. The proposed model is simple and requires only the information of Soil-Water Characteristic Curve (SWCC) and Grain Size Distribution curve (GSD), which can be obtained from conventional laboratory tests.

To investigate the influence of microstructure, a practical and reliable estimation approach for predicting the evolution of the microstructural void ratio of compacted clayey soils subjected to wetting and drying paths is proposed. The microstructural evolution of 13 examined soils were investigated quantitatively using the mercury intrusion porosimetry (MIP) results. The investigated soils include four high-plasticity clays, eight low-plasticity clays and a glacial till, which is a relatively coarse-grained soil with some fines. Based on this study, a novel criterion has been developed for identifying different pore populations of compacted clayey soils. The “as-compacted state line” (ACSL) was proposed to estimate the initial microstructural void ratio based on the compaction water ratio. A constitutive stress is derived to interpret and predict the volumetric

deformation of compacted clay aggregates. The linear elastic constitutive model is used for predicting the microstructural void ratio of the examined compacted soils following monotonic wetting and drying paths. The developed approach (i.e. the ACSL and the linear elastic constitutive model) is validated by providing comparisons between the predicted and interpreted microstructural void ratios for all the examined soils.

In addition to the matric suction and microstructure, the confining pressure also influences the tensile strength of unsaturated compacted clayey soils. The tensile strength tests on a compacted clayey soil by both the direct method (i.e. triaxial tensile test) and the indirect method (i.e. Brazilian split test) were performed. It is found that the tensile strength increases as the compaction water content decreases for the range investigated in this study, which could be explained by the variation of the inter-aggregated capillary bonding force and the change in microstructure. The increase in the confining pressure has been found to induce the change in failure mode (i.e. from pure tensile failure mode to combined tensile-shear failure mode). In spite of limitations associated with the Brazilian split test, tensile strength is widely determined using this test due to the simple procedure of specimen preparation and wide availability of test equipment in conventional laboratories. However, the Brazilian tensile strength is found to overestimate the tensile strength of compacted specimens with water content greater than the plastic limit. This is due to the considerable plastic deformation associated with the ductile failure instead of brittle failure.

In summary, this thesis is devoted to providing insight into the fundamental mechanisms associated with the desiccation-induced crack initiation by quantitatively investigating the various factors that influence the tensile strength of unsaturated soils, which include the matric suction, the microstructure, and the confining pressure from theoretical studies and laboratory investigations.

Acknowledgments

The research work presented in this thesis is conducted under the supervision of Prof. Sai K. Vanapalli at the Department of Civil Engineering, University of Ottawa. I would like to express my sincere appreciation to Prof. Vanapalli. I attended the lectures on unsaturated soils given by Prof. Vanapalli in April 2013 at Wuhan University when I first met him. Since then, I have received continuous encouragement from Prof. Vanapalli not only in the research program but also in my personal life.

The financial supports from China Scholarship Council (CSC) and University of Ottawa are greatly appreciated. In addition, I would like to express my gratitude to Mitacs Globalink Research Award which provided me an opportunity to have a short visit to Texas A&M University as a visiting scholar.

I would like to extend my appreciation to the thesis committee including Prof. Siva Sivathayalan, Prof. Sedano Julio Angel Infante, Prof. Rozalina Dimitrova and Prof. Marcelo Javier, Sánchez Castilla. Their insightful comments and suggestions were very helpful for improving the thesis. I thank the technical officers, Jean Claude Célestin, John Perrins and Leo Denner for their assistance with the test equipment.

I would like to thank my girlfriend, Mengxi who has supported and encouraged me during my Ph.D. studies. Acknowledgements are also extended to my colleagues, Zhong, Shunchao, Ping, Jiaying, Yunlong, Mohammed, Xiaokun, Hongyu, Junping, Guanlong, Xiuhan, Kun, Mingshu, Xinting, Xingyi, Yao, and Junjie from the Geotechnical group, University of Ottawa.

Last but not the least, I would like to express my appreciation to my mother, Jianru Lyu who selflessly supported me to pursue my dreams. I would like to dedicate the thesis to my father, Yugui Yin who never saw my exciting adventure during the past five and a half years.

Table of Contents

List of Figures

List of Tables

Chapter 1. Introduction

1.1 Research Motivation

1.1.1 Motivations for investigating tensile strength of unsaturated soils

Soil cracking is ubiquitous and alters the hydraulic, mechanical, thermal and other physico-chemical properties of soils. Therefore, as illustrated in Figure 1.1, soil cracking is of significant interest in several engineering and science fields (Kodikara and Costa 2013), (i) in geotechnical engineering, for example, cracking at the crest area of the slopes which could trigger the initiation of slope failure (e.g., Take 2003; Zhou et al. 2009), desiccation cracking induced progressive failures of embankment dams or flood dykes (e.g., Sherard 1973; Dyer et al. 2009), and tensile cracking for shallow anchors (e.g., Rowe and Davis 1982); (ii) in geo-environmental engineering, for example, leaching of waste liquid and gas from compacted and geosynthetic landfill liners and covers (e.g., Daniel and Wu 1993; Miller and Mishra 1989; Chen 2016), and gas migration through sealing or buffer materials which is referred as "engineered barrier system (EBS)" in the deep geological disposal of high-level and long-lived radioactive nuclear waste (e.g., Kim et al. 2011; Wiseall et al. 2015); (iii) mining and resources engineering, for example, cracking in mine tailings which influence the drying rate and stability (e.g., Morris et al. 1992; Rodríguez 2002); (iv) agricultural engineering and soil science, for example, water and solute transportation through the cracked soils in irrigated lands (e.g., Bronswijk et al. 1995), and the crumbility and friability of soils during wetting and drying or during tillage operations which is an important consideration in agricultural engineering (e.g., Dexter and Watts 2000); (v) planetary sciences, for example, formation of giant polygons on Earth and Mars which provides the evidence for presence of water (e.g., El Maarry et al. 2014); and (vi) paleontology, such as desiccation-induced cracks in the paleo-ecological and paleo-environmental setting which have influence on the quantitative interpretation of track fossils (e.g., Schanz et al. 2016).

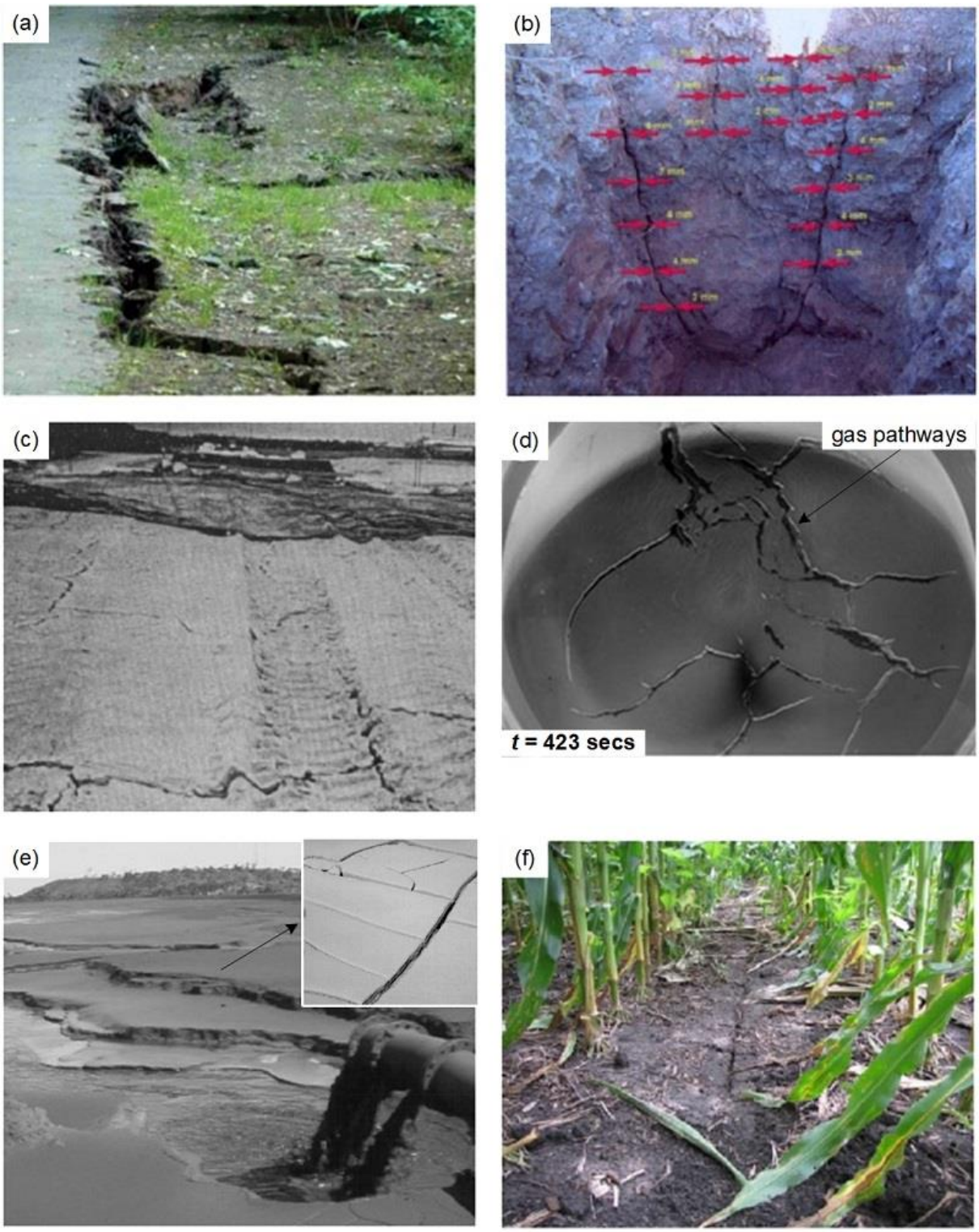

Figure 1.1 Scheme of (a) tensile crack at the upper part of a slope (after Vaníček 2013); (b) cracking in trail trench at Thorngumbald Flood defence embankment (after Dyer et al. 2009); (c) cracking in compacted clay liner after several days of unprotected exposure to air (after Daniel and Wu 1993); (d) Crack network development in kaolin paste due to gas injection (after Wiseall et al. 2015); (e) metallurgical waste discharge in Cuban nickel industry (after Rodríguez 2002); (f) surface cracks in the irrigated lands after wetting-drying cycles (after Sanders 2010).

The soil cracking phenomenon is commonly observed in slopes, earth dams, embankments, landfill liners and covers, deep geological disposal of nuclear waste, etc. Cracking in clayey soils is typically found under one or more of the following circumstances (Williams and Jennings 1977): (i) during the consolidation process; (ii) a decrease in overburden pressure during swelling of the clay; (iii) syneresis which is the spontaneous contraction of a gel accompanied by expulsion of liquid from the pores; (iv) chemical reactions in the clay induce volume distortions with cracks; (v) tectonic stresses; (vi) as the clay dries; (vii) be inherited from the bedrock; (viii) large lateral stresses induced cracking. The various types of soil cracking in geotechnical and geoenvironmental engineering have been classified into four categories (Fang 1997): (i) shrinkage cracks (referred as "desiccation-induced cracks" in the remainder of this thesis), which are generated when tensile stresses develop as water is lost from a soil mass; (ii) thermal cracks, which are caused by the change in thermal stresses as the soil is heated and then suddenly cooled or by a significant change in temperature as a result of freezing-thawing or wet-dry process; (iii) tensile cracks, which are attributed to the overburden pressure including structural loading, rainfall, ice and snow loads, vegetation, and seasonal creep loads; and (iv) fracture cracks, which are related to the change in the pore-water pressure within the existing fractures along with the change of environmental conditions due to daily moisture or temperature changes, to seasonal groundwater table fluctuation, rainfall or melting snow filling into the cracks or voids in the soil. From continuum mechanics point of view, the fourth category of cracks is essentially different from the former three which are associated with the transformation from intact soils (i.e. continuum) to cracked soils (i.e. material containing discontinuities). This study on the tensile strength of unsaturated soils is motivated by the fundamental mechanism of soil cracking initiation induced by desiccation in the context of geotechnical and geoenvironmental engineering.

1.1.2 Theoretical challenges for interpreting soil cracking in the context of fracture mechanics

Fracture mechanics is a well-developed and investigated subject for the past century, including linear elastic fracture mechanics (LEFM, e.g., Griffith 1921; Irwin 1957) and elastic-plastic fracture mechanics (EPFM, e.g., Rice 1968; Barenblatt 1962; Xu and Needleman 1994). However, the application of fracture mechanics to practical soil cracking due to drying could be challenging due to the following reasons. First, fracture in solids, like turbulence in fluids, is an incompletely solved problem (Goehring and Morris 2014). Soil cracking is a nonequilibrium and irreversible

dynamic process that cannot be entirely explained by global energy balance or local stress concentration arguments. Secondly, for desiccation-induced soil cracking, environmental load (i.e. evaporation) is the driven forces for shrinkage and subsequent cracking, rather than the mechanical loads in the context of classical fracture mechanics. For the initially saturated soil, desiccation induced shrinkage and cracking involve the invasion of the air-water interface, which makes the hydromechanical response significantly different from that of saturated soils (e.g., Terzaghi 1943; Fredlund and Rahardjo 1993). Thirdly, fracture mechanics deals only with the crack propagation phenomena of the existing cracks, the crack initiation criterion is not addressed. Technically, cracking of a soil mass with an initially intact state includes three successive stages (e.g., Wei et al. 2016; Wang et al. 2018): (i) crack initiation; (ii) crack propagation and bifurcation; and (iii) crack coalescence. Therefore, an appropriate crack initiation criterion is needed to interpret the fundamental mechanisms of desiccation-induced soil cracking using fracture mechanics incorporated with unsaturated soil mechanics (e.g., Lakshmikantha et al. 2012; Levatti et al. 2019). Lastly, soil cracking is not only controlled by the determinative factor, i.e. stress field generated during drying under certain boundary conditions, but also by the statistical factors, i.e. the randomly distributed flaws or large pores in the desiccating soils (e.g., Lau 1987; Costa et al. 2013). The intrinsic heterogeneity and anisotropy of desiccating soils make it more complicated for the interpretation of desiccation-induced crack initiation and propagation. For this reason, the tensile strength of unsaturated soils is chosen as topic in this thesis to investigate the underlying mechanism associated with crack initiation.

1.2 Objectives of the research

To better understand the various factors that influence the tensile strength of unsaturated soils, this study is devoted to the following objectives which focus on theoretical studies and experimental investigations (Figure 1.2):

Objective 1: To investigate the relationship between desiccation-induced crack initiation and the tensile strength of unsaturated soils by comprehensively and critically reviewing the published studies from the literature on desiccation cracking in cohesive soils and tensile strength of unsaturated soils.

Objective 2: To study the effect of matric suction on the tensile strength of unsaturated cohesionless soils by revealing the underlying mechanism and developing the mechanics-based prediction model which correlates the matric suction and tensile strength.

Objective 3: To evaluate the change in microstructure of compacted clayey soils upon wetting and drying by developing the predictive model which reflects the internal stress transmission among clay aggregates.

Objective 4: To experimentally investigate the effect of confining pressure as well as matric suction on the tensile strength of compacted clayey soils by performing direct tensile tests (i.e. triaxial tensile test) and indirect tensile tests (i.e. Brazilian split test) on compacted Indian Head till specimens with different compaction water contents.

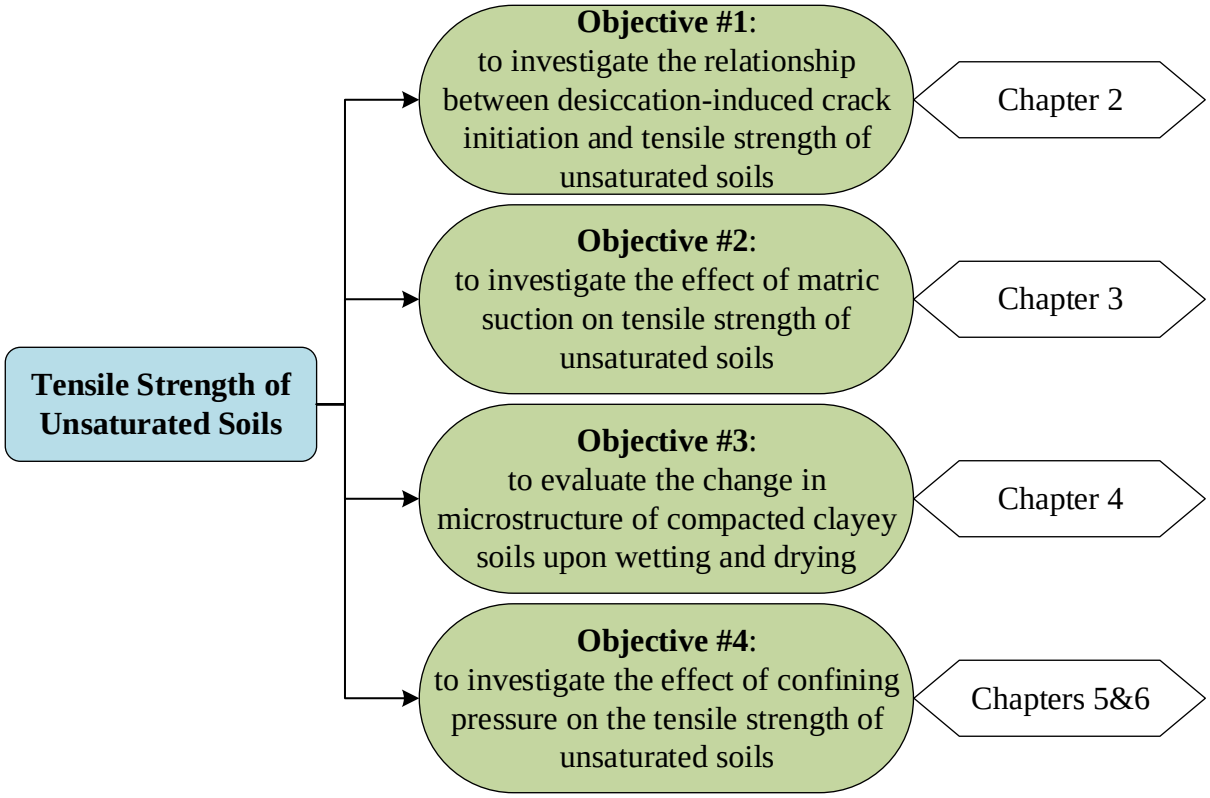

Figure 1.2 Research scope and thesis objectives.

1.3 Layout of the thesis

A detailed organization of this thesis is summarized below:

Chapter 1 is entitled, “Introduction”. This chapter provides a general introduction to highlight the motivation for investigating the tensile strength of unsaturated soils for better understanding the soil cracking behavior. The objectives and layout of this study are also summarized.

Chapter 2 is entitled, “Literature review”. A comprehensive review on desiccation-induced cracking of cohesive soils is presented, including the motivation, crack formation and crack patterns, and main research challenges. The existing methods for measuring the tensile strength of unsaturated soils and models for predicting the tensile strength of unsaturated cohesionless and cohesive soils are reviewed as well. The gap in the literature regarding the tensile strength of unsaturated soils is highlighted.

Chapter 3 is entitled, “Model for predicting the tensile strength of unsaturated cohesionless soils: accounting for the air-water interfacial tension”. This chapter presents a semi-empirical model for predicting tensile strength of unsaturated cohesionless soils using Soil-Water Characteristic Curve (SWCC) and Grain Size Distribution curve (GSD) as a tool. The proposed model accounts for the contribution to the tensile strength of unsaturated cohesionless soils from the suction (or negative pore water pressure) and surface tension. Experimental measurements of tensile strength for ten cohesionless soils (including five sandy soils and five silty soils) from the literature are used to validate the proposed model.

Chapter 4 is entitled, “Evolution of microstructural void ratio in compacted clayey soils upon wetting and drying”. The objective of this chapter is to provide a practical and reliable estimation approach for predicting the evolution of the microstructural void ratio of compacted clayey soils subjected to wetting and drying paths. The microstructural evolution of 13 examined soils were investigated quantitatively using the mercury intrusion porosimetry (MIP) results. The investigated soils include four high-plasticity clays, eight low-plasticity clays and a glacial till, which is a relatively coarse-grained soil with some fines. Based on this study, a novel criterion has been developed for identifying different pore populations of compacted clayey soils. The “as-compacted state line” (ACSL) has been proposed to estimate the initial microstructural void ratio based on the compaction water ratio. A constitutive stress is derived to interpret and predict the volumetric deformation of compacted clay aggregates. The linear elastic constitutive model is used for predicting the microstructural void ratio of the examined compacted soils following monotonic wetting and drying paths. The developed approach (i.e. the ACSL and the linear elastic constitutive

model) is validated by providing comparisons between the predicted and interpreted microstructural void ratios for all the examined soils.

Chapter 5 is entitled, “Geological and geotechnical characteristics of the investigated soil”. This chapter is devoted to present the geological origin, microstructure characteristics and conventional geotechnical properties of the investigated soil (i.e. Indian Head till). Scanning Electron Microscope (SEM) and Mercury Intrusion Porosimetry (MIP) are used to investigate the microstructural characteristics of the compacted Indian Head till specimens both at wet side and at dry side. The grain size distribution, Atterberg’s limits, consolidation characteristics, compaction curve, and Soil water characteristic curve (SWCC) are measured as well.

Chapter 6 is entitled, “Experimental studies on tensile strength of compacted clayey soil”. This chapter is devoted to present the experimental investigation of the tensile strength of a compacted clayey soil by both the direct method and the indirect method is presented. The effects of matric suction as well as confining pressure on the tensile strength of compacted Indian Head till are investigated by performing triaxial tensile tests on compacted specimens at different levels of confining pressures and various initial water content (i.e. various matric suction). Brazilian split test is conducted to investigate the variation of Brazilian tensile strength with respect to the compaction water contents.

Chapter 7 is entitled, “Conclusions and recommendations for future work”. This chapter presents five main conclusions from this study. Due to some limitations in this study, several recommendations for future research are provided, as well.

1.4 Related Publications

Journal Publications:

(1) **Penghai Yin** and Sai K. Vanapalli. (2018) Model for predicting tensile strength of unsaturated cohesionless soils. *Canadian Geotechnical Journal*. 55(9): 1313-1333. DOI: 10.1139/cgj-2017-0376.

(2) **Penghai Yin** and Sai K. Vanapalli. Model for predicting evolution of microstructural void ratio in compacted clayey soils upon wetting and drying. *Submitted for publication to an International Geotechnical Journal* (under review).

(3) **Penghai Yin** and Sai K. Vanapalli. Desiccation-induced cracks in cohesive soils: A review. *Submitted for publication to an International Geotechnical Journal*.

(4) **Penghai Yin** and Sai K. Vanapalli. The effects of matric suction and confining pressure on tensile strength of compacted clayey soil. *Geotechnical Testing Journal* (in-preparation).

Conference Publications:

(5) **Penghai Yin**, Sai K. Vanapalli. (2018). Prediction of tensile strength of compacted soils: A review. *In Proceedings of the 7th International Conference on Unsaturated Soils*, Hong Kong, China.

(6) **Penghai Yin**, Sai K. Vanapalli. (2018). Predicting the depth of desiccation-induced cracks in cohesive soils extending cohesive zone model. *In Proceedings of the Symposium on Engineering Properties and Applications of Fissured Clayey Soils*, Wuhan, China. [in Chinese]

(7) **Penghai Yin**, Sai K. Vanapalli. (2017). A unified failure criterion for saturated clayey soils under tension and compression. *In Proceedings of the 70th Canadian Geotechnical Conference*, Ottawa, Canada.

(8) Shunchao Qi, Sai K. Vanapalli, and **Penghai Yin**. (2017). Slope stability analysis of unsaturated expansive soils under rainfall infiltration using VADOSE/W and SLOPE/W. *In Proceedings of the 70th Canadian Geotechnical Conference*, Ottawa, Canada.

(9) **Penghai Yin**, Shunchao Qi, and Sai K. Vanapalli. (2016). A framework for predicting the depth of desiccation-induced cracks in clayey soils. *In Proceedings of the 69th Canadian Geotechnical Conference*, Vancouver, Canada.

1.5 References

Barenblatt, G.I. 1962. The mathematical theory of equilibrium cracks in brittle fracture. In Advances in applied mechanics (Vol. 7, pp. 55-129). Elsevier.

Bronswijk, J.J.B., Hamminga, W. and Oostindie, K. 1995. Field-scale solute transport in a heavy clay soil. Water Resources Research, 31(3): 517-526.

Chen, Z. 2016. Gas breakthrough and emission in unsaturated landfill final cover considering cracking effect. Doctoral dissertation, Hong Kong University of Science and Technology, China.

Costa, S., Kodikara, J.K. and Shannon, B. 2013. Salient factors controlling desiccation cracking of clay in laboratory experiments. Géotechnique, 63(1): 18-29.

Daniel, D.E. and Wu, Y.K. 1993. Compacted clay liners and covers for arid sites. Journal of Geotechnical Engineering, 119(2): 223-237.

Dexter, A.R. and Watts, C.W. 2000. Tensile strength and friability. In Soil and environmental analysis: Physical methods, Vol. 2, pp. 405-433.

Dyer, M., Utili, S. and Zielinski, M. 2009. Field survey of desiccation fissuring of flood embankments. In Proceedings of the Institution of Civil Engineers-Water Management, Vol. 162, No. 3, pp. 221-232. Thomas Telford Ltd.

El-Maarry, M.R., Watters, W., McKeown, N.K., Carter, J., Dobrea, E.N., Bishop, J.L., Pommerol, A. and Thomas, N. 2014. Potential desiccation cracks on Mars: A synthesis from modeling, analogue-field studies, and global observations. Icarus, 241: 248-268.

Fang, H. Y. 1997. Introduction to Environmental Geotechnology, volume 14 of New Directions in Civil Engineering. CRC Press.

Fredlund, D.G., Rahardjo, H. and Rahardjo, H. 1993. Soil mechanics for unsaturated soils. John Wiley and Sons, New York.

Goehring, L. and Morris, S.W. 2014. Cracking mud, freezing dirt, and breaking rocks. Physics Today, 67(11): 39-44.

Griffith, A.A. 1921. VI. The phenomena of rupture and flow in solids. Philosophical transactions of the Royal Society of London. Series A, containing papers of a mathematical or physical character, 221(582-593): 163-198.

Horseman, S.T., Harrington, J.F. and Sellin, P. 1999. Gas migration in clay barriers. Engineering Geology, 54(1-2): 139-149.

Irwin, G.R. 1957. Analysis of stresses and strains near the end of a crack traversing a plate. Journal of Applied Mechanics, 24: 361-364.

Lau, J.T.K. 1987. Desiccation cracking of soils. Master's dissertation, University of Saskatchewan, Canada.

Levatti, H.U., Prat, P.C. and Ledesma, A. 2019. Numerical and experimental study of initiation and propagation of desiccation cracks in clayey soils. Computers and Geotechnics, 105: 155-167.

Kim, J.S., Kwon, S.K., Sánchez, M. and Cho, G.C. 2011. Geological storage of high level nuclear waste. KSCE Journal of Civil Engineering, 15(4): 721-737.

Kodikara, J. and Costa, S. 2013. Desiccation cracking in clayey soils: Mechanisms and Modelling. In Multiphysical testing of soils and shales (pp. 21-32). Springer, Berlin, Heidelberg.

Konrad, J.M. and Ayad, R. 1997. Desiccation of a sensitive clay: field experimental observations. Canadian Geotechnical Journal, 34(6): 929-942.

Lakshmikantha, M.R., Prat, P.C. and Ledesma, A. 2012. Experimental evidence of size effect in soil cracking. Canadian Geotechnical Journal, 49(3): 264-284.

Miller, C.J. and Mishra, M. 1989. Modeling of leakage through cracked clay liners-II: A new perspective. Journal of the American Water Resources Association, 25(3): 557-563.

Morris, P. H., Graham, J. and Williams, D. J. 1992. Cracking in drying soils. Canadian Geotechnical Journal, 29(2): 263–277.

Wiseall, A.C., Cuss, R.J., Graham, C.C. and Harrington, J. F. 2015. The visualization of flow paths in experimental studies of clay-rich materials. Mineralogical Magazine, 79(6): 1335–1342.

Rice, J.R. 1968. A path independent integral and the approximate analysis of strain concentration by notches and cracks. Journal of Applied Mechanics, 35(2): 379-386.

Rodríguez Pacheco, R. L. 2002. Experimental study of flow and transport of chromium, nickel and manganese in residues of the Moa mining area (Cuba): Influence of the hydromechanical behavior. Doctoral dissertation, Universidad Politécnica de Cataluña, Spain. [in Spanish].

Rowe, R.K. and Davis, E.H. 1982. The behaviour of anchor plates in clay. Géotechnique, 32(1): 9-23.

Sanders, E.C. 2010. Characterizing flow through the soil matrix and preferential flow pathways (PFPs). Masters dissertation, Purdue University, USA.

Schanz, T., Datcheva, M., Haase, H. and Marty, D. 2016. Analysis of desiccation crack patterns for quantitative interpretation of fossil tracks. Dinosaur Tracks: The Next Steps, 367-379.

Sherard, J.L. 1973. Embankment dam cracking. In Embankment-Dam Engineering (Casagrande Volume, pp. 271-353). John Wiley and Sons, New York.

Take, W.A. 2003. The influence of seasonal moisture cycles on clay slopes. Doctoral dissertation, University of Cambridge, UK.

Terzaghi, K. 1943. Theoretical soil mechanics, Wiley, New York.
Vaníček, I. 2013. The importance of tensile strength in geotechnical engineering. Acta Geotechnica Slovenica, 10(1): 5–17.
Wang, L.L., Tang, C.S., Shi, B., Cui, Y.J., Zhang, G.Q. and Hilary, I. 2018. Nucleation and propagation mechanisms of soil desiccation cracks. Engineering Geology, 238: 27-35.
Wei, X., Hattab, M., Bompard, P. and Fleureau, J.M., 2016. Highlighting some mechanisms of crack formation and propagation in clays on drying path. Géotechnique, 66(4): 287-300.
Williams, A.A.B. and Jennings, J.E. 1977. The in-situ shear behaviour of fissured soils. In Proceedings of the 9th International Conference on Soil Mechanics and Foundation Engineering, pp. 169-176.
Xu, X.P. and Needleman, A. 1994. Numerical simulations of fast crack growth in brittle solids. Journal of the Mechanics and Physics of Solids, 42(9): 1397-1434.
Zhou, Y.D., Cheuk, C.Y. and Tham, L.G. 2009. Deformation and crack development of a nailed loose fill slope subjected to water infiltration. Landslides, 6(4): 299-308.

Chapter 2. Literature Review

2.1 Desiccation-induced cracks in cohesive soils: formation and patterns

2.1.1 Introduction

Soil scientists, geologists, civil and chemical engineers as well as physicists are interested in desiccation-induced cracks in soils (e.g., Bronswijk 1995; El Maarry et al. 2014; Dyer et al. 2009; Lee and Routh 2004; Goehring et al. 2011). Several researchers have contributed towards better understanding desiccation-induced cracks over the past century (e.g., Kindle 1917; Corte and Higashi 1964; Morris et al. 1992; Blight 1997; Kodikara et al. 2000; Goehring et al. 2015). However, this topic has received more attention during the last decade to understand climate change effects associated with extended drought periods. The focus of these studies were directed to understand the soil-atmosphere interaction, i.e. evaporation, which would induce shrinkage and cracking in the surficial soils especially in the arid and semi-arid areas (e.g., Omer and Mohd 2011; Kodikara and Costa 2013; Cordero et al. 2016; Zeng et al. 2019). Desiccation-induced surface cracks significantly alter the thermo-hydro-mechanical-chemical (THMC) responses of soils exposed to mechanical and environmental loads, which tend to damage the nearby geotechnical structures (e.g., retaining wall, shallow foundations), to exacerbate geo-environmental issues (e.g., preferential pathways for contaminants in covers and liners of the landfill), and to trigger the instability of slopes, earth dams, and embankments (e.g., Evans and Hughes 1968; Buzzi et al. 2010; Miller and Mishra 1989; Zhou et al. 2009; Sherard 1973).

The fundamental mechanism underpinning desiccation cracking is useful to bridge the gap between theoretical research and engineering practice applications. There are various factors which influence the formation and patterns of desiccation-induced cracks in soils, such as the composition of soils (e.g., Kleppe and Olson 1985; Rayhani et al. 2007; Costa et al. 2013), initial water content and density (e.g., Varsei et al. 2016; Demagistri et al. 2018), soil layer thickness (e.g., Tang et al. 2008), desiccation rate (e.g., Ávila et al. 2013), temperature (e.g., Tang et al. 2008), humidity (e.g., Rodríguez 2006), solvent (e.g., Shin and Santamarina 2011; Khatun et al. 2015; Zhang et al. 2019), substrate (e.g., Corte and Higashi 1964; DeCarlo and Shokri 2014), and external fields (e.g., Tarafdar and Dutta 2018). Kodikara and Costa (2013)

presented a succinct review of experimental and modelling studies on desiccation cracking of clayey soils, highlighting the Monash University research contributions. Shi et al. (2014) summarized research related to the formation of expansive soil cracks and their influences on the stability of expansive soil slopes. Sun et al. (2017) reviewed different research approaches and related techniques on soil desiccation cracking and concluded that there was no clear consensus on the formation mechanism of desiccation cracking. The purpose of this paper is to provide a theoretical framework to explain desiccation-cracking mechanism in cohesive soils and to rationally interpret the published experimental results based on unsaturated soil mechanics and fracture mechanics.

This state-of-the-art review is laid out in five sections. The first section introduces the current research advances and the purpose of this study. The second section summarizes the research motivation related to desiccation-induced cracks. The studies on the formation (i.e. initiation and propagation) of desiccation cracks are comprehensively reviewed in the third section, based on the information derived from large-scale field observations and small-scale laboratory tests from the literature. The desiccation crack patterns observed both in the field and laboratory studies are then summarized and interpreted based on fracture mechanics in the fourth section. Finally, the key research challenges that are related to the multiscale and multiphysics coupled features of desiccating cohesive soils are put forward in the last section.

2.1.2 Motivation for research related to desiccation-induced cracks

Cohesive soils, especially expansive soils are prone to shrink and crack upon drying due to considerable changes that arise in the soil microstructure, e.g., the increase in the frequency of macropores. Desiccation cracks have a paramount influence on the soil microstructure and subsequently on the soil responses to the mechanical and environmental loads (Gens 2010; Tang et al. 2018a). The motivation to study desiccation-induced cracks is discussed taking account of various needs in geotechnical and geo-environmental engineering, mining engineering, and agricultural engineering practice applications.

2.1.2.1 Desiccation-induced cracks in geotechnical and geo-environmental engineering

Desiccation-induced cracks are strongly related to failure events of earth structures, such as the slopes, dams and embankments. A better understanding of the adverse effect of cracks on the

stability of these infrastructures is vital for safe and economical designs. During the past two decades, many researchers attempted to understand the mechanism of the rainfall-induced failure of expansive soil slopes through field investigations, laboratory experiments, and numerical modelling studies (e.g., Bao et al. 1998; Ng et al. 2003; Kong et al. 2007; Cheng et al. 2014; Chen et al. 2018; Qi and Vanapalli 2018). Cracks resulting from desiccation (e.g., Yao et al. 2001; Chen et al. 2006; Huang and Wu 2007; Chen et al. 2014; Shi et al. 2014; Qi and Vanapalli 2015) and swelling and softening of the expansive soil induced by water infiltration (e.g., Huang et al. 2014; Ding et al. 2015; Qi and Vanapalli 2016) are regarded as two main contributors to surficial failure of expansive soil slopes. Cracks in the surficial soil layer of a slope will provide preferential flow channels and increase the coefficient of permeability (e.g., Návar et al. 2002; Zhan et al. 2007; Fredlund et al. 2010; Abbaszadeh 2011; Krisnanto et al. 2014; Li et al. 2016) and decrease the shear strength (e.g., Skempton 1964; Blight 1967; Thorne 1984; Yuan and Yin 2004; Lv et al. 2009; Xu et al. 2011; Wu and Yuan 2013; Cheng et al. 2016). Additionally, water-filled cracks may exert an additional driving force on the slope and form a part of the critical slip surface (e.g., Baker 1981; Chowdhury and Zhang 1991; Wang et al. 2012; Utili 2013; Li and Yang 2016). Figure 2.1(a) presents details related to the increase in the in-situ water infiltration rate of the expansive soil slope due to the surficial open cracks (Zhan et al. 2007). Figure 2.1(b) indicates that cracks resulting from drying-wetting cycles would decrease the shear strength of expansive soils derived from the saturated triaxial Consolidated-Undrained tests (Xu et al. 2011). Wu and Yuan (2013) conducted direct shear tests with large undistributed expansive soil samples and found significant decrease in peak shear strength after wetting-drying cycles (Figures 2.1(c)-(f)). Lv et al. (2009) investigated the change in microstructure (i.e. pore size distribution) and unsaturated shear strength (i.e. derived from triaxial Unconsolidated-Undrained tests) of expansive soils upon drying-wetting cycles (Figure 2.2). In summary, the complex failure mechanism of expansive soil slopes triggered by rainfall infiltration is due to the intrinsic characteristics of expansive soils (potential of swelling and shrinkage, abundance of cracks, and over-consolidated nature), and the coupled interaction between surficial soil layer and atmosphere (Bao et al. 2004; Yin and Xu 2011; Zhang et al. 2011; Cheng and Gong 2015).

The Dale Dyke dam failed on 11 March 1864, which led the flood to sweep throughout the City of Sheffield killing 250 people and causing extensive damage to property (Blight 1997). The failure and crest subsidence was initiated by the formation of an erosion pipe through the ruptured

puddle clay core. The hydraulic fracturing in the clay core seems to be linked to an existing desiccation crack running horizontally which was noticed 1.2 m below the crest before the breach. It is widely accepted in the literature that desiccation is one of the possible causes of hydraulic fracturing in earth dams which is related to concentrated leak and initiation of internal erosion (e.g., Fell et al. 2003). Based on the studies related to the stability of flood defense embankments (e.g., Cooling and Marsland 1953; Dyer 2004; Aubeny and Lytton 2004; Zielinski 2009), desiccation cracking was identified as a major contributor to embankment collapse under overflow conditions. Dyer et al. (2009) conducted in-situ double-ring infiltrometer tests on an embankment and found that interconnected cracks contributed to an increase in the coefficient of permeability by three orders. They proposed a failure mechanism of embankments responsible for desiccation-induced cracks (Figure 2.3): (i) interconnected cracks allow rapid preferential water flow into a desiccated zone; (ii) subsequently, excessive internal seepage during overflow conditions leads to hydraulic fracturing and the uplift of the desiccated clay blocks on the inward slope face; and (iii) progressive failure of the inward slope eventually results in a breach.

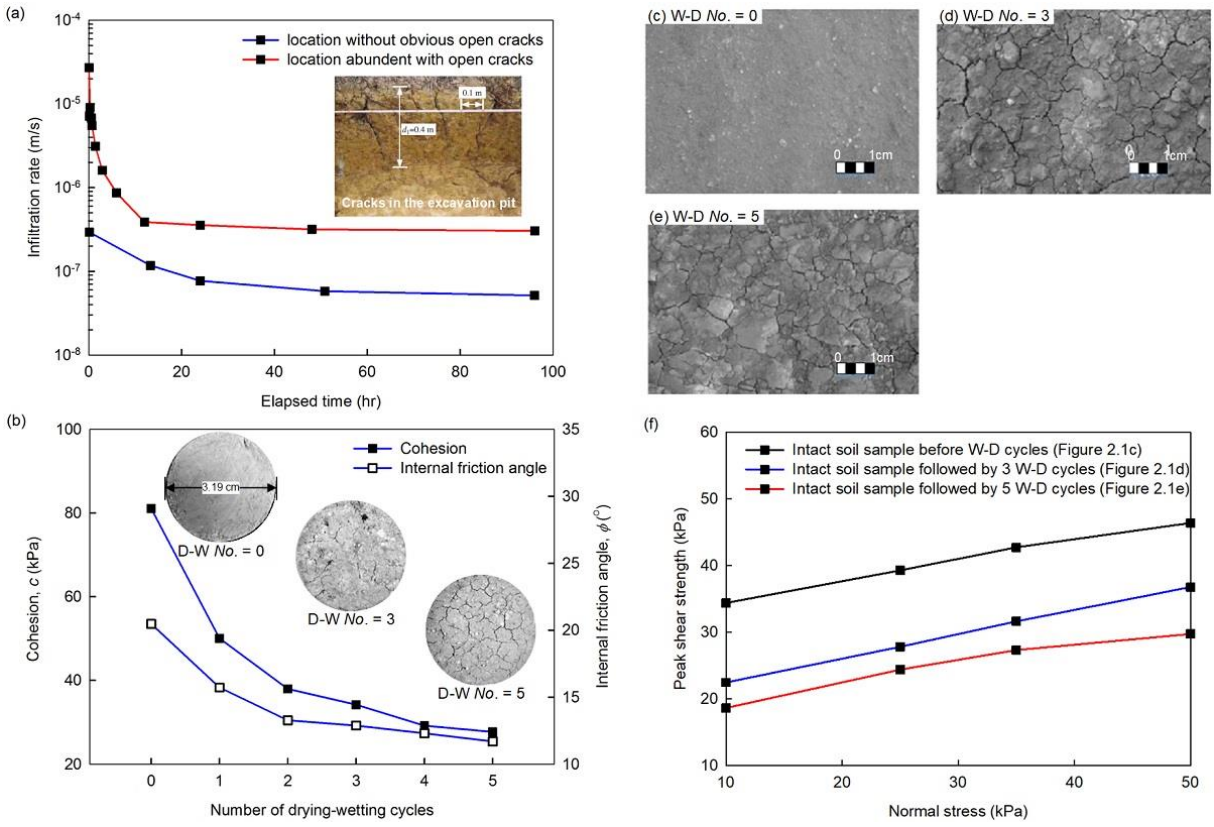

Figure 2.1 (a) In-situ double-ring infiltration test on Zaoyang expansive soil at locations with and without open surficial cracks (modified after Zhan et al. 2007); (b) Crack development along with drying-wetting (D-W) cycles and the corresponding decrease in saturated shear strength parameters of Xinxiang expansive

soil derived from saturated Consolidated-Undrained triaxial test results (modified after Xu et al. 2011); (c), (d), and (e) are the photos of in-situ natural soil samples before wetting-drying (W-D) cycles, after 3 W-D cycles, and after 5 W-D cycles, respectively (modified after Wu and Yuan 2013); (f) Effect of W-D cycles on the peak shear strength of the natural specimens of Xinxiang expansive soil obtained from the in-situ direct shear tests (modified after Wu and Yuan 2013).

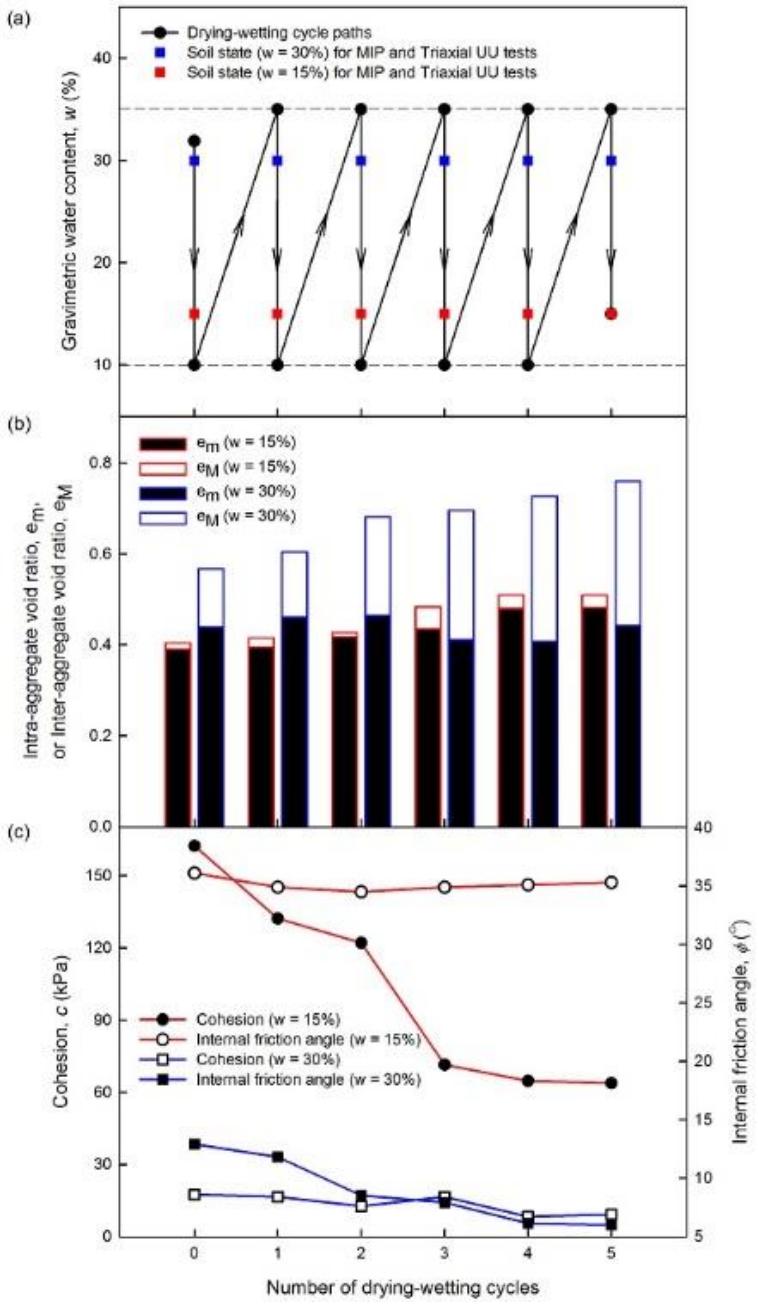

Figure 2.2 Schematic illustration of the effect on the shear strength of Nanning expansive soil of drying-wetting cycles and associated cracks (modified after Lv et al. 2009): (a) cyclic drying-wetting paths and soil states with different gravimetric water contents for MIP tests and Unconsolidated-Undrained (UU) triaxial compression tests; (b) evolution of intra- and inter- aggregate void ratios along with the drying-wetting cycles derived from MIP test results; (c) evolution of cohesion and internal frictional angle along with the drying-wetting cycles derived from the UU triaxial test results.

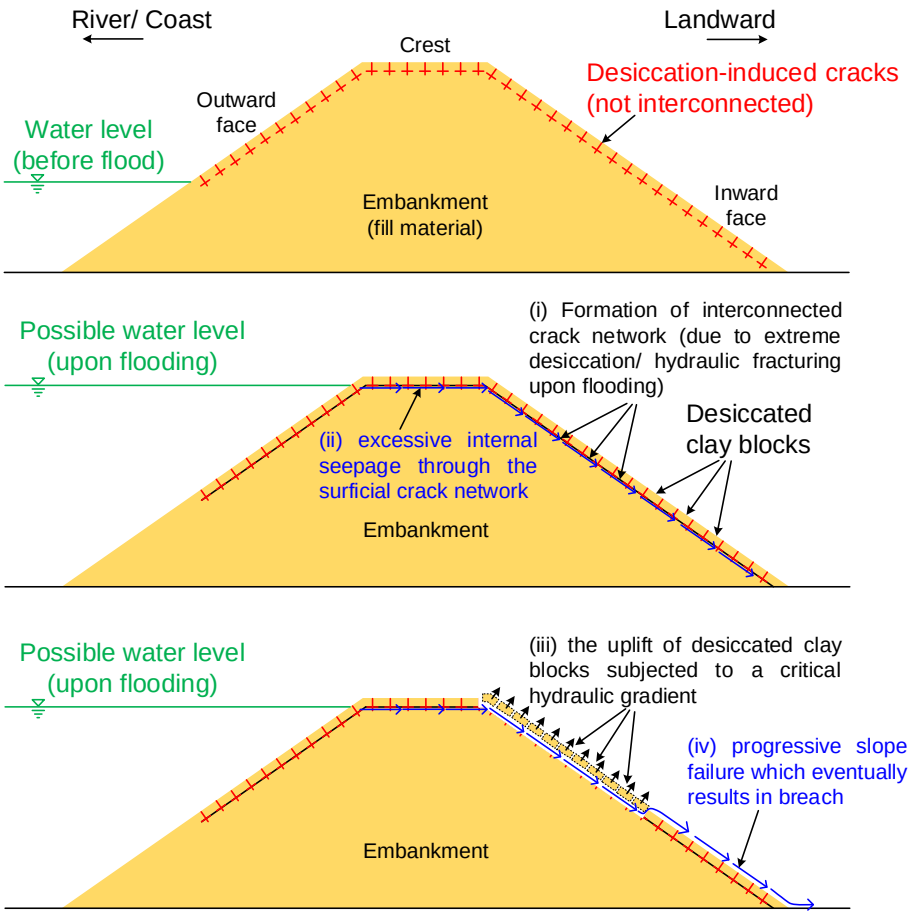

Figure 2.3 Schematic illustration of the failure mechanisms of embankment upon flooding with breach proposed by Dyer et al. (2009).

Desiccation-induced cracking is also of a major concern in engineering barrier systems. Clay (e.g., bentonite) is the most important constituent of geosynthetic liners and covers for hydraulic isolation of hazardous waste landfill, due to the favorable hydraulic properties (i.e. low coefficient of permeability), and large surface area and associated adsorption capacity of contaminants (Gebrenegus et al. 2011; Chen 2016). United States Environmental Protection Agency (USEPA) suggested that the maximum saturated coefficient of permeability should not exceed a value of 10^{-9} m/s for compacted clay liners to ensure protection of the environment (USEPA 1989). However, the presence of desiccation cracks will deteriorate the integrity and significantly increase the coefficient of permeability of landfill liners and covers. Based on the test data collected from the literature (e.g., USEPA 1989; Rayhani et al. 2007; Li et al. 2016; Chen 2016), the saturated and unsaturated coefficient of permeability of soil, and gas emission rate increase by at least one order; in some scenarios it increases by several orders of magnitude, due to the influence of desiccation cracks (Figure 2.4). In addition, Rayhani et al. (2007) found that the effect of drying-wetting cycles

on the cracking potential and the coefficient of permeability in the first cycle were much greater in comparison to the second cycle due to the self-healing upon wetting, which is related to the swelling potential of the soil (Figure 2.4(b)). In order to suppress the formation of desiccation cracks in engineering barrier systems, various techniques have been proposed, which include reinforcement by fibers (e.g., Fodor 1999; Tang et al. 2012; Chaduvula et al. 2017), addition of appropriate chemicals (e.g., Uday and Singh 2013), and microbial-induced calcite precipitation (MICP, e.g., Liu et al. 2020).

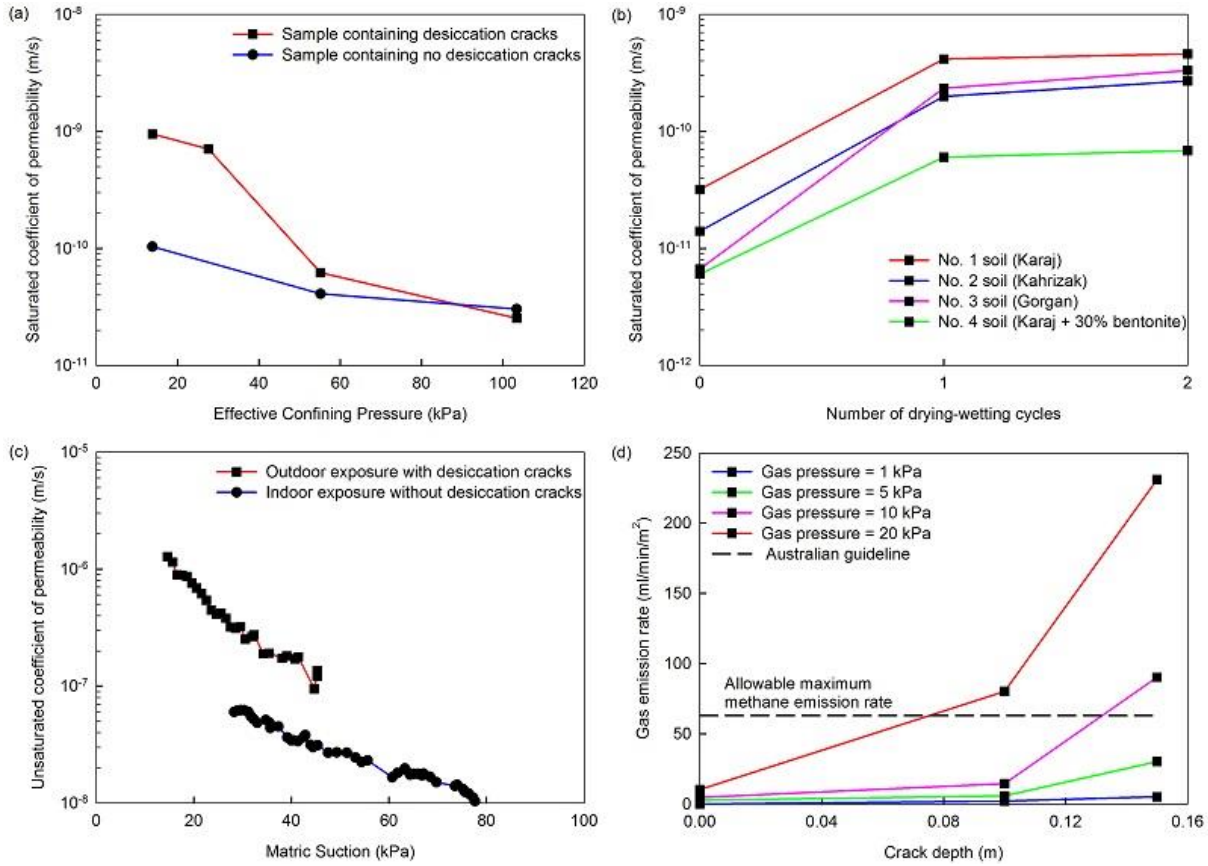

Figure 2.4 Schematic illustration of (a) effect of cracks and confining stress on the saturated hydraulic conductivity of a compacted clay (adapted from USEPA 1989); (b) effect of desiccation cracks on saturated hydraulic conductivity of four compacted soils along with different drying-wetting cycles (adapted from Rayhani et al. 2007); (c) effect of cracks on the unsaturated hydraulic conductivity of a compacted clay column on drying (adapted from Li et al. 2016); (d) effect of crack depth and applied gas pressure on gas emission rate of a 0.4-m-thick compacted soil layer (adapted from Chen 2016).

2.1.2.2 Desiccation-induced cracks in mining and agricultural engineering

The drying technique is widely used as a tool to increase the density and strength of tailings to assist stabilization and reclamation of tailings impoundments (e.g., Morris et al. 1992; Simms 2016). The high evaporation rates upon drying can have a beneficial effect on the behavior of

tailings; thus, an understanding of the evaporation and associated shrinkage and cracking behavior of tailings is important for the management of tailings disposal (Fujiyasu et al. 2000). It was found that the desiccation-induced cracks play a vital role in maintaining high actual evaporation rates in fine-graded tailings (e.g., Innocent-Bernard 2013; Simms et al. 2017). Rodríguez et al. (2006) found that the saturated coefficient of permeability of the tailings pond samples with desiccation cracks is typically one order of magnitude higher than those without cracks and the subsequent wetting following drying does not eliminate the original discontinuities.

Vertisols, which are typically clay-rich soils and known for their high shrinking and swelling characteristics are widely distributed across the world, such as the United States, the Netherlands, Israel, India, Australia, and Africa. The formation of cracks in agricultural soils due to the seasonal wetting-drying cycles, which subsequently increases the coefficient of permeability, poses a challenge for the irrigation management (e.g., Ritchie et al. 1972; Bronswijk 1991; Mitchell and van Genuchten 1993; Chertkov and Ravina 2000; Somasundaram et al. 2018). The preferential flow through soil cracks results in rapid transport of irrigation water, solutes and agrochemicals through the unsaturated zones and consequently reduces irrigation efficiency and leads to ground water contamination (e.g., Weaver et al. 2005; Kazemi et al. 2008; Baer et al. 2009). Therefore, investigation of the crack formation mechanism and the hydrological properties of agricultural soils is the first and useful step to improve and optimize the irrigation management (e.g., Kosmas et al. 1991; Bronswijk et al. 1995; Lin and McInnes 1995; Greve et al. 2010).

2.1.3 Mechanism of crack initiation and propagation induced by desiccation

As the moist soil dries, water retreats from the pores between the soil grains (in coarse-grained soils) or aggregates (in fine-grained soils). This phenomenon results in the invasion of air-water interface into the soil pores and the generation of capillary force at the interfaces (e.g., Fisher 1926; Hotta et al. 1974). The capillary force at a particle-scale tends to pull the soil grains or aggregates closer (Figure 2.5(a)). If the desiccating soil cannot contract freely due to the boundary constraints (e.g., the adhesion and friction between the soil and the container) or to the internal heterogeneity (e.g., defects such as air bubbles, larger pores compared to the surrounding pores), the unbalanced internal stress field out of the initial equilibrium state will be built up. Typically, a single crack initiates along the boundaries or around a defect (e.g., Kodikara and Costa 2013; Wang et al. 2018), due to the nucleation of large drained pores driven by the unbalanced internal stress field (Figure

2.5(a)). Thus, the change in soil microstructure (e.g., pore size distribution), especially the large pores, is strongly related to the shrinkage and crack initiation upon drying (e.g., Haigh et al. 2014). Once the crack initiates, it will rapidly propagate across the soil layer until it hits a boundary, e.g., an existing crack or a defect. Based on the hypothesis of continuum, saturated soils (two-phase porous media) or unsaturated soils (four-phase porous media, e.g., Fredlund and Rahardjo 1993) can be treated as a single-phase medium through the averaging technique. A heterogeneous medium at microscopic scale can be upscaled to be a homogenous medium at macroscopic scale associated with a representative elementary volume (REV) which is relevant for all the physical phenomena involved (Coussy 2010). From a macroscale perspective, soils tend to crack when the generated tensile stresses upon constrained shrinkage exceed the tensile strength (Figure 2.5(b)), based on the rupture criterion of solids, e.g., Griffith's theory of fracture (Griffith 1921). Subsequently, a crack pattern can develop subdividing the soil into blocks of various sizes (Kodikara et al. 1999; Goehring and Morris 2014), which will be discussed in greater detail in the fourth section. In this section, both large-scale field investigations and small-scale laboratory tests from the literature are summarized. Desiccation cracking behavior can be best interpreted from field investigation studies. However, field investigations are expensive, time-consuming and often involve complex, uncontrolled, and sometimes have undefinable boundary mechanical and hydraulic conditions which are obstacles to identify the crack formation mechanisms. Due to this reason, focus of various studies published in the literature are based on laboratory studies to interpret the complex mechanisms associated with desiccation cracking processes.

2.1.3.1 Large-scale field investigations

Various in-situ investigation studies of desiccation-induced cracking of cohesive soils are summarized in Table 2.1. The key findings on crack initiation and propagation induced by desiccation are also included.

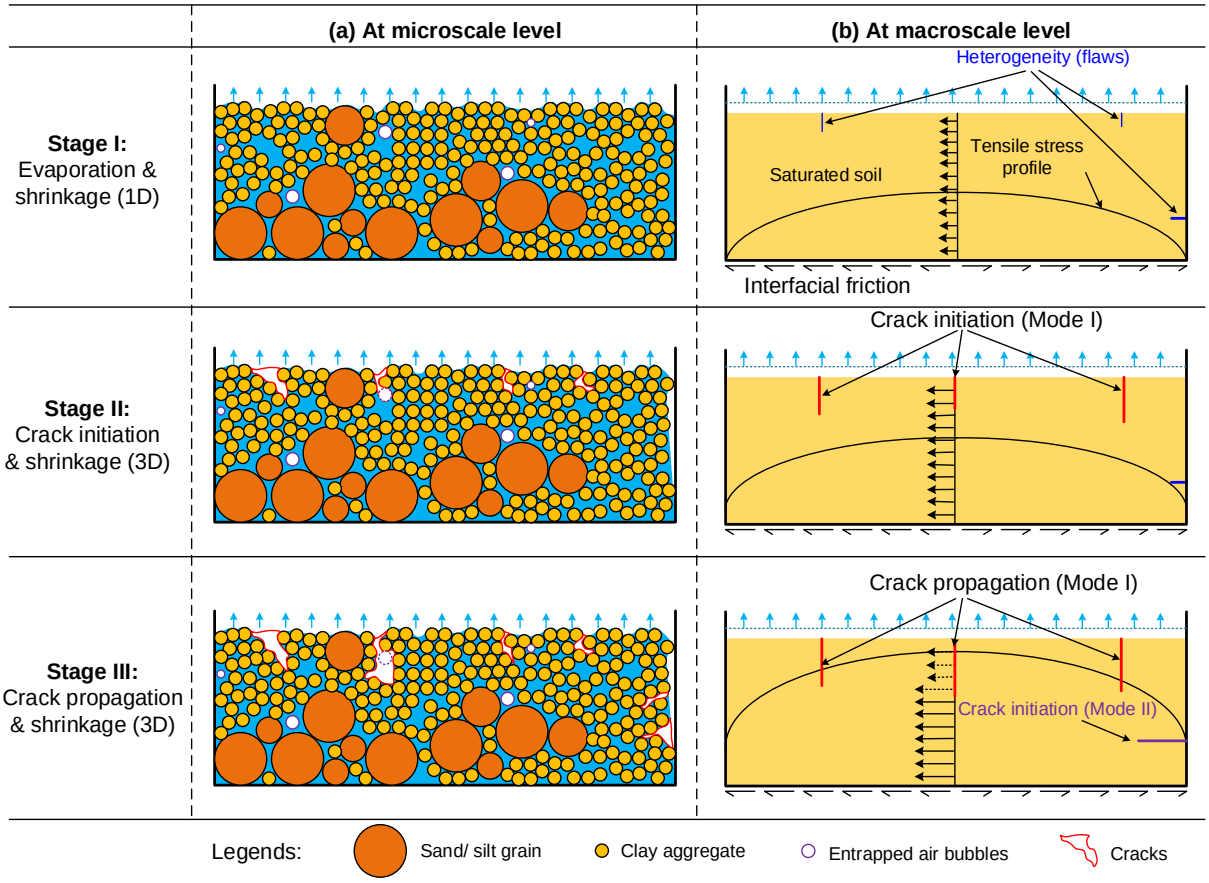

Figure 2.5 Schematic illustration of the initiation and propagation of desiccation cracking of cohesive soils from the aspects of: (a) at microscale level, and (b) at macroscale level. (Note: mode-I crack is the tension-induced crack; mode-II crack is the shear-induced crack.)

Table 2.1 List of several seminal research studies on desiccation cracking from field observations.

Reference	Site details and in-situ measurements	Key observation and conclusions
Konrad and Ayad (1997a)	A field study on St Alban's clay was conducted at Saint-Alban test site near Québec City, Canada. The test site was extensively instrumented to determine moisture content changes, temperature distribution, settlement and suctions with time (Figure 2.6).	• The primary cracks were first observed in the intact clay about 17 hours after the beginning of desiccation. By 22.5 hours after the start of desiccation, a complete network of cracks was observable. • After 96-hour evaporation (when the opening between primary cracks was 5 mm), most of the soil polygons showed new secondary cracks which could be identified by their small opening.
Weinberger (1999)	The well-developed surface morphology of natural mud cracks was studied in dehydrating mud puddles in the Dead Sea region, Israel. Several polygons containing a pair of desiccated layers were lifted out of the dried puddles and their walls were examined under optimal	• In the absence of surface defects, crack origins are consistently located at or near the bottom of the polygons, which strongly suggests that stress concentration at flaw discontinuities and layer boundaries play a fundamental role during mud fracturing. During desiccation, cracks initiated at the bottom and propagated

	oblique illumination (Figure 2.7). Plumose structures were utilized to examine the features of the mud cracks, such as the crack origin location, propagation direction.	vertically upward the free surface and laterally outward toward adjacent cracks. The vertical and lateral terminations of a mud crack occur at an intersection between the crack and the free surface and at an intersection with another crack, respectively.
Philip et al. (2002)	A field test cell was constructed at Heathfield landfill site in England, comprising a 300-mm-thick compacted Abbrook Clay layer with two different slope angles (i.e. sloping square, and flat basal square). Temperature, relative humidity, moisture content profile, and cracking characteristics were monitored during desiccation.	• Cracking initiates rapidly and continue to propagate after an initial moisture loss on the sloping square. Once the crack network had formed, cracks continue to propagate downwards and widen. Stabilization of the surface crack network is thought to occur when the moisture content approaches the shrinkage limit. Very small, shallow, polygons approximately 20 mm-spacing and 2 mm-deep developed at later stages of the test. • Compared with the sloping square, fewer cracks developed on the flat basal square as the horizontal surface would retard the moisture loss.
Li and Zhang (2011)	A field study was conducted to gain insight into the mechanisms of desiccation crack development on a backfilling soil and a residual soil located at the foot of the Huangshan Slope in Zhenjiang, China. Imaging analysis technique was used to measure the crack development in the surface soils (Figure 2.8). The crack porosity, crack aperture, and crack density were measured for each crack network during desiccation.	• Desiccation cracks developed in three stages, namely (i) the initial stage, (ii) the primary stage, and (iii) the steady state stage. In the initial stage, no or few cracks appear and soil water evaporates one-dimensionally and slowly from the soil matrix. In the primary stage, cracks initiated quickly as the water content reached a critical value. Cracking approached a steady state when water content approached the shrinkage limit. • The crack development in small-scale laboratory tests was different from that in the field tests due to boundary effect.
Cordero et al. (2016)	The field test was designed and installed in the Agropolis open research laboratory field of Technical University of Catalonia, Spain, to analyze the characteristics of desiccation-induced cracking. A large square container (i.e. 3 m by 3 m and 0.5 m height) filled with a reconstituted silty clay specimen was exposed to open atmosphere conditions. The time evolution of the main physical variables including meteorological data and internal variables in the soil, like suction, water content, temperature and heat flux, are automatically recorded by external and internal sensors.	• The preliminary results corresponding to a 160-day test suggest a global desiccation of the soil mass and subsequent cracking, which is consistent with the Mediterranean climate in Barcelona, i.e. water was always lost unless some precipitation occurred. The weight loss of water is almost linear at the beginning, but then slow down when cracks develop (i.e. crack initiation water content was about 35% with initial water content as 45% which equals to 1.5 times the liquid limit). Small rainfall events have not changed significantly that global tendency of weight loss.

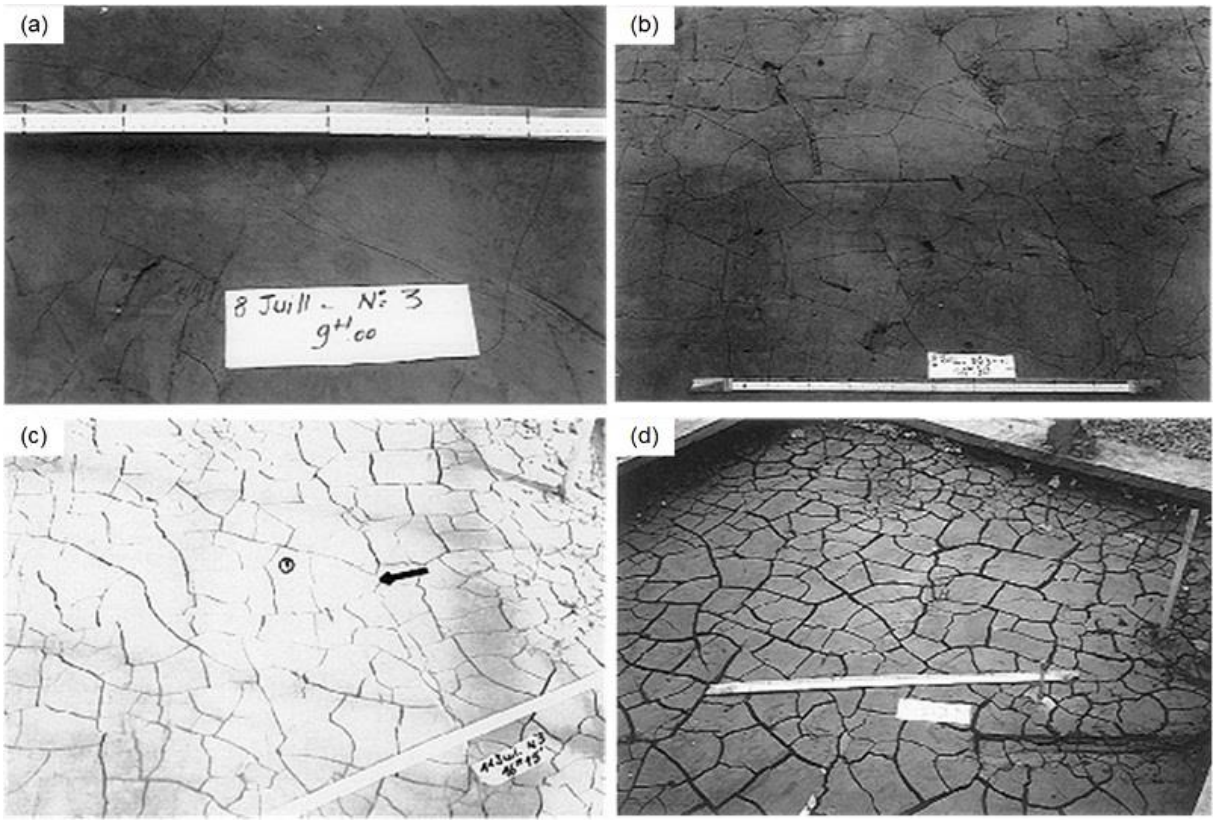

Figure 2.6 The evolution of crack patterns with time: (a) after 17 h of evaporation at which primary cracks initiate, (b) after 22.5 h of evaporation, (c) after 96 h of evaporation at which secondary cracks initiate, and (d) after 192 h of evaporation (adapted from Konrad and Ayad 1997a).

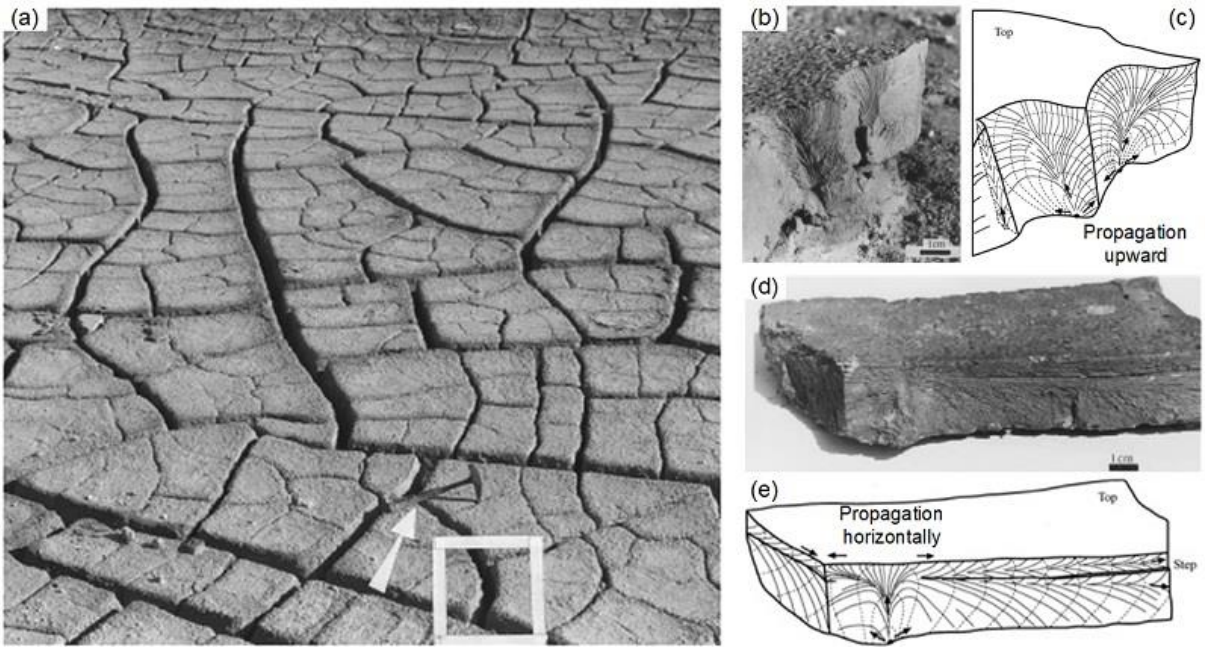

Figure 2.7 (a) Field investigation of mud cracks forming in a muddy sediment at the foot of Massada, Dead Sea region, Israel; (b) Oblique view of two adjacent cracks and (c) Their surface-morphology referred as type 1 plumose structure which shows no relation to layering; (d) Oblique view of a recovered polygon and

(e) Surface-morphology interpretation of an associated bounded crack referred as type 2 plumose structure which has an asymmetric plumose structure about a curved plume axis (adapted from Weinberger 1999).

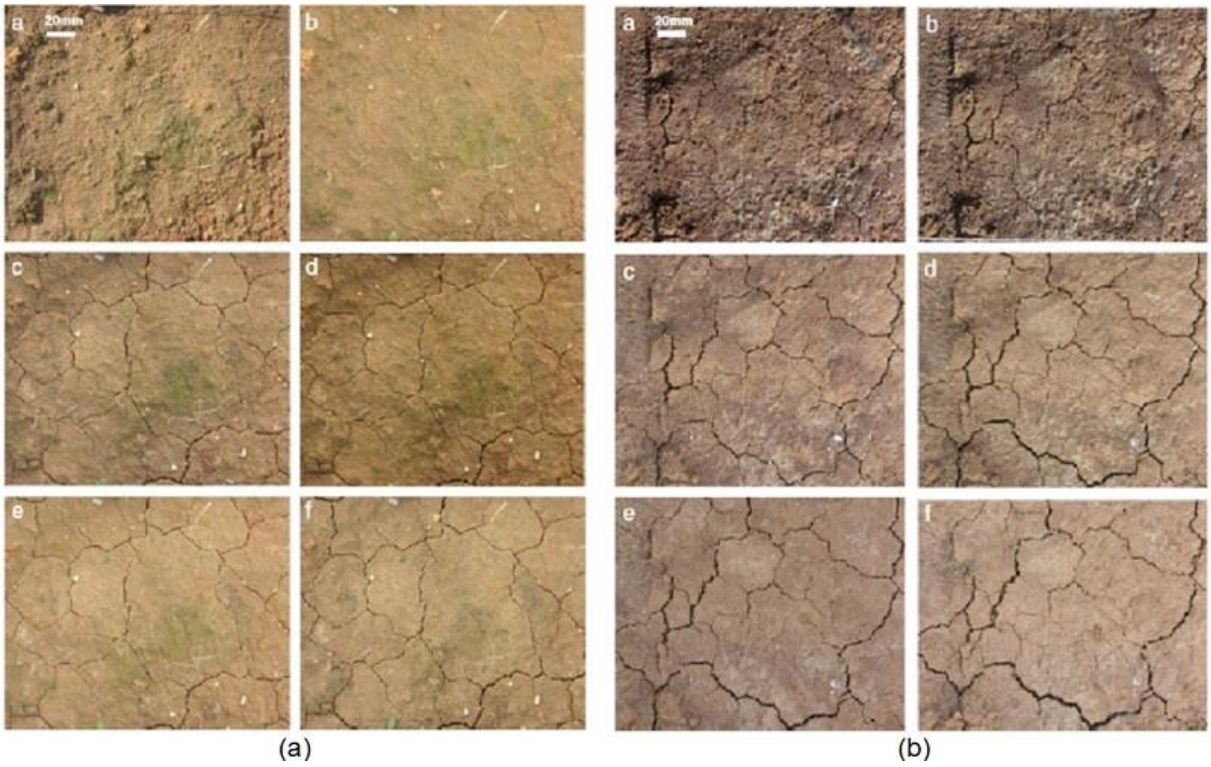

Figure 2.8 (a) Crack development on the backfilling soil ground during a drying process from 1 day to 11 days after rain at test site 1; (b) Crack development on the residual soil ground during a drying process from 1 day to 11 days after rain at test site 2 (adapted from Li and Zhang 2011).

2.1.3.2 Small-scale laboratory experiments

Desiccation-induced cracks in cohesive soils have been of interest in the literature dating back to the 1910s (e.g., Kindle 1917). The laboratory tests in the literature are classified into three categories according to the mould shape, namely (i) rectangular mould and long mould test, (ii) circular mould test, (iii) restrained ring test. Figure 2.9 presents the setup of several representative studies on desiccation cracking. Table 2.2 and Table 2.3 summarize the details of laboratory desiccation cracking tests on 21 different soils by rectangular, or long, or circular containers.

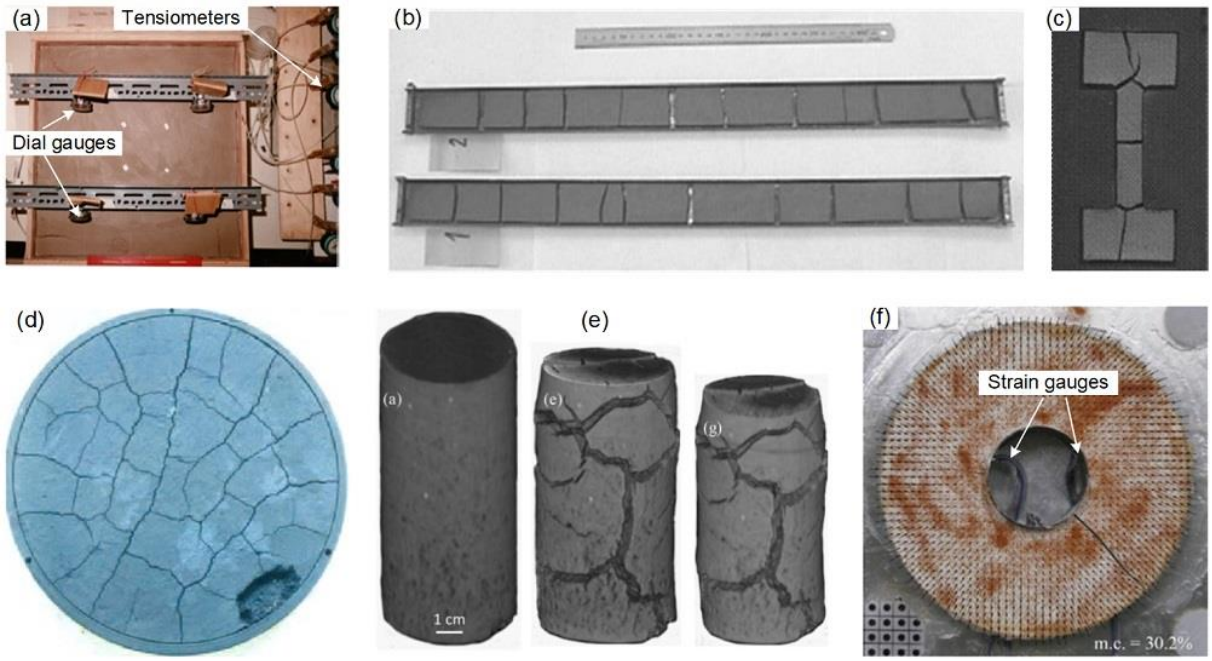

Figure 2.9 Desiccation cracking tests by different shaped moulds: (a) rectangular mould test (adapted from Lau 1987); (b) long mould test (adapted from Nahlawi and Kodikara 2006); (c) double-T shaped mould test (adapted from Ávila 2005); (d) circular mould test (adapted from Rodríguez 2006); (e) Three-dimensional reconstruction of a compacted cylinder-shaped clay specimen during desiccation based on X-ray computed tomography (XCT) observation (adapted from Tang et al. 2019); (f) restraint ring test with surficial strain field interpreted by Particle Image Velocimetry (PVI) technique (adapted from Shannon et al. 2014).

(1) Crack initiation criterion

The crack initiation criterion in desiccating soils is one of the key issues that need to be resolved. The cracking moisture content has been studied for the past five decades because the cracking moisture content is easier to monitor in comparison to stress state variables (e.g., Corte and Higashi 1964; Ávila et al. 2005). Figure 2.10(a) shows the change in water content prior to crack initiation for 17 of the 21 soils investigated in this study, including the initial water contents (w_i) and the corresponding crack water contents (w_c). A quick conclusion that can be drawn from Figure 2.10(a) is that the crack water content is not an intrinsic soil property, such as the liquid limit. The crack water content depends not only on the soil stress-strain response upon desiccation but also on the initial and boundary conditions, such as initial water content, interaction between soils and test containers and desiccation rate. From close examination of summarized results in Figure 2.10(a), it can be derived that the crack water content is independent on the initial water content, which is consistent with the conclusion by Towner (1987). The crack water content is strongly correlated to the liquid limit for the reconstituted soil specimens which were prepared at higher initial water contents than their

liquid limits (Figure 2.10(b)). The reason is that liquid limit is related to the saturated water content, and the crack initiation upon drying tend to occur once the transformation from the saturated to unsaturated state takes place. Moreover, the soil-water characteristic curve (SWCC) and the soil shrinkage characteristic curve (SSCC), which indicate the transformation process, have been intensively used as tools to interpret the hydromechanical responses of soils upon desiccation and cracking (e.g., Corte and Higashi 1964; Rodríguez 2006; Péron et al. 2009a; Trabelsi et al. 2012; Wei et al. 2016). The conclusion that can be derived from these studies is that crack initiation induced by desiccation takes place in saturated or quasi-saturated conditions, which means the degree of saturation is close to unity and the matric suction approximately equals air-entry value at crack initiation at a macroscale level. The discrepancies in some thin reconstituted soil specimens from above conclusion can be attributed to the difference in the two factors compared to the SWCC or SSCC measurements: (i) external boundary conditions, desiccation cracking tests may have different boundary constraints from the test container and environmental conditions; and (ii) initial soil states, the soil specimens subjected to desiccation cracking tests may have different initial states (e.g., water content, dry density, and soil structure).

In recent studies, in addition to water content the variations of matric suction and strain accompanied with desiccation cracking processes are monitored via tensiometers and image techniques, respectively (e.g., Lakshmikantha 2009; Wei et al. 2016). These studies were valuable to interpret the desiccation-induced crack initiation in a more rigorous way, e.g., extending the unsaturated soil mechanics (e.g., Fredlund and Rahardjo 1993). The maximum tensile stress criterion (or Rankine theory) is widely accepted by most researchers to explain the desiccation-induced soil crack initiation, which simulates the experimental studies on the tensile strength of unsaturated soils in the recent two decades (e.g., Tang and Graham 2000; Thusyanthan et al. 2007; Lu et al. 2009; Tang et al. 2014; Stirling et al. 2015; Trabelsi et al. 2018b; Murray and Tarantino 2019). The historical development of prediction models for the tensile strength of unsaturated cohesionless soils and that of compacted clays, taking account of the influence of matric suction were comprehensively reviewed by Yin and Vanapalli (2018a) and Yin and Vanapalli (2018b), respectively. For example, Yin and Vanapalli (2018a) proposed and validated a semi-empirical model for predicting the tensile strength of unsaturated cohesionless soils, including the contributions both from the matric suction and

from the air-water interfacial tension. For unsaturated cohesive soils, the effect of soil microstructure on tensile strength and desiccation cracking behavior has been investigated more recently (e.g., Trabelsi et al. 2018b; Cheng et al. 2020a). Only limited number of studies focus on the desiccation cracking behavior of compacted soil specimens compared to that of the reconstituted soil specimens in the literature (Kleppe and Olson 1985; Nahlawi and Kodikara 2006; Elghezal et al. 2015; Julina and Thyagaraj 2018, 2019; Cheng et al. 2019). Additionally, the influence of pore fluid and environment temperature on the crack initiation (e.g., Kindle 1917; Péron et al. 2007; Tang et al. 2010) can be explained by the changes in the tensile strength of unsaturated soils due to different pore fluids and temperature.

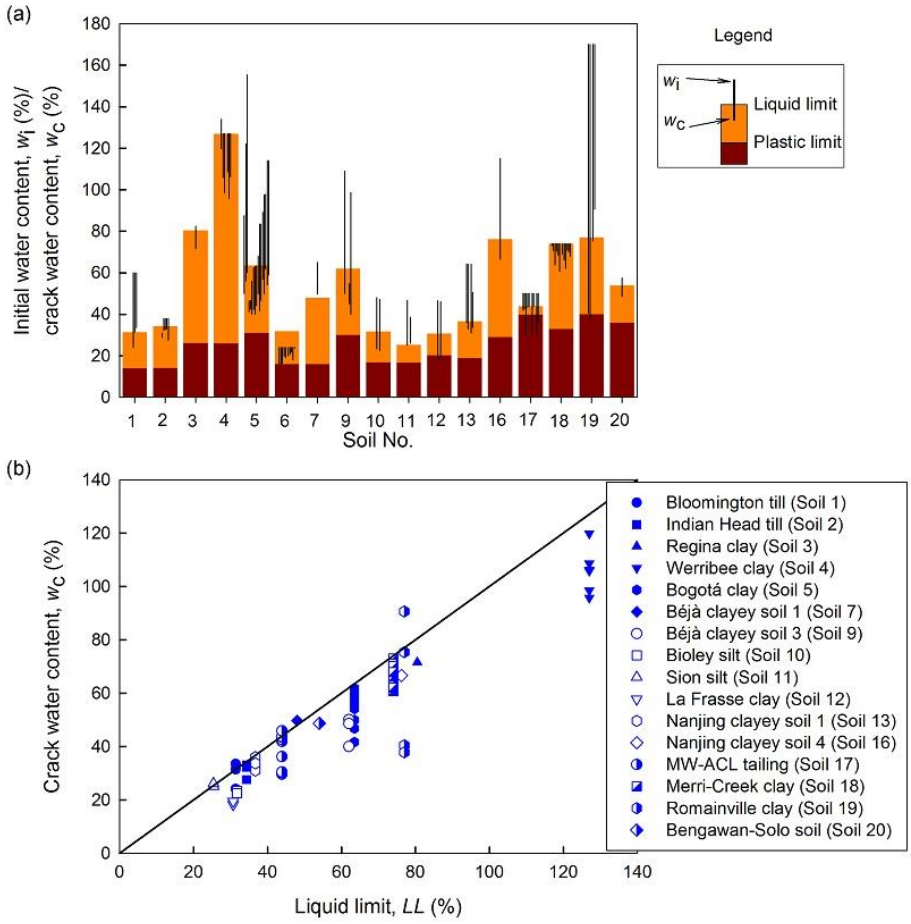

Figure 2.10 (a) Initial water contents and the corresponding crack water contents of 17 soils (Table 2.2) subjected to desiccation cracking tests with initially reconstituted state; (b) Crack water contents of reconstituted specimens which have initial water contents no lower than its liquid limit.

The prediction of the initiation points and orientation of desiccation-induced cracks is complex due to multiple factors that influence the crack formation processes. The process of soil crack initiation in the constrained desiccation test is essentially an initial and boundary

value problem. For example, the effect of mould shape on desiccation-induced cracking behavior was investigated by Ávila et al. (2005, 2013). They proposed a conceptual model based on mould shape factor (i.e. length to width ratio), initial moisture content and evaporation rate to predict crack initiation time and identify the location and direction of primary and secondary cracks. For the desiccation tests using the long mould, crack initiation can be predicted extending analytical method based on the hypothesis that one-dimensional shrinkage takes place prior to crack initiation (e.g., Kodikara and Choi 2006). Costa et al. (2013) postulated that desiccation-induced soil cracking is controlled by two factors, namely (i) the deterministic control which arises from the tensile stress distribution generated as a result of the constrained shrinkage, and (ii) the stochastic control which comes from the randomly distributed flaws, e.g., relatively large pores or foreign matters (e.g., Corte and Higashi 1964; Lau 1987) and entrapped air bubbles (e.g., Lau 1987; Péron et al. 2009a; Shin and Santamarina 2011). The latter factor provides insights into the mechanism for the cracks which do not initiate from the locations with the maximum tensile stress (Figure 2.5(b)), such as from inside or the bottom the specimen (e.g., Corte and Higashi 1964; Lakshmikantha et al. 2013b).

(2) Crack propagation

Once a desiccation crack initiates in a fine-grained soil, it tends to propagate and dissipate the accumulated strain energy surrounding the existing crack tip. In addition to the crack initiation, the soil crack propagation in desiccation cracking tests that are summarized in Table 2.2 and Table 2.3 can be interpreted extending fracture mechanics taking into account the soil heterogeneity. The soil crack after initiation propagates rapidly and reaches a stabilized state (Tang et al. 2010). For example, soil 20 in Table 2.2 reached the maximum depth and two thirds of the final aperture in a short period (around one hour) after crack initiation (Sánchez et al. 2013). Moreover, Corte and Higashi (1964) concluded that crack propagation speed in the drying soil (i.e. soil 1 in Table 2.2) was lower than that in solid materials. Such a behavior may be associated with the driving source, i.e. the desiccation-induced potential shrinkage strain energy, which is relatively lower at the initial stage of the soft soil cracking than mechanical load induced strain energy in the conventional scenario for solid materials. The crack propagation speed was also found to decrease if the soil layer thickness increased. Recently, Zeng et al. (2019) investigated the influence of interface friction and soil layer

thickness on the soil crack propagation behavior. The propagation velocity of soil cracks was found to be higher along with increase in interface roughness between soil and the container bottom. It can be explained by more strain energy accumulated prior to crack formation during the more strictly constrained shrinkage with larger interface roughness. The influence of interface friction on soil cracking decreases with an increase in the soil layer thickness.

Typically, cracks in soils propagate laterally and downward from the surface initiation point in straight lines which is perpendicular to tensile stresses from the fracture mechanics point of view (i.e. model I cracks). Based on the principle of linear elastic fracture mechanics (Griffith 1921; Irwin 1948), the crack propagation is governed by the interaction between the local fracture energy (or fracture toughness) at the existing crack tip and the available strain energy developed through the stress buildup upon desiccation (e.g., Lachenbruch 1961; Morris et al. 1992; Konrad and Ayad 1997b; Blight 1997; Lakshmikantha et al. 2012). More recently, the restrained ring test (RTT, Figure 2.9(f)) has been developed by Monash University geotechnical research group (e.g., Costa and Kodikara 2012; Shannon 2013; Shannon et al. 2014; Costa et al. 2015) to experimentally determine the parameter, *J* integral extending elastoplastic fracture mechanics. Compared with the linear elastic fracture mechanics, the *J* integral first introduced by Rice (1968) is calculated as the summation of four line integral along a rectangular loop around the crack based on the material plasticity at crack tip. Additionally, the heterogeneity induced by the internal soil structure, or pore water distribution, or local stress concentration resulting from the external constraints (e.g., the interaction between soil and the container) would deviate the direction of crack propagation from straight lines. For example, Wei et al. (2016) found that the propagation direction may change from perpendicular direction to soil extension to that coincides with the maximum principal strain ahead of the crack tip if shear strains are encountered within the vicinity of the propagating crack.

Table 2.2 Physical properties of the studied soils for desiccation cracking tests extracted from the literature.

No.	Reference	Soil name	Location	Specific gravity, G_s	Grain size distribution			Atterberg's limits				USCS	Dominate clay minerals	Proctor standard characteristics
					Sand size fraction (%)	Silt size fraction (%)	Clay size fraction (%)	Liquid limit (%)	Plastic limit (%)	Plasticity index (%)	Shrinkage limit (%)			
1	Corte and Higashi (1964)	Bloomington till	Illinois, US	2.63	28.9	67.6	3.5	31.4	13.9	17.5	12.0	CL	N/A	N/A
2	Lau (1987)	Indian Head till	Saskatchewan, Canada	N/A	37.5	34.0	28.5	34.3	14.2	20.1	14.0	CL	N/A	N/A
3	Lau (1987)	Regina clay	Saskatchewan, Canada	N/A	0	27.0	73.0	80.5	26.2	54.3	22.0	CH	N/A	N/A
4	Nahlawi and Kodikara (2006); Costa and Kodikara (2009); Costa et al. (2013)	Werribee clay	Melbourne, Australia	2.66	N/A	N/A	62.0	127.0	26.0	101.0	22.0	CH	Ca-Smectite; illite; kaolinite	OMC = 27.5; MDD = 1420
5	Ávila et al. (2005, 2013)	Bogotá clay	Bogotá, Colombia	2.60-2.70	4.0-5.0	33.0-34.0	61.0-63.0	62.0-65.0	28.0-32.0	30.0-35.0	13.0-23.0	CH	Kaolinite; smectite; illite	N/A
6	Lakshmikantha et al. (2006, 2009, 2012, 2013a, 2013b), Levatti et al. (2017);	Barcelona silty clay	Barcelona, Spain	2.71	46.8	44.6	8.6	32.0	16.0	16.0	N/A	CL	Illite	OMC = 13.0; MDD = 1890

	Ledesma et al. (2018)													
7	Trabelsi et al. (2012)	Béjà clayey soil 1	Beja, Tunisia	2.70	10.8	57.1	32.1	48.0	16.0	32.0	13.0	CL	Illite; semectite	N/A
8	Elghezal et al. (2015)	Béjà clayey soil 2	Beja, Tunisia	2.70	8.9	58.9	32.2	58.0	26.0	32.0	14.0	CH	Illite; semectite	OMC = 18.0; MDD = 1500
9	Trabelsi et al. (2018a)	Béjà clayey soil 3	Beja, Tunisia	2.70	3.0	79.0	18.0	62.0	30.0	32.0	15.0	CH	Illite; semectite	OMC = 23.0; MDD = 1520
10	Péron et al. (2007; 2009a)	Bioley silt	Switzerland	2.76	1.2	73.8	25.0	31.8	16.9	14.9	20.5-22.5	CL	Illite; chlorite; Smectite	N/A
11	Péron et al. (2007; 2009a)	Sion silt	Switzerland	2.79	9.7	80.3	10.0	25.4	16.7	8.7	>24.0	CL	Illite; chlorite; smectite	N/A
12	Péron et al. (2007; 2009a)	La Frasse clay	Switzerland	2.73	21.2	49.8	29.0	30.7	20.3	10.4	<16.5	CL	N/A	N/A
13	Tang et al. (2008); Tang et al. (2018); Zeng et al. (2019)	Nanjing clayey soil 1	Jiangsu, China	2.73	2.0	76.0	22.0	36.7	18.9	17.8	N/A	CL	N/A	OMC = 16.0; MDD = 1710
14	Tang et al. (2008)	Nanjing clayey soil 2	Jiangsu, China	2.70	4.0	67.0	29.0	34.5	22.7	11.8	N/A	CL	N/A	OMC = 16.5; MDD = 1700

15	Tang et al. (2008)	Nanjing clayey soil 3	Jiangsu, China	2.62	2.0	48.0	50.0	52.6	32.9	19.7	N/A	CL	N/A	OMC = 16.3; MDD = 1750
16	Wang et al. (2018); Tang et al. (2019)	Nanjing clayey soil 4	Jiangsu, China	2.71	24.0	34.0	42.0	76.2	29.1	47.1	N/A	CH	Montmorillonite; illite; kaolinite	OMC = 18.3; MDD = 1690
17	Lloret et al. (1998); Rodríguez (2006)	MW-ACL tailing	Holguín, Cuba	3.97	7.5	76.8	15.7	43.9	39.9	4.0	N/A	ML	No clay minerals	N/A
18	Costa and Kodikara (2007); Costa et al. (2008); Costa et al. (2013)	Merri-Creek clay	Melbourne, Australia	2.62	N/A	N/A	N/A	74.0	33.0	41.0	13.0	CH	Smectite; kaolinite	OMC = 26.0; MDD = 1360
19	Tang et al. (2010); Tang et al. (2011a); Tang et al. (2011b)	Romainville clay	Paris, France	2.79	N/A	N/A	79.0	77.0	40.0	37.0	12.0	CH	Illite; smectite	N/A
20	Sánchez et al. (2013); Antique (2013); Zielinski et al. (2014)	Bengawan-Solo soil	Surabaya, Indonesia	2.73	30.0	57.0	13.0	54.0	36.0	18.0	24.2	MH	Montmorillonite (88%); kaolinite (12%)	OMC = 28; MDD = 1470

21	Julina and Thyagaraj (2018; 2019)	Kishkinta expansive soil	Tamil Nadu, India	2.71	3.0	15.0	82.0	78.0	27.0	51.0	9.0	CH	N/A	OMC = 28.0; MDD = 1340

Note: USCS, Unified Soil Classification System (ASTM D2487-17, ASTM International 2017); N/A: information is not available in the cited studies; OMC: optimum moisture content (%); MDD: maximum dry density (kg/m^3).

Table 2.3 Summarized information on the initial states of studied soils, the boundary conditions and the environmental conditions for desiccation cracking tests.

No.	Soil name	Initial soil states	Initial soil thickness	Container		Environmental conditions	
				Shape and size	Bottom substrate	Drying/ drying-wetting cycles	Temperature and humidity
1	Blooming ton till	Reconstituted (w = 60%, ρ_d = 1.8 g/cm^3)/ loosely compacted (ρ_d = 1.5 g/cm^3)	0~50 mm (after complete drying)	Rectangular (600 mm by 840 mm/ 870mm by 1220 mm)	Wooden (plain/ greased) container with 20-mm thick sand layer on the bottom/ glass container	Drying	Air-dry, room temperature (original: 22 °C/ cold: 5 °C), humidity (regular: 30-40%; special plastic tent: 90%/ cold: 70%)
2	Indian Head till	Reconstituted (w = 31%, 38%, LL = 34.3%)	30~60 mm	Rectangular (610 mm by 610 mm)	Wooden	Drying	Air-dry, room temperature (23~25 °C) and humidity (25%-30%)
3	Regina clay	Reconstituted (w = 82.5%, LL = 80.5%)	60 mm	Rectangular (610 mm by 610 mm)	Wooden	Drying	Air-dry, room temperature (23~25 °C) and humidity (25%-30%)
4	Werribee clay	Reconstituted (w = 127% (close to LL); ρ_d = 0.54-0.62 g/cm^3)/ compacted	5~30 mm	Semi-cylindrical (25/ 50 mm by 250/ 600 mm)	Perspex/ metal	Drying	A humidity chamber for reconstituted specimens (temperature= 23 C; humidity=20-40%), and controlled room for compacted specimens (temperature= 23 °C; humidity= 50%)

		(w=32.5%; ρ_d = 1.32-1.56 g/cm^3)					
		Reconstituted (w = 127%)	3 mm	Rectangular (80 mm by 80 mm)	Glass	Drying	Air-dry, reasonably constant temperature (50 °C) and humidity (20%), at varying lamp distance (350/500/750 mm)
5	Bogotá clay	Reconstituted at various water content (w = 40%-160%)	5/ 10 mm (rectangular mould); 2/ 5 mm (double-T shape mould)	Rectangular (200 mm by 200 mm)/ double-T shaped (35 mm by 80 mm)/ micro double-T shaped (10 mm by 22 mm)	Perspex	Drying	Air-dry
6	Barcelona silty clay	Reconstituted (w=26%/24.5% for rectangular/ w=30% for circular)	10/ 15/ 20 mm (rectangular); 4/8/16 mm (circular)	Rectangular (geometrically similar with aspect ratio 1.5 and increasing surface area from 350 cm^2 to 1450 cm^2, and from 0.0625 m^2 to 1 m^2)/ circular (225 mm diameter)	PVC plastic tray with different roughness of the base (smooth, circular grooved, and with a square grid pattern)	Drying	An environment-controlled room (temperature=21±5 °C; humidity=52±2%)
		Reconstituted (w=30%)	200/ 100/ 50 mm	Circular (800/400/200 mm diameter)	PVC plastic tray with a grooved bottom surface	Drying	Different combinations of temperature and humidity were imposed by an environmental chamber
		Reconstituted	100 mm	Circular (800 mm diameter)	PVC plastic	Drying/ Drying-Wetting-Flooding-Drying-Wetting	Drying in the laboratory-controlled environment (temperature= 24 °C; humidity= 60%)/ cyclic tests with temperature and humidity cycles in an environmental chamber

7	Béjà clayey soil 1	Reconstituted (*w* = 65%)	5 mm	Circular (100 mm diameter)	Recipient with a frictional bottom	Drying	Air-dry in controlled climate conditions (temperature = 40 °C; humidity = 60%)
8	Béjà clayey soil 2	Compacted (*w* = 13%/ 26%)	5 mm	Rectangular (100mm by 100mm)	Glass	Drying	A climatic enclosure with controlled relative humidity and temperature
9	Béjà clayey soil 3	Reconstituted (*w* = 65%)	10/ 80/ 140/ 190 mm	Circular (80 mm diameter)	Glass	Drying	Air-dry in controlled climate conditions (temperature = 35±1 °C; humidity = 60±5 %)
10	Bioley silt	Reconstituted (*w* = 48%)	12/ 4 mm	Rectangular; 295 mm by 49 mm/ 300 mm by 300 mm	Aluminium mould with/ without notched metallic surface	Drying	A climate chamber with controlled temperature (19±1 °C) and humidity (40%)
11	Sion silt	Reconstituted (*w* = 1.5×liquid limit)	12 mm	Rectangular; 295 mm by 49 mm	Aluminium mould with notched metallic surface	Drying	A climate chamber with controlled temperature (19±1 °C) and humidity (40%)
12	La Frasse clay	Reconstituted (*w* = 1.5×liquid limit)	12 mm	Rectangular; 295 mm by 49 mm	Aluminium mould with notched metallic surface	Drying	A climate chamber with controlled temperature (19±1 °C) and humidity (40%)
13	Nanjing clay 1	Reconstituted (*w* = 90%)	5/ 8/ 11 mm	Rectangular (160mm by 160mm)	Glass	Drying-wetting cycles	Oven-dry under different temperatures (30/40/50 °C) and wetting by adding sufficient water
		Reconstituted (*w* = 50.5%)	20 mm	Rectangular (30 mm by 290 mm)	Plexiglass	Drying	An air-conditioned room
		Reconstituted (*w* = 64.1%)	5/ 10/ 15 mm	Rectangular (200 mm by 200 mm)	Glass container with standard sandpaper or	Drying	Air-dry under room temperature (30±1.5 °C)

					grease treated bottom		
14	Nanjing clay 2	Reconstituted (w = 90%)	5/ 8/ 11 mm	Rectangular (160mm by 160mm)	Glass	Drying-wetting cycles	Oven-dry under different temperatures (30/40/50 °C) and wetting by adding sufficient water
15	Nanjing clay 3	Reconstituted (w = 90%)	5/ 8/ 11 mm	Rectangular (160mm by 160mm)	Glass	Drying-wetting cycles	Oven-dry under different temperatures (30/40/50 °C) and wetting by adding sufficient water
16	Nanjing clay 4	Reconstituted (w = 15%)	8 mm	Circular (117 mm diameter)	Glass	Drying	Air-dry under laboratory conditions (temperature = 25±0.5 °C, humidity = 50±3%)
		Statically compacted (w = 25%, ρ_d = 1.3 g/cm^3) and saturated (w = 42.5%)	100 mm	Cylindrical (50 mm diameter)	------	Drying	Oven-dry at a constant temperature (30 °C)
17	MW-ACL tailing	Reconstituted (w = 50%)	40/ 4/ 8/ 16 mm	Circular (250 mm diameter)	Plate with smooth bottom/ plate with a 1.5-mm-depth grooved bottom	Drying	Open laboratory atmosphere (22 °C and 60%)/ Hermetic container condition with different imposed humidity (97.8%/ 75%/ 15.6%)
18	Merri-Creek clay	Reconstituted (w = 74%)	3/ 5/ 10/ 20 mm	Circular (140 mm diameter)	Glass	Drying	Air-dry, reasonably constant temperature (50 °C) and humidity (20%), at varying lamp distance (350/500/750 mm)
19	Romainville clay	Reconstituted (w = 170%)	10/ 8 mm	Circular (117 mm diameter)	Glass	Drying-Wetting cycles	Air-dry in constant room conditions (temperature = 22±1 °C; humidity = 55±5%) or (temperature = 25±1 °C; humidity = 50±5%); oven-dry conditions (temperature = 60 °C; humidity = 5±2%) or (temperature = 105 °C; humidity = 0%)

20	Bengawan-Solo soil	Reconstituted (w = 56.0%-57.0%)	10/ 20 mm	Rectangular (175 mm by 175 mm/ 295 mm by 95 mm)	Perspex with grooved bottom	Drying	Air-dry with controlled environment (temperature = 20.0 °C; humidity = 28%-36%)
		Reconstituted (w = 56.0%-57.0%)	5/ 10/ 20 mm	Circular (125 mm diameter)	Perspex with grooved or smooth bottom	Drying	Air-dry with controlled environment (temperature = 20.0 °C; humidity = 28%-36%)
		Reconstituted (w = 57.7%)	13 mm	Circular (97 mm diameter)	Glass	Drying	Air-dry with controlled environment (temperature = 19.5±0.3 °C; humidity = 37±4%)
21	Kishkinta expansive soil	Compacted (w = 28%, ρ_d = 1.34 g/cm^3)	20 mm	Circular (75 mm diameter)	Modified oedometer with filter paper on the bottom base	Wetting-drying cycles	Cyclic swell-shrink in the modified oedometer assemblies with the overburden stress (12.5 kPa) under constant temperature (45±2 °C)

Note: w: gravimetric water content, ρ_d: dry density.

2.1.4 Characteristics of crack patterns induced by desiccation

Tang et al. (2008; 2011b) identified three distinct stages on the basis of the laboratory observation of desiccation cracking tests on four clayey soils (i.e. soils 13, 14, 15, and 19 in Table 2.2), i.e. (i) initiation of primary cracks and formation of main-aggregates, (ii) initiation of sub-cracks (or secondary cracks) which split main-aggregates to several sub-aggregates, and (iii) relative stable stage without new cracks initiating and all aggregate size stabilizes, which was confirmed by several field observation (e.g., Konrad and Ayad 1997a; Li and Zhang 2011). Typically, a complex three-dimensional crack network forms at the steady stage under the given environmental conditions.

2.1.4.1 Large-scale field investigations

(1) Crack patterns on the desiccation soil surface

Konrad and Ayad (1997a) found that the intact marine clay deposit (i.e. Saint-Alban clay) with an initial water content of 103% produced successively the primary and the secondary crack networks when it was exposed to continued evaporation for 35 days. The spacing and opening of primary cracks were 200 to 240 mm and 17 to 21 mm, respectively. The secondary cracks split the original polygons into several parts (Figure 2.11(a)). Philip et al. (2002) found that the thin Abbrook clay layer, which was placed at dry of optimum, was found to generate primary crack polygons and secondary cracks on the slopping ground with an approximated spacing of 70 to 110 mm and 20 mm, respectively, after the 36-day evaporation period. On the other hand, the same clay layer on the horizontal ground surface cracked less due to differences in the moisture loss mechanism. Baer et al. (2009) investigated the evolution of crack pattern for exposed surfaces using saturated Mexico silt loam placed at two different sheltered locations to alleviate rainfall effects on a continuous cool-season grass and legume plot near Centralia (United States). From these investigations, they concluded that the higher clay concentration and the higher shrinkage potential closer to the soil surface contributed to more surface crack area. Dyer et al. (2009) carried out field survey on a naturally desiccated flood embankment (i.e. Thorngumbald embankment) near the city of Hull (UK) with alluvial clays. They identified the polygonal pattern of desiccation cracks along the crest of the embankment with a width varying from 5 to 25 mm (Figure 2.11(b)). Li and Zhang (2010) studied the crack pattern in the shallow expansive soil layer on the Huangshan Slope (Zhenjiang, China) that was subjected to evaporation. From statistical analysis on the crack patterns (Figure 2.11(c)), it was also found that the locations and orientations of the desiccation cracks followed a uniform

distribution, while the lengths and apertures followed a lognormal distribution. Cordero et al. (2016) installed a large-scale test cell in the field to investigate the desiccation cracking behavior of a reconstituted silty clay with initial water content of 1.5 times liquid limit in the natural atmospheric conditions. It was found that rainfall events during the drying period may affect the crack pattern by closing some small cracks and generating new ones (Figure 2.11(d)). Based on the information on the soil types, initial soil states, and drying environmental conditions summarized in Table 2.4, a general conclusion that can be drawn is that longer, wider and deeper cracks will occur for soils with higher shrinkage potential, higher initial water content under higher evaporation rate. Additionally, the vegetation cover will suppress the crack development due to the reinforcement effect of roots, which is also confirmed by Ravina (1983) and Morris et al. (1992).

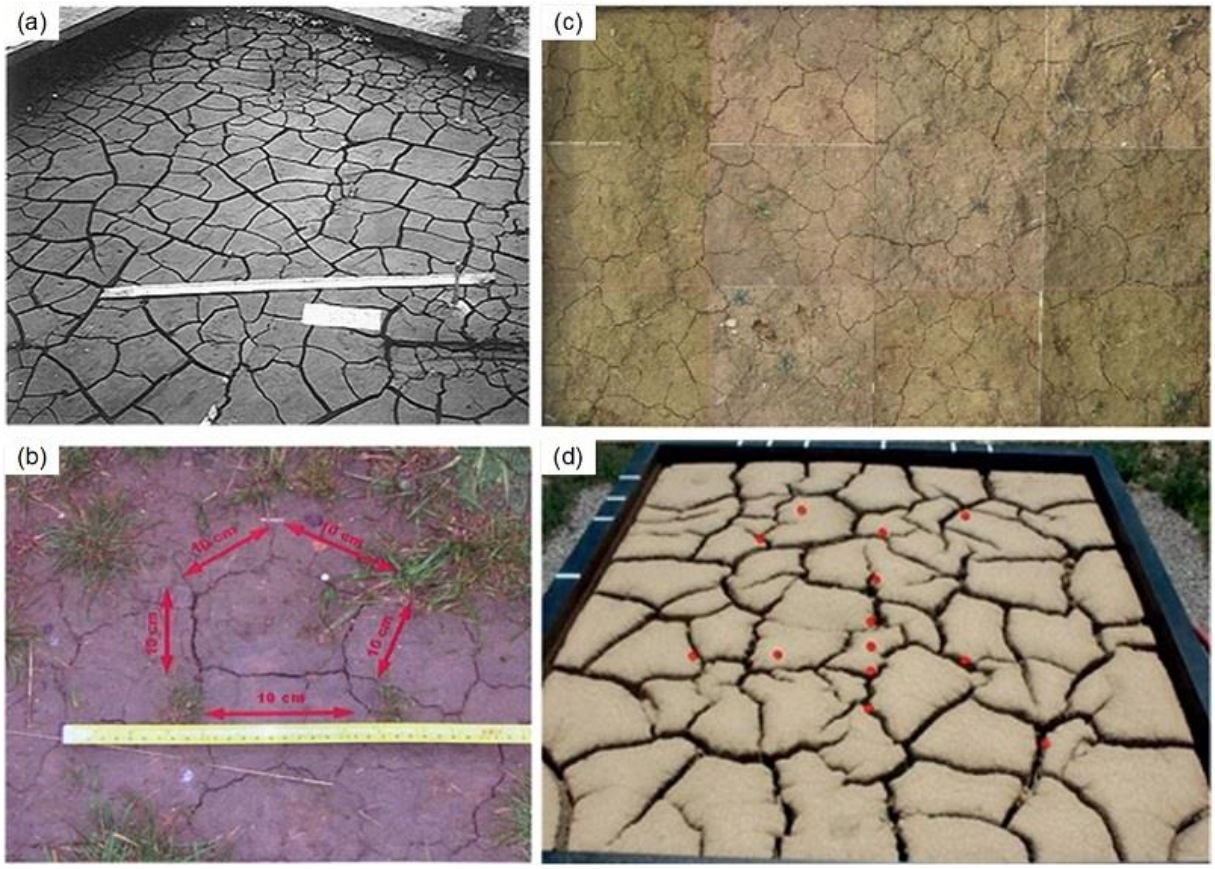

Figure 2.11 Photos of crack patterns induced by desiccation in the field: (a) the intact Saint-Alban clay, 8 days after the exposure to shrinkage (adapted from Konrad and Ayad 1997a), (b) the compacted alluvial clay on the crest of an embankment, 3 years after the construction (adapted from Dyer et al. 2009), (c) Huangshan Slope ground surface (actual picture size: 820 mm by 525 mm) at water content of shrinkage limit after desiccation (adapted from Li and Zhang 2010), (d) a silty clay in the large-scale field test cell (size: 3000 mm by 3000 mm), 150 days after the start of desiccation (adapted from Cordero et al. 2016).

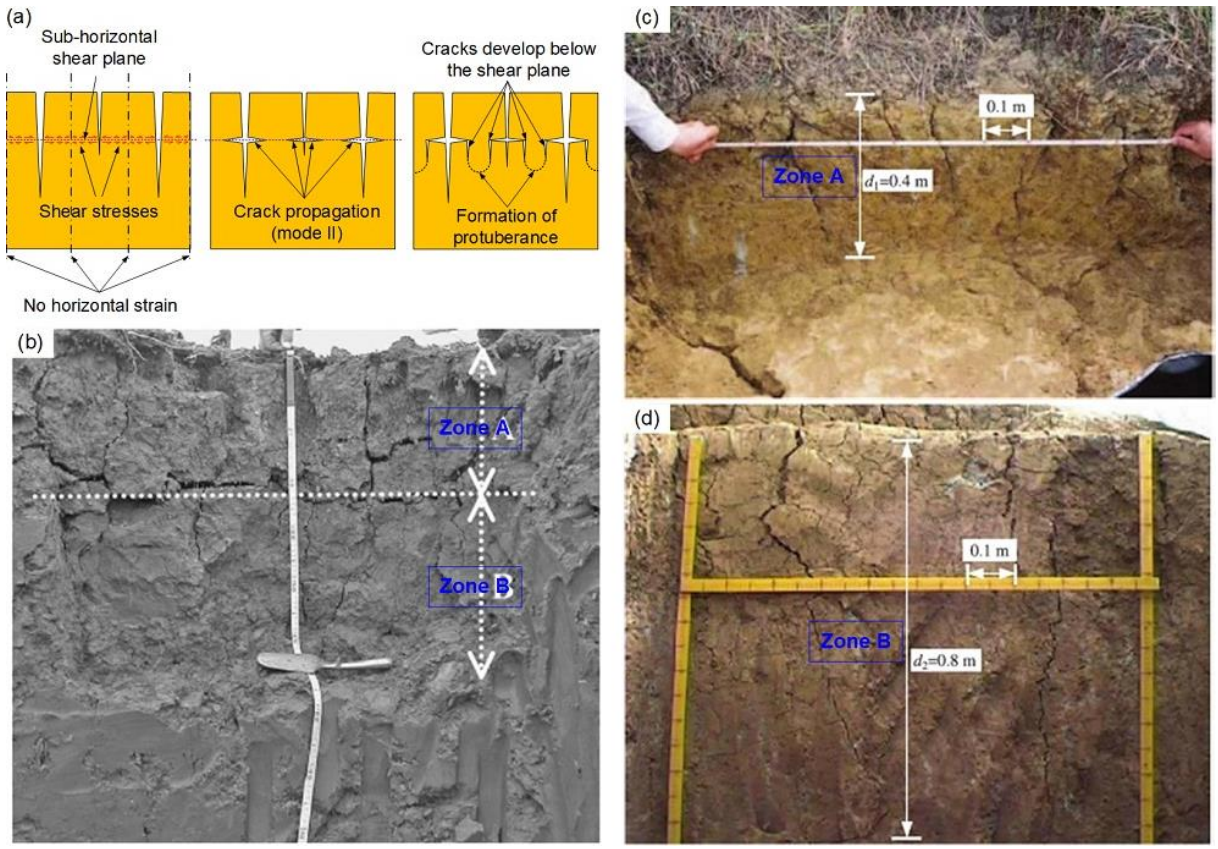

Figure 2.12 (a) Development mechanisms of sub-horizontal mode II cracks, cracks below the shear plane and protuberance suggested by Konrad and Ayad (1997a); (b) Pattern of desiccation cracks in trial trench at Thorngumbald flood embankment at an approximate depth of 600 mm below crest level (adapted from Dyer et al. 2009); Crack pattern observed in the excavation pit near the studied expansive soil slope (adapted from Zhan et al. 2007): (c) upper part (depth of 0-0.4 m), and (d) lower part (depth of 0.4-1.2 m).

(2) Crack characteristics in the desiccated soil profile

Based on the field observations of desiccation-induced cracking in the Saint Alban clay, Konrad and Ayad (1997a) proposed cracking mechanisms which include six successive phases (Figure 2.12(a)); namely: (i) the initiation of primary cracks under restrained conditions, (ii) the opening and propagation of the primary cracks and the progressive buildup of tensile stresses within each polygonal desiccated blocks, (iii) the initiation and sudden propagation of the secondary cracks, (iv) the appearance of the sub-horizontal shear planes and the development of the sub-horizontal cracks at certain depth within the polygonal desiccated blocks due to the differential horizontal shrinkage along the soil profile, (v) the initiation and propagation of a new sets of vertical cracks below the horizontal cracks, and (vi) the formation of protuberance in each desiccated block due to continued evaporation and shrinkage. This proposition was corroborated by Dyer et al. (2009) (Figure 2.12(b)) and Zhan et al. (2007) (Figures 2.12(c) and (d)) from field observations. In the desiccated soil profile, two distinct zones can be identified, namely the upper part (zone A) with a dense two-dimensional

array of cracks both perpendicular and parallel to the drying surface and the lower part (zone B) with a sparse crack array extending vertically from the horizontal cracks and terminate in intact soil at certain depth. The existence of two distinct zones was consistent with the observations in the region scale as well, such as Ruland et al. (1991) and Morris et al. (1992).

The depth of desiccation-induced cracks has received considerable attention in the literature. For example, Ruland et al. (1991) determined the maximum depth of hydraulic active, vertical fractures which is greater than 4.5 m at the 12 sites studied on the St. Clair Plain in southwestern Ontario (Canada), using the hydrogeological survey approach with both hydraulic and isotropic evidence. Morris et al. (1992) found the depth of desiccation-induced cracks strongly correlates to (or, typically coincides approximately with) the depth of seasonal moisture changes in ground, by analyzing the typical crack depths in several Australian tailing deposits and the Lake Agassiz clay near Winnipeg in Canada. For similar tailing deposits in Australia, the climate condition is the determinative factor for the crack patterns (i.e. the crack depth increases from 0.5 m to 3.0 m with distance from the east coast as the annual rainfall diminishes). In Canada, on the other hand, much deeper cracks were revealed (i.e. greater than 4.5 m in southwestern Ontario, and 6.0 m near Winnipeg) when compared with those in Australia. This can be attributed to two factors, namely (i) intrinsic soil properties, the Australian tailing deposits which include a considerable portion of coarse-grained particles show less shrinkage potential than the Lake Agassiz clays and clay-rich glacial tills in Canada, and (ii) environmental conditions, the climate condition in Australia (i.e. a temperate oceanic climate) is wetter and warmer than that in eastern Canada (i.e. a humid continental climate) which suppresses the development of shrinkage cracks, and the intensive freezing-thawing cycles in Canada can induce deeper soil cracks. The soil cracks observed by Ruland et al. (1991) and Morris et al. (1992) are much deeper than those summarized in Table 2.4 due to the differences in the environmental conditions to which the soils were exposed. For example, the 6-m-deep cracks in the Lake Agassiz clays were regarded to be formed during the Hypsithermal period 9000-4500 years ago following the draining of proglacial Lake Agassiz (Morris et al. 1992) and to be affected by thousands of drying-wetting cycles and freezing-thawing cycles (Graham and Au 1985). As suggested by D'Astous et al. (1989), the clay-rich glacial tills in southwest Ontario had undergone weathering from the surface to the depth greater than three meters. However, the crack patterns observed in field studies summarized in Table 2.4 were produced by one specific drying process, excluding the effect of the long-term soil-atmosphere interaction in a large geological time scale.

Table 2.4 Characteristics of desiccated soils and desiccation-induced crack patterns investigated from several field tests.

Soil type	Saint-Alban clay	Abbrook clay (compacted)	Thorngumbald clay	Huangshan Slope clay
References	Konrad and Ayad (1997a)	Philip et al. (2002)	Dyer et al. (2009); Jones et al. (2014)	Li and Zhang (2010)
Atterberg limits				
Liquid limit	50%	42-58%	57%	40.4%
Plastic limit	25%	20-23%	29%	15.6%
Plasticity index	25%	22-35%	28%	24.8%
Shrinkage limit		12.5-13%	14%	13%
USCS	CH	CL/CH	CH	CL
Grain size distribution				
Gravel size fraction	0%	0%	0%	8%
Sand size fraction	1%	3%	35%	23%
Silt size fraction	18%	25%	48%	34%
Clay size fraction	81%	72%	17%	35%
Dominate clay minerals	Montmorillonite	Kaolinite	Illite, kaolinite	Illite, montmorillonite
Initial soil states				
Gravimetric water content	103%	17.5-18%		30%
Dry density (kN/m^3)	14.4–16.0	17.5-17.9		16.7
Environmental conditions				
Average evaporation rate	0.18 mm/h (first 18 h)	0.05 mm/h (24-336 h)		0.06 mm/h (daily potential evaporation)
Surface cover condition	Uncovered	Covered (HDPE geomembrane)	Covered (poor grass)	Uncovered
Crack pattern at steady state stage				
Water content on the top surface	25%	9%	21.7%	13%
Average spacing of primary cracks	200–240 mm	70-110 mm	5–25 mm	31.6 mm
Main intersection angle	90° (quadrilateral), and 120° (hexagon)		144° (pentagon)	90° (quadrilateral), and 120° (hexagon)
Average aperture of primary cracks	17 – 21 mm	3 mm (width index)		0.49 mm
Average depth of primary cracks	50 mm (at onset of primary crack structure)	18 mm		

The inclination of desiccation-induced cracks in the desiccated soil profile is also investigated by several researchers. For instance, Blight (1997) interpreted the inclination of cracks based on the Griffith theory of fracture (Hoek 1964; Bishop and Garga 1969) and concluded that cracks vary from

inclined at the surface, to vertical terminating at a depth equal to half the water table depth, and to inclined near the ground water table. This interpretation was justified by Williams's in-situ observation (Williams 1965), in which no inclined cracks usually exist at depths of less than about 0.5 m and the range in crack inclinations at depths greater than 0.5 m was 39° to 78° off-vertical. From the histogram of crack orientation by analyzing a total of 192 observations, there is a subsidiary but significant peak showing a concentrated inclination at about 35° in addition to the definite peak of near vertical cracks. However, there is limited field evidence in the literature focused on inclined cracks near the ground water table provided in comparison to the vertical or subvertical cracks at a shallow depth. The lack of information on the inclination of cracks at a relatively great depth may be attributed to the difficulty in observing the cracks accurately in the desiccated soil profile because of the disturbance and stress-release during exploratory excavation.

2.1.4.2 Small-scale laboratory experiments

The crack evolution is found to be stable during the laboratory tests when the water content approaches the shrinkage limit (e.g., Tang et al. 2008; Tang et al. 2010; Julina and Thyagaraj 2018), which is consistent with the findings from the field observation (e.g., Li and Zhang 2011). Based on the extensive studies reported in the literature (e.g., Shorlin et al. 2000; Tang et al. 2008; Lakshmikantha et al. 2009; Péron et al. 2009a; Trabelsi et al. 2012; Antique 2013; Ledesma et al. 2018), it can be concluded that the geometry of the crack pattern at the stable stage is determined by (i) the soil properties (i.e. internal factors), such as fines contents, plasticity index, and mineralogy, and (ii) the existing mechanical and hydraulic boundary conditions (i.e. external factors), which are related to the desiccation surface geometry, boundary constraints and boundary flux conditions (e.g., desiccation rate). In addition, the crack patterns were found to evolve along with the drying-wetting cycles and gradually stabilize after two or three cycles which is associated with the evolution of soil microstructure (e.g., Yesiller et al. 2000; Tang et al. 2008; Tang et al. 2011a; Miedema 2015; Julina and Thyagaraj 2019). The key findings from the laboratory investigations on the crack intersection angle, the crack block size (or crack spacing) and crack depth are summarized in this subsection.

(1) Crack intersection angle

The first concern about the crack pattern is the shape of the desiccation blocks, which is essentially determined by the crack intersection angle. The intersection angles also provide an insight into the mechanism of crack formation. Soil crack patterns are classified into two categories; namely, the

orthogonal pattern and the non-orthogonal pattern, based on the examination of the thermal contraction cracks and ice-wedge polygons in permafrost by Lachenbruch (1962). More recently, though the comparative studies on the desiccation cracking behavior of the clayey soil (i.e. soil 18 in Table 2.2) and potato starch, Costa and Kodikara (2007) and Costa et al. (2013) found the interesting and distinctly different cracking phenomenon in the clayey soil specimens which cracked mainly orthogonally by sequential subdivision. However, the potato starch produced non-orthogonal (close to hexagonal) and simultaneous cracks. From fracture energy point of view, the theoretically plausible crack pattern forms in the most energy efficient way that a minimum amount of fracture energy will be released by creating new solid surfaces for the same amount of strain energy buildup upon desiccation (Corte and Higashi 1964; Péron et al. 2009a; Costa et al. 2013). Based on the Griffith theory of fracture (Griffith 1921), the strain energy released due to the relief of shrinkage stresses is converted into the surface energy of the cracks can be mathematically expressed as below:

$$\gamma_s \cdot (L dz) = G \cdot (A dz) \tag{2.1}$$

in which γ_s is the crack surface energy per unit area, G is the stored strain energy per unit volume of clay immediately before the soil crack initiation, L is the length of the created crack walls, A is the area of the desiccation blocks, dz is the soil layer thickness and the crack is assumed to propagate through the whole layer. Then, the length of crack walls per unit area can be represented as

$$l_{cw} = \frac{L}{A} = \frac{G}{\gamma_s} \tag{2.2}$$

By close examination of the three possible cases of crack intersection angles (Figure 2.13), it is found that cracks intersecting at 120° (i.e. hexagonal shape) have the minimum value of l_{cw} which is the most plausible crack pattern and the most energy efficient. Costa and Kodikara (2007) found that the hexagonal crack pattern is more likely to occur when cracking under conditions that are conducive to simultaneous cracking (i.e. high strain energy, uniform stress and uniform material). Potato starch that has a relatively large pore sizes and relatively uniform particle size distribution tends to simultaneously crack intersecting at 120°. The clayey soil, on the other hand, is prone to crack orthogonally by sequential subdivision after crack initiation, especially when the soil layer is thick and the desiccation rate is low. The marked hierarchy of desiccation-induced cracks in cohesive soils, i.e. secondary cracks occur between the primary ones (which have larger width) after the initiation and propagation of primary cracks, was also corroborated by experimental studies that were

consistent with field test results (e.g., Lau 1987; Nahlawi and Kodikara 2006; Costa and Kodikara 2007; Trabelsi et al. 2012; Lakshmikantha et al. 2013a; Antique 2013). Lakshmikantha et al. (2013a) attributed the hierarchical nature to (i) stress buildup beyond the soil strength, (ii) direction of stress generation, and (ii) stress redistribution in the vicinity or inside the newly formed domain. This interpretation provides insight into the occurrence frequency of crack intersection angles. Once a crack forms, tensile stresses perpendicular to the crack axis are released near the crack; when approaching the vicinity of another existing crack, a propagating crack tends to orient in the direction perpendicular to the local maximum tensile stress and to intersect the existing crack orthogonally. Tang et al. (2008), Tang et al. (2011b), and Antique (2013) observed that the shape of '+' or 'T' at the crack intersection regardless of the experimental conditions, which confirmed further this theoretical analysis. Costa et al. (2013) interpreted that the sequential cracking is a result of the tensile stress buildup and the activation of the randomly distributed flaws in the soil specimens (e.g., large pores, entrapped air bubbles). Hence, it is possible to obtain mixtures of sequential orthogonal and simultaneous hexagonal crack patterns, when the flaws in the soil are activated rapidly in succession. It is worth noting that not all the flaws may be activated because of the influence of the existing cracks in the vicinity of which there is a low-stress zone.

It is interesting to note that the soil layer thickness has significant influence on the crack pattern including the crack intersection angle. Figure 2.14(a) presents the probability distribution of side numbers of desiccation blocks observed by Corte and Higashi (1964). It is indicated that cracks intersect at 120° (i.e. hexagons) prevail when the thickness is less than 4 mm while cracks at 90° (i.e. quadrilaterals) are predominant where the thickness is more than 4 mm. Studies by Péron (2008) highlight that some groups of cracks intersecting at around 120° arise simultaneously in the thinner specimens (i.e. 4 mm-thick) especially at the beginning. On the other hand, secondary cracks exhibit the tendency to meet other existing cracks at a right angle upon further desiccation (Figure 2.14(b)). Similarly, Antique (2013) found that for very thin soil layer (i.e. 5 mm-thick), non-orthogonal primary crack patterns occurred simultaneously and propagated at a relatively faster rate especially at the beginning; upon further desiccation, secondary cracks make bridges between the primary ones and induce around 90° intersection angles. The mechanism underlying those phenomena can be interpreted based on their crack formation conditions. The thinner is the soil layer, the higher is the desiccation rate. Due to this reason, a relatively uniform stress field and the high strain energy accompanied with the constrained shrinkage prior to cracking, which are the favorable conditions for producing the simultaneous orthogonal crack pattern in the most energy efficient way. Based on the

above discussions, the successive cracks would tend to intersect the existing cracks due to the local stress field. In addition, Corte and Higashi (1964) argued that the final crack patterns will predominantly have pentagon shape if the primary cracks mainly form hexagonal pattern from the geometrical consideration of the successive subdivision process. This characteristic provides insight into the relatively higher frequency of occurrence of the five-side polygons and the intersection angle ranging from 100° to 110° especially for the thin soil layer as shown in Figures 2.14(a) and (b), respectively.

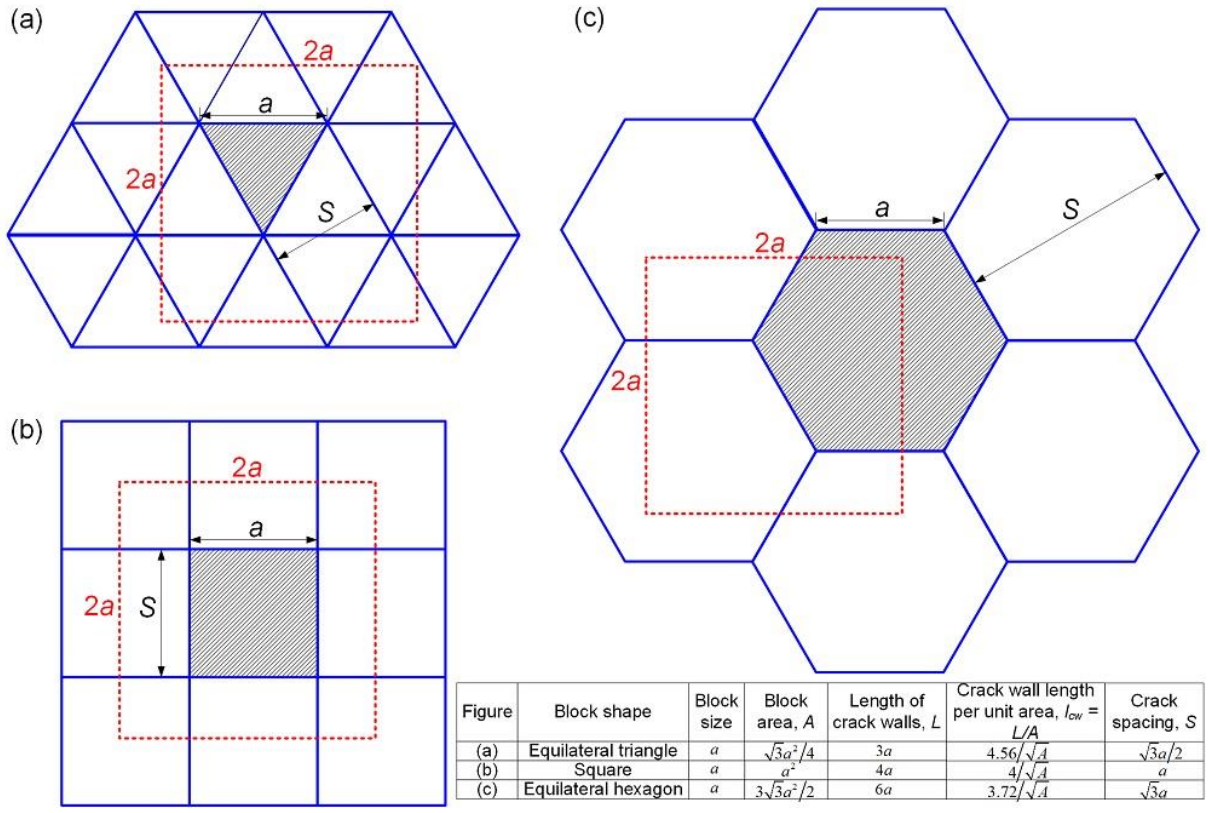

Figure	Block shape	Block size	Block area, A	Length of crack walls, L	Crack wall length per unit area, $l_{cw} = L/A$	Crack spacing, S
(a)	Equilateral triangle	a	$\sqrt{3}a^2/4$	$3a$	$4.56/\sqrt{A}$	$\sqrt{3}a/2$
(b)	Square	a	a^2	$4a$	$4/\sqrt{A}$	a
(c)	Equilateral hexagon	a	$3\sqrt{3}a^2/2$	$6a$	$3.72/\sqrt{A}$	$\sqrt{3}a$

Figure 2.13 Three possible geometric shape of the crack blocks with identical block size, a: (a) equilateral triangle; (b) square; and (c) equilateral hexagon. (Note: blue solid lines represent crack segments; red dash lines represent an identical square area with side length of 2*a*.)

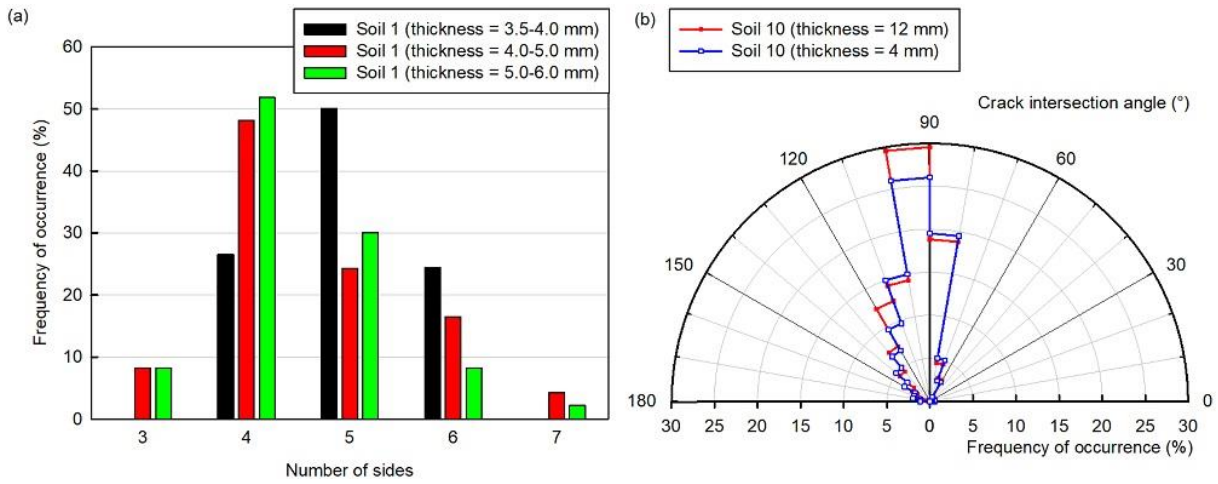

Figure 2.14 (a) Probability distribution of the number of sides of desiccation blocks at various thicknesses of soil 1 (data from Corte and Higashi 1964); (b) Probability distribution of the intersection angle of desiccation cracks in soil 10 (data from Péron 2008).

(2) Crack block size (or crack spacing)

Most of the earlier works on the shrinkage and cracking of soils were performed by geologists and soil scientists, mainly focusing on the aerial patterns (e.g., the spacing) of desiccation cracks. Kindle (1917) conducted the pioneering experimental investigation on desiccation cracking of mud samples originated from Ontario Lake clay and blue marine clay of Pleistocene age from Ottawa valley. From these investigations it was demonstrated that the external factor (i.e. temperature that is associated with the desiccation rate. In addition, the cohesion between soil and bottom base) and the internal factor (i.e. soil composition, water salinity) are two primary factors in controlling the crack formation and crack pattern. Twenhofel (1950) pointed out that crack spacing depended on many physical factors, including the character of the mud, the character of the water in which the mud was deposited, the thickness of the mud, the nature of the underlying material, the desiccation rate, and the presence of foreign matters. Lachenbruch (1962) studied the ice-wedge polygons in permafrost and theorized that crack spacing of any polygonal pattern ground is a function of the frequency of flaws (or heterogeneities) in the ground. The heterogeneities included non-uniform strength within the soil mass and the non-uniform drying conditions or thermal conditions in case of frozen patterned ground caused by local variation in relief and shrinkage properties. Discussion in those previous studies included the physical observations and qualitative analysis, without investigating any measurable parameters that control the crack patterns. Later, Corte and Higashi (1964) found that crack patterns depended largely on the thickness of the soil layer and the base friction. Lau (1987) concluded that crack pattern depended on the soil layer thickness, the presence of heterogeneities (e.g., foreign matter), boundary conditions, stress conditions, and material properties. Kodikara et al. (2000)

revisited the experimental investigation studies by Corte and Higashi (1964) and Lau (1987) and found that the area of desiccation blocks followed a log-normal distribution and the mean block area was a function of soil thickness, base adhesion, and initial soil density, but not strongly related to the desiccation rate.

A theoretical framework can be used based on fracture mechanics to obtain a quantitative relationship between the crack block size (or crack spacing) and the influencing factors in a desiccating soil element. Assuming an approximately uniform tensile stress profile across the soil layer is generated upon desiccation and the whole strain energy developed prior to crack initiation is consumed by creating crack surfaces (i.e. Eq. (2.1)), then the crack block size can be estimated as

$$a = \xi \frac{\gamma_s}{G} \tag{2.3}$$

in which ξ is the parameter associated to block shape and equals $4\sqrt{3}$, 4, and $4/\sqrt{3}$ for the block shape of equilateral triangle, square, and equilateral hexagon, respectively (Figure 2.13). Kodikara (2012) provided the following constitutive relationship to describe the stress-strain behavior of the desiccating soil prior to cracking:

$$dp = K\left(d\varepsilon_v - d\varepsilon_f\right) \tag{2.4}$$

in which dp is the incremental net mean stress, K is the bulk modulus at a given water content, $d\varepsilon_v$ and $d\varepsilon_f$ are the incremental actual shrinkage strain under constrained conditions and the incremental free shrinkage strain without any constraints. The difference in actual shrinkage strain and free shrinkage strain due to the constraints (i.e. $d\varepsilon_f$ - $d\varepsilon_v$), which was referred as "virtual strain" by Corte and Higashi (1964), provides the origins of generated stresses upon constrained shrinkage (Péron et al. 2009a) and stores the strain energy in the desiccating soil. For the preliminary investigation, the three-dimensional linearly elastic and isotropic shrinkage of the desiccating soil element and full constrained conditions prior to cracking can be assumed (i.e. K is constant, and $d\varepsilon_v = 0$),

$$p = -K\varepsilon_f \tag{2.5}$$

Hence, the stored elastic strain energy per unit volume prior to cracking can be given by the area under the net mean stress-virtual strain curve for the desiccating soil element (e.g., Corte and Higashi 1964; Blight 1997) as below:

$$(2.6)\quad G = \left| \int_0^{\varepsilon_{sh}} p d\varepsilon_f \right| \approx \frac{1}{2} K \left(\varepsilon_{sh} \right)^2$$

where ε_{sh} is the total free shrinkage strain until the onset of crack initiation. In addition, the free shrinkage strain is assumed to be linearly proportional to the reduction in moisture content of the desiccating soil as a first approximation (e.g., Corte and Higashi 1964; Kodikara and Choi 2006), which can be represented as

$$(2.7)\quad \varepsilon_{sh} = \alpha \triangle w$$

in which α is the proportional coefficient and Δw is the change in moisture content prior to cracking. Therefore, by substituting Eq. (2.6) and (2.7) into Eq. (2.3), the crack block size can be estimated as

$$(2.8)\quad a = \frac{2\xi\gamma_s}{K\left(\alpha \triangle w\right)^2}$$

The crack surface energy, γ_s is small (e.g., 1 N/m for soil 18 in Table 2 measured by Costa (2010)) for soft wet clayey soils (e.g., slurry). Blight (1997) suggested that γ_s is approximately a constant value and is twice the surface energy of the water. There are three variables in Eq. (8): (i) the bulk modulus K, (ii) the proportional coefficient α, and (iii) the reduction in moisture content Δw. Both K and α depend on soil intrinsic properties and initial soil states (i.e. the compressibility due to suction contraction and the shrinkage potential). However, Δw depends on the initial water content, the evaporation surface area and the desiccation rate which is associated with the soil layer thickness. Eq. (2.8) can be used as a tool to explain the complex mechanisms associated with desiccation cracking. For example, Lau (1987) reported from experimental studies clayey soils have a smaller crack spacing than silty soils. Typically, a clayey soil has higher compressibility due to suction contraction and a higher shrinkage potential (i.e. ε_{sh}) than a silty soil does because of the higher plasticity. The findings by Tang et al. (2008), Uday and Singh (2012), and Singh et al. (2018) that the crack spacing and the extent of cracking (i.e. crack intensity factor, CIF) is correlated directly to the clay content and plasticity index corroborates the applicability of Eq. (2.8) as well.

The soil layer thickness has been found to have a remarkable influence on the geometrical characteristics of crack patterns. Corte and Higashi (1964), Nahlawi and Kodikara (2006), Rodríguez (2006), Tang et al. (2008), Antique (2013) and Singh et al. (2018) found that the crack pattern

depends upon the thickness of the drying soil, e.g., along with the increase in soil layer thickness, the mean crack block size (or, crack spacing), the mean area of the crack blocks, and the number of large blocks increases, whereas the total length of cracks decreases. Corte and Higashi (1964) and Nahlawi and Kodikara (2006), from desiccation cracking tests on soil 1 and soil 4 (Table 2.2), respectively, found that both the desiccation rate and reduction in water content at the onset of crack initiation decreases. This is because water has to travel a greater distance for evaporation on the soil surface with an increase in the soil layer thickness. Hence, the block size will increase as the decrease in the reduction of moisture content upon crack initiation (Δw) according to Eq. (2.8). In addition, a further increase in soil layer thickness (e.g., larger than 20 mm) will result in a larger difference in the desiccation rates of the upper and bottom soil layers (Nahlawi and Kodikara 2006). Due to this reason, there will be a differential shrinkage deformation and the formation of the "effective layer" (Costa et al. 2013) above the sub-horizontal shear plane as shown in Figure 2.12(a) (Konrad and Ayad 1997a). Different total thickness of soil layer may correspond to different thickness of the "effective layer" due to differences in the desiccation rate and the transfer of thermal energy (Tang et al. 2008).

The base friction is another factor that controls the crack patterns of the desiccating soil. The base friction acts as the mechanical boundary constraint for the desiccating soil and consequently affects the soil stress-strain behavior including soil cracking (i.e. the actual shrinkage strain $d\varepsilon_v$ in Eq. (2.4)) and the generated tensile stress. Under fully constrained conditions, $d\varepsilon_v = 0$ will give rise to the development of the maximum tensile stress (i.e. $dp = K \cdot (-d\varepsilon_f)$). On the other hand, the partially constrained condition with a low base friction contributes to low shrinkage strains (i.e. $d\varepsilon_v > 0$) and generates lower tensile stresses. Therefore, the lower tensile stresses will result in lower stored shrinkage strain energy and larger crack block size (or crack spacing) according to the estimation by Eq. (2.3). The theoretical analysis can be validated from the observations by Corte and Higashi (1964) and Antique (2013); these studies suggest the more adhesive is the container bottom, the smaller are the crack blocks. For a soil layer with a great thickness, however, the above conclusion may not be valid. For example, Antique (2013) found that for the 5-mm-thick soil layer, the above conclusion applies, whereas the opposite result was observed for the 10-mm-thick soil layer. Essentially, the effect of base friction on the desiccation cracking behavior is coupled with the influence of the soil layer thickness. Due to this reason, the interface friction effect is more pronounced for thinner soil layers (Zeng et al. 2019).

The environmental condition is one of the key factors that influence the formation of desiccation cracks as well. Due to the difference in environmental conditions in the laboratory and those in the field, the

applicability is limited when comparing laboratory-scale and field-scale desiccation cracking behaviors. For example, Tang et al. (2008) indicated that the geometrical structure of crack patterns is significantly influenced by the imposed temperature (e.g., oven temperatures of 30, 40 and 50 °C). The contrasting observation by Rodríguez (2006) on soil 17 (Table 2.2) that the distance between cracks seems not to be affected by the imposed relative humidity and the corresponding suction may be due to the almost same reduction in water content at the onset of cracking which means the same crack spacing (see Eq. (2.8)) even imposed at different environmental conditions. Additionally, the surface area of the desiccating soil affects the desiccation rate and consequently the crack pattern (e.g., Lakshmikantha et al. 2006; Ledesma et al. 2018). The geometry of the test plate or the aspect ratio of the desiccating soil layer is found to have influence on the crack patterns as well (Lakshmikantha et al. 2006; Antique 2013), which probably due to the more pronounced effect of boundary disturbance to the formation of crack patterns in smaller soil specimens.

(3) Crack depth

As the soil layer thickness increases, the desiccation cracks may not propagate throughout the entire depth of the soil layer thickness, which was termed as “non-propagating cracks” by Julina and Thyagaraj (2018). The existence of non-propagating cracks is evident from the laboratory observations through the surface image (e.g., Costa et al. 2013) and through the X-ray computed tomography (e.g., Julina and Thyagaraj 2018; Tang et al. 2019). From engineering practice point of view, the crack depth which is associated with the crack volume is a key parameter for evaluating the characteristics of cracked soils, e.g., coefficient of permeability, shear strength, etc. However, the measurements of crack depth cannot be achieved by the commonly used image technique in the laboratory. Electrical resistivity tomography (e.g., Samouëlian et al. 2004; Khandelwal 2011; Jones et al. 2012; Tang et al. 2018b), laser microscope (e.g., Uday and Singh 2012), laser scanning technique (e.g., Sánchez et al. 2013), ground penetration radar (Levatti et al. 2017), and computed tomography (e.g., Julina and Thyagaraj 2018; Tang et al. 2019) have been used to capture the crack propagation in the soil profile and to measure the crack depth in the laboratory. Uday and Singh (2012) applied laser microscopy to study the three-dimensional cracking geometric characteristics of four fine-grained soils and derived an empirical correlation between the crack depth (D_c) and crack width (W_c) and crack length (L_c), i.e.

(2.9) $$D_c = m \times W_c^n \times L_c^{0.5}$$

in which both *m* and *n* are fitting parameters associated with soil properties, such as clay content, plasticity index, swelling index, and specific gravity. Two mathematical models, i.e. the triangular model (TM) and the square root model (SRM), which were proposed by Ringrose-Voase and Sanidad (1996) are examined based on the measured crack volume (Uday and Singh 2012). It was found that the former one is better than the latter one to define the crack geometry in the soil profile. Wang et al. (2013) proposed a simplified and linear relationship (i.e. Eq. (2.10)) between the crack depth and the crack width based on the measurements of the three-dimensional crack geometry of desiccation cracks on Huangshan Slope clay in a rectangular drying box extending the electrical resistivity technique:

$$D_c = \eta \times W_c \tag{2.10}$$

in which η is the proportional coefficient and related to the soil properties. Figure 2.15 shows the measurements of crack depth and its correlation to crack width by Uday and Singh (2012) and Wang et al. (2013). It can be concluded that the linear relationship (i.e. Eq. (2.10)) which correlates the crack depth exclusively with the crack width is reliable against the laboratory measurements. The reliable measurement of crack depth using special techniques such as electrical resistivity technique in the laboratory or in the field is expensive in comparison with monitoring the crack pattern in the soil surface. Therefore, the research on the prediction of desiccation-induced crack depth is an emergency but challenge task (e.g., Lau 1987; Morris et al. 1992; Konrad and Ayad 1997b; Chertkov and Ravina 1998). Furthermore, the contribution to the cracking depth from the stress field in the soil profile including the overburden stress and lateral earth stress should be taken into account (e.g., Blight 1997; Yin et al. 2012; Shahrokhabadi et al. 2019).

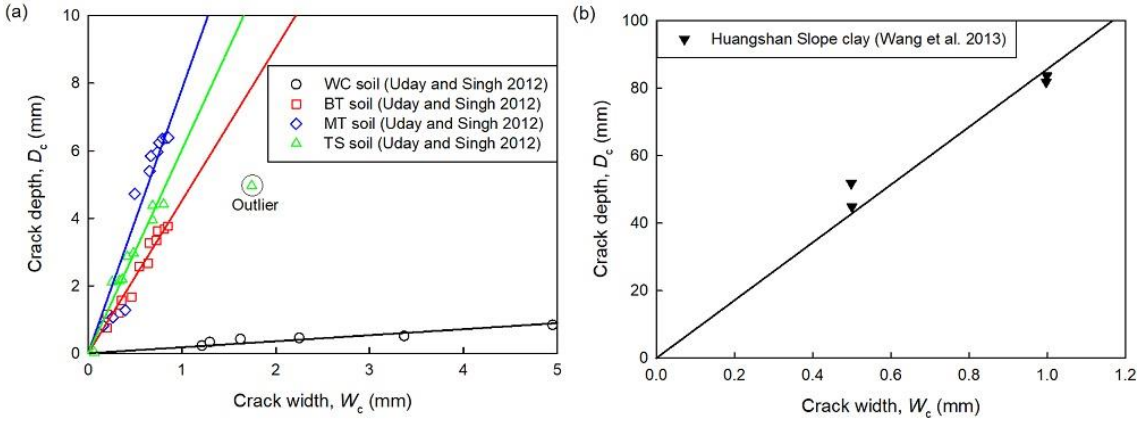

Figure 2.15 The linear relationship between the crack depth and the crack width (i.e., Eq. (2.10)) against experimental data for different cohesive soils: (a) data from Uday and Singh (2012); (b) data from Wang et al. (2013).

2.1.5 Numerical modelling desiccation-induced cracks

Desiccation cracking in cohesive soils and especially in expansive soils is unavoidable in semi-arid and arid regions of the world. These cracks significantly alter the hydraulic, mechanical, thermal properties of the cohesive soils. In many scenarios, these cracks likely contribute to the failure of soil slopes, embankments, and clay covers and liners for landfills due to the influence of the soil-atmosphere interaction (e.g., drying-wetting cycles). The depth of cracks is one of the key parameters required for the rational interpretation of the hydro-mechanical behavior of cracked soils. The commonly available image technique can only capture the characteristics of the surficial cracks, without the information on crack development inside the soil mass. The current available techniques for determining the three-dimensional development of the desiccation cracks, e.g., X-ray computed tomography (XCT), electrical resistivity technique (ERT), ground-penetrating radar (GPR), are time or cost consuming and employed mostly in the laboratory tests rather in the field. Therefore, to develop a prediction model for desiccation crack depth is emergency for engineering practice. The various prediction models of crack depth induced by desiccation are summarized and classified into three categories according to Potts and Zdravković (1999), namely (i) closed-form solutions, (ii) simple methods, and (iii) numerical analysis.

2.1.5.1 Close-form solution

The soil mass is assumed to be an elastic, homogeneous, and isotropic porous media. For the close-form solution, as the first step the variation of matric suction with depth or with depth and time is solved analytically through the one-dimensional steady-state unsaturated flow equation or one-dimensional transient diffusion equation with constant diffusion coefficient, respectively. The depth of desiccation cracks can subsequently be predicted, on the basis of a certain criterion (e.g., stress, strain, or fracture toughness) at the crack tip accompanied with the known variation of matric suction (e.g., Lau 1987; Shi et al. 2014; Morris et al. 1994). Lau (1987) and Shi et al. (2014) calculated the strains by the elastic constitutive model of unsaturated soils (e.g., Fredlund and Morgenstern 1976) and derived the arrested depth of desiccation cracks from the assumptions that the lateral restraint is removed after crack initiation and the crack is arrested when the lateral stain reaches the maximum tensile strain. Morris et al. (1992), Al-Dakheeli (2016), Chen and Bulut (2017) reputed that crack would be arrested when the total lateral stress reaches the maximum tensile stress (i.e. tensile strength) at the crack tip. The depth of cracks can therefore be deduced by the elastic constitutive model of unsaturated soils at K_0 stress state, which is similar as the real stress state in the field. Salganik and Chertkov (1969) obtained the distribution of water content with respect to depth and time by the analytical solution of one-dimensional diffusion equation

with constant coefficient of diffusion, which was related to the variation of total lateral stress with depth and time. The Stress Intensity Factor (SIF) (Cherepancv 1979) at the crack tip could then be determined in the framework of Linear Elastic Fracture Mechanics (LEFM) (e.g., Irwin 1948). The arrested crack depth following the stable propagation could be deduced based on the fracture toughness criterion after a specific period of drying time. Morris et al. (1992; 1994), Harison and Hardin (1994) derived the distribution of the lateral stress with depth for soil mass at K_0 stress state with elastic constitutive model and assumed the distribution of matric suction (constant or linear distribution with depth). Subsequently, the arrested depth of cracks was obtained by comparing the fracture toughness of the soil and the Stress Intensity Factor (SIF), which varies along with the crack propagation depth (Hartranft and Sih 1973), at the crack tip based on the Bueckner's approach (Bueckner 1958).

2.1.5.2 Simple method

For this category of approach, the stress field in the vicinity of the crack tip is assumed to be at the plastic limit state when the crack is arrested (e.g., Morris et al. 1994; Lau 1987; Morris et al. 1992); and the distribution of matric suction is assumed to be constant or linear distributed along with the depth. Morris et al. (1992) extended the Mohr-Coulomb failure criterion for unsaturated soils (Fredlund and Morgenstern 1978) and derived the depth of desiccation cracks in the basis of the assumption that the stress state of the soil mass in the vicinity of the crack tip is at the Rankine active earth pressure state and the crack would be arrested when the total lateral stress is null. Taking the contribution from matric suction to the shear strength of unsaturated soils into account, Mohr-Paul strength model (Paul 1961) and Griffith-Brace strength model (McClintock and Walsh 1962) were developed. Based on this model, Lau (1987), Morris et al. (1992; 1994) assumed that the crack would be arrested when the total lateral stress at the crack tip reached the tensile strength and derived the arrested depth of cracks through iteration algorithm.

2.1.5.3 Numerical analysis

The numerical methods which are adopted to simulate the desiccation-induced crack initiation and propagation of cohesive soils mainly include three approaches: (i) Finite Element Method (e.g., Shen and Deng 2004; Levatti et al. 2007; Sánchez et al. 2014; Matsubara et al. 2016; Vo et al. 2017; Cajuhi et al. 2018); (ii) Discrete Element Method (e.g., Nishimoto et al. 2007; Péron et al. 2009b; Sima et al. 2014; Asahina et al. 2014; Guo et al. 2018); (iii) Mesh Free Method (Bui et al. 2015; Hirobe and Oguni 2016). In the remainder of this chapter, the numerical techniques based on finite element method for simulating

the crack initiation and propagation, which can be classified into three categories, i.e. continuous approach, discontinuous approach, and interface element model are briefly reviewed.

The continuous approach is typically implemented by introducing the degradation at the constitutive model level in order to simulate the progressive fracturing of porous media. From the physical point of view, the discontinuity of displacement, i.e. the formation of cracks, is reproduced by the degradation of the material within a characteristic width, which makes this approach take advantage of the well-developed framework of continuum mechanics to simulate the issue of discontinuous displacement field. The specific locations of the cracks are not necessary to be predetermined, which means the crack propagation is less dependent on the geometric characteristics of the mesh. Trabelsi et al. (2012) developed the evolution model of cohesion and tensile strength with respect to matric suction for the unsaturated soil dried from initially slurried state. The Thermo-Hydro-Mechanical (THM) coupled visco-elastic-plastic model based on the principle of the two independent stress state variables for unsaturated soils was proposed. In their model, porosity was regarded as an internal variable, as the same as the damage variable in the damage model from the philosophy point of view, the spatial variation of which was implemented by introducing the concept of “cluster”, i.e. a group of elements with homogeneous porosity and therefore with homogeneous properties. In this model, the crack intersects the element when the cohesion of the element vanishes, i.e. the porosity reaches a certain critical value. The crack propagation is implemented by introducing the additional viscoelastic deformation as the viscosity of cracked elements decreases. From a mechanical point of view, this approach to treat the cracked elements is equivalent to removing the elements from the mesh and overcomes the disadvantage that hydraulic boundary conditions would have to be changed on the crack boundaries. Matsubara et al. (2016) proposed a novel non-increment-type of the smeared crack model based on three-dimensional finite element method for crack growth in Bentonite pastes during desiccation. In this model, the maximum tensile stress criterion was considered as the condition for crack initiation and the calculated physical variables of all the elements are modified by a specific factor related to the current principle stress and the tensile strength. Cajuhi et al. (2018) proposed a coupled hydro-mechanical model for simulating the desiccation-induced shrinkage and subsequent crack initiation and propagation base on the phase-field method. The hydro-mechanical behavior of porous media and the crack development (i.e. evolution of phase-field) is coupled through the evolution of the generalized effective stress and fracture toughness of unsaturated soils with water content during the desiccation.

Discontinuous approach to simulate the formation of discontinuity in displacement field is implemented through the rupture of the FEM mesh with the path along the boundaries of elements or through the

elements. For example, Extended Finite Element Method (X-FEM, e.g., Moës et al. 1999) simulates the discontinuity of displacement field across the cracks through the discontinuous Heaviside function. Abu-Hejleh and Znidarčić (1995) developed a novel desiccation theory which includes four consecutive segments that correspond chronologically to the phases that a soft fine-grained soil undergoes in the field after deposition based on effective stress path and total stress path, i.e. (i) consolidation under one-dimensional compression, (ii) desiccation under one-dimensional shrinkage, (iii) propagation of vertical cracks and tensile stress release, and (iv) desiccation under three-dimensional shrinkage. In their model, the depth of crack propagation of the drying soil is obtained through the crack initiation function, i.e. the relationship between the critical porosity in the vicinity of the crack tip and the total vertical stress, which is based on the maximum tensile stress criterion. The one-dimensional non-linear consolidation theory of saturated clays (Gibson 1967) was modified to be capable of modelling both the one-dimensional shrinkage and the three-dimensional shrinkage by incorporating the proportion function, which characterize the proportion of vertical and lateral deformation along the incremental isotropic effective stress paths. The crack propagation in the vicinity of the crack due to stress concentration is not included in their model. Shen and Deng (2004) simulate the whole process of initiation, propagation and close-up of cracks in clay surface during a drying and wetting cycle based on the simplified consolidation theory of unsaturated soils (Shen 1996). In this approach, the three-dimensional crack propagation is modelled by a simplified soil prism surround by cracks (i.e. the diameter is the crack space, and the circumferential surface is the surface of the crack wall), and the detachable double nodes and release node technique after crack formation is utilized to simulate the crack initiation and propagation. The effect on evaporation and rainfall infiltration of the induced crack wall was included in this model. Besides the above maximum tensile stress criterion (local criterion), the fracture toughness can be taken as the crack propagation criterion as well in the framework of Linear Elastic Fracture Mechanics (LEFM). Konrad and Ayad (1997b) developed an idealized framework for modelling desiccation cracking of cohesive soils. The one-dimensional evaporation process is solved numerically by the Richards Eq. with the outcome of the matric suction profile which varies with depth from the ground, which was subsequently taken as an input for calculating the lateral tensile stress profile at K_0 stress state based on the elastic constitutive model of saturated and unsaturated soils. The crack initiates when the lateral tensile stress reaches the tensile strength on the ground surface. The arrested depth of the crack is determined by the variation of stress intensity factor (SIF) at the crack tip with depth incorporating with the fracture toughness criterion in the framework of linear elastic fracture mechanics (LEFM, e.g., Hartranft and Sih1973; Lachenbruch 1961). The ultimate depth after the stable propagation of the primary crack which initiates from the ground surface is predicted by their theoretical framework, not accounting for the ongoing propagation with the

following drying and the formation of secondary cracks, which were observed by laboratory tests (e.g., Nahlawi and Kodikara 2006; Li and Zhang 2010; Ledesma et al. 2016). Moreover, the model could overestimate the crack depth due to the assumptions of linear elasticity and the infinite tensile stress at the crack tip, which ignore the possible generation of plastic strain and energy dissipation in the vicinity of the crack tip, especially for soils with high plasticity and at high water content (Morris et al. 1994; Hallett and Newson 1998). Levatti et al. (2007) presented a general framework to simulate the desiccation cracking behavior of soils, using finite element method combining continuum mechanics, linear elastic fracture mechanics, and unsaturated soil mechanics, together with the re-meshing technique. The re-meshing technique permits to model the development of cracks in form of discrete fissures and independent on the mesh geometry. Levatti et al. (2019) proposed a theoretical and numerical formulation for modelling desiccation cracking in soils based on the fundamental principles of unsaturated soil mechanics (i.e. two stress state variables (Fredlund and Morgenstern 1977)) and strength of materials (i.e. Griffith theory of fracture (Griffith 1924)). Release node technique was implemented to simulate cracking in their model considering the effect of new boundaries induced by crack development on the continuing drying.

Interface element model is introduced to the standard finite element method in order to model the crack initiation and propagation. The path of crack development is dependent on the location of the preset interface elements with this approach. Sánchez et al. (2014) and Manzoli et al. (2017) proposed a novel approach to model the formation of drying cracks in soils, by fragmenting the conventional finite element mesh through the mesh fragmentation technique (MFT) and inserting specific interface elements, i.e. high aspect ratio (HSR) elements, between the regular finite elements. An isotropic (Sánchez et al. 2014) or an orthotropic (Manzoli et al. 2017) nonlinear constitutive mechanical models based on the damage theory was adopted for the HSR element. The progressive deterioration of soils subjected to hydraulic and mechanical loading is simulated by the evolution of the damage variable of HSR elements, which reproduced the main characteristics of desiccation cracking in the laboratory and in the field (e.g., Rodríguez 2006; Péron et al. 2009a; Konrad and Ayad 1997a). In order to simulate the Mode I cracks due to tensile failure, Stirling et al. (2017) developed the interface element incorporating the modified Mohr-Coulomb failure criterion, which is capable of modelling both shear failure and tensile failure, and extended a set of vertical interface elements with a predetermined space in the commercial software, FLAC (Itasca 2002). The two-phase flow module and the nonlinear elastic constitutive model with model parameters (e.g.., elastic modulus) varied with moisture content were employed to simulate the evaporation process and shrinkage deformation in soils. Moreover, the random distribution of crack

initiation location and strain localization were accounted for by incorporating the spatial variability of soil tensile strength. Recently, cohesive zone model (CZM, originated from Dugdale 1960; Barenblatt 1962) is widely used to simulate the desiccation cracking of soils as well. In this model, a linear or nonlinear cohesive softening law (Figure 2.16), i.e. the relationship between the normal bridging stress across the crack and the crack opening, is adopted to model the hardening and softening behavior of the virtual cracks before and after the crack initiation. Amarasiri and Kodikara (2010) employed the joint element to simulate the initiation and propagation of desiccation cracking of cohesive soils subjected to uniaxial tension, three-point bending, and evaporation in the field which was implemented in the commercial program UDEC (Itasca 2004). The failure criterion of joint elements is modified to accommodate to be capable of modeling the softening behavior of ductile cracks rather than brittle cracking behavior, when the normal stress reaches the tensile strength of joint elements. Gui et al. (2016) developed a mixed-mode cohesive fracture model, that combines tension, compression, and shear behavior of soil grain bonds, to simulate the desiccation cracking behavior of soils, extending the elastic-plastic-damage interface constitutive framework (Galvez et al. 2002). The cohesive fracture model was implemented by the commercial program UDEC, which has a considerable advantage over the traditional finite element method (FEM) and discrete element method (DEM), i.e. traditional FEM has a problem of handling multiple fractures; the particle deformation is not considered in conventional DEM. Vo et al. (2017) introduced a set of zero-thickness four-node joint elements (e.g., Goodman et al. 1968) in the standard finite element mesh to predetermine the development path for potential cracks. The hydro-mechanical coupling effect during the whole processes of evaporation, shrinkage deformation, crack formation and propagation was accounted for. The flow behavior through porous media and cracks are controlled by Darcy's law and cubic law, respectively. The isotropic and linear elastic constitutive model and cohesive crack model based on the damage theory were employed for the mechanical behavior modelling of soil matrix and cracks, respectively.

All the above three categories of modelling approaches (i.e. continuous approach, discontinuous approach, and interface element model) are determinative approaches based on mechanics principles. Based on the observations in the laboratory and in the field, however, the formation and development of desiccation cracks are essentially random and uncertain due to the intrinsic heterogeneity and/or external constraints. Therefore, several uncertain models have been developed based on mathematics and statistical physics to model the desiccation cracking behavior of soils (e.g., Chertkov and Ravina 1998; Horgan and Young 2000; Vogel et al. 2005).

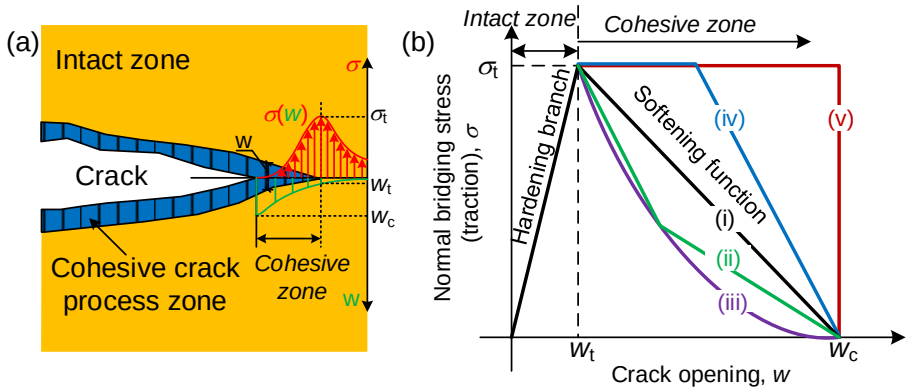

Figure 2.16 Schematic illustration of the cohesive zone model (CZM): (a) cohesive crack process zone (or, "cohesive zone") surrounding the crack (modified after Roth et al. 2014); (b) elastic-softening cohesive model including elastic hardening for intact zone and softening law for cohesive zone, i.e., (i) mono-linear, (ii) bi-linear, (iii) exponential, (iv) trapezoid shape, (v) rectangular shaped function.

2.1.6 Main challenges on the current research

In spite of extensive investigations, which include both large-scale field tests and small-scale laboratory tests that were undertaken over the past five decades, a thorough understanding of the intrinsic mechanisms related to desiccation cracking in cohesive soils is rather limited in the literature. To the best of the knowledge of authors, most of these studies extended unsaturated soil mechanics and fracture mechanics to interpret the desiccation cracking process in which three main successive stages are involved (e.g., Abu-Hejleh and Znidarčić 1995; Konrad and Ayad 1997b). The concepts of fracture mechanics are widely used to interpret soil cracking (e.g., Péron et al. 2009a; Lakshmikantha et al. 2012). However, there are many challenges, when applying principles of linear elastic fracture mechanics to the desiccation cracking in cohesive soils. The main challenges steam from the multiscale nature of the cohesive soils due to heterogeneity and the multiphysical coupling features of the desiccation cracking process.

The multiscale nature originates from the microstructure of the cohesive soils. Eghbalian et al. (2019) identified four scales to describe the hierarchical structure of clays, which include (i) nanoscale, (ii) microscale, (iii) mesoscale, and (iv) macroscale. The hierarchical structure produces a complicated pore structure in cohesive soils. For example, the compacted cohesive soils generally exhibit the pore structure of double levels, i.e. intra-aggregated pores and inter-aggregated pores. Upon drying, the inter-aggregate pores will desaturate firstly according to the well-known Yong-Laplace equation, which induces suction contraction of the aggregates and enlarger the inter-aggregated pores (e.g., Alonso et al. 2010; Guo and Fall 2018). The enlarged inter-aggregated pores which can be regarded as one source of defect, together with pores filled with entrapped air bubbles, act as crack initiators

(e.g., Snyder and Miller 1985) in the desiccating cohesive soils (Figure 2.5). This is how the multiscale nature of cohesive soils affects the heterogeneity and consequently affects the crack development upon drying, which adds complexity to the modelling studies of desiccation crack behavior of cohesive soils. Basically, desiccation and subsequent cracking result in the evolution of pore structure if the cracks are considered as extremely large pores. Therefore, the studies at the pore-scale or the local behavior are more meaningful and preferred than those base on the macro-scale or global behavior in an attempt to shed light on the mechanisms of desiccation cracking process (e.g., Shin and Santamarina 2011; Gui 2014; Hueckel et al. 2014; Wei et al. 2016; Eghbalian et al. 2019; Hueckel et al. 2019). In addition, due to the remarkable effect of the soil specimen geometry on soil cracking, the experimental investigations on a larger and thicker soil specimen incorporated with advanced monitoring techniques are recommended (e.g., Lakshmikantha et al. 2009; Khandelwal 2011; Simms et al. 2017; Ledesma et al. 2018).

The desiccation cracking processes in cohesive soils involves THM coupled processes (i.e. constrained shrinkage due to evaporation) interacting with the crack formation. The highly nonlinear processes (i.e. material non-linearity, and possible geometric non-linearity) pose great challenges to simulation studies on the desiccation cracking. Both continuum approach (e.g., Trabelsi et al. 2012; Sánchez et al. 2014; Hirobe and Oguni 2016; Stirling et al. 2017; Vo et al. 2017) and discontinuum approach (e.g., Amarasiri et al. 2011; Sima et al. 2014; Gui et al. 2016) have been developed to model the whole process of desiccation cracking including three stages (i.e. constrained shrinkage, crack initiation and crack propagation). However, the modelling studies reported in the literature are rarely capable to simulate the strong coupled process between the evaporation-induced shrinkage and the cracking development upon desiccation.

2.1.7 Summary

Desiccation cracking of cohesive soils is a multiphysical (i.e. thermo-hydro-mechanical) coupled and multiscale phenomenon, which has attracted attention both from researchers and practitioners. This study provides a comprehensive review on the desiccation-induced cracks in cohesive soils, which is summarized as follows.

(1) The published literature on desiccation-induced cracks in cohesive soils suggests the thermal-hydro-mechanical-chemical (THMC) significantly influences the ground and contributes to damage the nearby earth structures, such as slopes, dams and embankments. A better understanding of the desiccation cracking is necessary to further estimate the adverse effect of cracks on the geotechnical infrastructures.

(2) The observations on desiccation cracking in the large-scale field conditions as well as that in the controlled laboratory conditions are summarized. By analyzing the crack water contents of different soils reported in the literature, it is concluded that the crack water content is not the intrinsic soil property but is dependent on the soil properties, initial soil states, and the environmental conditions. Therefore, the crack initiation criterion should be derived in the framework of unsaturated soil mechanics and fracture mechanics (i.e. maximum tensile stress criterion). Based on the earlier observations and interpretations, the soil crack formation (i.e. initiation and propagation) is found to be controlled by both the deterministic factor (i.e. the generated stress field) and the stochastic factor (i.e. randomly distributed heterogeneities).

(3) The crack patterns induced by desiccation are presented based on extensive field and laboratory investigation studies. The origin of desiccation crack patterns is interpreted on the basis of fracture mechanics. The mixture of two typical patterns (i.e. the simultaneous hexagonal pattern, and the sequential orthogonal pattern) in cracked cohesive soils is a combined result of the strain energy release and the interaction between the generated stress field and the existing or induced heterogeneities. From the fracture mechanics standpoint of view, the effects of soil layer thickness, base friction, and environmental conditions on the crack block size (or crack spacing) can be better understood. Due to the non-visibility, the crack depth is more difficult to measure directly than the crack patterns on the soil surface.

(4) The multiscale nature associated with the heterogeneity of cohesive soils and the multiphysical coupled feature of the desiccation cracking processes pose significant challenges to the simulation studies on desiccation-induced cracking in cohesive soils.

2.2 Tensile strength of unsaturated soils

Tensile strength of soils is defined as the stress required to cause soil to failure in tension. From a historic point of view, the studies on the tensile strength of soils date back to 1920s in agricultural engineering (Hanies 1925; Fisher 1926), as the tensile strength is closely related to the crumbility and friability of soils during wetting and drying or during tillage operations (Dexter and Watts 2000). The tensile strength of soils is often assumed to be zero which means the soil cannot sustain any tensile stress. Such an assumption, considering the soil to be saturated with negligible tensile strength is regarded as the worst-case scenario and therefore conservative in conventional geotechnical engineering designs (Lakshmikantha et al. 2012). In recent two decades, there has been significant interest to investigate the

tensile strength of soils for the analysis of geotechnical and geoenvironmental engineering problems, because tensile strength is associated with the fundamental mechanism for soil cracking due to tensile stresses, wetting-drying cycles, or freeze-thaw cycles (e.g., Wang et al. 2007; Cordero et al. 2014; Li et al. 2018).

The tensile strength of unsaturated soils is widely explained by cohesion between soil particles (sand grains, or clay aggregates), which can be of two types, namely (i) the real cohesion due to cementing between soil particles, and (ii) the apparent cohesion due to suction (Lambe and Whitman 1979). Moreover, based on particle-scale force analyses, the tensile strength or more specifically, the "isotropic tensile strength" (Lu et al. 2007) of unsaturated soils is attributed to five types of interparticle physicochemical forces (Ingles 1962; Lu et al. 2007): (i) van der Waals attraction, (ii) electrical double layer repulsion or attraction, (iii) cementation due to solute precipitation, (iv) capillary stress due to the negative pore water pressure (i.e. matric suction), (v) capillary stress due to the surface tension. The contributions arising from the first three forces are for cohesionless soils is not pronounced, the tensile strength of cohesionless soils is mainly induced by capillary stresses due to matric suction (e.g., Lu et al. 2009) and surface tension (e.g., Jindal et al. 2016; Yin and Vanapalli 2018b). The tensile strength is essentially is the macroscopic response of the force transmission within the micro-fabric dependent unsaturated soil specimen under specific tensile stress conditions. From micromechanics studies, the mechanical responses including tensile strength of unsaturated soils also depend on the inherent or induced anisotropy which may influence the force transmission (e.g., Li 2003; Koliji 2008; Guo 2014). For compacted cohesive soils which typically exhibit double pore-structural levels (i.e. intra-aggregate and inter-aggregate pores), the fabric effect is as important as soil suction and degree of saturation in determining the macroscopic behavior during hydraulic and/or mechanical loading. Present evidence indicates that cohesion due to interparticle attractive forces are quite small in almost all cases, whereas that due to chemical cementation can be significant. If particle contacts cannot carry tension, it is often assumed that the tensile cracking occurs when the minor principal effective stress (σ_3') becomes zero. If the soil is cemented, cracking is generated when the minor principal effective stress is equal to the negative value of the tensile strength (Mitchell and Soga 2005). For cohesive soils especially soils with high plasticity index, the first three forces are significant due to complicated physicochemical activities. Even though the first three forces are significant, only cementation effect may influence the cohesion and tensile strength (Ingles 1962; Wollborn et al. 2017). Mullins and Panayiotopolous (1984), Koolen (1987), Snyder and Miller (1989) and Aluko and Koolen (2000) suggested that inter-aggregate capillary bonds constitute the dominant cohesion and tensile strength of aggregated soils. On the other hand, Chandler (1985) and

Guérif (1990) argued that it is the breakage of the weakest bonds which could be either intra-aggregate bonds or inter-aggregate bonds that drives the tensile failure of agricultural soils, which depends on the failure modes (brittle failure or ductile failure). In order to achieve a better understanding, the effect of microstructure on the tensile strength of cohesive soils needs more investigations.

2.2.1 Experimental determination of tensile strength of unsaturated soils

The laboratory test methods for determining the tensile strength of unsaturated soils can be mainly classified into two categories: (i) direct methods with direct application of tensile stress to a soil specimen, and (ii) indirect methods with indirect induced tensile failure by applying compressive forces or bending moments which generate tensile stress within a soil specimen. Direct methods mainly include uniaxial tensile test (e.g., Tschebotarioff et al. 1953; Rumpf 1961; Conlon 1966; Bofinger 1970; Schubert 1972; Ajaz and Parry 1974; Mikulitsch and Gudehus 1995; Tang and Graham 2000; Kim and Hwang 2003; Nahlawi et al. 2004; Tamrakar et al. 2005; Lu et al. 2005; Vesga and Vallejo 2006; Tang et al. 2015; Stirling et al. 2015; Murray and Tarantino 2019), triaxial tensile test (Péron 2008), hollow cylinder test (Al-Hussaini and Townsend 1974), centrifugation technique (Vomocil et al. 1961), and pneumatic fracture technique (Snyder 1980). Indirect methods mainly include flexure beam test (Leonards and Narain 1963; Ajaz and Parry 1975; Thusyanthan et al. 2007; Narvaez et al. 2015), double punch test (Fang and Chen 1970; Favaretti 1995; Li et al. 2011) or as referred as “unconfined penetration test” (Fang and Fernandez 1981; Kim et al. 2012), and Brazilian tensile test (Narain and Rawat 1970; Krishnayya and Eisenstein 1974; Das et al. 1995; Villar et al. 2009; Beckett et al. 2015; Akin and Likos 2017). Figures 2.17(a)~(g) and Figures 2.17(h)~(k) illustrate tension testing devices for determining the tensile strength of unsaturated soils in the literature based on direct method and indirect method, respectively. Table 2.5 summarizes the principle, strengths and limitations of each method.

Different test methods have been found to influence the tensile strength measurements (e.g., Bofinger 1970; Satyanarayana and Rao 1972; Favaretti 1995; Li et al. 2007; Stirling et al. 2015), due to the differences in stress state that the soil specimen is subjected to and the model used interpret the test results. Most direct methods involve pulling induced tensile failure, grasping a specimen at both ends by an adhesive or gripping a specimen along its sides by some form of grappling system. Although the principle and interpretation method is simple, direct tension tests are usually difficult to perform due to the following reasons: (i) the uniform tensile stress distribution on the failure plane is hard to be guaranteed, due to the emergence of bending momentum induced by the misalignment between the specimen and the gripping system or of disturbance from the specimen ends under grasping state with compression and shearing; (ii)

the dumbbell-shaped or dog-bone-shaped specimen used in some tests to induce cracking in the middle part (e.g., triaxial tensile test) is difficult to prepare without damage (Win 2006; Zhang et al. 2015). Compared to direct methods, indirect methods are easy-to-adopt. However, the assumptions on which the interpretation of test results by indirect methods based are not always valid. For example, the beam theory for interpreting the test results by flexure beam tests and the neglect of shear stress on the transverse section induced by self-weight may result in overestimation of tensile strength, especially for soft clay (Ammeri 2009). Additionally, the combination of tension and compression may invoke a complex mode of failure, rather than pure tensile failure mode, such as Brazilian split test (Leavell and Peters 1987; Namikawa and Koseki 2007). Table 2.5 summarizes the principle, technique, strength and limitations of various tension testing methods for unsaturated soils in the literature.

Numerous studies in the literature focused on desiccation cracking and tensile strength. The experimental studies on desiccation cracking, however have been typically decoupled from the determination of tensile strength. The soil undergoes increasing suction and decreasing lateral stress under nearly constant vertical stress and tensile stresses develop during constranined desiccation prior to cracking. On the other hand, the soil specimen is subjected to increasing tensile stresses up to cracking at nearly constant suction (or constant water content). However, it is well recognized that soil behavior is stress-path and stress-history dependent. Very recently, in several studies focused on the determination of the tensile strength of cohesive soils during desiccation, such as restrained ring test (e.g., Shannon et al. 2014; Cheng et al. 2020b), film test (e.g., Uday et al. 2014) and desiccation test using a novel desiccation-tensile strength apparatus (e.g., Varsei et al. 2016). It is rational to determine the tensile strength during desiccation than to drive tensile failure by applying tensile forces. However, complementary tensile strength determination by direct or indirect tensile tests is necessary due to the following reason. It is well accepted that tensile strength of cohesive soils typically depends on moisture content and dry density. The dry density of soil specimen and the constraint conditions during desiccation cannot be measured or controlled using the desiccation-tensile strength apparatus (Varsei et al. 2016). Thus, the tensile test is capable to identify the salient factors which influence the tensile strength with measured or controlled dry density and boundary conditions.

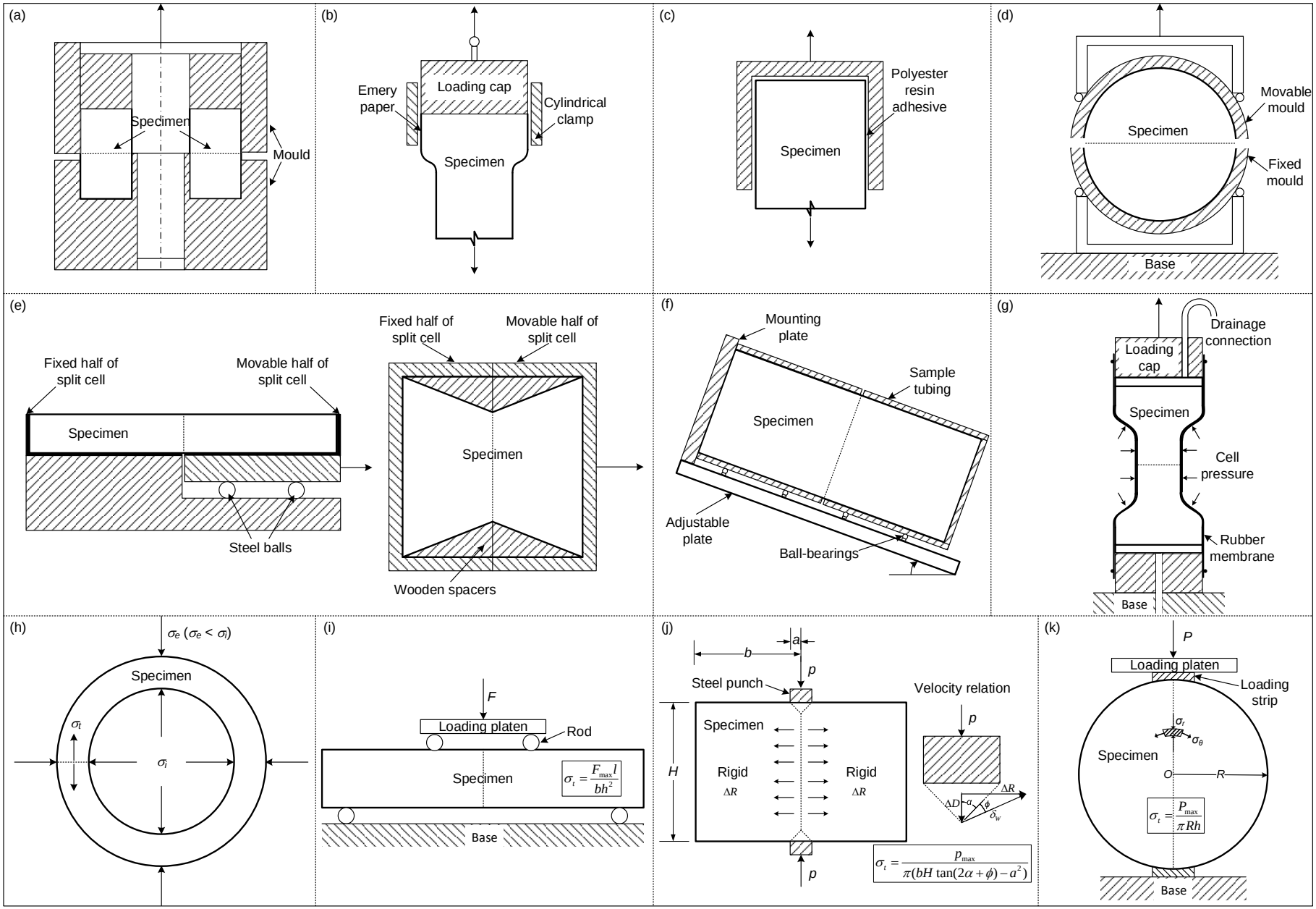

Figure 2.17 Illustration of direct method ((a)~(g)) and indirect method ((h)~(k)) for determining tensile strength of unsaturated soils.

Table 2.5 Summary of principle, technique, advantages and limitations of various tension testing methods for unsaturated soils.

Test method	Test technique and principle	Advantages and Limitations	References	Figure No.
Direct methods	**Uniaxial tensile test (wall adhesion method):** The tensile force in the fractured cross-section is transmitted through the end faces, the sidewall and the interior pin without using any adhesive.	**Limitations:** (i) This method is suitable for ductile soils which typically fail at a large tensile strain; (ii) this apparatus is not easy to set-up for use.	Rumpf (1961), Pietsch et al. (1969)	Figure 2.17(a)
	Uniaxial tension test (adhesion method): The specimen is similar to that used in conventional triaxial apparatus, except that its central portion is necked down in order to develop higher stresses in this zone.	**Advantages:** (i) Eccentricity is avoided during the application of the tension force by using the ball-and-socket arrangement at both ends of the specimen. **Limitations:** (i) This method can only be used for soils which are sufficiently strong for the two end faces of a cylindrical specimen to be bonded to the adapters without damage due to slippage; (ii) The effective length of the specimen is not accurately known; consequently, the tensile strain measurements are not reliable.	Conlon (1966)	Figure 2.17(b)
	Uniaxial tension test (adhesion method): The ends of the specimen are bonded to steel plates with quick-setting polyester resin. The tensile force is applied through a cap which is placed in a spherical seating to reduce the effect of end rotation.	**Advantages:** (i) The effect of stress concentration is reduced by utilizing the bonded side plates compared with Conlon (1966) apparatus. **Limitations:** (i) This method can only be used for soils which are sufficiently strong for the two end faces of a cylindrical specimen to be bonded to the adapters; (ii) The effective length of the specimen is not accurately known; consequently, the tensile strain measurements are not reliable.	Bofinger (1970)	Figure 2.17(c)
	Uniaxial tension test (adhesion method): The specimen is glued into the bottom and top moulds, then the tension force is applied by the load frame via the top transducers.	**Advantages:** (i) This apparatus is suitable for measurement tensile failure associated with both brittle and ductile fracture. **Limitations:** (i) Good alignment and reliable adhesion between the mould and the specimen should be ensured.	Tang and Graham (2000)	Figure 2.17(d)

	Uniaxial tension test (Split plate method): Pairs of split cells keep the sample in place. One pair is fixed, whereas the other rested on a ball-bearing and is pulled apart. This method is also be used by other researchers (e.g., Dawes 1952, Schubert 1972, Mikulitsch and Gudehus 1995, Nahlawi et al. 2004, Tamrakar et al. 2005, Lakshmikantha et al. 2012, Tang et al. 2015, Stirling et al. 2015). The main difference among these apparatus is the shape of the split cells.	**Advantages:** (i) This apparatus can overcome to some extent the typical disadvantages of adhesion-method based uniaxial tensile apparatus, such as stress concentration, misalignment, and eccentricity. (ii) This method is suitable for bulk materials with very low tensile strength. **Limitations:** (i) The adhesion conditions between the material and the support, and the height of the sample will influence the measurements; (ii) This apparatus involves a relatively large amount of soils and therefore causes challenges in obtaining multiple moist samples with a consistent porosity.	Perkins (1991), Kim and Hwang (2003), Jindal et al. (2016)	Figure 2.17(e)
	Uniaxial tension test (self-weight induced rupture method): The sample tubing filled with the compacted specimen is placed horizontally on a set of spherical ball-bearings on the adjustable table. The table is inclined progressively to increase the gravitational force along the longitudinal direction of the sample, thus applying a tensile force to the sample.	**Advantages:** (i) Simple test set-up and procedures with accurate and reliable measurements; (ii) This method can overcome the disadvantage of uniaxial tension tests based on adhesion method, which cannot be directly utilized to measure the tensile strength of cohesionless soils due to the stress magnitude and resolution and the required confinement. **Limitations:** (i) This method is suitable for unsaturated soils with low cohesion (e.g., sands and low-plastic silts).	Lu et al. (2005)	Figure 2.17(f)
	Triaxial tensile test: A triaxial apparatus is used with a soil specimen which is necked down at the central section. Confining pressure is used to produce tensile stresses, instead of pulling the ends of the specimen to the platens.	**Advantages:** (i) This apparatus could be used to investigate the effect of confining pressure on the tensile failure of unsaturated soils. **Limitations:** (i) Although the tensile strength of soils can be obtained with reasonable accuracy, accurate strain measurements are not possible. Because only the necked part of the specimen is in tension, while the rest of the specimen is in compression.	Péron (2008)	Figure 2.17(g)
	Hollow cylinder test: The soil samples have the form of hollow cylinders and fail at the combination of the internal and external hydrostatic pressures.	**Advantages:** (i) Well-defined stress states without uncontrolled stress concentration;	Al-Hussaini and Townsend (1974)	Figure 2.17(h)

		(ii) The possibility of investigating the deformability and strength for various stress states and for long-term and drained tests. **Limitations:** (i) Specimen preparation technique and apparatus set-up procedures are complicated.		
Indirect methods	**Flexure beam test:** The test produces a constant bending moment in the central zone of the specimen. The stress distribution on the failure cross section is assumed to be complied by the elastic beam theory.	**Advantages:** (i) This method is easy-to-adopt and the test results are easy to interpret. **Limitations:** (i) The test results would overestimate the tensile strength values compared with direct methods, due to the oversimplification of the linear elastic beam theory. (ii) This method is more suitable for cohesive soils.	Ajaz and Parry (1975), Narvaez et al. (2015)	Figure 2.17(i)
	Double punch test and Unconfined penetration test: The tensile failure is interpreted by the theory of upper bound limit analysis method.	**Advantages:** (i) This apparatus can overcome the disadvantage that the displacement or strain measurements are not reliable and the non-uniformity of the stress distribution within the specimen associated with most uniaxial tension tests. **Limitations:** (i) This type of test is suitable for the tensile failure associated with brittle fracture.	Fang and Chen (1970), Fang and Fernandez (1981), Kim et al. (2012)	Figure 2.17(j)
	Brazilian tensile test: A disc specimen is subjected to a compressive force which is applied over a short strip of the circumference at each end of a diameter. The soil specimen is assumed to be homogeneous, isotropic and linearly elastic before brittle failure occurs.	**Advantages:** (i) This type of test is easy-to-adopt and the test results are easy to interpret. **Limitations:** (i) The reliability of the interpreted tensile strength utilizing this method is questionable due to the assumptions for interpreting the test results (e.g., the specimen is linearly elastic).	Krishnayya and Eisenstein (1974), Das et al. (1995), Munkholm and Kay (2002), Villar et al. (2009), Akin and Likos (2017), Gaspar and Jacobsz (2021)	Figure 2.17(k)

2.2.2 Models for predicting the tensile strength of unsaturated cohesionless soils

Various models have been proposed in the literature from different research fields, for predicting the tensile strength of unsaturated granular materials. The existing models for unsaturated cohesionless soils can be classified into two categories, namely, (i) theoretical models based on micromechanics or macromechanics approach, and (ii) empirical models based on regression analysis using extensive test data.

Table 2.6 summarizes models developed from the micromechanics point of view from the literature. Haines (1925) investigated the relationship between pressure deficiency of pore water and the cohesion induced by capillary force of unsaturated soils. Fisher (1926) studied the contribution arising from both pore water and air-water interface on the cohesion of unsaturated soils. The relationships proposed by those investigators (i.e. Eq.s (2.11) and (2.12)) relate the cohesion of unsaturated soils, which must be overcome by the applied tensile stress for tensile failure, to water content and particle radius, for idealized noncolloidal soils consisting of uniformly rigid spheres at regular packing states (i.e. open or close). However, neither the water-soil surface contact angle (δ) nor the distance between adjacent particles (a) was taken into consideration in the Haines-Fisher theory.

Rumpf (1961; 1970) simplified the assembly of real soil particles as smooth particles with a finite surface separation. The relationship among the tensile strength, the interparticle forces between adjacent particles, the porosity, and the mean size of particles was derived statistically as Eq. (2.13) in the pendular regime. In addition, Rumpf assumed that the tensile strength of granular materials in the capillary regime can be approximated to the capillary pressure (P_c). Pietsch (1968) assumed that the relationship between the tensile strength and the degree of saturation increases linearly from a critical degree of saturation S^*, corresponding to the saturation where water bridges in the aggregates begin to connect to each other, to saturated state (i.e. S =1). Thus, the tensile strength of granular materials in the entire moisture range can be estimated using Eq. (2.14), by combining Rumpf's theory and Pietsch's assumption. Furthermore, the tensile strength of wet aggregates in the capillary regime was calculated by the product of degree of saturation and capillary pressure (Schubert 1973; 1975). The tensile strength in the funicular regime was estimated by superimposing linearly the bonding force originating from water bridges and that caused by saturated pores filled with bulk water (Eq. (2.15)).

The Haines-Fisher theory and the Rumpf-Schubert model provides explanation for the mechanical approach and facilitates to the fundamental understanding the tensile strength of unsaturated granular

materials. However, the micromechanical models have limitations for their use in practice because of oversimplified assumptions. The tensile failure will not take place until bonding forces acting on the contacting points between adjacent particles on the failure plane are overcome. This is equivalent to stating that the effective stress (carried on by the soil matrix in soil-water-air system subjected to external forces) is zero on the tensile failure plane at failure. Thus, the tensile strength can be obtained by macromechanics approach by equating the effective stress of unsaturated soils to zero (Table 2.7). Based on Bishop's effective stress principle (Bishop 1959), Snyder and Miller (1985) proposed a novel formula (Eq. (2.16)) to estimate the tensile strength of unsaturated soils, by combining Haines-Fisher theory and Griffith's theory (Griffith 1924) of fracture failure of cracked elastic solids. However, the comprehensive parameter, $F(S)$, which was introduced to reflect the tensile failure patterns associated with the complex mechanism of capillary effect and the soil structure characteristics, is difficult to estimate. Based on the concept of "suction stress" and the corresponding effective stress formulation for unsaturated soils (Lu and Likos 2006), Lu et al. (2009) proposed a theoretical formulation (Eq. (2.17)) to evaluate the uniaxial tensile strength by including it with the nonlinear Mohr-Coulomb failure criterion (Figure 2.18(a)).

Several empirical models have been proposed in the literature using regression analysis using extensive experimental data. Table 2.8 lists several empirical models proposed in recent years to predict the variation of the tensile strength of unsaturated cohesionless soils. For example, Kim (2001) proposed a formula (Eq. (2.18)) to evaluate the tensile strength of unsaturated sands in the pendular regime, considering effects of both water content and relative density. These empirical models are simple for use in engineering practice applications. However, most empirical models have several fitting parameters which are constants derived from regression analysis based on experimental data of several soils that belong to a specific group or variety. For this reason, such models are soil specific, which restricts the efficiency of those models for predicting the tensile strength for unsaturated soils with different properties. The empirical relationships could not yield a reliable and generalised method for determination of the tensile strength of unsaturated soils based on the critical review and comprehensive investigation of the empirical models by Venkataramana et al. (2009).

Table 2.6 Theoretical models for predicting the tensile strength of unsaturated cohesionless soils based on micromechanical approach.

Equation No. and Reference	Equation and Notations
(2.11) Haines (1925)	$\Pi = \zeta \frac{T_s}{R} \frac{1-2\tan(\theta/2)}{1+\tan(\theta/2)}$ where Π is cohesion due to capillary forces, ζ is a constant related to the packing state ($4\pi\sqrt{3}$ for close packing; π for open packing), T_s is surface tension of the wetting liquid, R is the radii of soil particles, and θ is the half-filling angle.
(2.12) Fisher (1926)	$\Pi = \xi \frac{T_s}{R} \frac{1}{1+\tan\theta}$ where ξ is a constant related to the state of packing ($\sqrt{2}\pi$ for close packing; $\pi/2$ for open packing).
(2.13) Rumpf (1961; 1970)	In pendular regime, $\sigma_{tp} = \frac{1-n}{n} \frac{F_t}{d^2}$ with $\begin{cases} F_t = \pi d T_s \sin\theta \left[\sin(\theta+\delta) + \frac{\sin\theta}{4}\left(\frac{1}{r^*} - \frac{1}{h^*}\right)\right] \\ r^* = \frac{r}{d} = \frac{(1-\cos\theta)+a/d}{2\cos(\theta+\delta)} \\ h^* = \frac{h}{d} = \frac{\sin\theta}{2} + \frac{r}{d}\left[\sin(\theta+\delta)-1\right] \end{cases}$; In capillary regime, $\sigma_{tc} \approx P_c = \eta \frac{1-n}{n} \frac{T_s}{d} f(\delta)$. where σ_{tp} is tensile strength of unsaturated soils in pendular regime, n is porosity, F_t is the total interparticle bonding force due to water bridges (i.e. the resultant of surface tension and capillary pressure), d is the mean diameter of soil particles, δ is contact angle between the solid and water phase, a is the surface separation between adjacent soil particles, h and r are two radii of curvature of the water bridge when taken as arcs of a circle; σ_{tc} is tensile strength of unsaturated soils in capillary regime, P_c is capillary pressure, $f(\delta)$ is a function of the contact angle, which is unity for water wetting the solid completely ($\delta = 0^\circ$), the constant η with values between 6 and 8 which can be measured by experiments.

(2.14) Pietsch (1968)	$\begin{cases} FZ = \frac{9}{8}\cdot\frac{1-n}{n}\cdot FH \quad for\ 0 \le S < S^*; \\ FZ = FZ_b^* + \frac{S-S^*}{1-S^*}\left(FPK - FZ_b^*\right) \quad for\ S^* < S < 100\%. \end{cases}$ with $\begin{cases} FZ_b^* = FZ\left(S=S^*\right) = \frac{9}{8}\cdot\frac{1-n}{n}\cdot FH\left(\theta^*, \delta^*, \left(\frac{a}{d}\right)^*\right); \\ FPK = FZ\left(S = 100\%\right). \end{cases}$ where $FZ = \sigma_t \cdot \frac{d}{T_s}$ is the dimensionless tensile strength; $FPK = P_c \cdot \frac{d}{T_s}$ is the dimensionless capillary pressure; $FH = FH\left(\theta, \delta, \frac{a}{d}\right)$ is a complicated function of half-filling angle (θ), contact angle (δ), and the dimensionless length ratio (a/d); S^* is the critical saturation.
(2.15) Schubert (1973; 1975)	In capillary regime, $\begin{cases} \sigma_{tc} = SP_c \\ P_c = \omega\frac{1-n}{n}\frac{T_s}{d} \end{cases}$; In funicular regime, $\sigma_{tf} = \frac{S_c - S}{S_c - S_r}\sigma_{tp} + \frac{S - S_r}{S_c - S_r}\sigma_{tc}$. where S is degree of saturation, ω is a constant related to the grain size distribution (6 - 8 for a narrow range, and 1.9 - 14.5 for a wide range (Schubert 1984)), σ_{tf} is tensile strength of unsaturated soils in the funicular regime.

Table 2.7 Theoretical models for predicting the tensile strength of unsaturated cohesionless soils based on macro-mechanical approach.

Equation No. and Reference	Equation and Notations
(2.16) Snyder and Miller (1985)	$\sigma_t = F\left(S\right)\left(u_a - u_w\right)$, with $F\left(S\right) = \frac{\chi}{f\left(S\right)}$ where $F\left(S\right)$ is a comprehensive parameter, χ is the Bishop (1959) effective stress parameter, $f\left(S\right)$ is a proportionality factor in the context of Griffith's stress concentration theory of fracture (Griffith 1924) and is a function of the degree of saturation, and $\left(u_a - u_w\right)$ is the matric suction or the difference between pore-air pressure and pore-water pressure.

(2.17) Lu et al. (2009)	$\sigma_{tu} = -[2\tan\phi_t \tan(\frac{\pi}{4} - \frac{\phi_t}{2})]\cdot\sigma^s$, with $\begin{cases} \sigma^s = -(u_a - u_w)S_e \\ S_e = \frac{S - S_r}{1 - S_r} = \left\{\frac{1}{1+\left[\alpha_{vg}(u_a - u_w)\right]^{n_{vg}}}\right\}^{1-1/n_{vg}} \end{cases}$ where σ_{tu} is the uniaxial tensile strength of unsaturated soils, σ^s is the "suction stress" proposed by Lu and Likos (2004; 2006), ϕ_t is the friction angle at low normal stress level.	

Table 2.8 Empirical models for predicting the tensile strength of unsaturated cohesionless soils.

Equation No. and Reference	Equation and Notations	Soil Name (USCS, Location)	Test Method
(2.18) Kim (2001)	$\sigma_{tp} = P_r \ln(D_r)\left[69\ln(w)+170\right]$ σ_{tf} or $\sigma_{tc} = S(u_a - u_w)$ where P_r is a reference pressure (1 Pa), w is gravimetric water content (%), D_r is relative density (%).	Ottawa sand (F75-C) (SP, Illinois, USA)	Uniaxial tensile test
(2.19) Munkholm and Kay (2002)	$\sigma_t = \beta\cdot\psi^{\alpha}$ where α and β are fitting parameters depending on soil aggregates of different particle diameters, σ_t and ψ are in kPa.	two cropping system samples, and two traffic experiment samples (SC/SM, South Denmark, Denmark)	Brazilian tensile test

Notations: SP, poorly-graded sand; SC/SM, Clayey/Silty sand.

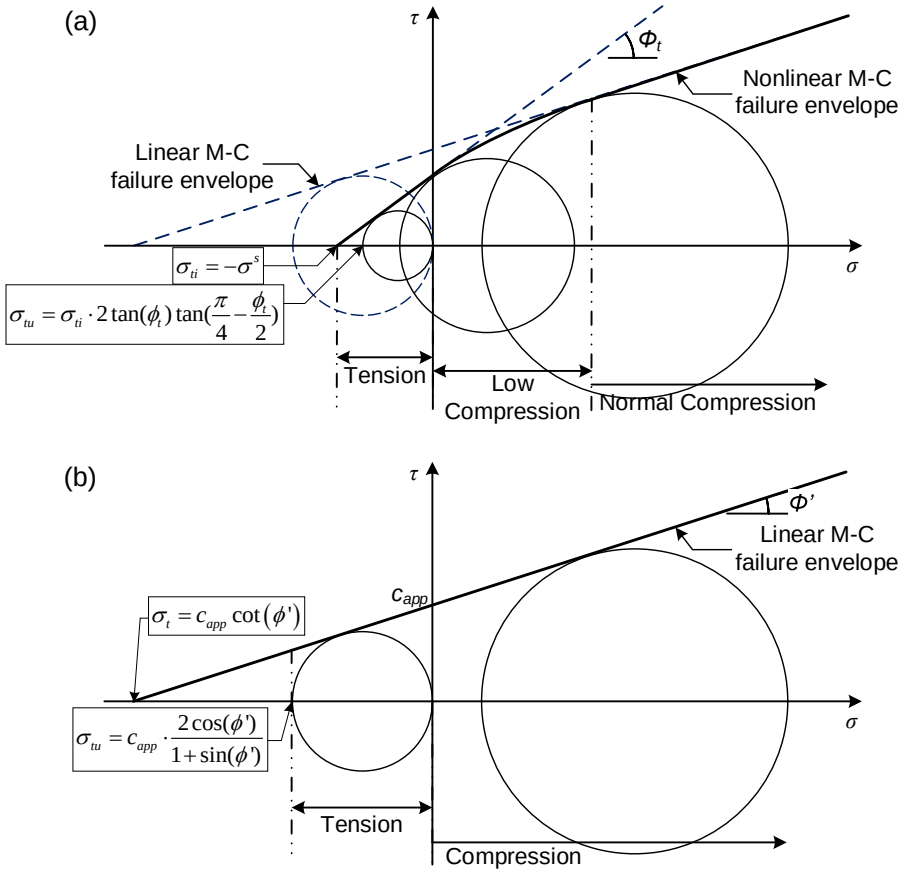

Figure 2.18 Conceptual illustration of tensile strength models of unsaturated soils proposed by (a) Lu et al. (2009); (b) Lakshmikantha et al. (2012) and Varsei et al. (2016).

2.2.3 Predictive models for the tensile strength of unsaturated cohesive soils

Several models have been proposed in the literature to predict the tensile strength of compacted cohesive soils. Generally, these models can be grouped into two categories: (i) empirical models (Table 2.9), and (ii) mechanics-based models (Table 2.10).

2.2.3.1 Empirical models

Zeh and Witt (2005) measured the tensile strength of a medium plasticity clay (called "Plessa clay") under constant initial soil structure (controlled by compaction conditions) by subsequently exposing to different suctions. The direct tensile test was conducted on hollow-cylinder-shaped specimens (in order to ensure the maximum tensile stresses to occur in the middle part of the specimen) by a modified triaxial apparatus. An exponent-form correlation on matric suction (Eq. (2.20)) was proposed for a wide range of degree of saturation (i.e. S_r = 0.1~0.9) to reproduce the dependency on the soil-water interactions by increasing up to a peak value and a slight decrease afterwards. Win (2006) performed a series of uniaxial tensile tests on three different soils from existing embankment dams and investigated the tensile strength of compacted

soils in relation to compaction water content, compaction density ratio, soil suction, the effect of drying and wetting, etc. Empirical relationships are given as Eqs. (2.21) and (2.22) for compacted path and compacted-desiccation path, respectively. Lutenegger and Rubin (2008) evaluated the tensile strength of four fine-grained soils using the double punch test for three different levels of compaction energy. The results show a general global linear trend between the normalized tensile strength and the water content deviation away from the optimal water content (w_{opt}), particularly in the range of w_{opt} ±4%, which is a typical working range for many field compaction specifications (Eq. (2.23)). Péron (2008) investigated the tensile failure criterion for the unsaturated Bioley silt (a clay with medium plasticity) by suction-controlled triaxial tensile tests with dog-bone shaped specimens imposed to different suction values. Based on the analysis of the measured data and other published data (e.g., Farrell et al. 1969; Rodriguez et al. 2007), an exponential Eq. expressed in the form of effective stress (Eq. (2.24)) is developed to include the matric-suction dependency. Venkataramana et al. (2009) evaluated the tensile strength of 14 fine-grained soils compacted at optimum water content by performing triaxial undrained shear tests interpreting the experimental data with Mohr-Coulomb failure criterion and developed a generalized relationship (Eq. (2.25)) utilizing multiple soil properties, such as clay content and cation-exchange capacity. Zhang et al. (2015) presented uniaxial tensile test results for two compacted soils used in the core walls of two high earth-rockfill dams and proposed an empirical formula (Eq. (2.26)) for estimating the tensile strength of compacted soils with water content close to the optimum water content (which is the interested condition for engineering practice).

2.2.3.2 Mechanics-based models

Based on Bishop's effective stress principle (Bishop 1959), Mullins and Panayiotopoulos (1984) proposed a formula (Eq. (2.27)) to estimate the tensile strength of unsaturated soils based on experimental data of Brazilian tensile tests on unsaturated two sand-kaolin mixtures. Snyder and Miller (1985) proposed a novel formula (Eq. (2.16)) to estimate the tensile strength of unsaturated soils, by combining the Haines–Fisher theory and Griffith's theory (Griffith 1924) for fracture failure of cracked elastic solids. However, the comprehensive parameter, F(S), which was introduced to reflect the tensile failure patterns associated with the complex mechanism of the capillary effect and the soil structure characteristics, is difficult to estimate. Based on the modified Griffith theory of brittle fracture (Brace 1960) and the shear strength envelope of unsaturated soils (Fredlund and Morgenstern 1978), Morris et al. (1992) correlated the uniaxial tensile strength of compacted soils to matric-suction derived cohesion (Eq. (2.28)). With a linear relationship between matric suction and water content on a semilogarithmic plot and accounting for the compaction effects (i.e. static compaction pressure), Leavell and Peters (1987) further developed a semiempirical

relationship (Eq. (2.29)) for the variation of uniaxial tensile strength with water content and void ratio (or density). According to experimental investigation on the indirect tensile strength of a Wageningen silty clay loam by Brazilian tensile tests, Aluko and Koolen (2000) developed a model of mechanics of capillary crumbling in structured agricultural soils, which indicated that the inter-aggregate bonding strength determined the tensile strength of aggregated soils (Eq. (2.30)). Thusyanthan et al. (2007) performed flexure beam tests on a remoulded kaolin clay which is at initially slurry state and then drying to target suction values (less than air entry value, the specimens remained saturated throughout) before subjected to bending momentum load. Analyzing test results from the point view of critical state soil mechanics framework (e.g., Modified Cam-Clay model, Schofield and Wroth 1968), zero effective tension cut-off was observed for pure mode I crack initiation (tensile failure), and a trend line with reasonable bounds (Eq. (2.31)) was offered to estimate the total maximum tensile stress for crack initiation during flexure beam tests, which depends on the preconsolidation pressure and initial mean effective stress (i.e. matric suction in this study). Shin and Santamarina (2011) implemented the study of desiccation crack initiation and propagation on a remoulded saturated Ca-montmorillonite using a combination of experimental and numerical methods. Based on particle-level and macro-scale analysis of desiccation crack formation stages, it concluded that once the air-water membrane invades the specimen, the crack will grow normal to the applied tensile load, eventually giving the appearance of a tensile failure, while the soil mass has remained in effective compression and saturated states at all times before crack initiation. Therefore, an upper bound for the apparent tensile strength was estimated in terms of the air-entry value of soils (Eq. (2.32)), which is consistent with the argument by Mitchell and Soga (2005). Murray and Tarantino (2019) developed an experimental apparatus for uniaxial tensile tests with suction monitoring facility (i.e. high-capacity tensiometers) on two clayey soils under saturated and unsaturated conditions. It was found that the tensile failure of normally consolidated specimens occurs as a combined mode I and mode II crack and the Mohr-Coulomb failure criterion can be extended to predict the tensile strength of both saturated and unsaturated soils in terms of effective stress and average skeleton stress, respectively (Eq. (2.33)).

A similar approach of extending the Mohr-Coulomb failure criterion for interpreting the shear strength of unsaturated soils (e.g., Fredlund et al. 1978) can also be followed for tensile strength of unsaturated soils to include the effect of soil suction. Extending the same philosophy, the tensile strength of unsaturated soil can also be predicted by combining the Mohr-Coulomb shear strength parameters which reflect the macromechanical properties and the SWCC which includes the micromechanics associated to water retention characteristics. Lakshmikantha et al. (2012) investigated the tensile strength of a low-plasticity clay (Barcelona silty clay) by direct tensile tests for two specific bulk densities and two specific dry

densities with different compaction water content. Taking advantage of the shear strength Eq. with the effective degree of saturation introduced by Alonso et al. (2010) and the "apparent cohesion" concept for unsaturated soils, Eq. (2.34) was derived to determine the tensile strength of compacted soils. Following Lakshmikantha et al. (2012) model, Varsei et al. (2016) proposed Eq. (2.35), which was derived for two clayey soils using the experimental results obtained from split plate method to predict the uniaxial tensile strength of unsaturated soils. This relation can be obtained from Mohr's circle with zero major principal stress (Figure 2.18(b)). Following the tensile strength model for unsaturated sands (Eq. (2.17)) proposed by Lu et al. (2009), Tang et al. (2015) proposed Eq. (2.36) to estimate the tensile strength of compacted clayey soils based on experimental data of uniaxial tensile tests on a low plasticity clay. Figure 2.18 illustrates the tensile strength models for unsaturated cohesionless soils and cohesive soils proposed by Lu et al. (2009), Lakshmikantha et al. (2012) and Varsei et al. (2016), respectively. Trabelsi et al. (2012) proposed a formula for the tensile strength of unsaturated soils (Eq. (2.37)) accounting for the significance of both suction and porosity for the variation of "apparent cohesion" and consequently tensile strength of unsaturated clayey soils. More recently, Trabelsi et al. (2018b) investigated the tensile strength as well as the water retention property and microstructural characteristics of an unsaturated clay exposed to three hydro-mechanical paths (i.e. "C", "CD", and "SD") prior to the uniaxial tensile loading. A simple but comprehensive model (Eq. (2.38)) was proposed for the variation of tensile strength of remoulded and compacted soils including the role of soil fabric and its effect on the soil water retention capability, dry density and initial water content.

2.2.4 Discussion and concluding remarks

This subchapter 2.2 is devoted to a comprehensive review on experimental determination and theoretical prediction of the tensile strength of unsaturated cohesionless soils and cohesive soils. The concluding remarks regarding the tensile strength of unsaturated soils are made as follows:

(1) For the various methods for experimental determination, the direct method is recommended due to the pure tensile failure could be guaranteed, such as the uniaxial tensile test. However, the direct method has relatively stringent requirements of the specimen preparation and test equipment, such as the triaxial tensile test. In contrast, the indirect method is commonly used due to the simple procedure of specimen preparation and the availability of test equipment, such as the Brazilian split test. Indirect methods are still widely used in spite of some limitations for determining the tensile strength of soils. More recently, direct methods are being recommended as they provide reliable measurements of tensile strength of unsaturated soils (e.g., Tang et al. 2015; Trabelsi et al. 2018b; Murray and Tarantino 2019). However, there are several

researchers who encourage the interpretation of indirect tensile tests as they are simple for implementing in engineering practice (Stirling et al. 2015; Gaspar and Jacobsz 2021).

(2) As the various prediction models of tensile strength of unsaturated soils, two main categories could be identified; namely, empirical models and mechanics-based models. Mechanics-based models are preferred due to reliability and rationality. The core motivation of mechanics-based models is to formulate the tensile resistance as the macroscopic response of unsaturated soils which reflects the stress transmission at the microscale. For example, the concept of suction stress proposed by Lu and Likos (2006) reflects the contribution of suction in unsaturated cohesionless soils to the internal stress state at the level of representative elementary volume (REV). The variation of microstructure in compacted cohesive soils with different water contents adds the complexity when applying the concept of suction to unsaturated cohesive soils (e.g., Tang et al. 2015). The effect of microstructure on the internal stress transmission in unsaturated cohesive soils remains not well understood, even though some research work by theoretical and numerical investigation has been published recently (e.g., Eghbalian et al. 2019). As another estimation method, the concept of “apparent cohesion” of unsaturated cohesive soils is widely accepted and used for interpreting the tensile strength. However, the “apparent cohesion” is not the “real cohesion” (Lambe and Whitman 1979) or the “true cohesion” (Mitchell and Soga 2005) due to the natural or artificial cementing among soil particles or aggregates. The “apparent cohesion” in the Mohr-Coulomb failure envelope is essential the shear strength without any confining pressure. Moreover, the nonlinearity of failure envelope of saturated and unsaturated soils has been observed under low compressive and tensile normal stresses (e.g., Sture et al. 1998; Lu et al. 2009; Lade 2010). Therefore, the estimation of tensile strength using the “apparent cohesion” determined by the linear Mohr-Coulomb criterion appears questionable from the theoretical point of view.

(3) The investigation on the effect of confining pressure on the tensile strength of unsaturated soils is limited in the literature. Even though some researchers have proposed the unified failure criterion considering the various failure modes (i.e. shear failure, tensile failure, combined tensile-shear failure) under different stress conditions (e.g., Guan 1983; Zhang and Chen 1987; Lu et al. 2009), those models are not well established due to the limited test results of specimens failure at tension, especially for considering the influence of confining on the tensile strength of soils. For this reason, in the present thesis, the influence of confining stress on the tensile strength is investigated using the triaxial tensile tests.

Table 2.9 Empirical models for predicting the tensile strength for unsaturated cohesive soils.

Equation No. and Reference	Equation and notations	Testing technique; (hydro-mechanical path)
(2.20) Zeh and Witt (2005)	$\sigma_{tu} = a + b \cdot \exp\left\{-0.5 \cdot \left[\frac{\ln(s/c)}{d}\right]^2\right\}$ where σ_{tu} = uniaxial tensile strength, kPa; s = matric suction, kPa; a, b, c, d = soil parameters to be determined experimentally.	Uniaxial tensile test; ("CD")
(2.21) Win (2006)	$\sigma_{tu} = a(w - w_{opt}) + b$, or $\sigma_{tu} = a \cdot s + b$ where w = water content; w_{opt} = optimum moisture content;	Uniaxial tensile test; ("C")
(2.22) Win (2006)	$\sigma_{tu} = b \cdot \exp\left[a(w - w_{opt})\right]$	Uniaxial tensile test; ("CD")
(2.23) Lutenegger and Rubin (2008)	$\frac{\sigma_t}{\sigma_{t,opt}} = 1 + \zeta(w - w_{opt})$ where $\sigma_{t,opt}$ = σ_t at optimum moisture content condition, kPa; ζ = soil parameter.	Double punch test; ("C")
(2.24) Péron (2008)	$\sigma'_t = \sigma'_{t,sat} + k_6\left[1 - \exp\left(-\frac{k_5 s}{k_6}\right)\right]$ where σ'_t = effective tensile strength, kPa; $\sigma'_{t,sat}$ = effective saturated tensile strength, kPa; k_5 (expresses the initial tangent at low suction level), k_6 (has the dimension of stress, and expresses the ultimate tensile strength at high suction level) = soil parameters to be determined experimentally.	Triaxial tensile test; ("SD")
(2.25) Venkataramana et al. (2009)	$\sigma_t = 0.001 \cdot CC^{1.5} \cdot CEC^{0.5} \cdot s^{0.5}$ for tensile strength at optimum moisture content, where CC is clay content in percentages, CEC is cation-exchange capacity in milliequivalents per 100 g.	Triaxial test (results are interpreted by Mohr-Coulomb criterion); ("C")
(2.26) Zhang et al. (2015)	$\frac{\sigma_{tu}}{P_r} = a\left(\frac{w}{w_{opt}} - 1\right) + b$ where P_r is 1 kPa; a, b = fitting parameters to be determined experimentally.	Uniaxial tensile test; ("C")

Table 2.10 Mechanical-based models for predicting the tensile strength of unsaturated cohesive soils.

Equation No. and Reference	Equation and notations	Testing technique; (hydro-mechanical path)
(2.27) Mullins and Panayiotopoulos (1984)	$\sigma_t = c' + \chi s = c' + sS_r$ where c' is the effective cohesion at a saturated state, χ is the Bishop's effective stress parameter which equates the degree of saturation, S_r.	Brazilian tensile test; ("SD")
(2.16) Snyder and Miller (1985)	$\sigma_t = sF(S_r) = s\frac{\chi}{f(S_r)}$ where F(S_r) is a comprehensive parameter, f(S_r) is a proportionality factor in the context of Griffith's stress concentration theory of fracture and is a function of the degree of saturation.	pneumatic fracture technique; ("SD")
(2.28) Morris et al. (1992)	$\sigma_{tu} = c_{app}/2 = \left[c' + s\cdot\tan(\phi^b)\right]/2$ where c_{app} is the apparent cohesion of unsaturated soils representing the intercept when net normal stress equal to zero in the net normal stress-shear stress plane, ϕ^b is the angle of shearing resistance with respect to matric suction.	N/A (Theoretical analysis); ("SD")
(2.29) Leavell and Peters (1987)	$\lg(\sigma_{tu}/P_e) = a(w - w_{opt}) + b$ with $P_e = P_a \cdot \exp\left(\frac{e_a - e}{\lambda}\right)$ where w_{opt} = optimum moisture content; P_a = atmospheric pressure; λ = slope of virgin curve on e-ln(p) plot for saturated soil under isotropic compression; e_a = void ratio on virgin compression curve at P_a; e = void ratio of soil.	Uniaxial tensile test; ("C")
(2.30) Aluko and Koolen (2000)	$\sigma_t = sS_r^i$ where S_r^i is the degree of inter-aggregate pore saturation which is defined as the fraction of the inter-aggregate pore space occupied by water.	Brazilian tensile test; ("CD")
(2.31) Thusyanthan et al. (2007)	$\sigma_t = (0.45\pm0.15)\sqrt{p_0' p_i'} = (0.45\pm0.15)\sqrt{p_0' s}$ where p_0' is the preconsolidation pressure; p_i' is the initial mean effective stress which equates the initial suction, s in the unloaded and saturated beam.	Flexure beam test; ("SD")
(2.32) Shin and Santamarina (2011)	$\sigma_t \le s_0 \frac{2\sin(\phi')}{1+\sin(\phi')}$ where s_0 is the initial air entry value, and ϕ' is the internal friction angle of soils at a saturated state.	Desiccation tests and theoretical analysis (tensile strength is not measured); ("SD")
(2.33) Murray and Tarantino (2019)	$q = M_e\left[p + s(S_r)^k\right]$, or $\sigma_{tu} = s(S_r)^k \frac{6\sin(\phi')}{\left[1+\sin(\phi')\right]\left[3+\sin(\phi')\right]}$	Uniaxial tensile test; ("SD")

	with $S_r = \left\{1+\left[\left(\frac{e}{a_t}\right)^{1/b_t} s\right]^{n_t}\right\}^{-b_t/n_t}$ where q is deviator stress, p is mean stress, M_e is the slope of the critical state line (CSL) for saturated soils at triaxial extension tests, k is a scaling parameter for the degree of saturation (Vanapalli et al. 1996), a_t, b_t, and n_t are model parameters of Tarantino's SWCC model for deformable soils (Tarantino 2009).	
(2.34) Lakshmikantha et al. (2012)	$\sigma_{tu} = c_{app}\cot\phi' = \left(c' + sS_r^e \tan\phi'\right)\cot\phi'$ with $S_r^e = \left(S_r\right)^{\alpha}$ where S_r^e is an effective degree of saturation, and α ($\alpha \geq 1$) is a material parameter related to pore size distribution.	Uniaxial tensile test; ("C")
(2.35) Varsei et al. (2016)	$\sigma_{tu} = c_{app}\frac{2\cos\phi'}{1+\sin\phi'} = \left[c' + sS_r^e \tan\phi'\right]\frac{2\cos\phi'}{1+\sin\phi'}$ with $S_r^e = \left(S_r\right)^{\alpha}$	Desiccation test and tensile stresses are measured ("CD")
(2.36) Tang et al. (2015)	$\sigma_{tu} = \begin{cases} -2\sigma^s \tan\phi_t \tan\left(\frac{\pi}{4}-\frac{\phi_t}{2}\right), & 0 \leq S_r \leq S_r^{cr}; \\ -2\sigma^s \tan\phi_t \tan\left(\frac{\pi}{4}-\frac{\phi_t}{2}\right) + \sigma_{tu}^{res}, & S_r^{cr} \leq S_r \leq 1. \end{cases}$ With $\sigma^s = -s \cdot S_e$ and $S_e = \frac{1}{\left[1+\left(\alpha_{vg}\cdot s\right)^{n_{vg}}\right]^{1-1/n_{vg}}}$ where σ^s is the "suction stress" proposed by Lu and Likos (2006), ϕ_t is the friction angle corresponding to the nonlinear Mohr-Coulomb failure envelope at tensile normal-stress range, α_{vg} and n_{vg} are fitting parameters of van Genuchten's SWCC model (van Genuchten 1980), σ_{tu}^{res} is a residual tensile strength at the saturated state, S_r^{cr} is the critical degree of saturation corresponding to the maximum tensile strength over the entire saturation range, and S_e is the equivalent degree of saturation.	Uniaxial tensile test; ("C")
(2.37) Trabelsi et al. (2012)	$\sigma_{tu} = c_{app}\frac{2\cos\phi'}{1+\sin\phi'}$ with $\begin{cases} c_{app} = c_n(n)c_s(s) = \frac{\lvert f(n)\rvert + f(n)}{2}\left(A\cdot s + B\right) \\ f(n) = 1-\left(\frac{n}{n_0}\right)^C \end{cases}$ where $c_n(n)$ is a variable function of cohesion with porosity (n), $c_s(s)$ is a variation function of cohesion with soil suction (s), n_0 is the reference porosity, and C is a material parameter related to the shape of the cohesion-porosity function, $c_n(n)$.	Uniaxial tensile test; ("SD")

(2.38) Trabelsi et al. (2018b)	$\sigma_{tu} = \left(a^m S_r^m + a^M S_r^M\right) s + \sigma_{tu}^{res}$ where S_r^m is a microscopic degree of saturation which describes the water within micropores, S_r^M is a macroscopic degree of saturation which describes the water within macropores, a^m is a microstructural parameter linked to the initial water content (a^m = 0, for compacted soil with hydraulic path "C"), and parameter a^M is linked to S_r^M at inter-aggregate scale.	Uniaxial tensile test; ("SD" & "CD" & "C")

Note: "C", as-compaction; "CD", compaction and desiccation under a controlled condition; "SD", slurry and desaturation by imposing a suction level or drying under a controlled condition.

2.3 References

Abbaszadeh, M.M. 2011. The effect of cracks on unsaturated flow and volume change properties of expansive clays and impacts on foundation performance. Doctoral dissertation, Arizona State University, USA.

Abu-Hejleh, A.N. and Znidarčić, D. 1995. Desiccation theory for soft cohesive soils. Journal of Geotechnical Engineering, 121(6): 493-502.

Ajaz, A. and Parry, R.H.G. (1974). An unconfined direct tension test for compacted clays. American Society for Testing and Materials Journal of Testing and Evaluation, 2(3): 163–172.

Ajaz, A. and Parry, R. H. G. (1975). Stress-strain behaviour of two compacted clays in tension and compression. Géotechnique, 25(3): 495–512.

Akin, I.D. and Likos, W.J. 2017. Brazilian tensile strength testing of compacted clay. Geotechnical Testing Journal, 40(4): 608–617.

Al-Hussaini, M.M. and Townsend, F.C. 1974. Investigation of Tensile Testing of Compacted Soils. No. AEWES-Misc-Paper-S-74-10. Army Engineer Waterways Experiment Station Vicksburg Miss.

Alonso, E.E., Pereira, J.M., Vaunat, J. and Olivella, S. 2010. A microstructurally based effective stress for unsaturated soils. Géotechnique, 60(12): 913-925.

Aluko, O.B. and Koolen, A.J., 2000. The essential mechanics of capillary crumbling of structured agricultural soils. Soil and Tillage Research, 55(3-4): 117-126.

Al-Dakheeli H. 2016. Hydro-mechanical analysis of shrinkage and shrinkage cracking due to environmental loads on saturated to unsaturated expansive soils. Doctoral dissertation, Oklahoma State University, USA.

Amarasiri, A. and Kodikara, J., 2010. Use of material interfaces in DEM to simulate soil fracture propagation in Mode I cracking. International Journal of Geomechanics, 11(4): 314-322.

Amarasiri, A.L., Kodikara J.K. and Costa, S. 2011. Numerical modelling of desiccation cracking. International Journal for Numerical and Analytical Methods in Geomechanics, 35(1): 82-96.

Ammeri, A. 2009. Contribution to the experimental and numerical study of the behavior of a limon stressed in traction: approach by discrete elements. Ph.D. dissertation, National Engineers School of Tunis. [In French.]

Asahina, D., Houseworth, J.E., Birkholzer, J.T., Rutqvist, J. and Bolander, J.E. 2014. Hydro-mechanical model for wetting/drying and fracture development in geomaterials. Computers & Geosciences, 65: 13-23.

ASTM International. 2017. D2487-17 Standard Practice for Classification of Soils for Engineering Purposes (Unified Soil Classification System). West Conshohocken, PA.

Atique, A. 2013. Investigation of desiccation cracks in drying soil. Doctoral dissertation, University of Strathclyde, UK.

Aubeny, C.P. and Lytton, R.L. 2004. Shallow slides in compacted high plasticity clay slopes. Journal of Geotechnical and Geoenvironmental Engineering, 130(7): 717-727.

Ávila, G., Ledesma, A. and Lloret, A. 2005. Hydro-mechanical processes in soil desiccation problems. Application to Bogotá clay. In Proceedings of the 16th International Conference on Soil Mechanics and Geotechnical Engineering, Osaka, Vol. 4, pp. 2353-2356.

Ávila, G., Ledesma, A. and Lloret, A. 2013. One-dimensional cracking model in clayey soils. In Proceddings of the 18th International Conference on Soil Mechanics and Geotechnical Engineering, Paris, pp. 1077-1080.

Baer, J.U., Kent, T.F. and Anderson, S.H. 2009. Image analysis and fractal geometry to characterize soil desiccation cracks. Geoderma, 154(1-2): 153-163.

Baker, R. 1981. Tensile strength, tension cracks, and stability of slopes. Soils and Foundations, 21(2): 1-17.

Bao, C.G. 2004. Behavior of unsaturated soil and stability of expansive soil slope. Chinese Journal of Geotechnical Engineering, 26(1): 1-15. [in Chinese]

Bao, C.G., Gong, B.W. and Zhan, L.T. 1998. Properties of unsaturated soils and slope stability of expansive soils. In Proceedings of the 2nd International Conference on Unsaturated Soils, Beijing, Vol. 2, pp. 71-98.

Barenblatt, G.I. 1962. The mathematical theory of equilibrium cracks in brittle fracture. In Advances in applied mechanics (Vol. 7, pp. 55-129). Elsevier.

Beckett, C.T.S., Smith, J.C., Ciancio, D. and Augarde, C.E. 2015. Tensile strengths of flocculated compacted unsaturated soils. Géotechnique Letters, 5(4): 254–260.

Bishop, A.W. 1959. The principle of effective stress. Teknisk Ukeblad, 106: 859–863.

Bishop, A.W. and Garga, V.K. 1969 Drained tension tests on London clay. Géotechnique, 19(2): 309-313.

Blight, G.E. 1967. Observations on the shear testing of indurated fissured clays. In Proceedings of the Geotechnical Conference on Shear Strength Properties of Natural Soils and Rocks, Oslo, Vol. 1, pp. 97-102.

Blight, G.E. 1997. Interactions between the atmosphere and the earth. Géotechnique, 47(4): 715-767.
Bofinger, H.E. 1970. The measurement of the tensile properties of soil cement. RRL Report LR 365, Road Research Laboratory, Ministry of Transport, Crowthorne, Berkshire.
Brace, W. F. 1960. An extension of the Griffith theory of fracture to rocks. Journal of Geophysical Research, 65(10): 3477–3480.
Bronswijk, J.J.B. 1991. Drying, cracking and subsidence of a clay soil in a lysimeter. Soil Science, 152(2): 92-99.
Bronswijk, J.J.B., Hamminga, W. and Oostindie, K. 1995. Field-scale solute transport in a heavy clay soil. Water Resources Research, 31(3): 517-526.
Bueckner, H.F. 1958. The propagation of cracks and the energy of elastic deformation. Transaction of the ASME, Series E, 80(6): 1225-1230.
Bui, H.H., Nguyen, G.D., Kodikara, J. and Sánchez, M. 2015. Soil cracking modelling using the mesh-free SPH method. In Proceedings of the 12th Australia New Zealand Conference on Geomechanics, Willington, New Zealand, Vol. 1, pp. 120-127.
Buzzi, O., Fityus, S. and Sloan, S.W. 2010. Use of expanding polyurethane resin to remediate expansive soil foundations. Canadian Geotechnical Journal, 47(6): 623-634.
Cajuhi, T., Sanavia, L. and De Lorenzis, L. 2018. Phase-field modeling of fracture in variably saturated porous media. Computational Mechanics, 61(3): 299-318.
Chaduvula, U., Viswanadham, B.V.S. and Kodikara, J. 2017. A study on desiccation cracking behavior of polyester fiber-reinforced expansive clay. Applied Clay Science, 142: 163-172.
Chandler, H.W. 1985. Topsoils and cultivations. In Span, 28(3): 106-107.
Chen, L. and Bulut, R. 2017. Development and Application of a New Tensile Stress Model for Expansive Soils. Geotechnical and Geological Engineering, 35(3): 1067-1077.
Chen, S.X., Dai, Z.J., Lu D.J., Luo, H.M. and Li, Y.F. 2014. Stability analysis considering fracture distribution and strength for expansive soil slope. Shuili Xuebao, 45(12): 1442-1449. [in Chinese]
Chen T.L., Deng G., Chen S.S. and Shen Z.J. 2006. Effect of fissures on stability of unsaturated soil slope. Chinese Journal of Geotechnical Engineering, 28(2): 210-215. [in Chinese]
Chen, T.L., Zhou, C., Wang, G.L., Liu, E.L. and Dai, F. 2018. Centrifuge model test on unsaturated expansive soil slopes with cyclic wetting–drying and inundation at the slope toe. International Journal of Civil Engineering, 16(10): 1341-1360.
Chen, Z. 2016. Gas breakthrough and emission in unsaturated landfill final cover considering cracking effect. Doctoral dissertation, Hong Kong University of Science and Technology, China.
Cheng, M.S., Wang, S.J., Mao, X., Chen, Z.H. and Jiang, S.H. 2016. Fissure morphology and mechanical characterization for structure-damaged expansive soil under triaxial compression tests. Chinese Journal of Geotechnical Engineering, 38(s2): 73-78. [in Chinese]
Cheng, Q., Tang, C.S., Zeng, H., Zhu, C., An, N. and Shi, B. 2020a. Effects of microstructure on desiccation cracking of a compacted soil. Engineering Geology, 265: p.105418.
Cheng, Q., Tang, C.S., Chen, Z.G., El-Maarry, M.R., Zeng, H. and Shi, B. 2020b. Tensile behavior of clayey soils during desiccation cracking process. Engineering Geology, 279, p.105909.
Cheng, Z.L., Ding, J.H., Rao, X.B., Cheng, Y.H. and Xu, H. 2014. Physical model tests of expansive soil slopes. Chinese Journal of Geotechnical Engineering, 36(4): 716-723. [in Chinese]
Cheng, Z.L. and Gong, B.W. 2015. Expansive Soil Slope. Science Press. [in Chinese]
Cherepancv, G. 1979. Mechanics of brittle fracture. McGraw-Hill, New York.
Chertkov, V.Y. and Ravina, I. 1998. Modeling the crack network of swelling clay soils. Soil Science Society of America Journal, 62(5): 1162-1171.
Chertkov, V.Y. and Ravina, I. 2000. Shrinking–swelling phenomenon of clay soils attributed to capillary-crack network. Theoretical and Applied Fracture Mechanics, 34(1): 61-71.
Chowdhury, R.N. and Zhang, S. 1991. Tension cracks and slope failure. In Proceedings of the International Conference on Slope Stability, the Isle of Wight, pp. 27-32.
Conlon, R.J. 1966. Landslide on the Toulnustouc River, Quebec. Canadian Geotechnical Journal, 3(3): 113–144.
Cordero, J., Cuadrado, A., Ledesma, A. and Prat, P. 2014. Patterns of cracking in soils due to drying and wetting cycles. In Unsaturated Soils: Research and Applications, pp. 381–387.

Cooling, L.F. and Marsland, A. 1953. Soil mechanics studies of failures in the sea defense banks of Essex and Kent. In Proceedings of the ICE Conference on the North Sea Floods of 31 January/1 February 1953, London, pp. 58-73.

Cordero, J., Cuadrado, A., Prat, P. and Ledesma, A. 2016. Description of a field test involving cracking in a drying soil. In E3S Web of Conferences, Vol. 9, p.12005.

Corte, A. and Higashi, A. 1964. Experimental research on desiccation cracks in soil (Research report 66). Cold Regions Research and Engineering Lab, Hanover NH, USA.

Costa, S. 2010. Study of desiccation cracking and fracture properties of clay soils, Doctoral dissertation, Monash University, Australia.

Costa, S., Htike, W.Y., Kodikara, J. and Xue, J. 2015. Determination of J-integral for clay during desiccation. Environmental Geotechnics, 3(6): 372-378.

Costa, S. and Kodikara, J. 2007. Investigation of desiccation cracking using automated digital photography. In Proceedings of the 10th Australia-New Zealand Conference on Geomechanics, Brisbane (Australia), pp. 338-343.

Costa, S. and Kodikara, J. 2009. Shrinkage development during soil desiccation. In Proceedings of the 4th Asia Pacific Conference on Unsaturated Soils, Newcastle, Vol. 2, pp. 433-436.

Costa, S. and Kodikara, J. 2012. Evaluation of J integral for clay soils using a new ring test. Geotechnical Testing Journal, 35(6): 981-989.

Costa, S., Kodikara, J. and Shannon, B. 2013. Salient factors controlling desiccation cracking of clay in laboratory experiments. Géotechnique, 63(1): 18-29.

Costa, S., Kodikara, J. and Thusyanthan, N.I. 2008. Study of desiccation crack evolution using image analysis. In Proceedings of the 1st European Conference on Unsaturated Soils, Durham, pp. 159-164.

Coussy, O. 2010. Mechanics and Physics of Porous Solids. John Wiley and Sons.

Das, B. M., Yen, S. C. and Dass, R. N. 1995. Brazilian tensile strength test of lightly cemented sand. Canadian Geotechnical Journal, 32: 166–171.

D'Astous, A.Y., Ruland, W.W., Bruce, J.R.G., Cherry, J.A. and Gillham, R.W. 1989. Fracture effects in the shallow groundwater zone in weathered Sarnia-area clay. Canadian Geotechnical Journal, 26(1): 43-56.

DeCarlo, K.F. and Shokri, N. 2014. Effects of substrate on cracking patterns and dynamics in desiccating clay layers. Water Resources Research, 50(4): 3039-3051.

Demagistri, A., Ledesma Villalba, A., Cordero Arias, J.A., Moreno, R., Prat Catalán, P. and Jacinto, A.C. 2018. Effects of compaction on desiccation cracking of clayey soils. In Proceedings of the 7th International Conference on Unsaturated Soils, Hong Kong, pp. 1273-1278.

Dexter, A.R. and Watts, C.W. 2000. Tensile strength and friability. In: Smith, K.A., Mullins, C.E. (Eds.), Soil and Environmental Analysis Physical Methods. Marcel Dekker, NY, USA.

Ding J.H., Chen R.P., Tong J. and Gong B.W. 2015. Research on failure mechanism of shallow instability of expansive soil slope based on multi-field coupling numerical analysis. Rock and Soil Mechanics, 36(s1): 159-168. [in Chinese]

Dugdale, D.S. 1960. Yielding of steel sheets containing slits. Journal of the Mechanics and Physics of Solids, 8(2): 100-104.

Dyer, M. 2004. Performance of flood embankments in England and Wales. In Proceedings of the Institution of Civil Engineers-Water Management, 157(4): 177-186.

Dyer, M., Utili, S., and Zielinski, M. 2009. Field survey of desiccation fissuring of flood embankments. In Proceedings of the Institution of Civil Engineers-Water Management, 162(3): 221-232.

Eghbalian, M., Pouragha, M., and Wan, R. 2019. Micromechanical approach to swelling behavior of capillary-porous media with coupled physics. International Journal for Numerical and Analytical Methods in Geomechanics, 43(1): 353-380.

El-Maarry, M.R., Watters, W., McKeown, N.K., Carter, J., Dobrea, E.N., Bishop, J.L., Pommerol, A. and Thomas, N. 2014. Potential desiccation cracks on Mars: A synthesis from modeling, analogue-field studies, and global observations. Icarus, 241: 248-268.

Elghezal, L., Trabelsi, H., Jamei, M. and Romero, E.E. 2015. Desiccation effects on clay-based engnieered barriers. In Proceedings of the 1st International Symposium on Energy Geotechnics, Barcelona.

Evans, E.P. and Hughes, B.P. 1968. Shrinkage and thermal cracking in a reinforced concrete retaining wall. In Proceedings of the Institution of Civil Engineers, 39(1): 111-125.

Fang, H.Y. and Chen, W. 1970. New method for determination of tensile strength of soils. Report No. 348.5, Lehigh University, Bethlehem, Pennsylvania.

Fang, H. and Fernandez, J. 1981. Determination of tensile strength of soils by unconfined-penetration test. In Laboratory shear strength of soil, STP28748S. Edited by R. Yong and F. Townsend. ASTM International, West Conshohocken, Pa., pp. 130–144.

Farrell, D. A., Greacen, E. L. and Larson, W. E. 1967. The effect of water content on axial strain in a loam soil under tension and compression. Soil Science Society of America Journal, 31(4): 445-450.

Favaretti, M. 1995. Tensile strength of compacted clays.pdf. In Proceedings of the 1st International Conference on Unsaturated Soils. Barcelona, Spain, pp. 51–56.

Fell, R., Wan, C.F., Cyganiewicz, J. and Foster, M. 2003. Time for development of internal erosion and piping in embankment dams. Journal of Geotechnical and Geoenvironmental Engineering, 129(4): 307-314.

Fisher, R.A. 1926. On the capillary forces in an ideal soil; correction of formulae given by WB Haines. The Journal of Agricultural Science, 16(03): 492–505.

Fodor, A. 1999. Inhibition of desiccation cracking of clayey barriers through the addition of polymers. Doctoral dissertation, University of Massachusetts Lowell, USA.

Fujiyasu, Y., Fahey, M. and Newson, T. 2000. Field investigation of evaporation from freshwater tailings. Journal of Geotechnical and Geoenvironmental Engineering, 126(6): 556-567.

Fredlund, D.G. and Morgenstern, N.R. 1976. Constitutive relations for volume change in unsaturated soils. Canadian Geotechnical Journal, 13(3): 261-276.

Fredlund, D.G. and Morgenstern, N.R. 1977. Stress state variables for unsaturated soils. Journal of Geotechnical and Geoenvironmental Engineering, 103: 447–466.

Fredlund, D.G., Morgenstern, N.R. and Widger, R.A. 1978. The shear strength of unsaturated soils. Canadian Geotechnical Journal, 15(3): 313-321.

Fredlund, D.G. and Rahardjo, H. 1993. Soil Mechanics for Unsaturated Soils. John Wiley and Sons.

Fredlund, D.G., Houston, S.L., Nguyen, Q. and Fredlund, M.D. 2010. Moisture movement through cracked clay soil profiles. Geotechnical and Geological Engineering, 28(6): 865-888.

Galvez, J.C., Cervenka, J., Cendon, D.A. and Saouma, V. 2002. A discrete crack approach to normal/shear cracking of concrete. Cement and Concrete Research, 32: 1567–1585.

Gaspar, T.A.V. and Jacobsz, S.W. 2021. Brazilian tensile strength test conducted on ductile unsaturated soil samples. Geotechnical Testing Journal, 44. https://doi.org/10.1520/GTJ20190078.

Gens, A. 2010. Soil-environment interactions in geotechnical engineering. Géotechnique, 60(1): 3-74.

Gebrenegus, T., Ghezzehei, T.A. and Tuller, M. 2011. Physicochemical controls on initiation and evolution of desiccation cracks in sand–bentonite mixtures: X-ray CT imaging and stochastic modeling. Journal of Contaminant Hydrology, 126(1-2): 100-112.

Gibson, R.E., England, G.L. and Hussey, M.J.L. 1967. The Theory of one-dimensional consolidation of saturated clays: 1. finite non-Linear consolidation of thin homogeneous layers. Géotechnique, 17(3): 261-273.

Goehring, L., Clegg, W.J. and Routh, A.F. 2011. Wavy cracks in drying colloidal films. Soft Matter, 7(18): 7984-7987.

Goehring, L. and Morris, S.W. 2014. Cracking mud, freezing dirt, and breaking rocks. Physics Today, 67(11): 39-44.

Goehring, L., Nakahara, A., Dutta, T., Kitsunezaki, S. and Tarafdar, S. 2015. Desiccation cracks and their patterns: Formation and Modelling in Science and Nature. John Wiley and Sons.

Goodman, R.E., Taylor, R.L. and Brekke, T.L. 1968. A model for the mechanics of jointed rock. Journal of the Soil Mechanics and Foundations Division, 94(3): 637-660.

Graham, J. and Au, V.C.S. 1985. Influence of freeze-thaw and softening effects on stress-strain behaviour of natural plastic clay at low stresses. Canadian Geotechnical Journal, 22(1): 69-78.

Greve, A., Andersen, M.S. and Acworth, R.I. 2010. Investigations of soil cracking and preferential flow in a weighing lysimeter filled with cracking clay soil. Journal of Hydrology, 393(2010): 105–113.

Griffith, A.A. 1921. The phenomena of rupture and flow in solids. Philosophical Transactions of the Royal Society of London. Series A, containing papers of a mathematical or physical character, 221(582-593): 163-198.

Griffith, A.A. 1924. The theory of rupture. In Proceedings of the 1st International Congress on Applied Mechanics, Delft, the Netherlands, pp. 55–62.

Guan, D. 1983. Combined Griffith-Mohr strength theory of rupture in soils. Proceedings of the 4th Academic Conference of China Civil Engineering Society for Soil Mechanics and Foundation Engineering, Beijing, China, pp. 124-131. [in Chinese]

Guérif, J. 1990. Factors influencing compaction-induced increases in soil strength. Soil and Tillage Research, 16(1–2): 167–178.

Gui, Y.L. 2014. Desiccation cracking in unsaturated soils. Doctoral dissertation, The University of New South Wales, Australia.

Gui, Y.L., Zhao, Z.Y., Kodikara, J., Bui, H.H. and Yang, S.Q. 2016. Numerical modelling of laboratory soil desiccation cracking using UDEC with a mix-mode cohesive fracture model. Engineering Geology, 202: 14-23.

Guo, G. and Fall, M. 2018. Modelling of dilatancy-controlled gas flow in saturated bentonite with double porosity and double effective stress concepts. Engineering Geology, 243: 253-271.

Guo, P. 2014. Coupled effects of capillary suction and fabric on the strength of moist granular materials. Acta Mechanica, 225(8): 2261-2275.

Guo, Y., Han, C. and Yu, X. 2018. Laboratory characterization and discrete element modeling shrinkage and cracking. Canadian Geotechnical Journal, 55(5): 680-688.

Haigh, S.K., Vardanega, P.J. and Bolton, M.D. 2014. Authors' reply to discussion of "The plastic limit of clays". Géotechnique, 64(7): 584-586.

Haines, W. B. 1925. Studies in the physical properties of soils: II. A note on the cohesion developed by capillary forces in an ideal soil. The Journal of Agricultural Science, 15(4): 529–535.

Hallett, P.D. and Newson, T.A. 1998. Desiccation of a sensitive clay: Application of the model CRACK: Discussion. Canadian Geotechnical Journal, 35(6): 1109-1110.

Harison, J.A. and Hardin, B.O. 1994. Cracking in clays: solutions to problems in earth structures. International Journal for Numerical and Analytical Methods in Geomechanics, 18(7): 467-484.

Hartranft, R.J. and Sih, G.C. 1973. Alternating method applied to edge and surface crack problems. In Methods of analysis and solutions of crack problems (pp. 179-238). Springer.

Hirobe, S. and Oguni, K. 2016. Coupling analysis of pattern formation in desiccation cracks. Computer Methods in Applied Mechanics and Engineering, 307: 470-488.

Hoek. 1964. Rock fracture under static stress conditions. Doctoral dissertation, University of Cape Town, South Africa.

Horgan, G.W. and Young, I.M. 2000. An empirical stochastic model for the geometry of two-dimensional crack growth in soil (with Discussion). Geoderma, 96(4): 263-276.

Hotta, K., Takeda, K. and Iinoya, K. 1974. The capillary binding force of a liquid bridge. Powder Technology, 10(4–5): 231–242.

Huang, B., Cheng, Z.L. and Xu, H. 2014. Expansion model of expansive soil and its application to slope engineering. Rock and Soil Mechanics, 35(2): 3550-3555. [in Chinese]

Huang, R.Q. and Wu, L.Z. 2007. Stability analysis of unsaturated expansive soil slope. Earth Science Frontiers, 14(6): 129-133.

Hueckel, T., Mielniczuk, B., El Youssoufi, M.S., Hu, L.B. and Laloui, L. 2014. A three-scale cracking criterion for drying soils. Acta Geophysica, 62(5): 1049-1059.

Hueckel, T., Mielniczuk, B. and El Youssoufi, M.S. 2019. Adhesion-force micro-scale study of desiccating granular material. Géotechnique, https://doi.org/10.1680/jgeot.18.P.298.

Ingles, O. 1962. Bonding forces in soils. Part 3. Theory of tensile strength for stabilized and naturally coherent soils. In Proceedings of the 1st Australian Road Research Board Conference, pp. 1025–1047.

Innocent-Bernard, T. 2013. Evaporation, cracking, and salinity in a thickened oil sands tailings, Doctoral dissertation, Carleton University, Canada.

Irwin, G.R. 1948. Fracture dynamics. In Fracturing of Metals, American Society for Metals, Cleveland, OH, pp. 147-166.

Itasca. 2002. Fast Lagrangian Analysis of Continua, Version 4.0 User's Guide, Itasca Consulting Group. Inc., Minneapolis, USA.

Itasca. 2004. Universal Distinct Element Code, Version 4.0 User's Guide, Itasca Consulting Group. Inc., Minneapolis, USA.

Jindal, P., Sharma, J. and Bashir, R. 2016. Effect of pore-water surface tension on tensile strength of unsaturated sand. Indian Geotechnical Journal, 46(3): 276–290.

Jones, G., Zielinski, M. and Sentenac, P. 2012. Mapping desiccation fissures using 3-D electrical resistivity tomography. Journal of Applied Geophysics, 84: 39-51.

Jones, G., Sentenac, P. and Zielinski, M. 2014. Desiccation cracking detection using 2-D and 3-D electrical resistivity tomography: Validation on a flood embankment. Journal of Applied Geophysics, 106: 196-211.

Julina, M. and Thyagaraj, T. 2018. Determination of volumetric shrinkage of an expansive soil using digital camera images. International Journal of Geotechnical Engineering, 2018: 1-9.

Julina, M. and Thyagaraj, T. 2019. Quantification of desiccation cracks using X-ray tomography for tracing shrinkage path of compacted expansive soil. Acta Geotechnica, 14(1): 35-56.

Kazemi, H.V., Anderson, S.H., Goyne, K.W. and Gantzer, C.J. 2008. Atrazine and alachlor transport in claypan soils as influenced by differential antecedent soil water content. Journal of Environmental Quality, 37(4): 1599-1607.

Khandelwal, S. 2011. Effect of Desiccation Cracks on Earth Embankments. Master's dissertation, Texas A&M University, USA.

Khatun, T., Dutta, T. and Tarafdar, S. 2015. Topology of desiccation crack patterns in clay and invariance of crack interface area with thickness. The European Physical Journal E, 38(8): 83-93.

Kim, T.H. 2001. Moisture-induced tensile strength and cohesion in sand. Ph.D. dissertation, University of Colorado at Boulder.

Kim, T.-H., Kim, T.-H., Kang, G.-C. and Ge, L. 2012. Factors Influencing Crack-Induced Tensile Strength of Compacted Soil. Journal of Materials in Civil Engineering, 24(3): 315–320.

Kim, T. H. and Hwang, C. 2003. Modeling of tensile strength on moist granular earth material at low water content. Engineering Geology, 69(3–4): 233–244.

Kindle, E.M. 1917. Some factors affecting the development of mud-cracks. The Journal of Geology, 25(2): 135–144.

Kleppe, J. and Olson, R. 1985. Desiccation Cracking of Soil Barriers. In Hydraulic Barriers in Soil and Rock, ed. Johnson, A., Frobel, R., Cavalli N., and Pettersson C. (West Conshohocken, PA: ASTM International, 1985), pp. 263-275.

Kodikara, J. 2012. New framework for volumetric constitutive behaviour of compacted unsaturated soils. Canadian Geotechnical Journal, 49(11): 1227-1243.

Kodikara, J., Barbour, S.L. and Fredlund, D.G. 1999. Changes in clay structure and behaviour due to wetting and drying. In Proceedings of the 8th Australia-New Zealand Conference on Geomechanics: Consolidating Knowledge, Hobart, pp. 179-186.

Kodikara, J.K., Barbour, S.L. and Fredlund, D.G. 2000. Desiccation cracking of soil layers. In Proceedings of the Asian Conference in Unsaturated Soils, Singapore, pp. 693-698.

Kodikara, J.K. and Choi, X. 2006. A simplified analytical model for desiccation cracking of clay layers in laboratory tests. In Proceedings of the 4th International Conference on Unsaturated Soils, Arizona, pp. 2558-2569.

Kodikara, J. and Costa, S. 2013. Desiccation cracking in clayey soils: mechanisms and modelling. In Multiphysical Testing of Soils and Shales, pp. 21-32. Springer, Berlin, Heidelberg.

Koliji, A. 2008. Mechanical behaviour of unsaturated aggregated soils. Doctoral dissertation, École Polytechnique Fédérale de Lausanne, Switzerland.

Kong, L.W., Chen, J.B., Guo, A.G., Zhao, Y.L. and Lv, H.B. 2007. Field response tests on expansive soil slopes under atmosphere. Chinese Journal of Geotechnical Engineering, 29(7): 1065-1073. [in Chinese]

Konrad, J.M. and Ayad, R. 1997a. Desiccation of a sensitive clay: field experimental observations. Canadian Geotechnical Journal, 34(6): 929-942.

Konrad, J.M. and Ayad, R. 1997b. An idealized framework for the analysis of cohesive soils undergoing desiccation. Canadian Geotechnical Journal, 34(4): 477-488.

Koolen, A.J. 1987. Workability limits and their soil physical background. PAGV-Verslag No. 64 Lelystadm, The Netherlands, pp. 21-41. [In Dutch]

Kosmas, C., Moustakas, N., Kallianou, C. and Yassoglou, N. 1991. Cracking patterns, bypass flow and nitrate leaching in Greek irrigated soils. Geoderma, 49(1–2): 139–152.

Krishnayya, A. V. G. and Eisenstein, Z. 1974. Brazilian Tensile Test for Soils. Canadian Geotechnical Journal, 11: 632–642.

Krisnanto, S., Rahardjo, H., Fredlund, D.G. and Leong, E.C. 2014. Mapping of cracked soils and lateral water flow characteristics through a network of cracks. Engineering Geology, 172: 12-25.

Lachenbruch, A.H. 1961. Depth and spacing of tension cracks. Journal of Geophysical Research, 66(12): 4273-4292.

Lachenbruch, A.H. 1962. Mechanics of thermal contraction cracks and ice-wedge polygons in permafrost (Vol. 70). Geological Society of America.

Lade, P.V. 2010. The mechanics of surficial failure in soil slopes. Engineering Geology, 114(1-2): 57-64.

Lakshmikantha, M.R. 2009. Experimental and theoretical analysis of cracking in drying soils. Doctoral dissertation, Universitat Politècnica de Catalunya, Spain.

Lakshmikantha, M.R., Prat, P.C. and Ledesma, A. 2006. An experimental study of cracking mechanisms in drying soils. In Proceedings of the ISSMGE's 5th ICEG Environmental Geotechnics, Cardiff, pp. 533-540.

Lakshmikantha, M.R., Prat, P.C. and Ledesma, A. 2009. Image analysis for the quantification of a developing crack network on a drying soil. Geotechnical Testing Journal, 32(6): 505-515.

Lakshmikantha, M.R., Prat, P.C. and Ledesma, A. 2012. Experimental evidence of size effect in soil cracking. Canadian Geotechnical Journal, 49(3): 264-284.

Lakshmikantha, M.R., Prat, P.C. and Ledesma, A. 2013a. Evidences of hierarchy in cracking of drying soils. ASCE Geotechnical Special Publication, 231: 782-789.

Lakshmikantha, M.R., Reig, R., Prat, P.C. and Ledesma, A. 2013b. Origin and mechanism of cracks seen at the bottom of a desiccating soil specimen. ASCE Geotechnical Special Publication, 231: 790-799.

Lambe, T.W. and Whitman, R.V. 1979. Soil mechanics, SI Version. John Wiley and Sons, New York.

Lau, J.T.K. 1987. Desiccation cracking of soils. Masters' dissertation, University of Saskatchewan, Canada.

Leavell, D. A. and Peters, J. F. 1987. Uniaxial tensile test for soil. No. WES/TR/GL-87-10). Army Engineer Waterways Experiment Station, Vicksburg, Mississippi.

Ledesma, A. 2016. Cracking in desiccating soils. In E3S Web of Conferences (Vol. 9, p. 03005). EDP Sciences.

Ledesma, A., Lakshmikantha, M.R. and Prat, P.C. 2018. Boundary effects in the desiccation of soil layers with controlled environmental conditions. Geotechnical Testing Journal, 41(4): 675-697.

Lee, Wai Peng and Routh, Alexander F. 2004. Why do drying films crack? Langmuir, 20(23): 9885-9888.

Leonards, G.A. and Narain, J. 1963. Flexibility of clay and cracking of earth dams. Journal of the Soil Mechanics and Foundations Division, 89(2): 47-98.

Levatti, H.U., Prat, P.C. and Ledesma, A. 2007. Numerical modelling of formation and propagation of drying cracks in soils. In Proceedings of the 9th International Conference on Computational Plasticity, Barcelona, Spain.

Levatti, H.U., Prat, P.C., Ledesma, A., Cuadrado, A. and Cordero, J.A. 2017. Experimental analysis of 3D cracking in drying soils using ground-penetrating radar. Geotechnical Testing Journal, 40(2): 1-23.

Levatti, H.U., Prat, P.C. and Ledesma, A. 2019. Numerical and experimental study of initiation and propagation of desiccation cracks in clayey soils. Computers and Geotechnics, 105: 155-167.

Li, J., He, C. and Tang, H. 2007. The comparative study on the tensile strength test of soft clay. Subgrade Engineering, 131(2): 104-105. [In Chinese]

Li, J.H., Li, L., Chen, R. and Li, D.Q. 2016. Cracking and vertical preferential flow through landfill clay liners. Engineering Geology, 206: 33-41.

Li, J.H. and Zhang, L.M. 2010. Geometric parameters and REV of a crack network in soil. Computers and Geotechnics, 37(4): 466-475.

Li, J.H. and Zhang, L.M. 2011. Study of desiccation crack initiation and development at ground surface. Engineering Geology, 123(4): 347-358.

Li, X.J., Liu, Y.R., Jiang, L.H. and Tang, Y.C. (2011). Determination of tensile strength of compacted loess by double punch test. Advanced Materials Research, 194–196: 1176–1179.

Li, X.S. 2003. Effective stress in unsaturated soil: a microstructural analysis. Géotechnique, 53(2): 273-277.

Li, Y., Ling, X., Su, L., An, L., Li, P. and Zhao, Y. 2018. Tensile strength of fiber reinforced soil under freeze-thaw condition. Cold Regions Science and Technology, 146: 53–59.

Li, Y.X. and Yang, X.L. 2016. Stability analysis of crack slope considering nonlinearity and water pressure. KSCE Journal of Civil Engineering, 20(6): 2289-2296.

Lin, H. and McInnes, K. 1995. Water-flow in clay soil beneath a tension infiltrometer. Soil Science, 159(6): 375–382.

Liu, B., Zhu, C., Tang, C.S., Xie, Y.H., Yin, L.Y., Cheng, Q. and Shi, B. 2020. Bio-remediation of desiccation cracking in clayey soils through microbially induced calcite precipitation (MICP). Engineering Geology, 264, p.105389.

Lloret, A., Ledesma, A., Rodriguez, R. L., Sánchez, M. J., Olivella, S. and Suriol, J. 1998. Crack initiation in drying soils. In Proceedings of the 2nd International Conference on Unsaturated Soils, Beijing, pp. 497–502.

Lu, N., Kim, T.H., Sture, S. and Likos, W.J. 2009. Tensile strength of unsaturated sand. Journal of Engineering Mechanics, 135(12): 1410-1419.

Lu, N. and Likos, W.J. 2006. Suction stress characteristic curve for unsaturated soil. Journal of Geotechnical and Geoenvironmental Engineering, 132(2): 131–142.

Lu, N., Wu, B. and Tan, C. P. 2007. Tensile strength characteristics of unsaturated sands. Journal of Geotechnical and Geoenvironmental Engineering, 133(2): 144–154.

Lu, N., Wu, B. and Tan, C.P. 2005. A tensile strength apparatus for cohesionless soils. In Advanced experimental unsaturated soil mechanics. Edited by A. Tarantino, et al. Trento, Italy, pp. 105–110.

Lutenegger, A.J. and Rubin, A. 2008. Tensile strength of some compacted fine-grained soils. In Proceedings of the 1st European Conference on Unsaturated Soils, pp. 411-415.

Lv, H.B., Zeng Z.T., Zhao, Y.L. and Lu, H. 2009. Experimental studies of strength of expansive soil in drying and wetting cycle. Rock and Soil Mechanics, 30(12): 3797-3802. [in Chinese]

Manzoli, O., Sánchez, M., Maedo, M., Hajjat, J. and Guimarães, L.J. 2017. An orthotropic interface damage model for simulating drying processes in soils. Acta Geotechnica, 13(5): 1171-1186.

Matsubara, H., Hirose, K., Edo, T.A., Tamanaha, K.I., Hara, H. and Yamada, T. 2016. Numerical modelling of mudcrack growth. Japanese Geotechnical Society Special Publication, 2(31): 1143-1147.

McClintock, F.A. and Walsh, J.B. 1962. Friction on Griffith cracks in rock under pressure. In Proceedings of the 4th US National Congress on Applied Mechanics, New York, Vol. 2, pp. 1015-1021.

Miedema, M. 2015. Mud-crack pattern evolution in iterated drying cycles. Undergraduate report (unpublished), University of Toronto, Canada.

Mikulitsch, W.A. and Gudehus, G. 1995. Uniaxial tension, biaxial loading and wetting tests on loess. In Proceedings of the 1st International Conference on Unsaturated Soils, Paris, France, Vol. 1, pp. 145-150.

Miller, C.J. and Mishra, M. 1989. Modeling of leakage through cracked clay liners-II: A new perspective. Journal of the American Water Resources Association, 25(3): 557-563.

Mitchell, A. and van Genuchten, M. 1993. Flood irrigation of a cracked soil. Soil Science Society of America Journal, 57 (2): 490-497.

Mitchell, J.K. and Soga, K. 2005. Fundamentals of soil behavior (Vol. 3). John Wiley and Sons, New York.

Moës, N., Dolbow, J. and Belytschko, T. 1999. A finite element method for crack growth without remeshing. International Journal for Numerical Methods in Engineering, 46(1): 131-150.

Morris, P.H., Graham, J. and Williams, D.J. 1992. Cracking in drying soils. Canadian Geotechnical Journal, 29(2): 263-277.

Morris, P.H., Graham, J. and Williams, D.J. 1994. Crack depths in drying clays using fracture mechanics. Geotechnical special publication, 43:40-53.

Mullins, C. E. and Panayiotopoulos, K. P. 1984. The strength of unsaturated mixtures of sand and kaolin and the concept of effective stress. Journal of Soil Science, 35(3): 459–468.

Munkholm, L. J. and Kay, B. D. 2002. Effect of water regime on aggregate-tensile strength, rupture energy, and friability. Soil Science Society of America Journal, 66(3): 702-709.

Murray, I. and Tarantino, A. 2019. Mechanisms of failure in saturated and unsaturated clayey geomaterials subjected to (total) tensile stress. Géotechnique, 69(8): 701-712.

Nahlawi, H., Chakrabarti, S. and Kodikara, J. 2004. A direct tensile strength testing method for unsaturated geomaterials. Geotechnical Testing Journal, 27(4): 1-6.

Nahlawi, H. and Kodikara, J.K. 2006. Laboratory experiments on desiccation cracking of thin soil layers. Geotechnical and Geological Engineering, 24(6): 1641-1664.

Namikawa, T. and Koseki, J. 2007. Evaluation of tensile strength of cement-treated sand based on several types of laboratory tests. Soils and Foundations, 47(4): 657–674.

Narain, J. and Rawat, P.C., 1970. Tensile strength of compacted soils. Journal of Soil Mechanics and Foundations Div., 96(6): 2185-2190.

Narvaez, B., Aubertin, M. and Saleh-Mbemba, F. 2015. Determination of the tensile strength of unsaturated tailings using bending tests. Canadian Geotechnical Journal, 52(11): 1874–1885.

Návar, J., Mendez, J., Bryan, R.B. and Kuhn, N.J. 2002. The contribution of shrinkage cracks to bypass flow during simulated and natural rainfall experiments in northeastern Mexico. Canadian Journal of Soil Science, 82(1): 65-74.

Ng, C.W.W., Zhan, L.T., Bao, C.G., Fredlund, D.G. and Gong, B.W. 2003. Performance of an unsaturated expansive soil slope subjected to artificial rainfall infiltration. Géotechnique, 53(2): 143-157.

Nishimoto, A., Mizuguchi, T. and Kitsunezaki, S. 2007. Numerical study of drying process and columnar fracture process in granule-water mixtures. Physical Review E, 76(1): p.016102.

Omer, M. and Mohd, R.T. 2011. Cracks in soils related to desiccation and treatment. Australian Journal of Basic and Applied Sciences, 5(8): 1080-1089.

Paul, B. 1961. A modification of the Coulomb-Mohr theory of fracture. Journal of Applied Mechanics, 28(2): 259-268.

Perkins, S.W. 1991. Modeling of regolith structure interaction in extraterrestrial constructed facilities. Doctoral dissertation, University of Colorado at Boulder, USA.

Péron H. 2008. Desiccation cracking of soils. Doctoral dissertation, École polytechnique fédérale de Lausanne, Switzerland.

Péron, H., Hu, L., Hueckel, T. and Laloui, L. 2007. The influence of the pore fluid on desiccation of a deformable porous material. In Experimental Unsaturated Soil Mechanics, pp. 413-420. Springer.

Péron, H., Hueckel, T., Laloui, L. and Hu, L. 2009a. Fundamentals of desiccation cracking of fine-grained soils: experimental characterisation and mechanisms identification. Canadian Geotechnical Journal, 46(10): 1177-1201.

Péron, H., Delenne, J.Y., Laloui, L. and El Youssoufi, M.S. 2009b. Discrete element modelling of drying shrinkage and cracking of soils. Computers and Geotechnics, 36(1-2): 61-69.

Philip, L.K., Shimell, H., Hewitt, P.J. and Ellard, H.T. 2002. A field-based test cell examining clay desiccation in landfill liners. Quarterly Journal of Engineering Geology and Hydrogeology, 35(4): 345-354.

Pietsch, W.B. 1968. Tensile strength of granular materials. Nature, 217: 736–737.

Pietsch, W., Hoffman, E. and Rumpf, H. 1969. Tensile strength of moist agglomerates. Industrial and Engineering Chemistry Product Research and Development, 8(1): 58–62.

Potts, D.M. and Zdravkovic, L., 1999. Finite Element Analysis in Geotechnical Engineering: Theory (Vol. 1). Thomas Telford.

Qi, S. and Vanapalli, S.K. 2015. Hydro-mechanical coupling effect on surficial layer stability of unsaturated expansive soil slopes. Computers and Geotechnics, 70: 68-82.

Qi, S. and Vanapalli, S.K. 2016. Influence of swelling behavior on the stability of an infinite unsaturated expansive soil slope. Computers and Geotechnics, 76: 154-169.

Qi, S. and Vanapalli, S.K. 2018. Simulating hydraulic and mechanical responses of unsaturated expansive soil slope to rainfall: case study. International Journal of Geomechanics, 18(6): p.05018002.

Ravina, I. 1983. The influence of vegetation on moisture and volume changes. Géotechnique, 33(2): 151-157.

Rayhani, M.H., Yanful, E.K. and Fakher, A. 2007. Desiccation-induced cracking and its effect on the hydraulic conductivity of clayey soils from Iran. Canadian Geotechnical Journal, 44(3): 276-283.

Rice, J. R. 1968. A path independent integral and the approximate analysis of strain concentrations by notches and cracks. Journal of Applied Mechanics, 35: 379–386.

Ringrose-Voase, A.J. and Sanidad, W.B. 1996. A method for measuring the development of surface cracks in soils: application to crack development after lowland rice. Geoderma, 71(3-4): 245-261.

Ritchie, J.T., Kissel, D.E. and Burnett, E. 1972. Water movement in undisturbed swelling clay soil. Soil Science Society of America Journal, 36(6): 874-879.

Rodríguez, R. 2006. Hydrogeotechnical characterization of a metallurgical waste. Canadian Geotechnical Journal, 43(10): 1042-1060.

Rodríguez, R., Sánchez, M., Ledesma, A. and Lloret, A. 2007. Experimental and numerical analysis of desiccation of a mining waste. Canadian Geotechnical Journal, 44(6): 644–658.

Roth, S., Hütter, G. and Kuna, M. 2014. Simulation of fatigue crack growth with a cyclic cohesive zone model. International Journal of Fracture, 188(1): 23-45.

Ruland, W.W., Cherry, J.A. and Feenstra, S. 1991. The depth of fractures and active ground-water flow in a clayey till plain in southwestern Ontario. Groundwater, 29(3): 405-417.

Rumpf, H. 1961. The strength of granules and agglomerates. In International Symposium on Agglomeration. Edited by W.A. Knepper. Knepper, Interscience, New York, pp. 379–418.

Rumpf, H. 1970. Zur theorie der zugfestigkeit von agglomeraten bei kraftuebertragung an kontaktpunkten. Chemie Ingenieur Technik, 42(8): 538–540. [in German]

Salganik, R.L. and Chertkov, V.Y. 1969. Reduction of strength under the action of shrinkage stresses. Mechanics of Solids, 4: 118-124.

Samouëlian, A., Richard, G., Cousin, I., Guerin, R., Bruand, A. and Tabbagh, A. 2004. Three-dimensional crack monitoring by electrical resistivity measurement. European Journal of Soil Science, 55(4): 751-762.

Sánchez, M., Atique, A., Kim, S., Romero, E. and Zielinski, M. 2013. Exploring desiccation cracks in soils using a 2D profile laser device. Acta Geotechnica, 8(6): 583-596.

Sánchez, M., Manzoli, O.L. and Guimarães, L.J. 2014. Modeling 3-D desiccation soil crack networks using a mesh fragmentation technique. Computers and Geotechnics, 62: 27-39.

Satyanarayana, B. and Rao, K. S. 1972. Measurement of tensile strength of compacted soil. Geotechnical Engineering, 3: 61–66.

Schofield, A. and Wroth, P. 1968. Critical State Soil Mechanics (Vol. 310). McGraw-Hill, UK.

Schubert, H. 1972. Investigations on the determination of capillary pressure and tensile strength of wet granular materials. Doctoral dissertation, University of Karlsruhe, Germany. [in German]

Schubert, H. 1973. Kapillardruck und Zugfestigkeit von feuchten Haufwerken aus körnigen Stoffen. Chemie Ingenieur Technik, 45(6): 396–401. [in German]

Schubert, H. 1975. Tensile strength of agglomerates. Powder Technology, 11(2): 107–119.

Shahrokhabadi, S., Vahedifard, F., Ghazanfari, E. and Foroutan, M. 2019. Earth pressure profiles in unsaturated soils under transient flow. Engineering Geology, 260: p.105218.

Shannon, B.M. 2013. Fracture propagation of cohesive soils under tensile loading and desiccation. Doctoral dissertation, Monash University, Australia.

Shannon, B., Kodikara, J. and Rajeev, P. 2014. The use of restrained ring test method for soil desiccation studies. Geotechnical Testing Journal, 38(1): 98-112.

Shen, Z.J. 1996. Reduced suction and simplified consolidation theory for expansive soils. In Proceedings of the 1st International Conference on Unsaturated Soils, Paris, France, Vol. 3.

Shen Z.J. and Deng G. 2004. Numerical simulation of crack evolution in clay during drying and wetting cycle. Rock and Soil Mechanics, 25(s2): 1-6. [in Chinese]

Sherard, J.L. 1973. Embankment dam cracking. In Embankment-Dam Engineering (Casagrande Volume), John Wiley and Sons, New York, NY, pp. 271-353.

Shi, B.X., Zheng, C.F. and Wu, J.K. 2014. Research progress on expansive soil cracks under changing environment. The Scientific World Journal, vol. 2014, Article ID 816759.

Shin, H. and Santamarina, J. C. 2011. Desiccation cracks in saturated fine-grained soils: particle-level phenomena and effective-stress analysis. Géotechnique, 61(11): 961–972.

Shorlin, K.A., de Bruyn, J.R., Graham, M. and Morris, S.W. 2000. Development and geometry of isotropic and directional shrinkage-crack patterns. Physical Review E, 61(6): 6950-6957.

Sima, J., Jiang, M. and Zhou, C. 2014. Numerical simulation of desiccation cracking in a thin clay layer using 3D discrete element modeling. Computers and Geotechnics, 56: 168-180.

Simms, P. 2016. 2013 Colloquium of the Canadian Geotechnical Society: geotechnical and geoenvironmental behaviour of high-density tailings. Canadian Geotechnical Journal, 54(4): 455-468.

Simms, P., Soleimani, S., Mizani, S., Daliri, F., Dunmola, A., Rozina, E. and Innocent-Bernard, T. 2017. Cracking, salinity and evaporation in mesoscale experiments on three types of tailings. Environmental Geotechnics, 6(1): 3-17.

Singh, S.P., Rout, S. and Tiwari, A. 2018. Quantification of desiccation cracks using image analysis technique. International Journal of Geotechnical Engineering, 12(4): 383-388.

Skempton, A.W. 1964. Long-term stability of clay slopes. Géotechnique, 14(2): 77-102.

Snyder, V.A. 1980. Theoretical aspects and measurement of tensile strength in unsaturated soils. Doctoral dissertation, Cornell University, USA.

Snyder, V. A. and Miller, R. D. 1989. Soil deformation and fracture under tensile forces. In the NATO Advanced Research Workshop on Mechanics and Related Processes in Structured Agricultural Soils (pp. 23–35). St. Paul, Minnesota, USA: Kluwer Academic Publisher.

Snyder, V.A. and Miller, R.D. 1985. Tensile strength of unsaturated soils. Soil Science Society of America Journal, 49(1): 58-65.

Somasundaram, J., Lal, R., Sinha, N.K., Dalal, R., Chitralekha, A., Chaudhary, R.S. and Patra, A.K. 2018. Cracks and potholes in vertisols: Characteristics, occurrence, and management. In Advances in Agronomy, Vol. 149, pp. 93-159. Academic Press.

Stirling, R.A., Hughes, P., Davie, C.T. and Glendinning, S. 2015. Tensile behaviour of unsaturated compacted clay soils - A direct assessment method. Applied Clay Science, 112–113: 123–133.

Stirling, R.A., Glendinning, S. and Davie, C.T. 2017. Modelling the deterioration of the near surface caused by drying induced cracking. Applied Clay Science, 146: 176-185.

Sture, S., Costes, N.C., Batiste, S.N., Lankton, M.R., AlShibli, K.A., Jeremic, B., Swanson, R.A. and Frank, M. 1998. Mechanics of granular materials at low effective stresses. Journal of Aerospace Engineering, 11(3): 67–72.

Sun K., Tang C., Liu C., Li H., Wang P. and Leng T. 2017. Research methods of soil desiccation cracking behavior. Rock and Soil Mechanics, 38(s1): 11-26. [in Chinese]

Tamrakar, S., Toshiyuki, Y. and Itoh, K. 2005. Development of a new soil tensile strength test apparatus. In Site Characterization and Modeling, pp. 1–10.

Tang, A.M., Hughes, P.N., Dijkstra, T.A., Askarinejad, A., Brenčič, M., Cui, Y.J., Diez, J.J., Firgi, T., Gajewska, B., Gentile, F. and Grossi, G. 2018a. Atmosphere–vegetation–soil interactions in a climate change context; impact of changing conditions on engineered transport infrastructure slopes in Europe. Quarterly Journal of Engineering Geology and Hydrogeology, 51(2): 156-168.

Tang, C.S., Cui, Y.J., Tang, A.M. and Shi, B. 2010. Experiment evidence on the temperature dependence of desiccation cracking behavior of clayey soils. Engineering Geology, 114(3-4): 261-266.

Tang, C.S., Cui, Y.J., Shi, B., Tang, A.M., and Liu, C. 2011a. Desiccation and cracking behaviour of clay layer from slurry state under wetting–drying cycles. Geoderma, 166(1): 111-118.

Tang, C.S., Pei, X.J., Wang, D.Y., Shi, B. and Li, J. 2015. Tensile strength of compacted clayey soil. Journal of Geotechnical and Geoenvironmental Engineering, 141(4): 04014122.

Tang, C.S., Shi, B., Cui, Y.J., Liu, C. and Gu, K. 2012. Desiccation cracking behavior of polypropylene fiber–reinforced clayey soil. Canadian Geotechnical Journal, 49(9): 1088-1101.

Tang, C., Shi, B., Liu, C., Zhao, L. and Wang, B. 2008. Influencing factors of geometrical structure of surface shrinkage cracks in clayey soils. Engineering Geology, 101(3-4): 204-217.

Tang, C.S., Shi, B., Liu, C., Suo, W.B., and Gao, L. 2011b. Experimental characterization of shrinkage and desiccation cracking in thin clay layer. Applied Clay Science, 52(1-2): 69-77.

Tang, C.S., Wang, D.Y., Zhu, C., Zhou, Q.Y., Xu, S.K. and Shi, B. 2018b. Characterizing drying-induced clayey soil desiccation cracking process using electrical resistivity method. Applied Clay Science, 152: 101-112.

Tang, C.S., Zhu, C., Leng, T., Shi, B., Cheng, Q., and Zeng, H. 2019. Three-dimensional characterization of desiccation cracking behavior of compacted clayey soil using X-ray computed tomography. Engineering Geology, 255: 1-10.

Tang, G. X. and Graham, J. 2000. A method for testing tensile strength in unsaturated soils. Geotechnical Testing Journal, 23(3): 377–382.

Tarafdar, S. and Dutta, T. 2018. Formation of desiccation crack patterns in electric fields: a review. Philosophical Transactions of the Royal Society A, 377(2136): p.20170398.

Tarantino, A. 2009. A water retention model for deformable soils. Géotechnique, 59(9): 751-762.

Thorne, C.P. 1984. Strength assessment and stability analyses for fissured clays. Géotechnique, 34(3): 305-322.

Thusyanthan, N.I., Take, W.A., Madabhushi, S.P.G. and Bolton, M.D. 2007. Crack initiation in clay observed in beam bending. Géotechnique, 57(7): 581-594.

Towner, G. D. 1987. The mechanics of cracking of drying clay. Journal of Agricultural Engineering Research, 36: 115-124.

Trabelsi, H., Hadrich, B. and Guiras, H. 2018a. Evaporation, shrinkage and intrinsic permeability of unsaturated clayey soil: analytical modelling versus experimental data. Arabian Journal of Geosciences, 11(8): p.184.

Trabelsi, H., Jamei, M., Zenzri, H. and Olivella, S. 2012. Crack patterns in clayey soils: experiments and modeling. International Journal for Numerical and Analytical Methods in Geomechanics, 36: 1410–1433.

Trabelsi, H., Romero, E. and Jamei, M. 2018b. Tensile strength during drying of remoulded and compacted clay: the role of fabric and water retention. Applied Clay Science, 162: 57-68.

Tschebatorioff, F.P., 1953. The tensile strength of disturbed and recompacted soils. In Proceedings of the 3rd International Conference of Soil Mechanics and Foundation Engineering, Vol. 1, pp. 207-210.

Twenhofel, W.H. 1950. Principles of Sedimentation. McGraw-Hill, New York.

Uday, K. V., Jayanthi, P. N. V. and Singh, D. N. 2014. A generalized relationship for determination of tensile strength of fine-grained soils from shrinkage characteristics. Drying Technology, 32(7): 869–876.

Uday, K.V. and Singh, D.N. 2012. Application of laser microscopy for studying crack characteristics of fine-grained soils. Geotechnical Testing Journal, 36(1): 146-154.

Uday, K.V. and Singh, D.N. 2013. Investigation on cracking characteristics of fine-grained soils under varied environmental conditions. Drying Technology, 31(11): 1255-1266.

United States Environmental Protection Agency (USEPA). 1989. Requirements for hazardous waste landfill design, construction and closure. Seminar Pub., EPA 625 4–89/022. Washington, USA.

Utili, S. 2013. Investigation by limit analysis on the stability of slopes with cracks. Géotechnique, 63(2): 140-154.

van Genuchten, M.T. 1980. A closed-form Eq. for predicting the hydraulic conductivity of unsaturated soils. Soil Science Society of America Journal, 44(5): 892–898.

Vanapalli, S.K., Fredlund, D.G., Pufahl, D.E. and Clifton, A.W. 1996. Model for the prediction of shear strength with respect to soil suction. Canadian Geotechnical Journal, 33(3): 379–392.

Varsei, M., Miller, G.A. and Hassanikhah, A. 2016. Novel approach to measuring tensile strength of compacted clayey soil during desiccation. International Journal of Geomechanics, 16(6): 1–10.

Venkataramana, K., Rao, B.H. and Singh, D.N. 2009. A critical review of the methodologies employed for determination of tensile strength of fine-grained soils. Journal of Testing and Evaluation, 37(2): 115–121.

Vesga, L. F. and Vallejo, L. E. 2006. Direct and indirect tensile tests for measuring the equivalent effective stress in a Kaolinite clay. ASCE Geotechnical Special Publication 147: 1290–1301.

Villar, L. F. S., De Campos, T. M. P., Azevedo, R. F. and Zornberg, J. G. 2009. Tensile strength changes under drying and its correlations with total and matric suctions. In Proceedings of the 17th International Conference on Soil Mechanics and Geotechnical Engineering: The Academia and Practice of Geotechnical Engineering, Vol. 1, pp. 793–796.

Vo, T.D., Pouya, A., Hemmati, S. and Tang, A.M. 2017. Numerical modelling of desiccation cracking of clayey soil using a cohesive fracture method. Computers and Geotechnics, 85: 15-27.

Vogel, H.J., Hoffmann, H., Leopold, A. and Roth, K. 2005. Studies of crack dynamics in clay soil: II. A physically based model for crack formation. Geoderma, 125(3-4): 213-223.

Vomocil, J.A., Waldron, L.J. and Chancellor, W.J. 1961. Soil tensile strength by centrifugation. Soil Science Society of America Journal, 25(3): 176–180.

Wang, Y., Feng, D. and Ng, C.W. 2013. Modeling the 3D crack network and anisotropic permeability of saturated cracked soil. Computers and Geotechnics, 52: 63-70.

Wang, Z.F., Li, J.H. and Zhang, L.M., 2012. Influence of cracks on the stability of a cracked soil slope. In Proceedings of the 5th Asia-Pacific Conference on Unsaturated Soils, Pattaya, pp. 721-728.

Wang, L.L., Tang, C.S., Shi, B., Cui, Y.J., Zhang, G.Q. and Hilary, I. 2018. Nucleation and propagation mechanisms of soil desiccation cracks. Engineering Geology, 238: 27-35.

Wang, J. J., Zhu, J. G., Chiu, C. F. and Zhang, H. 2007. Experimental study on fracture toughness and tensile strength of a clay. Engineering Geology, 94(1–2): 65–75.

Weaver, T., Hulugalle, N. and Ghadiri, H. 2005. Comparing deep drainage estimated with transient and steady state assumptions in irrigated vertisols. Irrigation Science, 23 (4): 183–191.

Wei, X., Hattab, M., Bompard, P. and Fleureau, J.M. 2016. Highlighting some mechanisms of crack formation and propagation in clays on drying path. Géotechnique, 66(4): 287-300.

Weinberger, R. 1999. Initiation and growth of cracks during desiccation of stratified muddy sediments. Journal of Structural Geology, 21(4): 379-386.

Williams, A.A.B. 1965. The deformation of roads resulting from moisture changes in expansive soils in South Africa. In Moisture equilibria and moisture changes in soils beneath covered areas (ed. Aitchison, G.D.), Butterworth, pp. 143-155.

Win, S. S. 2006. Tensile strength of compacted soils subject to wetting and drying. Master's dissertation, The University of New South Wales, Australia.

Wollborn, T., Schwed, M. F. and Fritsching, U. 2017. Direct tensile tests on particulate agglomerates for the determination of tensile strength and interparticle bond forces. Advanced Powder Technology, 28(9): 2177–2185.

Wu, J.H. and Yuan, J.P. 2013. Field tests on expansive soil during wetting-drying cycles using large shear apparatus. Chinese Journal of Geotechnical Engineering, 35(s1): 103-107. [in Chinese]

Xu, B., Yin, Z.Z. and Liu, S.L. 2011. Experimental study of factors influencing expansive soil strength. Rock and Soil Mechanics, 32(1): 44-50. [in Chinese]

Yao, H.L., Zheng, S.H. and Chen, S.Y. 2001. Analysis on the slope stability of expansive soils considering cracks and infiltration of rain. Chinese Journal of Geotechnical Engineering, 23(5): 606-609. [in Chinese]

Yesiller, N., Miller, C.J., Inci, G. and Yaldo, K. 2000. Desiccation and cracking behavior of three compacted landfill liner soils. Engineering Geology, 57(1-2): 105-121.

Yin, P. and Vanapalli, S.K. 2018a. Model for predicting tensile strength of unsaturated cohesionless soils. Canadian Geotechnical Journal, 55(9): 1313-1333.

Yin, P. and Vanapalli, S.K. 2018b. Prediction of tensile strength of compacted soils: A review. In Proceedings of the 7th International Conference on Unsaturated Soils, Hong Kong, China.

Yin, Z.Z. and Xu, B. 2011. Slope stability of expansive soil under fissure influence. Chinese Journal of Geotechnical Engineering, 33(3): 454-459. [in Chinese]

Yin, Z.Z., Yuan, J.P., Wei, J., Cao, X.S., Liu, H.Q. and Xu, B. 2012. Influence of fissures on slope stability of expansive soil. Chinese Journal of Geotechnical Engineering, 34(12): 2155-2161. [in Chinese]

Yuan, J.P. and Yin, Z.Z. 2004. Quantitative index of fissure and strength characteristics of fissured expansive soils. Shuili Xuebao, 06: 108-113. [in Chinese]

Zeng, H., Tang, C.S., Cheng, Q., Inyang, H.I., Rong, D.Z., Lin, L. and Shi, B. 2019. Coupling effects of interfacial friction and layer thickness on soil desiccation cracking behavior. Engineering Geology, 260: p.105220.

Zeh, R. M. and Witt, K. J. 2005. Suction-controlled tensile strength of compacted clays. In Proceedings of the 16th International Conference on Soil Mechanics and Geotechnical Engineering, Osaka, Japan, Vol. 4, pp. 2347–2352.

Zhan, T.L., Ng, C.W. and Fredlund, D.G. 2007. Field study of rainfall infiltration into a grassed unsaturated expansive soil slope. Canadian Geotechnical Journal, 44(4): 392-408.

Zhang, X.J. and Chen, W.F. 1987. Stability analysis of slopes with general nonlinear failure criterion. International Journal for Numerical and Analytical Methods in Geomechanics, 11(1): 33–50.

Zhang, B., Li, Q., Yuan, H. and Sun, X. 2015. Tensile fracture characteristics of compacted soils under uniaxial tension. Journal of Materials in Civil Engineering, 27(10), 04014274.

Zhang, L.L., Zhang, J., Zhang, L.M. and Tang, W.H. 2011. Stability analysis of rainfall-induced slope failure: A review. In Proceedings of the Institution of Civil Engineers-Geotechnical Engineering, 164(5): 299-316.

Zhang, T., Deng, Y., Cui, Y., Lan, H., Zhang, F. and Zhang, H. 2019. Porewater salinity effect on flocculation and desiccation cracking behaviour of kaolin and bentonite considering working condition. Engineering Geology, 251: 11-23.

Zhou, Y.D., Cheuk, C.Y. and Tham, L.G. 2009. Deformation and crack development of a nailed loose fill slope subjected to water infiltration. Landslides, 6(4): 299-308.

Zielinski, M. 2009. Influence of desiccation fissuring on the stability of flood embankments. Doctoral dissertation, University of Strathclyde, UK.

Zielinski, M., Sánchez, M., Romero, E. and Atique, A. 2014. Precise observation of soil surface curling. Geoderma, 226: 85-93.

Chapter 3. Model for Predicting the Tensile Strength of Unsaturated Cohesionless Soils

3.1 Background

The tensile strength is a key property that significantly influences the tensile cracking and subsequent tensile failure of earth structures such as the earth dams, slopes, highway embankments, the clay covers and liners of waste landfills, and the sand-bentonite package used for nuclear waste isolation systems. In conventional engineering practice, it is typically assumed that the cohesionless soils have no tensile strength. Unsaturated cohesionless soils, however, exhibit tensile strength that mainly arises from capillary forces which typically vary from several kilopascals in wet sands to several tens of kilopascals in wet silts (Ingles 1962a). In cohesionless (or, uncemented) soils, tensile strength is mainly induced by two types of interparticle capillary forces, namely (i) capillary force due to the matric suction (or, negative pore water pressure), and (ii) capillary force due to surface tension of wetting liquid acting on the air-water interface (e.g., Ingles 1962b; Lu et al. 2005). The former can exist in soils in either saturated or unsaturated state, while the latter can only act on air-water interface within unsaturated soils.

Various theoretical models (e.g., Fisher 1926; Rumpf 1961; Snyder and Miller 1985; Morris et al. 1992; Lu et al. 2009; Varsei et al. 2016) and empirical models (e.g., Kim and Hwang 2003) have been put forward for predicting the tensile strength of unsaturated granular materials. However, investigation studies related to the tensile strength of unsaturated soils taking account of the contribution from air-water interfaces over the entire saturation range is rather limited. From a behavioural standpoint, an unsaturated soil can be visualised as a mixture with two phases that come to equilibrium under applied stress gradients (i.e. soil particles and contractile skin) and two phases that flow under applied stress gradients (i.e. air and water). It is rational to recognise that the contractile skin (or, air-water interfaces) behaves as an independent phase, especially when performing stress analysis on an unsaturated soil element (Fredlund and Morgenstern 1977). The air-water interfaces have an important contribution to the bonding effects, which is the origin of the tensile strength of unsaturated soils. In early works, it was found that the bonding phenomenon is related to the amount of air-water interfaces by some pioneers who significantly contributed to our present understanding of unsaturated soil mechanics (e.g., Blight 1961; Matyas and Radhakrishna 1968). More recently, micromechanical studies (e.g., Coussy 2011; Nikooee et al. 2013; Likos and Jaafar 2013) and experimental investigations (e.g., Willson et al. 2012; Jindal et al. 2016) also

noted the importance of the air-water interface in the mechanical behavior of unsaturated soils. Therefore, it is necessary to consider the effect of the air-water interface on capillary force and consequently the tensile strength of unsaturated cohesionless soils by utilizing the classical "Bundle of Cylindrical Capillary" (BCC) model, in which the overall soil pore space is idealized as a bundled population of tubes with variable radius following the pore size distribution.

In this chapter, Soil-Water Characteristic Curve (SWCC) and Tensile Strength Characteristic Curve (TSCC) for unsaturated soils is first succinctly reviewed. A semi-empirical TSCC model is proposed using the SWCC as a tool. This model is capable of predicting the tensile strength which arises from both the matric suction within the saturated pores and the surface tension acting on the air-water interface associated with water bridges around the interparticle contacts in partially saturated pores. Moreover, the proposed model is validated by comparing the prediction results with measured tensile strength of ten different unsaturated cohesionless soils (which include five sandy soils and five silty soils) using a total of 21 sets of data from the literature. The proposed model is found to be suitable for predicting the variation of tensile strength with the degree of saturation, not only for unsaturated sandy soils but also for unsaturated silty soils, with the aid of two model parameters (k and η_s) which can be estimated from empirical relationships associated with the coefficient of uniformity (C_u). Lastly, various factors influencing the tensile strength of unsaturated cohesionless soils and the potential engineering practice applications of the proposed model are discussed.

3.1.1 Soil-Water Characteristic Curve (SWCC) and Tensile Strength Characteristic Curve (TSCC) for Unsaturated soils

Based on the idealisation of capillarity as the BCC model, many important concepts have been put forward for interpreting the behavior of unsaturated soils, such as the SWCC which establishes the relationship between the degree of saturation and the matric suction. Several mathematical functions for describing the SWCC can be found in the literature (e.g., Brooks and Corey 1964; van Genchten 1980; Fredlund and Xing 1994; Kosugi 1994). Among those SWCC models, the commonly used van Genuchten (1980) model is as follows:

$$(3.1a)\quad S_e = \frac{1}{\left\{1+\left[\alpha_{vg}(u_a-u_w)\right]^{n_{vg}}\right\}^{1-1/n_{vg}}}$$

(3.1b) $S_e = \dfrac{S - S_r}{1 - S_r}$

where (u_a - u_w) is matric suction (or, negative pore water pressure), α_{vg} and n_{vg} are least-square fitting parameters based on the measured water retention data, S_e is the effective degree of saturation, S_r is the residual degree of saturation. It is worth noting that, S_r might be negligible (i.e. close to zero) as a fitting parameter in Eq. (3.1) for cohesionless soils. The residual degree of saturation, S_r in the remainder of this chapter is determined by the graphical method (Vanapalli et al. 1999) instead of a fitting parameter. Figure 3.1 depicts a typical plot of the SWCC for unsaturated soils, highlighting three different saturation regimes: (i) capillary regime (or, boundary effect zone), (ii) funicular regime (or, transition zone), and (iii) pendular regime (or, residual zone), on the basis of the distribution of the water and air phases within the soil matrix (White et al. 1970; Orr et al. 1975; Vanapalli et al. 1996; Vanapalli et al. 1998). In addition, the capillary degree of saturation (S_c) corresponding to the air-entry value (AEV), and residual degree of saturation (S_r) corresponding to the residual suction are the lower saturation bounds to the capillary regime and funicular regime, respectively.

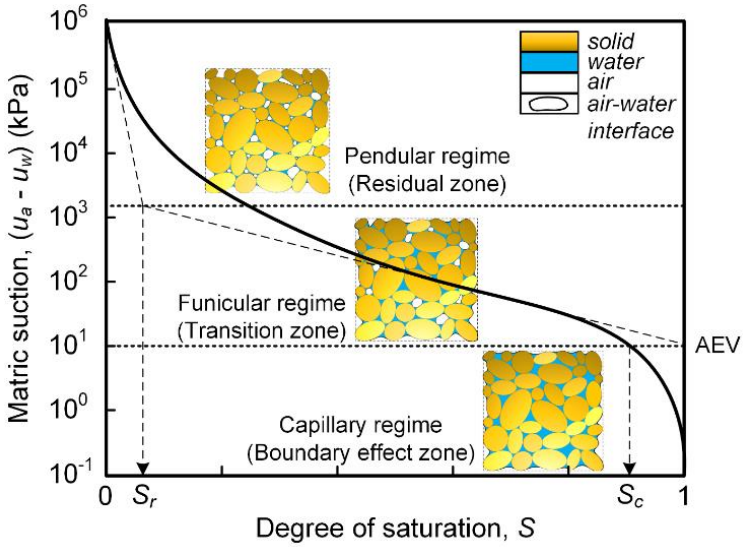

Figure 3.1 Schematic illustration of typical SWCC for unsaturated soils with three different saturation regimes: (i) the capillary regime (or, boundary effect zone), (ii) the funicular regime (or, transition zone), and (iii) the pendular regime (or, residual zone).

The terminology of "TSCC" (i.e. Tensile Strength Characteristic Curve) was proposed by Lu et al. (2007), in order to provide a comprehensive understanding of the tensile strength of unsaturated soils in different saturation regimes. It was suggested that the tensile strength of unsaturated sands originates only from the interparticle capillary forces, without any other physical or chemical mechanisms. The physical mechanisms contributing to the tensile strength of unsaturated sands could be quite different in each of the different saturation regimes (or, different zones, see Figure 3.1). In the capillary regime (or, boundary effect zone), the outside menisci at boundaries are pulled inward and the soil suction increases with small reductions in water content. The capillary force and consequently tensile strength mainly originate from the matric suction within the soil pores. When the soil suction reaches the air-entry value (AEV), the air phase breaks into the pore structure and the soil mass becomes unsaturated in the funicular regime (or, transition zone). As drying proceeds, the soil suction increases gradually with decreasing water content (or degree of saturation). And the water phase, which varies from continuous to disconnected state with desaturation, exists in two forms: (i) water filled in saturated pores, and (ii) water bridges around the particle contacts within unsaturated pores. Thus, in this saturation range, the capillary force and tensile strength are induced by not only matric suction but also surface tension associated with water bridges. In pendular regime (or, residual zone), water exists mainly in the form of water bridges around the particle contacts, and capillary force and tensile strength mainly result from the surface tension acting on the air-water interface. Therefore, there are two different mechanisms which contribute to the capillary force and consequently tensile strength of unsaturated cohesionless soils: (i) matric suction, and (ii) surface tension. In the capillary regime, matric suction predominantly contributes to the tensile strength; while surface tension is significant in the pendular regime. In the funicular regime, those two mechanisms jointly contribute to the overall tensile strength, which is consistent with "the superimposed theory" proposed by Schubert (1973, 1975).

3.1.2 Predicting the properties of unsaturated soils using the SWCC as a tool

The engineering behavior of an unsaturated soil is significantly influenced by the soil-water interaction and soil structure. As the SWCC reflects the integrated information related to soil-water interaction and soil structure, it has been successfully used as a tool to predict the nonlinear behavior of unsaturated soils, such as the hydraulic conductivity (e.g., Fredlund et al. 1994; Simms and Yanful 2001), volume change (e.g., Thu et al. 2007; Tu and Vanapalli 2016; Han and Vanapalli 2017), shear strength (e.g., Fredlund et al. 1996; Oh et al. 2011), and tensile strength (e.g., Kim and Stein 2008; Lu et al. 2009; Narvaez et al.

2015; Varsei et al. 2016). Most of the model parameters of the equations developed following this approach associate with the soil properties which can be obtained or estimated from conventional laboratory tests. For example, Vanapalli et al. (1996) proposed a simple model based on the SWCC and conventional shear strength parameters of saturated soils (i.e. cohesion, and internal friction angle) to predict the nonlinear shear strength behavior of unsaturated soils, τ_f:

(3.2a) $$\tau_f = c' + (\sigma_n - u_a)\tan\phi' + (u_a - u_w)\tan\phi^b$$

(3.2b) $$\tan\phi^b = (S^\kappa)\tan\phi'$$

where $(\sigma_n - u_a)$ is the net normal stress on the plane of failure at failure; ϕ^b is the angle of shearing resistance with respect to matric suction, $(u_a - u_w)$; and κ is a model parameter which is related to the plasticity index of the soil (Vanapalli and Fredlund 2000).

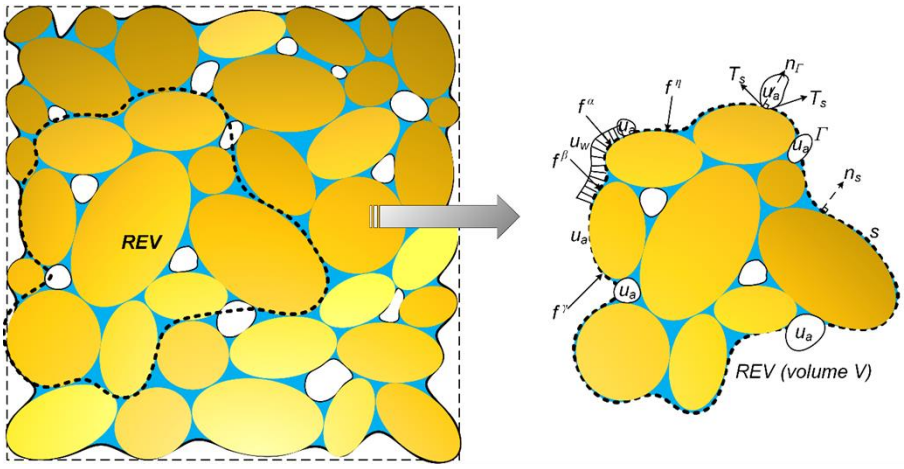

Figure 3.2 Conceptual illustration of a three-phase granular material and the external force system acting on the boundary of REV. (Note: *REV*, representative element volume; *S*, boundary of *REV* with unit outer normal vector, n_s; Γ, air-water interface with unit outer normal vector, n_Γ; u_a and u_w, pore air, and pore water pressure respectively; T_s, surface tension pre length that acts along the edge of the air-water interface; f^i, contact force at contact point *i*.)

Figure 3.2 illustrates the external force system acting on the boundaries of the representative element volume (REV) of a soil-water-air system. In unsaturated cohesionless soils, there are three types of forces acting on the boundary of the REV: (i) pore water pressure (which is a negative value compared with the atmosphere pressure); (ii) pore air pressure; (iii) surface tension acting along the air-water interface (or, contractile skin which pulls the soil particles together). When the pore air pressure is assumed to be equivalent to the atmospheric pressure, the second type of force is eliminated. Therefore, the unsaturated

cohesionless soil element is subjected to only two types of external forces at self-equilibrium state: matric suction and surface tension. The tensile strength is reached when the tensile stress developed on the plane of failure overcomes the interparticle bonding forces. According to Wheeler and Karube (1995) and Gallipoli et al. (2003), matric suction influences the mechanical behavior of unsaturated soils in two different ways: (i) by modifying intergranular stress through negative water pressure in the saturated portions of the pore structure, and (ii) by providing an interparticle bonding or stabilizing force through the water bridges. Therefore, the total tensile strength of unsaturated soils can be considered to have two parts: (i) tensile strength induced by matric suction, and (ii) tensile strength induced by water bridges associated surface tension acting on the air-water interface (Figure 3.3). Extending this philosophical approach to the SWCC and the TSCC, the distribution of saturated pores with negative pore water pressure and the amount of air-water interface varies with respect to degree of saturation. In the capillary regime, the tensile strength is predominately induced by matric suction, while the tensile strength resulting from surface tension is pronounced in the pendular regime. In funicular regime, both of those two mechanisms contribute to the tensile strength. From theoretical analysis, Goulding (2006) suggested that the tensile strength of unsaturated soils has two peak values in the entire range of degree of saturation: one at the capillary degree of saturation, and the other at the residual degree of saturation. Thus in this study, the first part of tensile strength (σ_{tun}) can be assumed to reach the peak value at the capillary degree of saturation, and the second part (σ_{tus}) can be assumed to reach the peak value at the residual degree of saturation.

3.2 Model formulation

3.2.1 Surface tension and specific air-water interfacial area

In order to consider the effect of surface tension on the tensile strength of unsaturated soils, the amount of air-water interfacial area should be quantified. Willson et al. (2012) investigated quantitatively the distribution of pore water and pore air variation along with desaturation in an unsaturated sand by X-Ray Computed Tomography (XCT) imaging. The results demonstrated that the air-water interfacial area increases from dry to low-level volumetric water contents, plateaus with the mid-range water contents, and then decreases at high water contents. In other words, the water bridges associated air-water interfacial area is a non-monotonic function of the degree of saturation. Based on the idealized geometry of the water bridge, Likos and Jaafar (2013) derived the air-water interfacial area in a unit pore (A_{aw}) and the specific

air-water interfacial area per pore volume (a_{aw}) by integrating over the range of pore size containing water bridges ($R_{fill} < R < R_{max}$):

$$(3.3a)\quad A_{aw} = 6\pi(r_1\frac{\pi}{2})\left[r_2 + r_1 - \frac{r_1\sin(\pi/4)}{\pi/4}\right]$$

$$(3.3b)\quad a_{aw} = \int_{R_{fill}}^{R_{max}} \frac{A_{aw}}{V_v} f(R)dR = \int_{R_{fill}}^{R_{max}} \frac{6\pi(r_1\frac{\pi}{2})\left[r_2 + r_1 - \frac{r_1\sin(\pi/4)}{\pi/4}\right]}{(8-\frac{4}{3}\pi)R^3} f(R)dR$$

where radii r_1 and r_2 are related to particle size, filling angle, and contact angle (Likos and Lu 2004), $f(R)$ is the pore-size distribution function (PDF) with respect to pore sizes, R. The simulation results by Eq. (3.3) agreed close with the experimental measurements by Willson et al. (2012). However, the oversimplification of geometric properties of the soil pore system contributes to limitations; and obtaining the PDF is expensive as it needs elaborate equipment facilities use the cumbersome analytical Eq.s. Therefore, a convenient estimation for the specific air-water interface area needs to be proposed for engineering practice applications.

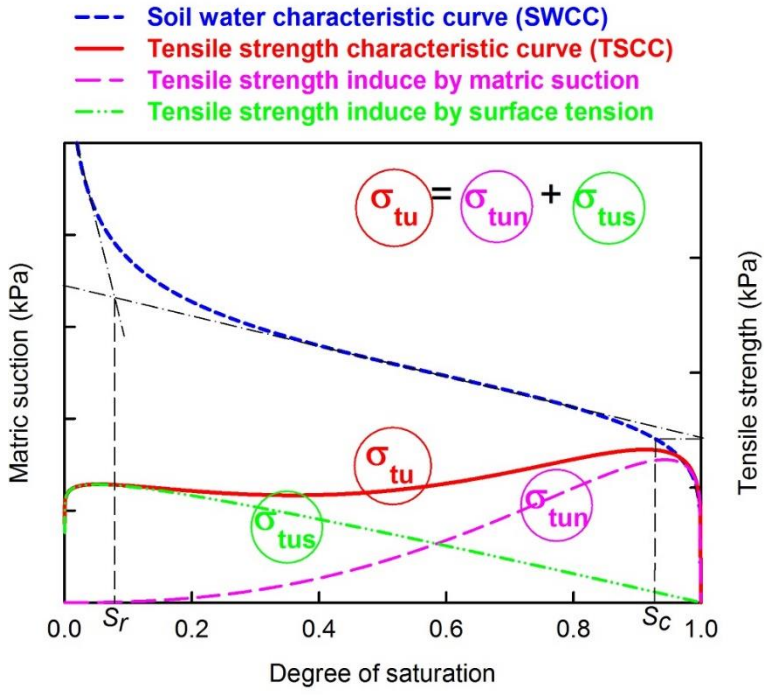

Figure 3.3 Conceptual illustration of the relationship between the SWCC and TSCC for unsaturated cohesionless soils. (Note: the capillary degree of saturation, S_c, and the residual degree of saturation, S_r, are determined by the commonly used tangent method from the SWCC.)

According to Rumpf (1961) and Schubert (1975), the component of tensile strength of moisture aggregates induced by surface tension in partially saturated pores (σ_{tus}) could be estimated by

$$(3.4)\quad \sigma_{tus} = \frac{\pi T_s}{ed} f(\theta, \delta)$$

where e is the void ratio, d is the mean diameter of soil particles, $f(\theta, \delta)$ is the function of half-filling angle (θ) determined by the degree of saturation, and contact angle between the soil particle and the pore fluid (δ). Moreover, the conceptualized "suction stress" is considered to be the isotropic tensile strength of unsaturated soils by Lu et al. (2009). Lu et al. (2010) derived a complex Eq. based on the principle of virtual work applied for a soil system, before simplifying the suction stress (σ^s) as Eq. (2.17). For $V_w \geq V_r$,

$$(3.5)\quad \sigma^s = -S_e(u_a - u_w) - \sum_i T_{si} \left.\frac{\partial A_i}{\partial V}\right|_{\mu,T}$$

where the first term, $-S_e (u_a - u_w)$ represents the contribution to suction stress from matric suction in saturated pores, and the second term, $-\sum_i T_{si} \left.\frac{\partial A_i}{\partial V}\right|_{\mu,T}$ stands for the contribution to suction stress from surface tension in partially saturated pores. T_{si} and A_i are the surface tension and area for interface i respectively, μ and T are chemical potential and temperature to which the soil system is subjected, respectively, V is the volume of soil system, and V_r is the residual volume occupied by the bound water layers adsorbed on the surface of soil particles. The second term, which suggests contribution from surface tension to the tensile strength of unsaturated soil, was ignored in order to simplify the complex mechanism. Furthermore, a general form was derived following similar procedures by quantifying the effect of surface tension on the suction stress (Nikooee et al. 2013; Likos 2014):

$$(3.6)\quad \sigma^s = -S_e(u_a - u_w) - T_s(a_{aw})$$

where T_s is surface tension acting on air-water interface depending on temperature (i.e. 72.2 mN/m at 20°C), and a_{aw} is the specific air-water interface area per pore volume. The influence of temperature and type of pore fluid on surface tension are not considered in this thesis. It is assumed that the environmental temperature is 20°C, and pore fluid is distilled water without solute.

In the spirit of Eqs. (3.4) and (3.6), a semi-empirical model is proposed to estimate the specific air-water interface area per pore volume (a_{aw}):

$$a_{aw} = \eta_s \frac{\pi}{e d_{50}} S_e^{\lambda_s} (1 - S_e) \tag{3.7}$$

where the value of d in Eq. (3.4) is taken equal to the mean particle diameter d_{50}, (1 - S_e) is the degree of air saturation, η_s and λ_s are two fitting parameters. The parameter η_s is introduced to reflect the anisotropy of the distribution of pore water, pore air and air-water interface, and therefore the anisotropic effect of surface tension on the suction stress and consequently the tensile strength of unsaturated soils. The parameter λ_s corresponding to the saturation value at which the maximum specific air-water interfacial area reaches can be determined by the assumption that the second tensile strength component due to the surface tension (σ_{tus}) reaches the peak value at the residual degree of saturation (S_r):

$$\lambda_s = \frac{S_r}{1 - S_r} \tag{3.8}$$

Thus Eq. (3.7) can be rewritten by

$$a_{aw} = \eta_s \frac{\pi}{e d_{50}} S_e^{S_r/(1-S_r)} (1 - S_e) \tag{3.9}$$

In order to validate the efficiency of the proposed model, the specific air-water interface area is simulated by Eq. (3.9) using the least-square fitting procedure based on the test data for Ottawa sand (F75) by Willson et al. (2012). The details of the prediction results are presented in Table 3.1. The prediction by Eq. (3.9) shows good agreement with the measurements, which provides evidence for the assumption that the specific air-water interfacial area increases with a decrease in saturation and reaches a maximum value at the residual degree of saturation (Figure 3.4).

Table 3.1 Details of the prediction results for the specific air-water interfacial area of Ottawa sand (F75).

Ottawa sand (F75) basic properties	Grain size distribution	d_{10} (mm)	0.11
		d_{30} (mm)	0.15
		d_{50} (mm)	0.185
		d_{60} (mm)	0.20
		C_u	1.8
		C_c	1.0
	Specific gravity, G_s		2.65
	Void ratio, e		0.67
	Classification (USCS)		SP
SWCC model (van Genuchten 1980)	α_{vg}		0.29
	n_{vg}		3.91
	S_r^a		0.13
Proposed model (Eq. (3.9)) parameters	η_s		0.22

Note: d_{10}, d_{30}, d_{60}, soil particle size at which 10%, 30%, and 60% of the mass of a soil specimen is finer, respectively; C_u, coefficient of uniformity; C_c, coefficient of curvature; G_s, specific gravity. [a]Estimated by the commonly used tangent method (Figure 3.4b).

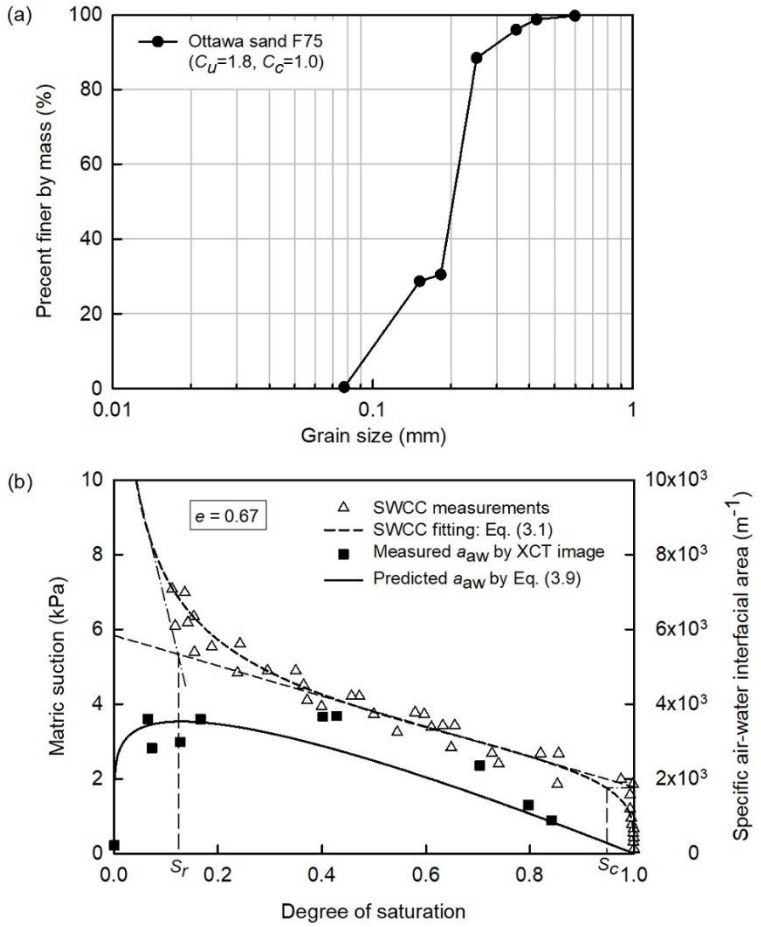

Figure 3.4 Performance of the proposed model (Eq. (3.9)) to estimate the specific air-water interface area (a_{aw}) as a function of the degree of saturation: (a) the grain size distribution of Ottawa sand (F75); (b) comparison between measurements of Willson et al. (2012) and the prediction results based on the SWCC.

3.2.2 Model for predicting tensile strength of unsaturated cohesionless soils

The proposed model is based on macromechanics approach by incorporating it along with the SWCC, which is a bridge connecting the micro-variable (i.e. soil suction) and macro-variable (i.e. the degree of saturation). Based on the relationship between the SWCC and the TSCC over the entire saturation range established by Figure 3.3, the total uniaxial tensile strength of unsaturated cohesionless soils (σ_{tu}) is the superimposition of the tensile strength component induced by the matric suction within the saturated pores (σ_{tun}), and the tensile strength component induced by the surface tension associated with water bridges (σ_{tus}):

(3.10a) $\sigma_{tu} = \sigma_{tun} + \sigma_{tus}$

(3.10b) $\sigma_{tun} = 2\tan(\phi_t)\tan(\frac{\pi}{4} - \frac{\phi_t}{2})[S_e{}^k(u_a - u_w)]$

(3.10c) $\sigma_{tus} = 2\tan(\phi_t)\tan(\frac{\pi}{4} - \frac{\phi_t}{2})(T_s \cdot a_{aw})$

Alternatively,

(3.11) $\sigma_{tu} = 2\tan(\phi_t)\tan(\frac{\pi}{4} - \frac{\phi_t}{2})(\sigma^s) = 2\tan(\phi_t)\tan(\frac{\pi}{4} - \frac{\phi_t}{2})[S_e{}^k(u_a - u_w) + T_s \cdot a_{aw}]$

where parameter k is introduced to facilitate flexibility of the first component (σ_{tun}) to accommodate the peak value to occur at the capillary degree of saturation, compared with the TSCC model proposed by Lu et al. (2009). In addition, the degree of saturation (S_0) corresponding to the peak tensile strength of the first component can be related to the parameter, k, and one of the SWCC model parameters, n_{vg}, as follows:

(3.12) $S_0 = \left[1 - \frac{1}{k(1-n_{vg})+1}\right]^{(1-n_{vg})/n_{vg}}$

3.3 Model validation

A total of 21 sets of data derived from ten different cohesionless soils (five sandy soils and five silty soils) listed in Table 3.2 are used to validate the proposed TSCC model (Eq. (3.11)). The details of the SWCC

of the ten cohesionless soils are summarized in Table 3.3. The fitting parameters (i.e. α_{vg} and n_{vg}) of the van Genuchten (1980) SWCC model (Eq. (3.1)) will be used in Eq. (3.11) for predicting the tensile strength, σ_{tu}.

3.3.1 Ottawa sand (soil 1) from Illinois, USA (Goulding 2006)

The tensile strength of unsaturated Ottawa sand (soil 1) was measured using the uniaxial tension apparatus which was modified by Kim (2001) from the original version developed by Perkins (1991). Goulding (2006) conducted direct shear and direct tension tests using three gradations (F40, F55, and F75) of Ottawa sand at relatively loose (e = 0.75) and relatively dense (e = 0.6) states over a wide saturation range (7% ~ 64%, for loose states; 8% ~ 80%, for dense states). The tensile strength of unsaturated sands exhibited double-peak behavior as a function of the degree of saturation, which tends to flatten out as the grain size increases. The maximum tensile strength of Ottawa sand at dense state is larger than that of Ottawa sand at loose state with the same gradation (Figures 3.5(b) and (c); Figures 3.5(d) and (e); Figures 3.5(f) and (g)).

The results of grain size analysis for Ottawa sand from Goulding (2006), are presented in Figure 3.5(a). The friction angle for Ottawa sand at low normal stress level (ϕ_t) is taken as 55° based on Kim (2001). Figure 3.5 presents the measured and predicted SWCC and TSCC by Eqs. (3.1) and (3.11), respectively. The SWCCs show different characteristics due to the difference in their soil structure resulting from different gradations and different relative densities. The proposed TSCC model (Eq. (3.11)) provides a reliable prediction for the tensile strength values of Ottawa sand for the entire range of saturation. The prediction results suggest that the second component of tensile strength (σ_{tus}) has a significant value compared with the first part (σ_{tun}), which validates the need for accounting for the tensile strength component induced by the surface tension. However, the predictions show poor agreements with the measured tensile strength values at relatively high saturation values. It is perhaps the sensitive variation of the measurements to the experimental instrument in Goulding's tests that results in the peak value of the first component (σ_{tun}) occurs far away from the capillary degree of saturation which undermines the model assumption.

Table 3.2 Soil properties of unsaturated cohesionless soils used in this study.

No.	Soil Name	Sub-type	Location	Grain size distribution						G_s	USCS	Reference
				d_{10} (mm)	d_{30} (mm)	d_{50} (mm)	d_{60} (mm)	C_u	C_c			
1	Ottawa sand	F40	IL, USA	0.25	0.27	0.33	0.38	1.52	0.77	2.65	SP	Goulding (2006)
		F55		0.18	0.23	0.25	0.27	1.50	1.09	2.65	SP	
		F75		0.15	0.18	0.21	0.26	1.73	0.83	2.65	SP	
2	Perth sand	Silty	WA, Australia	0.06	0.08	0.11	0.11	1.79	0.99	2.65	SP	Lu et al. (2007)
		Fine		0.12	0.14	0.17	0.17	1.47	0.97	2.65	SP	
		Medium		0.31	0.38	0.45	0.47	1.50	1.00	2.65	SP	
3	Esperance sand		WA, USA	0.13	0.15	0.23	0.24	1.88	0.71	N/A	SP	Lu et al. (2009)
4	Silica sand		AB, Canada	0.24	0.35	0.42	0.46	1.96	1.12	2.65	SP	Jindal et al. (2016)
5	Glass balls fraction G4		Bavaria, Germany	0.11	0.13	0.15	0.15	1.35	1.00	N/A	SP	Schubert (1972)
6	Limestone aggregates K1			0.053	0.064	0.071	0.087	1.64	0.89	N/A	ML	
7	Manchester silt		NH, USA	0.006	0.01	0.017	0.022	3.67	0.76	2.70	ML	Snyder (1980)
8	Tailings A		QC, Canada	0.002	0.008	0.012	0.019	9.50	1.68	2.75	ML	Narvaez et al. (2015)
9	Tailings B			0.003	0.015	0.030	0.042	14.00	1.79	2.77	ML	
10	Tailings C			0.002	0.008	0.021	0.040	20.00	0.80	2.93	ML	

Note: N/A, not available in the cited studies; ML, low-plastic silt.

Table 3.3 Details of the SWCC and the testing techniques of unsaturated cohesionless soils used in this study.

No	Soil Name	Sub-type	Void ratio, e	SWCC model (Eq. (3.1)) fitting results			Saturation boundaries[a]		Testing technique
				α_{vg} (1/kPa)	n_{vg}	R^2	S_r	S_c	
1	Ottawa sand	F40	0.75	0.255	7.78	0.96	0.03	0.92	Tempe cell, hanging column system, and tensiometer
			0.6	0.274	6.94	0.96	0.03	0.92	
		F55	0.75	0.476	3.55	0.90	0.10	0.95	
			0.6	0.398	4.13	0.94	0.08	0.95	
		F75	0.75	0.240	5.97	0.95	0.07	0.93	
			0.6	0.348	3.34	0.91	0.12	0.95	
2	Perth sand	Silty	0.82	0.297	2.99	0.99	0.02	0.90	Standard Tempe cell
		Fine	0.82	0.173[b]	3.12[b]	-	0.02	0.91	
			0.59	0.173	3.12	0.95	0.02	0.91	
		Medium	0.67	0.7[c]	4[c]	-	0.07	0.95	
			0.59	0.7[c]	4[c]	-	0.07	0.95	
3	Esperance sand		0.82	0.804[b]	3.35[b]	-	0.09	0.95	Standard Tempe cell
			0.67	0.804	3.35	0.98	0.09	0.95	
4	Silica sand		0.65	0.414	3.11	0.98	0.12	0.96	------
			0.61	0.414	3.11	0.98	0.12	0.96	
5	Glass balls fraction G4		0.59	0.197	6.77	0.94	0.08	0.93	Axis translation
6	Limestone aggregates K1		0.71	0.084	9.00	0.98	0.06	0.92	Axis translation
7	Manchester silt		0.73[d]	0.011	3.34	0.90	0.03	0.90	Axis translation
8	Tailings A		0.84	0.006	1.89	0.99	0.10	0.92	Pressure plate
9	Tailings B		0.79	0.012	2.35	0.99	0.02	0.91	
10	Tailings C		0.81	0.012	2.38	0.99	0.02	0.92	

Note: *a*: estimated by the commonly used tangent method (Figures 3.5-3.11); *b*: assumed to be identical to those for the same soil with different void ratio; *c*: assumed values by Lu et al. (2009); *d*: estimated value after Stevens (1973).

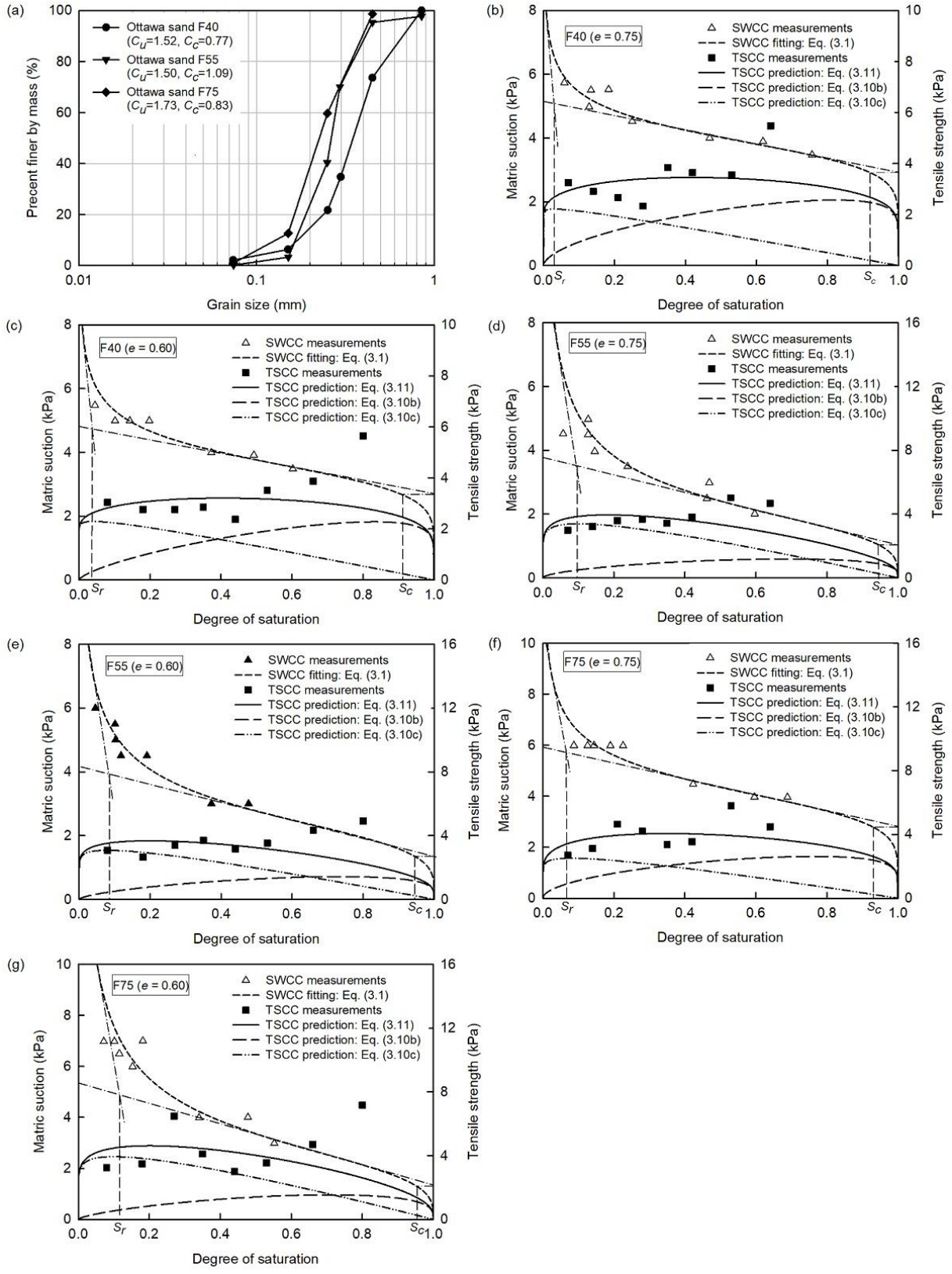

Figure 3.5 Ottawa sand: (a) the grain size distribution curves; the measured SWCC data and the corresponding fitting result based on van Genuchten (1980), and the comparison between the measured TSCC data and the predicted TSCC result by Eq. (3.11) for F40 (b, c), F55 (d, e), and F75 (f, g).

3.3.2 Perth sand (soil 2) from Western Australia, Australia (Lu et al. 2007)

Lu et al. (2007) conducted a series of tensile strength tests on unsaturated Perth sand (soil 2) using the uniaxial tension apparatus which was developed by Lu et al. (2005). The focus of these tests was to understand comprehensively the tensile strength characteristics of unsaturated sands induced by capillary forces. The sands were first sieved and separated into three groups; namely, silty sand, fine sand, and medium sand. Each group of specimens were compacted or cored into the sample tubing to different desired porosities (e.g., e = 0.82 and 0.59 for fine sand).

The grain size analysis results for Perth sand with three different gradations are presented in Figure 3.6(a). The friction angle for Perth sand at low normal stress level (ϕ_t) is taken as 48° based on Lu et al. (2009). The prediction results compared with the measurements of tensile strength are shown in Figures 3.6(b), (c), (d), (e) and (f). The prediction captures the variation of tensile strength over entire range of the degree of saturation. These results suggest that the maximum tensile strength value increases with the decrease in the mean particle size for the three gradations. The maximum tensile strength value will increase as the relative density increases (or, void ratio decreases). The most striking shift in tensile strength prediction is that the second component of tensile strength becomes less significant as mean particle size increases. It is worth noting that the prediction for medium sand is better than that for fine sand and silty sand. This can be attributed to the complex soil structure with the lower mean size of the soil particles is (especially combined with a larger value of coefficient of uniformity). The complex soil structure of fine sand and silty sand induce that the peak value of the second component (σ_{tus}) occurs at a higher saturation rather than the residual degree of saturation (which is typically a lower value for sandy soils). Moreover, the double-peak behavior of TSCC measurements for fine sand and silty sand is more evident than that for medium sand. The tensile strength for all soils has two components, each has one peak value occurring at capillary degree of saturation and residual degree of saturation respectively, according to the assumption of the proposed model (Eq. (3.11)). However, the total tensile strength over the entire range of saturation will exhibit the double-peak behavior only when those two peak values corresponding to each component are comparable (or even close) in terms of the value (Figure 3.6(d)). Otherwise, the total tensile strength will have only one peak value over the entire range of saturation (Figures 3.6(e) and (f)), by combining two components (σ_{tun}, and σ_{tus}).

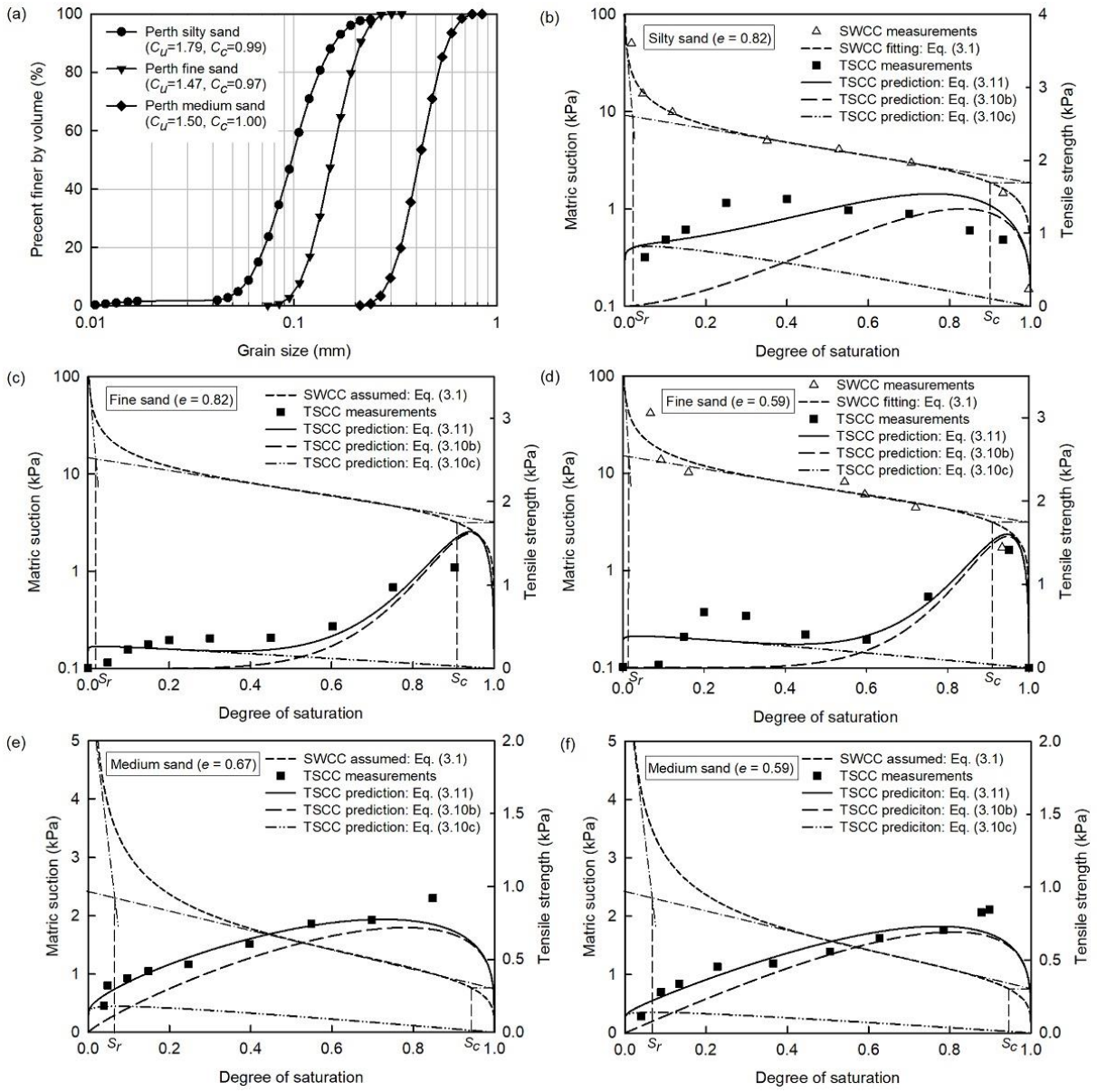

Figure 3.6 Perth sand: (a) the grain size distribution curves; the measured SWCC data and the corresponding fitting result based on van Genuchten (1980), and the comparison between the measured TSCC data and the predicted TSCC result by Eq. (3.11) for silty sand (b), fine sand (c, d), and medium sand (e, f).

3.3.3 Esperance sand (soil 3) from Washington, USA (Lu et al. 2009)

The tensile strength of Esperance sand (soil 3) was measured by Lu et al. (2009), using the uniaxial tension apparatus which was developed by Lu et al. (2005). The grain size distribution for Esperance sand is presented in Figure 3.7(a). The friction angle for Esperance sand at low normal stress level (ϕ_t) was determined as 50° from direct shear tests by Lu et al. (2009). The prediction results compared with the measurements of tensile strength are summarized in Figures 3.7(b) and (c). The prediction results reproduce the variation of tensile strength over the entire range of saturation for different void ratios (e = 0.82 and e = 0.67). It is worth noting that the first component of tensile strength (σ_{tun}) is predominant over

the entire saturation range; while the second component of tensile strength (σ_{tus}) is not significant and can be negligible (η_s = 0 for loose sands; and η_s = 0.10 for dense sand). There are perhaps two reasons responsible for this characteristic behavior. One reason is that Esperance sand has a narrow range of particle size distribution (i.e. between 0.1 mm and 0.6 mm for over 95% percent of the soil particles) which results in less probability of the simultaneous existence of saturated water pores and unsaturated pores associated with air-water interface over a large range of saturation. In other words, most saturated pores tend to drain (i.e. desaturate), which can be expected from the sharp slope of the SWCC during the funicular regime. Another reason is that a relatively large mean particle size of Esperance sand (d_{50} = 0.23 mm) could result in a relatively small specific air-water interface area (Willson et al. 2012) and therefore a relatively small value of the second component of tensile strength (σ_{tus}).

3.3.4 Silica sand (soil 4) from Alberta, Canada (Jindal et al. 2016)

The tensile strength of unsaturated Silica sand (soil 4) with two different void ratios (0.65, and 0.61) was measured by Jindal et al. (2016) using the uniaxial tension apparatus modified by Kim (2001). Due to the almost identical grain-size distribution, the SWCC of Ottawa sand F75 measured by Kim and Sture (2008) was used for the silica sand (Jindal et al. 2016). This approximation is also adopted in this study (i.e. Figures 3.8(b) and (c)), as estimating the SWCC from the grain size distribution was found to be reliable for cohesionless soils (e.g., Fredlund et al. 2002; Chin et al. 2010). The specimens were prepared by mixing oven-dried silica sand with two different liquids: distilled water and butanol solution at various water contents, in order to investigate the effect of surface tension of wetting liquid on the tensile strength. It is suggested that the specimen mixed with butanol solution (i.e. that has a lower surface tension in comparison to pure water) has a lower tensile strength compared with that mixed with distilled water at each saturation value for the entire range of saturation. Only the test results of specimens mixed with distilled water at two different void ratios (e = 0.65 and e = 0.61) were used in this study. Figure 3.8(a) shows the grain size distribution of Silica sand. The friction angle for Silica sand at low normal stress level (ϕ_t) is taken as 56° by Jindal et al. (2016). Figures 3.8(b) and (c) present the comparison between measurements and predictions by the proposed model (Eq. (3.11)) for the tensile strength. The predictions agree well with the measurements for both sets of data investigated. The second component of tensile strength (σ_{tus}) is significant compared with the first component (σ_{tun}) for Silica sand at loose state (Figure 3.8(b)), while the contribution from second component (σ_{tus}) to the tensile strength can be negligible at dense state (Figure 3.8(c)).

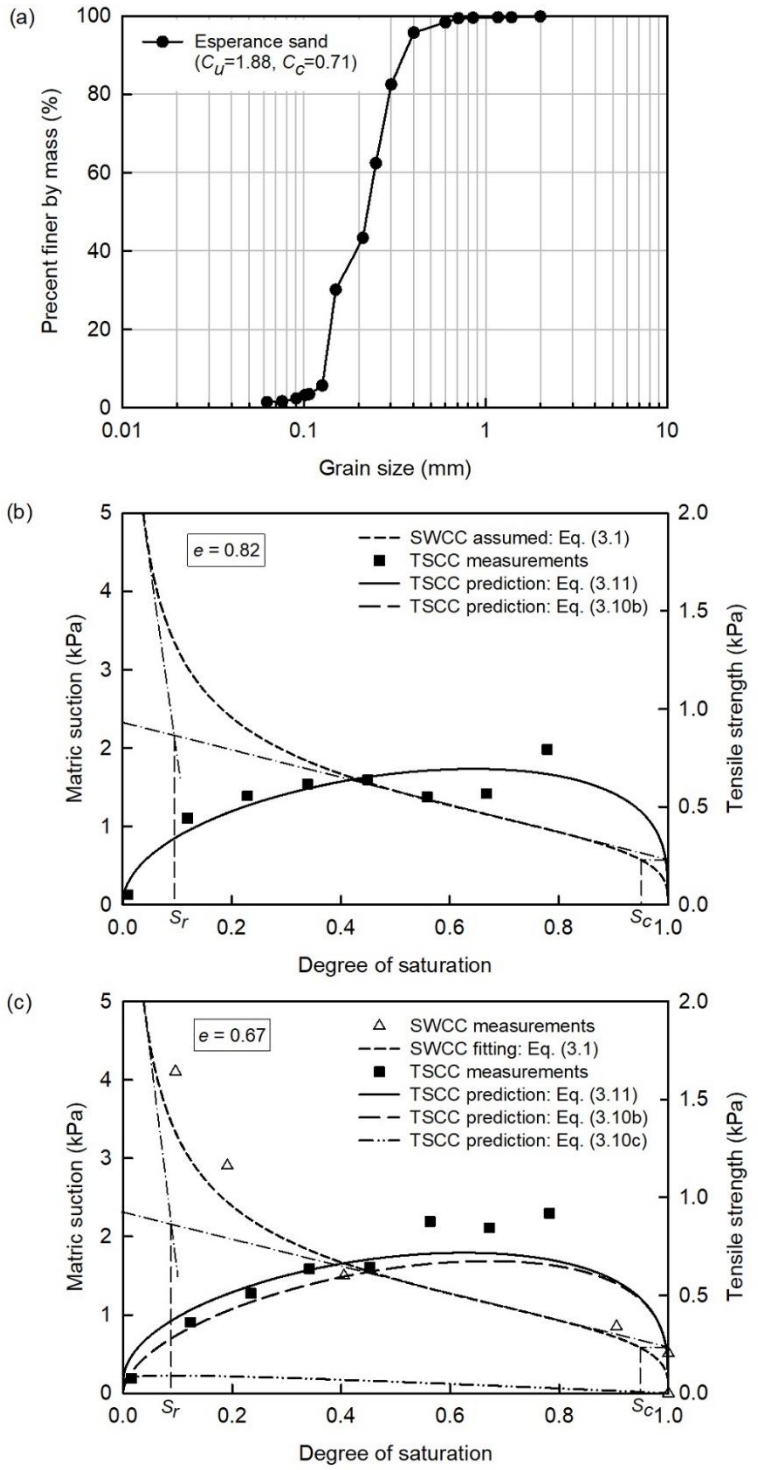

Figure 3.7 Esperance sand: (a) the grain size distribution curve; the measured SWCC data and the corresponding fitting result based on van Genuchten (1980), and the comparison between the measured TSCC data and the predicted TSCC result by Eq. (3.11) for e = 0.82 (b), e = 0.67 (c).

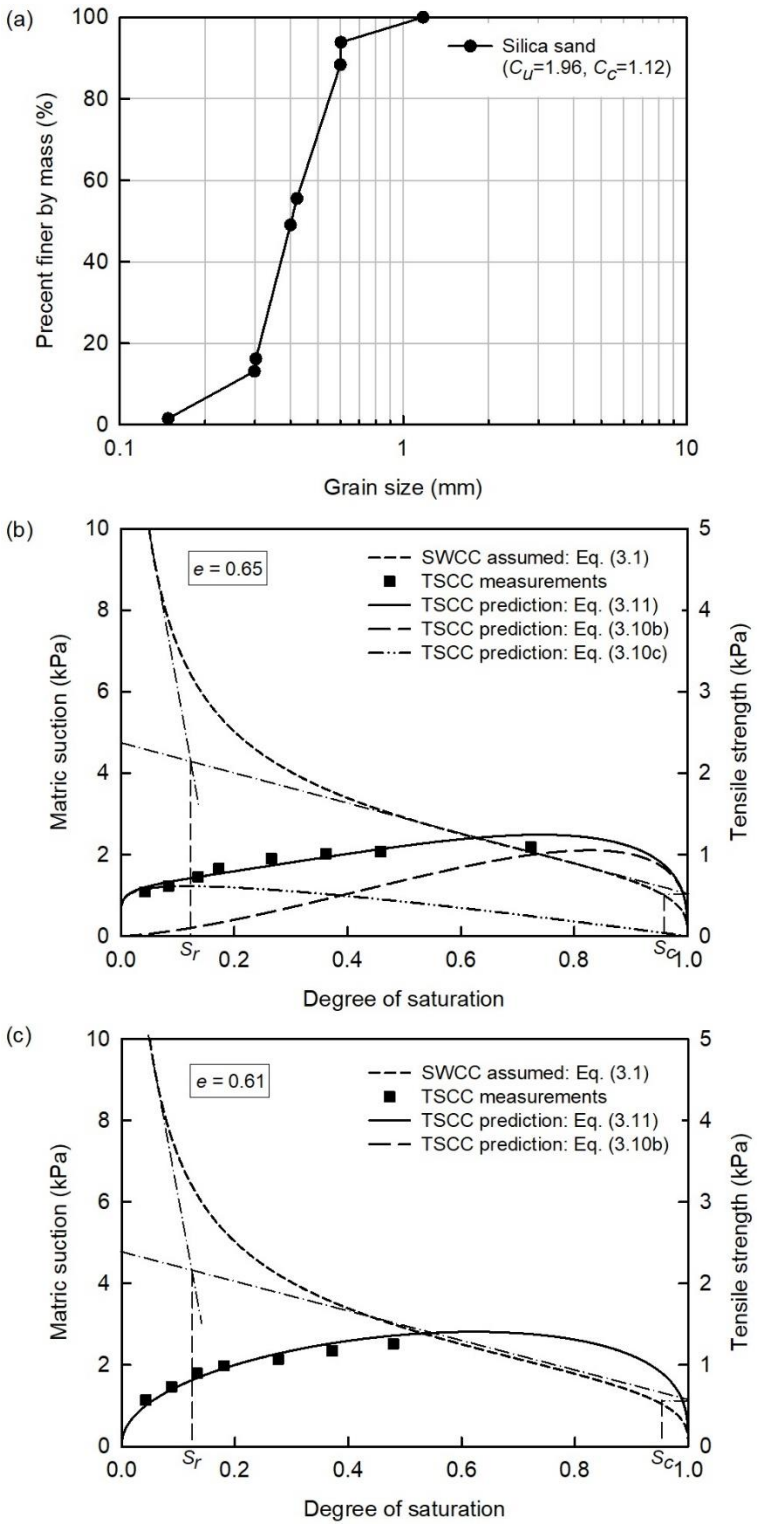

Figure 3.8 Silica sand: (a) the grain size distribution curve; the measured SWCC data and the corresponding fitting result based on van Genuchten (1980), and the comparison between the measured TSCC data and the predicted TSCC results by Eq. (3.11) for e = 0.65 (b), e = 0.61 (c).

3.3.5 Glass balls fraction G4 (soil 5) and Limestone aggregates K1 (soil 6) from Bavaria, Germany (Schubert 1972)

Schubert (1972) investigated the tensile strength of a series of Glass balls fraction (G1, G2, G3, G4, and G5) and a series of Limestone aggregates (K1, K2, K3, K4, and K5) over the entire range of saturation by the uniaxial tension apparatus developed by Dawes (1952). The test results for Glass balls fraction G4 (soil 5) and Limestone aggregates K1 (soil 6) were used to validate the efficiency of the proposed TSCC model (Eq. (23)). The maximum tensile strength of K1 (8.5 kPa) is greater than three times that of G4 (2.5 kPa) because the K1 has smaller mean particle size than G4. Figure 3.9(a) shows the grain size distributions of Glass balls fraction G4 and Limestone aggregates K1. Based on the direct shear tests under extremely low normal stress for unsaturated sands by Kim (2001) and Sture et al. (1998), the average friction angle over the entire range of saturation (ϕ_t) is around 40° ~ 60° under the normal stress range of 0.1 Pa ~ 0.25 Pa. This approach has not been extended to investigate the ϕ_t for silts, to best of the knowledge of the authors. Based on the variation of the predictions by the proposed model (Eq. (3.11)) with different ϕ_t values when the other two fitting parameters are fixed as the values in Table 3.4, ϕ_t is found to be 30° ~ 50° for silty soils 6, 7, 8, 9 and 10 (Figure 3.12). Based on the best-fit predictions (Figures 3.12(a) and (b)), the friction angles at low normal stress level (ϕ_t) for G4 and K1 are taken as 40° and 50° respectively. Figures 3.9(b) and (c) present the prediction results for G4 and K1 compared with the respective measurements. The prediction can capture the double-peak characteristic of the tensile strength for G4 over the entire range of saturation: one peak tensile strength near the residual degree of saturation and the other near the capillary degree of saturation. It is interesting to note that the peak value of the second component (σ_{tus}) of the tensile strength of G4 is comparable to that of the first component (σ_{tun}) (η_s = 1.33). Compared with G4, the second component is less significant for the tensile strength characteristics of K1 (η_s = 0.56).

3.3.6 Manchester silt (soil 7) from New Hampshire, USA (Snyder 1980)

Snyder (1980) developed a method to measure the tensile strength of unsaturated Manchester silt (soil 7) extending pneumatic fracture theory. The grain size distribution of Manchester silt (Figure 3.10(a)) shows that this silt has a relatively wide range of particle sizes (i.e. C_u=3.67) and has a higher air-entry value (i.e. around 40 kPa) in comparison to other sandy soils (Figure 3.10(b)). Based on the best-fit prediction (Figure 3.12(c)), the friction angle at low normal stress level (ϕ_t) is taken as 35°. Figure 3.10b presents the comparison between the measured and the predicted tensile strength (Eq. (3.11)) of Manchester silt. The predicted results capture the double-peak characteristics of the tensile strength, which has one peak value

at the capillary degree of saturation and the other one is close to the residual degree of saturation. It should be noted that for silty soils with a wide range of grain size distribution, the second component of tensile strength (σ_{tus}) could have a significant value, especially in the pendular regime (or, residual zone).

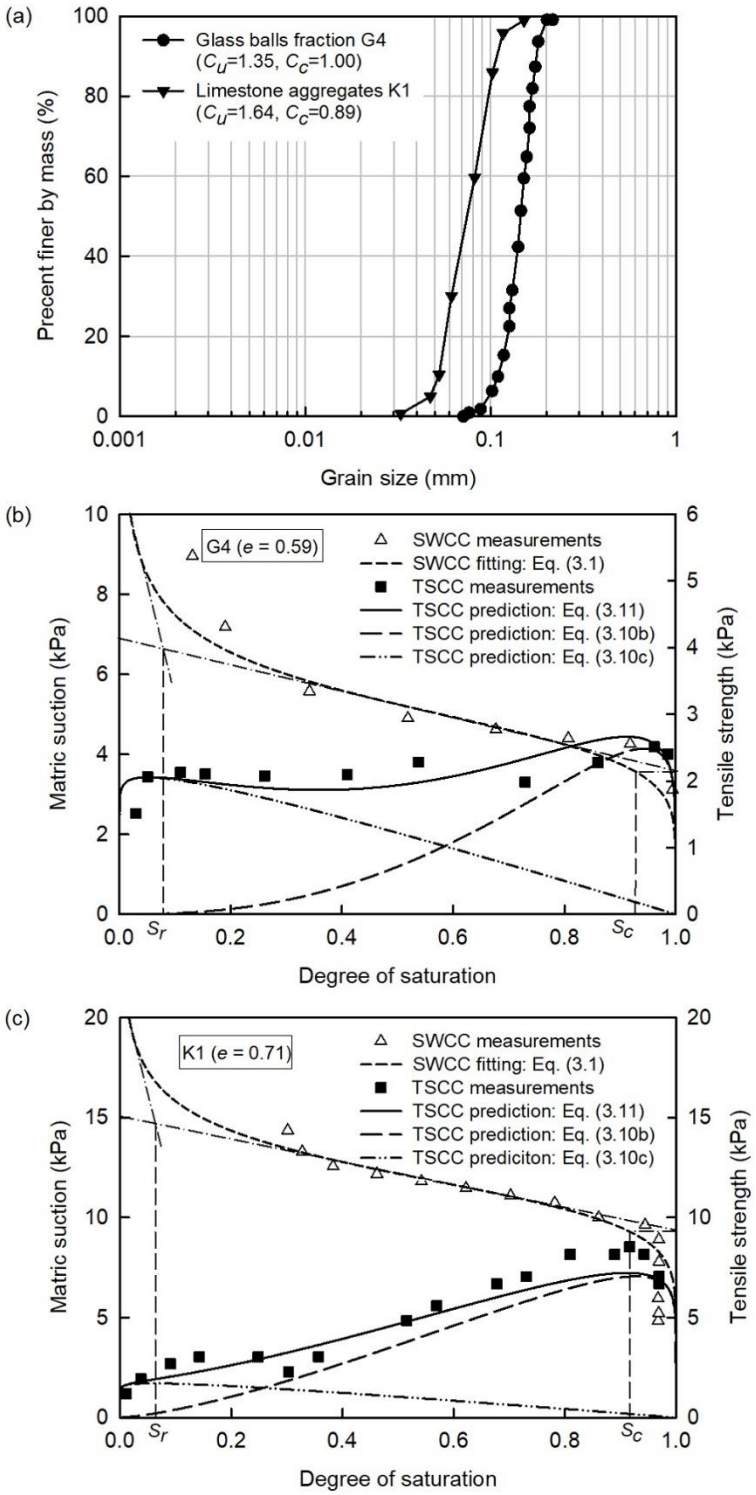

Figure 3.9 Glass balls fraction G4 and Limestone aggregates K1: (a) the grain size distribution curves; the measured SWCC data and the corresponding fitting result based on van Genuchten (1980), and the comparison between the measured TSCC data and the predicted TSCC results by Eq. (3.11) for G4 (b), K1 (c).

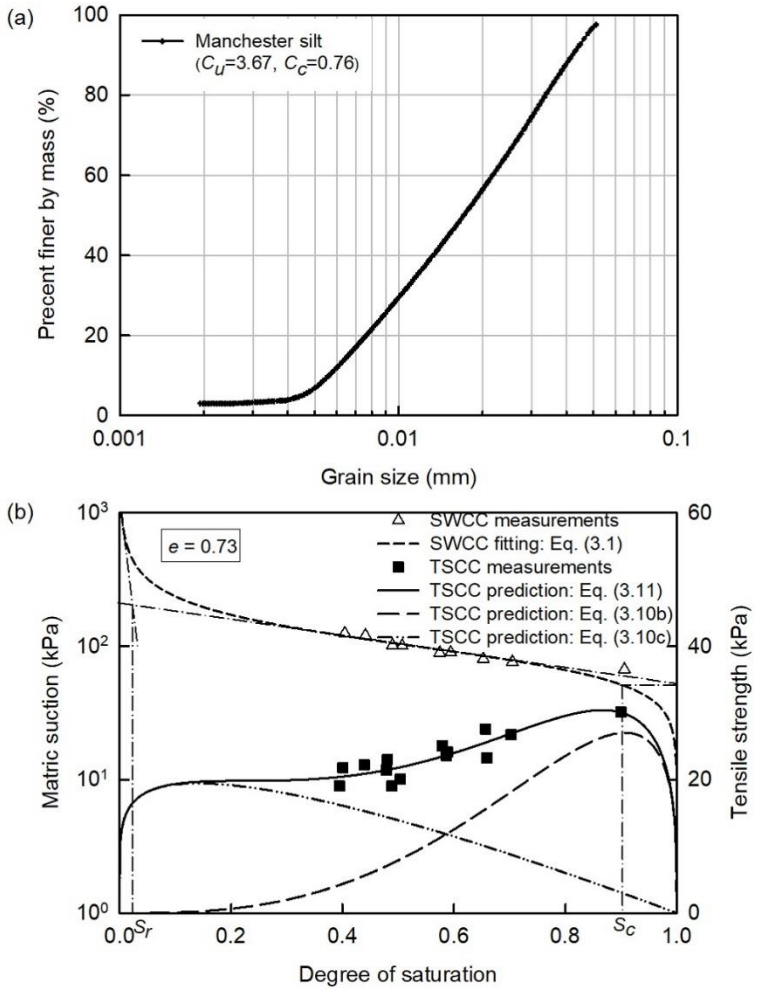

Figure 3.10 Manchester silt: (a) the grain size distribution curve; the measured SWCC data and the corresponding fitting result based on van Genuchten (1980), and the comparison between the measured TSCC data and the predicted TSCC results by Eq. (3.11).

3.3.7 Tailings A, B and C (soil 8, 9 and 10) from Quebec, Canada (Narvaez et al. 2015)

Narvaez et al. (2015) investigated the tensile strength of three unsaturated fine-grained tailings produced by hard rock mines, Tailings A, B and C (soils 8, 9, and 10) through flexure beam tests following ASTM D1635-00 (ASTM International 2006). All the three tailings can be classified as non-plastic silts (ML), according to the USCS (ASTM D2487-17, ASTM International 2017). The three tailings specimens were prepared at the same initial water content and then naturally air-dried to the desired state; followed by performing tests using a bending test apparatus. All the three tailings have a wide range of grain-size distribution (Figure 3.11(a)), and high AEV of around 100 kPa (Figures 3.11(b), (c), and (d)). Based on the best-fit predictions (Figures 3.12(d), (e), and (f)), the friction angles at low normal stress level, ϕ_t, for Tailings A, B and C are taken as 30°, 30°, and 50°, respectively. Figures 3.11(b), (c), and (d) present the prediction results by Eq. (3.11) for the tensile strength of Tailings A, B, and C, compared with the

measurements. It is interesting to note that the tensile strength of all the three tailings increases with decreasing degree of saturation until the maximum value is reached at a relatively dry condition (i.e. around S =10%). The tensile strength remains relatively high even at a dry state (S = 0). This trend is significantly different from the tensile strength behavior of most granular soils, for which the maximum value is reached at relative wet saturation (i.e. S > 0.7) and zero tensile strength at a dry state. The prediction results reproduce the characteristics of the tensile strength measurements for all the three tailings. By comparing the prediction results for all the three tailings, it can be concluded that the contribution from the second component to the total tensile strength becomes more significant with an increase in the uniformity coefficient, C_u. This is the result from a higher probability of coexistence of saturated pores and unsaturated pores associated with water bridges for a wider range of grain-size distribution (or, a larger value of C_u).

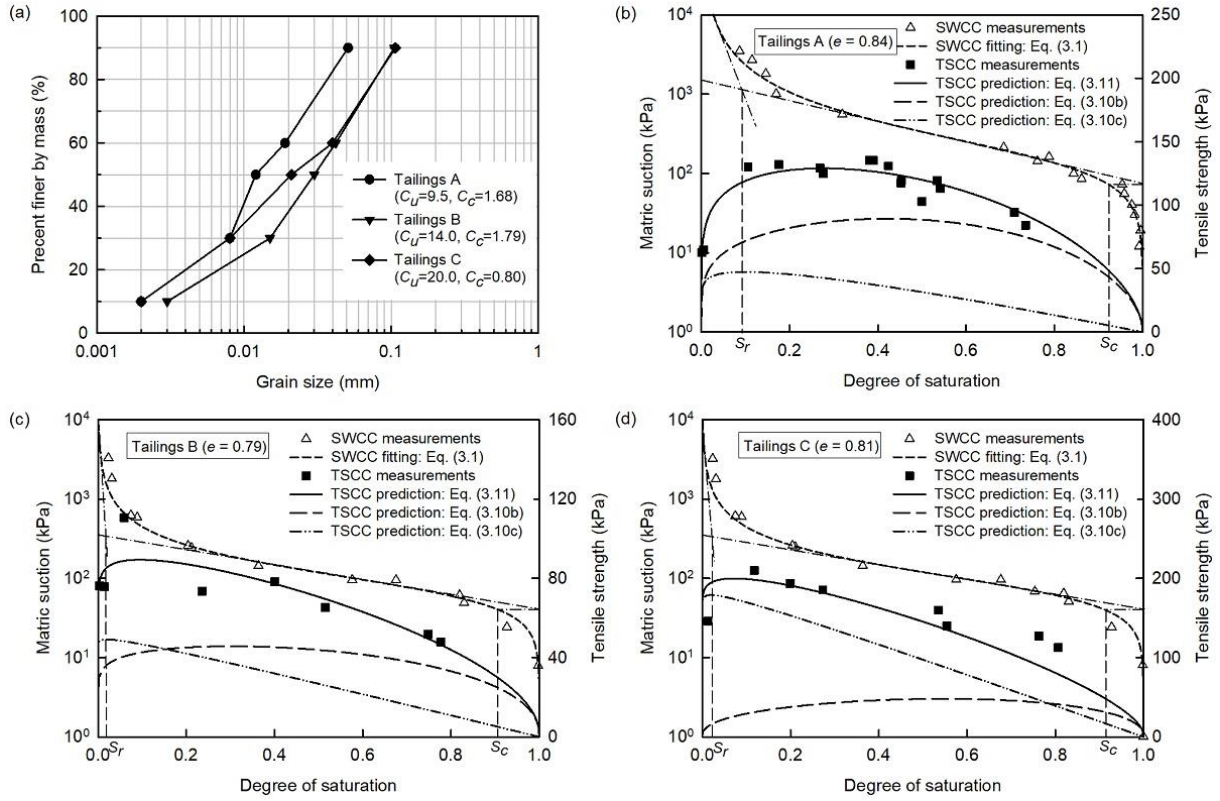

Figure 3.11 Tailings: (a) the grain size distribution curves; the measured SWCC data and the corresponding fitting result based on van Genuchten (1980), and the comparison between the measured TSCC data and the predicted TSCC results by Eq. (3.11) for tailings A (b), tailings B (c), and tailings C (d).

Table 3.4 Details of the TSCC predicted by proposed model (Eq. (3.11)) and the testing techniques of unsaturated cohesionless soils used in this study.

No	Soil Name	Sub-type	Void ratio, e	Proposed TSCC model (Eq. (3.11))			[a]Critical saturation, S_0	Testing technique
				k	η_s	ϕ_t		
1	Ottawa sand	F40	0.75	0.72	3.09	55	0.82	Uniaxial tension test
			0.6	0.85	2.57	55	0.83	
		F55	0.75	1.00	4.46	55	0.70	
			0.6	0.96	3.06	55	0.74	
		F75	0.75	0.72	2.53	55	0.76	
			0.6	1.14	3.67	55	0.72	
2	Perth sand	Silty	0.82	2.04	0.45	48	0.83	Uniaxial tension test
		Fine	0.82	5.75	0.20	48	0.92	
			0.59	6.20	0.21	48	0.95	
		Medium	0.67	1.19	0.33	48	0.78	
			0.59	1.34	0.27	48	0.81	
3	Esperance sand		0.82	0.91	0	50	0.64	
			0.67	0.98	0.10	50	0.67	
4	Silica sand		0.65	1.94	1.23	56	0.83	Uniaxial tension test
			0.61	0.94	0	56	0.62	
5	Glass balls fraction G4		0.59	2.52	1.33	[b]40	0.94	Uniaxial tension test
6	Limestone aggregates K1		0.71	1.54	0.56	[b]50	0.93	
7	Manchester silt		0.73	3.17	2.01	[b]35	0.90	Pneumatic fracture method
8	Tailings A		0.84	1.34	4.53	[b]30	0.42	Flexure beam test
9	Tailings B		0.79	0.85	8.51	[b]30	0.30	
10	Tailings C		0.81	1.12	17.09	[b]50	0.55	

Note: *a*: S_0 corresponding to the peak value of the first tensile strength component is evaluated by Eq. (3.12); *b*: assumed values based on the sensitivity analysis of ϕ_t by comparing the prediction utilizing different ϕ_t values with the measurements (see Figure 3.12).

3.4 Model parameters

Table 3.4 provides summary of the model parameters of the prediction for tensile strength of unsaturated cohesionless soils used in this study by Eq. (3.11). The two model parameters, k and η_s, are discussed below.

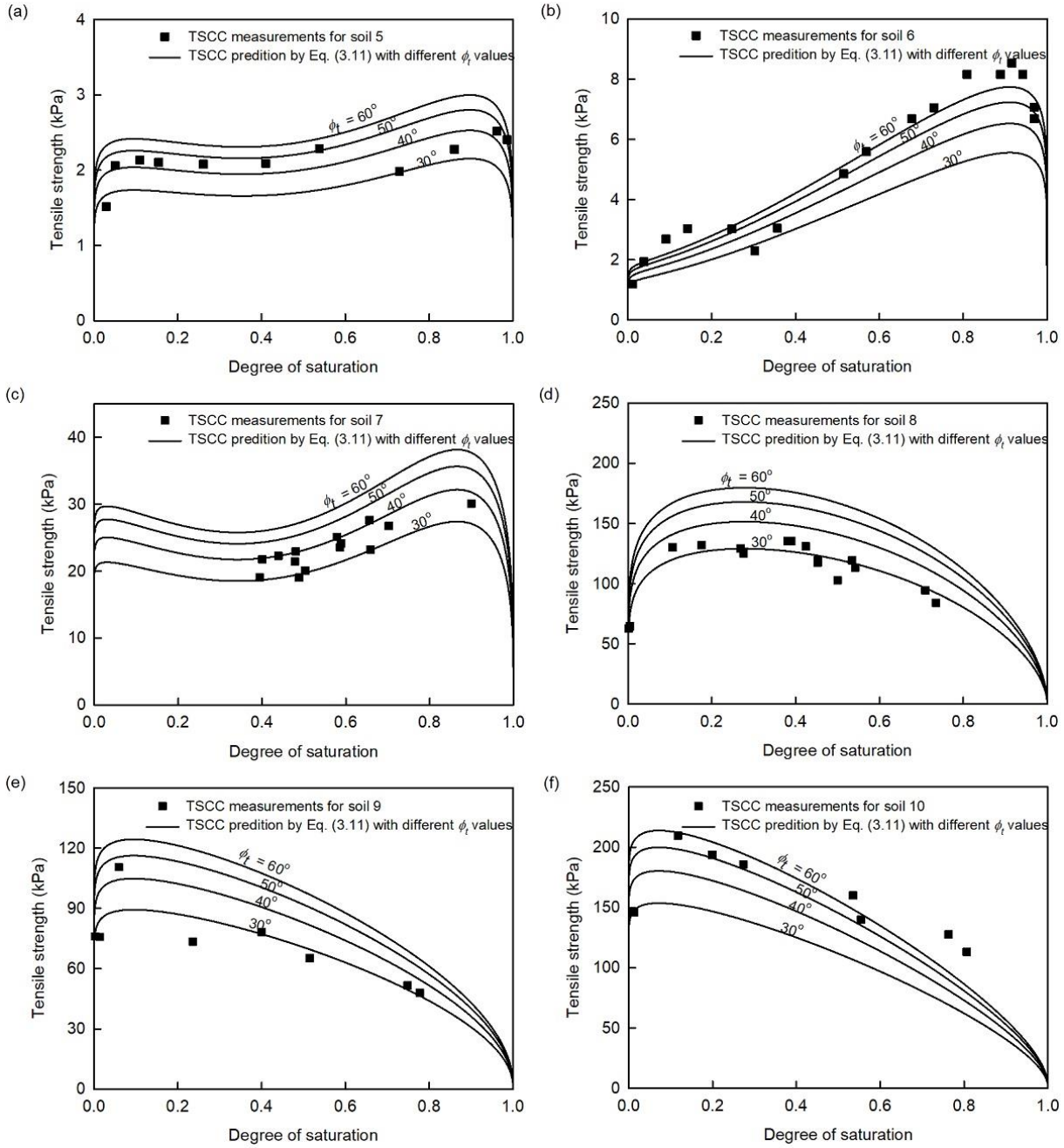

Figure 3.12 Variation of the prediction results by Eq. (3.11) with different values of ϕ_t compared with measurements for (a) Soil 5 (Glass balls fraction G4), (b) Soil 6 (Limestone aggregates K1), (c) Soil 7 (Manchester silt), (d) Soil 8 (Tailings A), (e) Soil 9 (Tailings B), and (f) Soil 10 (Tailings C).

3.4.1 Model parameter, *k*

The model parameter, *k*, bears a one-to-one relationship with the critical degree of saturation, S_0 corresponding to the peak value of the first component of the tensile strength (Eq. (3.12)). For all the soils, Table 3.4 lists S_0 calculated from parameter *k*. There can be considerable discrepancy between S_0 and the capillary degree of saturation S_c for some investigated soils, which indicates the simplification of the assumption that the first component of tensile strength reaches the peak value at S_c. The more uniform is the grain size distribution, the closer is the ratio of S_0/S_c to a value of unity due to the approximately concurrent drainage of all the soil pores near capillary degree of saturation upon drying. Figure 3.13(a) presents the variation of S_0/S_c with the coefficient of uniformity, C_u and the mean particle size, d_{50}. The S_0/S_c decreases significantly from unity as C_u increases. This behavior can be explained as follows. The degree of saturation decreases during drying at a faster rate for soils with uniform particle sizes. For soils that belong to this category, the first component of tensile strength induced by matric suction in saturated soil pores reaches the peak value near the capillary degree of saturation, S_c, corresponding to the AEV. In addition, S_0/S_c decreases with a decrease in mean particle size, which can also be explained by the combined effects of C_u and d_{50}. For example, soils 8, 9, and 10 that have a smaller mean particle size and a larger C_u corresponding to a wider range of grain size distribution (Figure 3.11(a)). The higher content of fine particles (i.e. smaller than 0.075 mm) accompanied with more widely distributed grain size (i.e. larger C_u) would likely induce more complex soil structure. Due to this reason, the degree of saturation decreases gradually during desaturation when the soil suction exceeds the AEV. Therefore, the first component of tensile strength (σ_{tun}) due to matric suction in saturated soil pores will reach the peak value far away from the capillary degree of saturation, S_c. Thus, the value of S_0/S_c will be much less than unity.

Moreover, the variation S_0/S_c is not sensitive to the mean particle size, especially for sandy soils (i.e. d_{50} larger than 0.075 mm). In other words, the C_u is more predominant in determining the value of S_0/S_c than the mean particle size (Figure 3.13(a)). A close look at the variations of S_0/S_c with C_u, for $C_u \leq 6$ and $C_u > 6$, are presented in Figures 3.13(b) and (c), respectively. The average value of S_0/S_c is found to be 0.85 for cohesionless soils with C_u less than 6, and 0.45 for C_u greater than 6 except for soil 4 (Silica sand). This is perhaps due to the approximation of the SWCC of the Silica sand without measurements (Jindal et al. 2016). Thus,

(3.13a) $$\frac{S_0}{S_c} = 0.85 \pm 0.15, \qquad for \;\; C_u \leq 6;$$

(3.13b) $\frac{S_0}{S_c} = 0.45 \pm 0.15, \quad for \;\; C_u > 6.$

The model parameter, k can be estimated based on Eq. (3.13), as follows:

(3.14a) $k = \frac{1}{n_{vg} - 1} \cdot \frac{1}{1 - \left[(0.85 \pm 0.15) S_c\right]^{n_{vg}/(n_{vg}-1)}}, \quad for \;\; C_u \le 6;$

(3.14b) $k = \frac{1}{n_{vg} - 1} \cdot \frac{1}{1 - \left[(0.45 \pm 0.15) S_c\right]^{n_{vg}/(n_{vg}-1)}}, \quad for \;\; C_u > 6.$

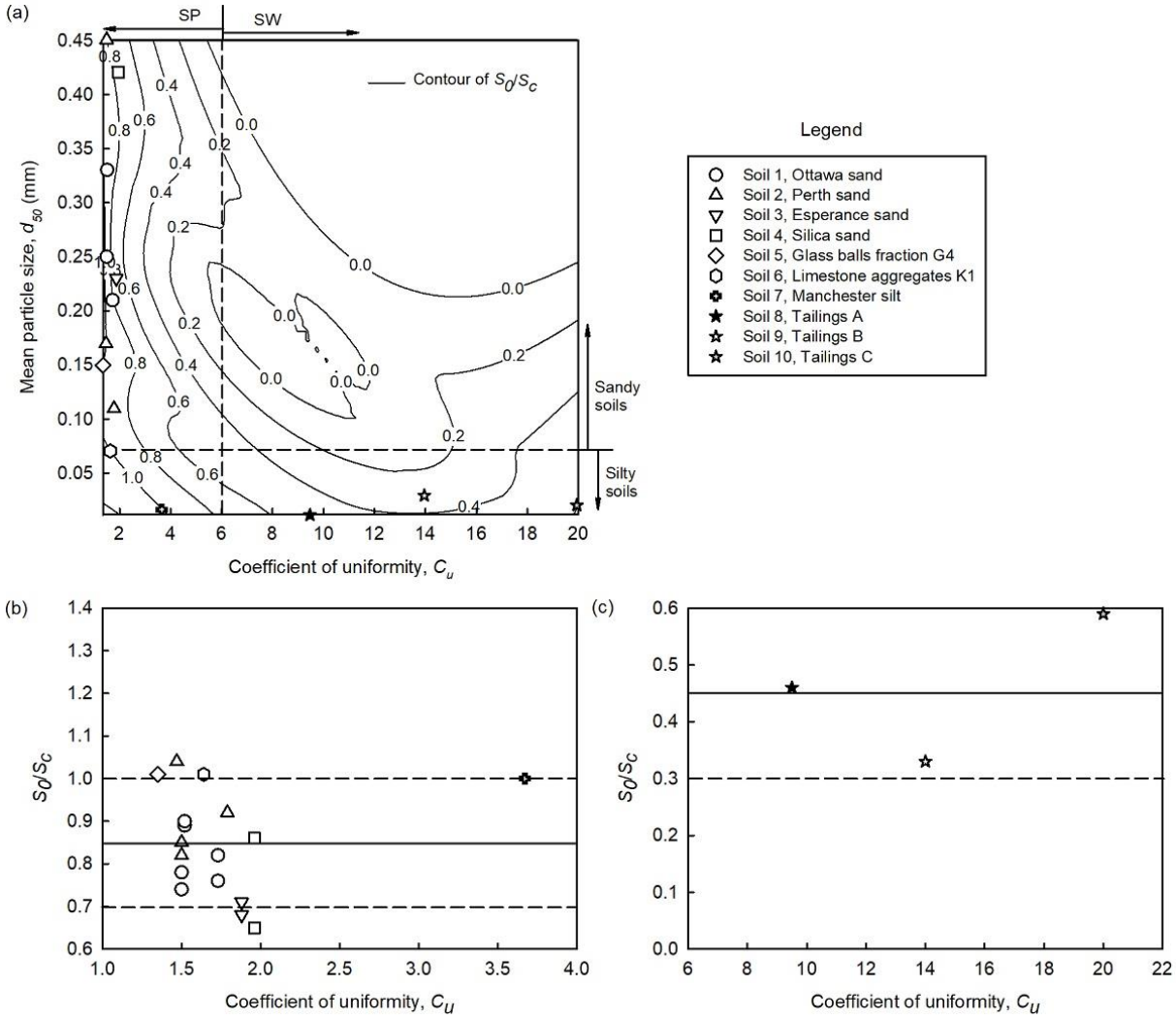

Figure 3.13 Distribution of the ratio, S_0/S_c, with respect to (a) coefficient of uniformity, C_u, and mean particle size, d_{50}, for all the soils in this study; (b) coefficient of uniformity, C_u, for all the soils except for soil 8, 9 and 10; (c) coefficient of uniformity, C_u, for soils 8, 9 and 10. (*SP*: Poorly graded sand; *SW*: Well graded sand.)

3.4.2 Model parameter, η_s

The second model parameter, η_s reflects the relative magnitude of the second component of tensile strength (σ_{tus}), compared to the first component (σ_{tun}). The variation of η_s with the coefficient of uniformity, C_u is presented in Figure 3.14. The linear regression result (solid line) can be expressed as

(3.15) $\eta_s = 0.73C_u$

The two dashed lines are regression lines presented with 95% prediction interval (Figure 3.14). The model parameter, η_s, falls in narrow range for all the soils. The discrepancies between the regression results and the parameters resulting from the prediction can be attributed to the anisotropy of the mechanical behavior of unsaturated soils. In the framework of suction stress characteristic curve (SSCC), the suction stress is regarded as an isotropic tensile strength of unsaturated soils (Lu et al. 2007). In the proposed TSCC model (Eq. (3.11)), an additional term (i.e. $T_s \bullet a_{aw}$) which doesn't represent isotropic conditions is added into the suction stress (σ^s). This is because the specific air-water interfacial area is closely related to the distribution of water and air, which is essentially anisotropic and depends on the soil pore structure (or, soil fabric) especially at low saturation level (Li 2003; Toker et al. 2014). Therefore, the model parameter, η_s reflects not only the contribution from surface suction to the tensile strength but also includes the anisotropy (i.e. direction dependent) of suction stress and consequently the tensile strength.

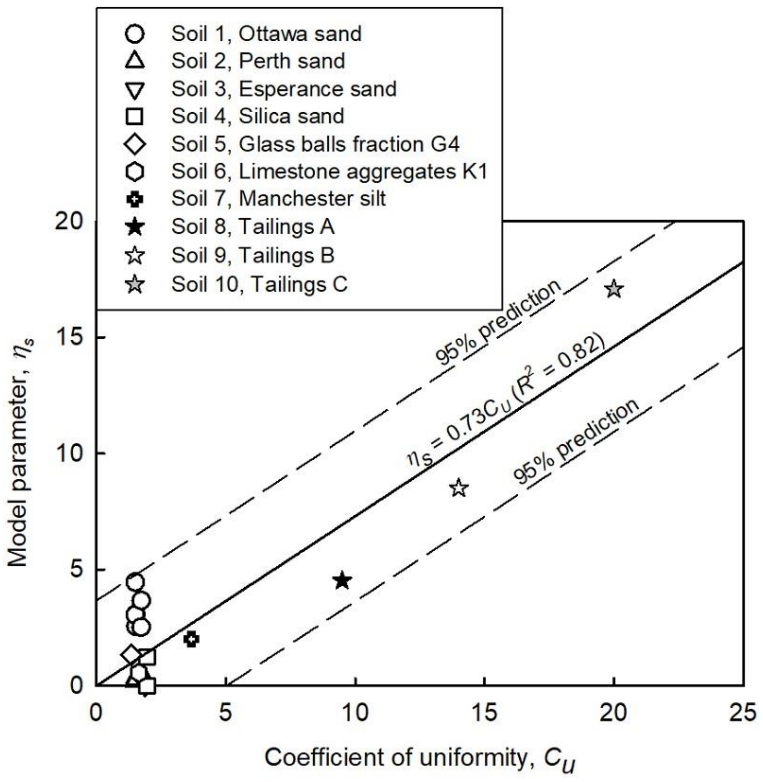

Figure 3.14 Distribution and prediction of model parameter, η_s, with respect to the coefficient of uniformity, C_u, for all the soils.

3.5 Discussion

3.5.1 Factors influencing the tensile strength of unsaturated cohesionless soils

In addition to the degree of saturation and matric suction, basic soil properties (e.g., grain size distribution), soil type (i.e. sandy or silty soils), relative density (or, void ratio) can influence the tensile strength of unsaturated cohesionless soils. The influence factors can be classified into two categories: namely, (i) internal factors (e.g., water content, soil structure), and (ii) external factors (e.g., stress state, temperature, etc.). The influence of these factors towards predictions are discussed below.

According to USCS (ASTM D2487-17, ASTM International 2017), soils 1, 2, 3, 4, and 5 in this study are classified as poorly-graded sands (SP); and soils 6, 7, 8, 9 and 10 are classified as non-plastic or low-plastic silts (ML). The tensile strength of soils 6, 7, 8, 9 and 10 should be larger than that of soils 1, 2, 3, 4, and 5, if the assumption in the proposed model that the tensile strength of unsaturated cohesionless soils is induced only by matric suction and surface tension without other interparticle forces (e.g., cementation between soil particles) is true. This is because finer grain size incorporated with wider grain size distribution typically leads to a larger number of contacts between particles. In addition, finer grain size combined with larger relative density (or lower void ratio) results in a closer distance between adjacent particles. The larger the number of contacts and closer interparticle distance can explain why the tensile strength of silts is much larger than that of sands. Moreover, the number of contacts and interparticle distance will have a significant effect on the second component (σ_{tus}) of tensile strength rather than the first component (σ_{tun}) according to the micromechanical models for tensile strength at low water content (e.g., Fisher 1926; Rumpf 1961). This can explain why the second component increases more significantly than the first component for silts compared to sands. In the present study, the peak value of the second component for soils 8, 9 and 10 exceeded that of the first component and the maximum value of the total tensile strength occurred at a relatively lower degree of saturation (e.g., $S < 0.5$).

The double-peak behavior in tensile strength of unsaturated cohesionless soils has been observed and documented by several researchers (e.g., Lu et al. 2007; Cai et al. 2020). The double-peak feature could be attributed to the different mechanisms that contribute to tensile strength at different levels of degree of saturation. In the residual zone with low degree of saturation, pore water exists mainly in the form of water bridges and tensile strength that arises is mainly from the second component (σ_{tus}). Tensile strength

increases due to an increase in the number of water bridges associated with an increase in the degree of saturation. In the boundary effect zone with high degree of saturation, water filled the soil pores and tensile strength comes from the negative pore water pressure (or matric suction). As the degree of saturation decreases to a value little lower than unity, the tensile strength increases due to increase in the matric suction. In the transition zone, the tensile strength stems from both the first component (σ_{tun}) and the second component (σ_{tus}). The double-peak feature would be pronounced if the two components reach their peaks at different levels of degree of saturation, e.g., the first component (σ_{tun}) reaches its peak at around the capillary degree of saturation and the second one (σ_{tus}) does at around the residual degree of saturation. For cohesionless soils with uniform grain size distribution (or low value of C_u), both the components are likely to reach their peaks concurrently. For cohesionless soils with non-uniform grain size distribution (or high value of C_u), the proposed model is capable to reproduce the double-peak feature of tensile strength characteristic curve if the values of the first peak and the second peak are comparable, such as Glass balls fraction G4 (soil 5) in Figure 3.9(b).

Besides, the tension test method and specimen preparation method can also influence the measurements of tensile strength. For a specific soil specimen, different measurements are possible due to different testing techniques. For example, bending test (interpreted with the elastic method) often overestimates the tensile strength in comparison with values measured by direct tension tests (Ammeri 2009). The uniaxial tension tests with different apparatus may also induce different measurements of tensile strength, because the tensile strength of unsaturated soils is stress-state dependent (e.g., the effect of confining pressure to the tensile strength). Different apparatus to which the soil specimens are subjected typically produce different stress states at tension failure. Additionally, whether the soil specimen is wetted or dried to reach the desired water content before subjecting to tension is expected to influence the measurements of tensile strength as well due to the hydraulic hysteresis effect.

3.5.2 Potential application

The tensile strength of cohesionless soils is rarely considered in the conventional geotechnical engineering practice. Such an assumption may lead to the conservative estimation of the stability of geotechnical structures, such as the durability of the earth dam cores, the stability of soil slopes including top tension cracks, especially under an unsaturated state.

It is also important to recognize that there are difficulties associated with the experimental determination of the tensile strength of unsaturated sands. First, the direct imposition of the soil specimen to a tension state is difficult. To alleviate some of the limitations associated with the testing techniques, several investigators developed different apparatus for obtaining direct tension measurements using different strategies to determine the tensile failure that takes place along the weakest cross section (e.g., Kim and Hwang 2003; Tamrakar et al. 2005; Tang et al. 2015). Secondly, the tensile strength measured using different devices may not be comparable. In fact, different stress states corresponding to tension failure can be expected, when the soil specimen is imposed to tension using different test devices. Moreover, the tensile strength measured by experimental tests cannot be used directly in engineering practice applications. This is because the stress state in the field condition may not necessarily be the same as that at failure state during experimental tests.

The proposed model, which provides a reasonable estimation of the tensile strength of unsaturated cohesionless soils based on the basic information of the soils (the SWCC and the grain-size distribution curve) would be promising for use in practice applications. Figure 3.15 shows the comparison between the measured and predicted σ_t values using the proposed TSCC model (Eq. (3.11)) incorporating with empirical estimation of model parameters (i.e. k and η_s) with Eqs. (3.14) and (3.15) for all the ten soils, which constitute a total of 201 measured data points. The proposed model provides predictions for these 201 data points with an overall R^2 value of 0.95. It should be noted that the physical parameter ϕ_t for soils 5, 6, 7, 8, 9, and 10 is taken as the best-fit prediction for this preliminary investigation. Reasonably good predictions were achieved for all soils except for soil 6 (Limestone aggregates K1). For this soil, there are considerable discrepancies between the measurements and the predictions with the 95% prediction interval. In fact, the large-valued tensile strength values can be predicted more reliably than the relatively small-valued values (typically, less than 5 kPa). This is because even a small error in this low range values on a percentage basis can translate into a significantly large experimental error. It should be expected that slight differences in initial density and water content at sample preparation, compaction, trimming and setting up for loading also could lead to significant variations of tensile strength measurements, especially for soils that have low tensile strength values. In addition, the tensile strength of unsaturated cohesionless soils is expected to be very low and negligible (e.g., less than 1 kPa) when the d_{50} is greater than 0.5 mm.

3.5.3 Summary

From a microscopic point of view, capillary force induced by matric suction from the voids filled with bulk water and surface tension along the air-water interface can be exerted on soil particles, resulting in

the bonding effect and developing tensile strength between adjacent soil particles. Based on this mechanism, the effects of both matric suction and surface tension on the tensile strength of unsaturated cohesionless soils are investigated using Eq. (3.11). The contribution arises independently towards the total tensile strength from the first component (σ_{tun}) and the second component (σ_{tus}). Following the framework of suction stress characteristic curve (SSCC) (Lu and Likos 2004, 2006) and tensile strength characteristic curve (TSCC) (Lu et al. 2007, 2009), a semi-empirical model (Eq. (3.9)) is used to simulate the amount of specific air-water interfacial area, which is a non-monotonic function of degree of saturation. Consequently, the second component of tensile strength (Eq. (3.10c)) which is induced by surface tension is added to the total tensile strength of unsaturated cohesionless soils (Eq. (3.11)). Some important conclusions associated with the proposed model are summarized below:

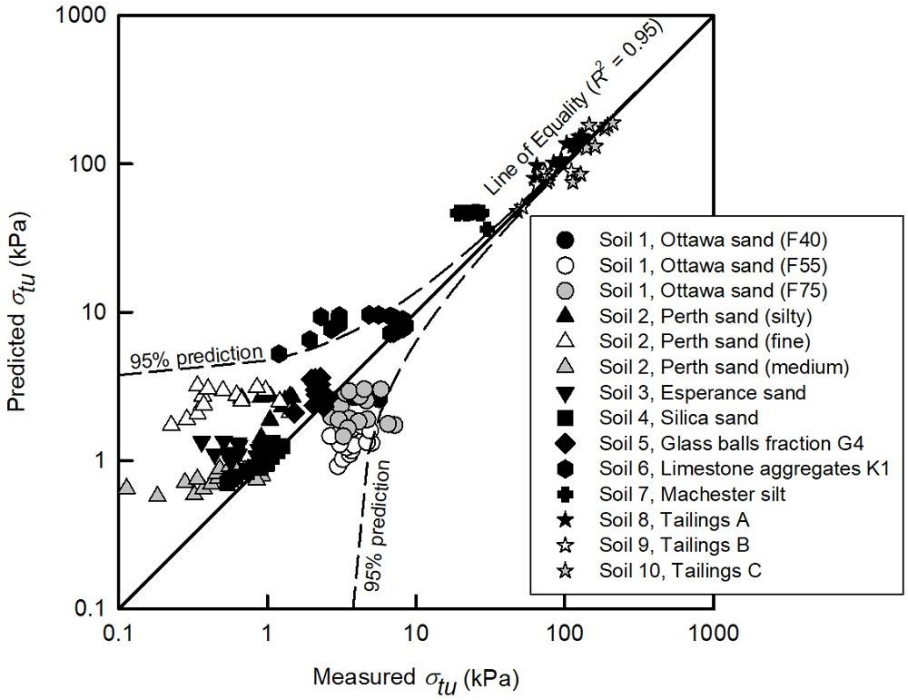

Figure 3.15 Comparisons between measured and predicted tensile strength (σ_{tu}) values using Eqs. (3.11), (3.14), and (3.15) for all the soils including a total of 201 data points.

(1) The required information to estimate the tensile strength of unsaturated cohesionless soils includes: the matric suction corresponding to a specific degree of saturation, the capillary degree of saturation (S_c), and residual degree of saturation (S_r) which can be derived from the SWCC; the mean particle size (d_{50}), and coefficient of uniformity (C_u) which can be obtained from the grain size distribution curve; the void ratio (e); and the friction angle (ϕ) at low normal stress level.

(2) It is necessary to consider the contribution from surface tension to the tensile strength of unsaturated cohesionless soils, especially for silty soils with well-graded grain size distribution at low water contents.

For silty soils, the peak value of the second component of the tensile strength (σ_{tus}) is comparable to that of the first component (σ_{tun}). However, the contribution from the surface tension to the tensile strength is less significant compared with the first component for sandy soils. In some cases, the second component can be negligible (e.g., $\eta_s = 0$ for soils 3 and soil 4) which means that the contribution from the first component to total tensile strength is predominant.

(3) The assumption that the first component of tensile strength (σ_{tun} in Eq. (3.10b)) reaches the peak value at the capillary degree of saturation and the second component (σ_{tus} in Eq. (3.10c)) does at the residual degree of saturation, for the proposed TSCC model (Eq. (3.11)) is valid, especially for cohesionless soils with uniform grain size distribution. In Eq. (3.11), parameter k reflects the relationship between the degree of saturation, S_0 corresponding to the peak value of the first component (σ_{tun}) and the capillary degree of saturation, S_c. Based on the prediction results of the total tensile strength of unsaturated cohesionless soils, the average ratio of S_0/S_c is 0.85 for cohesionless soils with C_u less than 6, and 0.45 for that with C_u greater than 6. The other parameter, η_s, which demonstrates the contribution from surface tension and the anisotropic nature of the mechanical behavior including tensile strength of unsaturated soils, could also be related to the coefficient of uniformity, C_u.

(4) The proposed TSCC model (Eq. (3.11)) is validated by providing comparisons with the measured TSCC data for ten soils (five sandy soils, and five silty soils). The proposed TSCC model is capable of reliably predicting the variation of tensile strength, σ_{tu}, with the degree of saturation, S, using two model parameters (i.e. k and η_s) which can be related to the coefficient of uniformity, C_u as Eqs. (3.14) and (3.15). The prediction is more accurately represented by plotting the results on an arithmetic scale and providing comparisons with the measured tensile strength values. The tensile strength values of certain cohesionless soils are rather small (for example, soils 2, 3, and 4 have values less than 2 kPa). Such measurements are more difficult to predict in comparison to relatively large values (i.e. tens of kilopascals for soils 7, 8, 9, and 10) due to the sensitive response of instrumentation used in tests and possible experimental errors to measure low values of stresses.

3.6 References

ASTM International. 2006. D1635-00 Standard Test Method for Flexural Strength of Soil-cement Using Simple Beam with Third-point Loading. West Conshohocken, PA.

ASTM International. 2017. D2487-17 Standard Practice for Classification of Soils for Engineering Purposes (Unified Soil Classification System). West Conshohocken, PA.

Ammeri, A. 2009. Contribution à l'étude expérimentale et numérique du comportement d'un limon sollicité en traction: Approche par éléments discrets. Doctoral dissertation, Université Joseph-Fourier, Grenoble, France. [in French]

Blight, G.E. 1961. Strength and consolidation characteristics of compacted soils. Doctoral dissertation, Imperial College London, UK.

Brooks, R.H. and Corey, A.T. 1964. Hydraulic properties of porous media. Hydrology Papers, No. 3, Colorado State University, Ft. Collins, Colo.

Cai, G., Shi, P., Kong, X., Zhao, C. and Likos, W.J. 2020. Experimental study on tensile strength of unsaturated fine sands. Acta Geotechnica, 15: 1057–1065.

Chin, K.B., Leong, E.C. and Rahardjo, H. 2010. A simplified method to estimate the soil-water characteristic curve. Canadian Geotechnical Journal, 47(12): 1382–1400.

Coussy, O. 2011. Mechanics and physics of porous solids. John Wiley and Sons, New York.

Dawes, J.G. 1952. Safety in Mines Res. Estab. Res. Rept. Nos. 36, 46, 49, Sheffield.

Fisher, R.A. 1926. On the capillary forces in an ideal soil; correction of formulae given by W.B. Haines. The Journal of Agricultural Science, 16(03): 492–505.

Fredlund, D.G. and Morgenstern, N.R. 1977. Stress state variables for unsaturated soils. Journal of Geotechnical and Geoenvironmental Engineering, 103: 447–466.

Fredlund, D.G. and Xing, A. 1994. Equations for the soil-water characteristic curve. Canadian Geotechnical Journal, 31(4): 521–532.

Fredlund, D.G., Xing, A. and Huang, S. 1994. Predicting the permeability function for unsaturated soils using the soil-water characteristic curve. Canadian Geotechnical Journal, 31(4): 533–546.

Fredlund, D.G., Xing, A., Fredlund, M.D. and Barbour, S.L. 1996. The relationship of the unsaturated soil shear to the soil-water characteristic curve. Canadian Geotechnical Journal, 33(3): 440–448.

Fredlund, M.D., Wilson, G.W. and Fredlund, D.G. 2002. Use of the grain-size distribution for estimation of the soil-water characteristic curve. Canadian Geotechnical Journal, 39(5): 1103–1117.

Gallipoli, D., Gens, A., Sharma, R. and Vaunat, J. 2003. An elasto-plastic model for unsaturated soil incorporating the effects of suction and degree of saturation on mechanical behaviour. Géotechnique, 53(1): 123–136.

Goulding, R.B. 2006. Tensile strength, shear strength, and effective stress for unsaturated sand. Ph.D. dissertation, University of Missouri-Columbia.

Han, Z. and Vanapalli, S.K. 2017. Normalizing variation of stiffness and shear strength of compacted fine-grained soils with moisture content. Journal of Geotechnical and Geoenvironmental Engineering, 143(9): 04017058.

Ingles, O.G. 1962a. Bonding forces in soils, Part III: A theory of tensile strength for stabilized and naturally coherent soils. In Proceedings of the 1st Conference of the Australian Road Research Board, Canberra, Australia, Vol. 1, pp. 1025–1047.

Ingles, O.G. 1962b. Bonding forces in soils, Part I: Natural soils- the physical factors responsible for cohesive strength. In Proceedings of the 1st Conference of the Australian Road Research Board, Canberra, Australia, Vol. 1, pp. 999–1013.

Jindal, P., Sharma, J. and Bashir, R. 2016. Effect of pore-water surface tension on tensile strength of unsaturated sand. Indian Geotechnical Journal, 46(3): 276–290.

Kim, T.H. 2001. Moisture-induced tensile strength and cohesion in sand. Doctoral dissertation, University of Colorado at Boulder, USA.

Kim, T.H. and Hwang, C. 2003. Modeling of tensile strength on moist granular earth material at low water content. Engineering Geology, 69(3): 233–244.

Kim, T.H. and Sture, S. 2008. Capillary-induced tensile strength in unsaturated sands. Canadian Geotechnical Journal, 45(5): 726–737.

Kosugi, K.I. 1994. Three-parameter lognormal distribution model for soil water retention. Water Resources Research, 30(4): 891–901.

Li, X.S. 2003. Effective stress in unsaturated soil: a microstructural analysis. Géotechnique, 53(2): 273–277.

Likos, W.J. 2014. Effective stress in unsaturated soil: accounting for surface tension and interfacial area. Vadose Zone Journal, 13(5), https://doi.org/10.2136/vzj2013.05.0095.

Likos, W.J. and Jaafar, R. 2013. Pore-scale model for water retention and fluid partitioning of partially saturated granular soil. Journal of Geotechnical and Geoenvironmental Engineering, 139(5): 724–737.

Likos, W.J. and Lu, N. 2004. Hysteresis of capillary stress in unsaturated granular soil. Journal of Engineering Mechanics, 130(6): 646–655.

Lu, N., Godt, J.W. and Wu, D.T. 2010. A closed-form Eq. for effective stress in unsaturated soil. Water Resources Research, 46(5): 1–14.

Lu, N., Kim, T.H., Sture, S. and Likos, W.J. 2009. Tensile strength of unsaturated sand. Journal of Engineering Mechanics, 135(12): 1410–1419.

Lu, N. and Likos, W.J. 2004. Unsaturated soil mechanics, John Wiley& Sons, New York.

Lu, N. and Likos, W.J. 2006. Suction stress characteristic curve for unsaturated soil. Journal of Geotechnical and Geoenvironmental Engineering, 132(2): 131–142.

Lu, N., Wu, B. and Tan, C.P. 2005. A tensile strength apparatus for cohesionless soils. In Advanced experimental unsaturated soil mechanics. Edited by A. Tarantino, et al. Trento, Italy, pp. 105–110.

Lu, N., Wu, B. and Tan, C.P. 2007. Tensile strength characteristics of unsaturated sands. Journal of Geotechnical and Geoenvironmental Engineering, 133(2): 144–154.

Matyas, E.L. and Radhakrishna, H.S. 1968. Volume change characteristics of partially saturated soils. Géotechnique, 18(4): 432–448.

Morris, P.H., Graham, J. and Williams, D.J. 1992. Cracking in drying soils. Canadian Geotechnical Journal, 29(2): 263–277.

Narvaez, B., Aubertin, M. and Saleh-Mbemba, F. 2015. Determination of the tensile strength of unsaturated tailings using bending tests. Canadian Geotechnical Journal, 52(11): 1874–1885.

Nikooee, E., Habibagahi, G., Hassanizadeh, S.M. and Ghahramani, A. 2013. Effective stress in unsaturated soils: a thermodynamic approach based on the interfacial energy and hydromechanical coupling. Transport in Porous Media, 96: 369–396.

Oh, S., Lu, N., Kim, Y.K., Lee, S.J. and Lee, S.R. 2011. Relationship between the soil-water characteristic curve and the suction stress characteristic curve: Experimental evidence from residual soils. Journal of Geotechnical and Geoenvironmental Engineering, 138(1): 47–57.

Orr, F.M., Scriven, L.E. and Rivas, A.P. 1975. Pendular rings between solids: meniscus properties and capillary force. Journal of Fluid Mechanics, 67(04): 723–742.

Perkins, S.W. 1991. Modeling of regolith structure interaction in extraterrestrial constructed facilities. Ph.D. dissertation, University of Colorado at Boulder.

Rumpf, H. 1961. The strength of granules and agglomerates. In Agglomeration. Edited by W.A. Knepper. Knepper, Interscience, New York, pp. 379–418.

Schubert, H. 1972. Untersuchungen zur Ermittlung von Kapillardruck und Zugfestigkeit yon feuchten HauFwerken aus kSrnigen Stoffen. Doctoral dissertation, University of Karlsruhe, Germany. [in German]

Schubert, H. 1973. Kapillardruck und Zugfestigkeit von feuchten Haufwerken aus körnigen Stoffen. Chemie Ingenieur Technik, 45(6): 396–401. [in German]

Schubert, H. 1975. Tensile strength of agglomerates. Powder Technology, 11(2): 107–119.

Simms, P.H. and Yanful, E.K. 2001. Measurement and estimation of pore shrink- age and pore distribution in a clayey till during soil-water characteristic curve tests. Canadian Geotechnical Journal, 38(4): 741–754.

Snyder, V.A. 1980. Theoretical aspects and measurement of tensile strength in unsaturated soils. Ph.D. dissertation, Cornell University.

Snyder, V.A. and Miller, R.D. 1985. Tensile strength of unsaturated soils. Soil Science Society of America Journal, 49(1): 58–65.

Stevens, H.W. 1973. Viscoelastic properties of frozen soil under vibratory loads. In North American Contribution to the 2nd International Conference on Permafrost, Yakutsk, Siverua, USSR, pp. 400–409.

Sture, S., Costes, N.C., Batiste, S.N., Lankton, M.R., AlShibli, K.A., Jeremic, B., Swanson, R.A. and Frank, M. 1998. Mechanics of granular materials at low effective stresses. Journal of Aerospace Engineering, 11(3): 67–72.

Tamrakar, S.B., Mitachi, T., Toyosawa, Y. and Itoh, K. 2005. Development of a new soil tensile strength test apparatus. In Proceedings of Geo-Frontiers Congress 2005, Austin, Texas, USA.

Tang, C.S., Pei, X.J., Wang, D.Y., Shi, B. and Li, J. 2015. Tensile strength of compacted clayey soil. Journal of Geotechnical and Geoenvironmental Engineering, 141(4): 04014122.

Thu, T.M., Rahardjo, H. and Leong, E.C. 2007. Elastoplastic model for unsaturated soil with incorporation of the soil-water characteristic curve. Canadian Geotechnical Journal, 44(1): 67–77.

Toker, N.K., Germaine, J.T. and Culligan, P.J. 2014. Effective stress and shear strength of moist uniform spheres. Vadose Zone Journal, 13(5), https://doi.org/10.2136/vzj2013.07.0129.

Tu, H. and Vanapalli, S.K. 2016. Prediction of the variation of swelling pressure and one-dimensional heave of expansive soils with respect to suction using the soil-water retention curve as a tool. Canadian Geotechnical Journal, 53(8): 1213–1234.

van Genuchten, M.T. 1980. A closed-form Eq. for predicting the hydraulic conductivity of unsaturated soils. Soil Science Society of America Journal, 44(5): 892–898.

Vanapalli, S.K. and Fredlund, D.G. 2000. Comparison of different procedures to predict unsaturated soil shear strength. In Proceedings of Geo-Denver, Denver, USA, pp. 195–209.

Vanapalli, S.K., Fredlund, D.G., Pufahl, D.E. and Clifton, A.W. 1996. Model for the prediction of shear strength with respect to soil suction. Canadian Geotechnical Journal, 33(3): 379–392.

Vanapalli, S.K., Sillers, W.S. and Fredlund, M.D. 1998. The meaning and relevance of residual state to unsaturated soils. In Proceedings of the 51st Canadian Geotechnical Conference, Edmonton, AB, Canada, pp. 4–7.

Vanapalli, S.K., Fredlund, D.G. and Pufahl, D.E. 1999. The influence of soil structure and stress history on the soil water characteristics of a compacted till. Géotechnique, 49: 143–159.

Varsei, M., Miller, G.A. and Hassanikhah, A. 2016. Novel approach to measuring tensile strength of compacted clayey soil during desiccation. International Journal of Geomechanics, 16(6): D4016011.

Wheeler, S. and Karube, D. 1995. Constitutive behaviour. In Proceedings of the 1st International Conference on Unsaturated Soils, Paris, France, Vol. 3, pp. 1323–1356.

White, N.F., Duke, H.R., Sunada, D.K. and Corey, A.T. 1970. Physics of desaturation in porous materials. Journal of the Irrigation and Drainage Division, 96(2), 165–191.

Willson, C.S., Lu, N. and Likos, W.J. 2012. Quantification of grain, pore, and fluid microstructure of unsaturated sand from X-ray computed tomography images. Geotechnical Testing Journal, 35(6), 911–923.

Chapter 4. Evolution of Microstructural Void Ratio in Compacted Clayey Soils upon Wetting and Drying

4.1 Background

It is widely recognized in the literature that the soil microstructure significantly influences the hydraulic and mechanical properties of compacted clayey soils. The pioneering studies linking the macroscopic behavior with the microstructure of compacted clays date back to the 1950s and the 1960s (e.g., Lambe 1958; Mitchell et al. 1965). During the last 25 years, information of soil fabric and pore-size distribution were possible using scanning electron microscopy (SEM) and mercury intrusion porosimetry (MIP), respectively from direct observations. Both the SEM and MIP serve as tools to provide insight into the microstructural evolution of compacted clayey soils (for example, Delage et al. 1996; Al-Mukhtar et al. 1996; Cuisinier and Laloui 2004; Monroy et al. 2010; Burton et al. 2015; Li et al. 2020). Several additional factors contribute to changes in the soil microstructure, which include the aging effect (e.g., Delage et al. 2006), low or high temperature (e.g., Xu et al. 2018; Villar et al. 2019), pore-water chemistry (e.g., Pedrotti 2016), and cementation (e.g., Di Sante et al. 2014); however, these factors are out of the scope for investigation in this study. During the past decade, remarkable advancements have been achieved in modelling the behavior of compacted clayey soils incorporating explicitly the microstructural evolution, such as the soil-water characteristic curve (SWCC) (e.g., Romero et al. 2011; Hu et al. 2013; Della Vecchia et al. 2015), hydraulic conductivity (e.g., Romero 2013; Wang et al. 2013; Azizi et al. 2020), mechanical constitutive behavior (e.g, Gens et al. 2010; Alonso et al. 2013; Qiao et al. 2019), and shear strength and tensile strength properties (e.g., Alonso et al. 2010; Trabelsi et al. 2018).

Most studies on the microstructure of compacted clayey soils are related to the double-porosity aggregated structure, which is a typical structural characteristic at the dry-of-optimum compaction state. The microstructural void ratio is strongly associated with the microstructural state, which influences the hydromechanical behavior of compacted clayey soils (e.g., Alonso et al. 2013; Mašín 2013; Qiao et al. 2019; Cheng et al. 2020a). The identification of different populations of soil pores (i.e. inter- and intra-aggregate pores) is the first step to investigate separately the soil behavior at two structural levels. However, this identification to a certain extent is subjective due to the overlapping of different pore size populations. Hydromechanical loading paths after compaction that might dramatically change the soil microstructure add complexity to this approach. Therefore, a reasonable criterion is required to discriminate the intra-aggregate pores from the inter-aggregate pores for compacted clayey soils following

hydromechanical loading paths. Moreover, in almost all the previous studies, the clay aggregates with intra-aggregate pores are assumed to remain fully saturated (e.g., Gens and Alonso 1992; Mašín 2013). This assumption is not valid for compacted clayey soils with low water content or the clayey soil that dries after compaction. If the clay aggregates desaturate, the volumetric behavior will be controlled by other constitutive stresses in unsaturated conditions instead of Terzaghi's effective stress used in the well-known model for expansive soils, BExM (Alonso et al. 1999; Sánchez et al. 2005). The objective of this study is to investigate quantitatively and propose a practical and reliable prediction procedure of the volumetric deformation of clay aggregates of compacted clayey soils following the wetting and drying paths.

This chapter is organized as follows. First, a brief introduction of the MIP technique is presented. Then, several MIP test results are summarized to highlight the typical structural characteristics of compacted clayey soils that follow the wetting or drying paths. A practical criterion for identifying different pore populations by interpreting the MIP results is suggested after evaluating the existing criteria. The as-compacted state line (ACSL) is proposed to predict the variation of microstructural void ratio with the compaction water ratio for compacted clayey soils. For the sake of generality, the constitutive stress that is regarded to control the volumetric deformation of unsaturated clay aggregates (referred as "microstructural average skeleton stress") is derived. Thereafter, the linear elastic constitutive model proposed by Alonso et al. (1999) is extended for predicting the change in the microstructural void ratio of the examined compacted clayey soils subjected to monotonic wetting or drying path. Lastly, the capability and limitations of the proposed approach are discussed.

4.2 Microstructural evolution of compacted clayey soils upon wetting and drying

4.2.1 Basic principle of mercury intrusion porosimetry (MIP) technique

The mercury intrusion porosimetry (MIP) and environmental scanning electron microscopy (ESEM) are the widely used approaches for investigating the features of the soil microstructure (Romero and Simms 2008). In the interpretation of MIP results, the theoretical entrance pore size, d is related to the applied pressure of nonwetting phase (i.e. mercury), p_{Hg} according to the Washburn (1921) equation:

$$p_{Hg} = -\frac{4T_{s,Hg}\cos\theta_{nw}}{d} \quad (4.1)$$

where $T_{s,Hg}$ is the surface tension of mercury (i.e. 0.484 N/m at 25 °C (Mitchell and Soga 2005)), θ_{nw} is the mercury-soil contact angle (e.g., 140° (Romero 1999)). The MIP results are often presented in terms

of the cumulative mercury volume intruded into the specimen per unit mass as the function of the entrance pore size, which is referred as “cumulative intrusion curve”. Two different approaches can be employed to illustrate the pore size frequency using the information of cumulative intrusion curve; (i) the intruded pore volume fraction associated with the increments of the applied mercury pressure corresponding to the changes in entrance pore size with the selected equally-spaced class width on the logarithmic axis (e.g., Simms and Yanful 2001), and (ii) the pore size density function (PSD) defined as the derivative of the normalised cumulative intruded mercury volume with respect to the logarithm of the entrance pore size. The appearance of the former plot depends largely on the selected number and size of the entrance pore size and the corresponding applied pressure intervals; therefore, pore size density (PSD) function is commonly exploited. The mathematical formulation of PSD is expressed by (Juang and Holtz 1986; Romero et al. 1999):

$$\text{(4.2)}\quad \mathrm{PSD}(d) = f(d_{\mathrm{m}}) = \frac{\delta\left(S_{\mathrm{r,nw}}\right)}{\delta(\log d)}$$

where normalised cumulative intruded volume (or, nonwetting phase degree of saturation), $S_{\mathrm{r,nw}} = V_{\mathrm{nw}}/V_{\mathrm{MIP}}$, V_{nw} and V_{MIP} are the cumulative intruded volume and total intruded volume by MIP technique, respectively; d_{m} is the mid-point of each class width $\delta(\log d)$. Other modified expressions can be (e.g., Koliji et al. 2010; Lloret et al. 2005; Monroy et al. 2010; Della Vecchia et al. 2015):

$$\text{(4.3)}\quad f^{\mathrm{V}}(d_{\mathrm{m}}) = V_{\mathrm{MIP}} f(d_{\mathrm{m}}) = \frac{\delta\left(V_{\mathrm{MIP}} S_{\mathrm{r,nw}}\right)}{\delta(\log d)} = \frac{\delta\left(V_{\mathrm{nw}}\right)}{\delta(\log d)}$$

$$\text{(4.4)}\quad f^{\mathrm{e}}(d_{\mathrm{m}}) = e_{\mathrm{MIP}} f(d_{\mathrm{m}}) = \frac{\delta\left(e_{\mathrm{MIP}} S_{\mathrm{r,nw}}\right)}{\delta(\log d)} = \frac{\delta\left(e_{\mathrm{nw}}\right)}{\delta(\log d)}$$

where $e_{\mathrm{nw}} = V_{\mathrm{nw}}/V_{\mathrm{s}}$, $e_{\mathrm{MIP}} = V_{\mathrm{MIP}}/V_{\mathrm{s}}$, and V_{s} is the volume of solid phase in the MIP specimen. It is worth noting that the derived PSD with respect to “entrance pore size” from MIP measurements might differ from the real pore size frequency. This is mainly attributed to the limitations of MIP technique, such as the pore entrapment and the ink-bottle effect (e.g., Simms and Yanful 2005), the disturbance on the soil structure during specimen preparation and testing (e.g., Diamond 1970; Delage and Pellerin 1984; Penumadu and Dean 2000; Yuan et al. 2018), the intruded minimal pore size and detectable maximal pore size limited by the applied mercury pressure provided by the MIP test apparatus (Koliji et al. 2010), and the influence of specimen size (Simms and Yanful 2001; Yuan et al. 2019).

4.2.2 Typical structural characteristics of compacted clayey soils upon wetting and drying

Based on the observation on the microfabric feature of natural soils using scanning electron microscopy (SEM), Collins and McGown (1974) divided the microfabric feature into three types, namely (i) elementary particle arrangements (type I), (ii) particle assemblages (type II), and (iii) pore spaces (type III). The type I with the matrix arrangement of individual clay particles (Figure 4.1(a)) is dominant in expansive soils, whereas the type II with the aggregation configuration of clay particles (Figure 4.1(b)) is predominant in collapsible soils (Alonso et al. 1987). Similarly, the type I and type II of microfabric typically appear in as-compacted clayey soils at the wet-of-optimum and the dry-of-optimum conditions, respectively (e.g., Tarantino 2010). Figure 4.2(a) shows the variation of PSD on three compacted kaolin specimens at the same vertical stress of 1200 kPa and different compaction water contents. It is found that specimen compacted at a water content of approximately 21.5% shows two dominant modal pore sizes in PSD (i.e. 0.2 μm and 0.6 μm), which correspond to the intra-aggregate pores and the inter-aggregates, respectively. It is interesting to note that mono-modal PSD appears in both the specimen compacted with a relatively high water content (i.e. 31.1%) and the one with extremely low compaction water content (i.e. 8.6%). The intra-aggregate pores are dominant in the specimens compacted at high compaction water content; whereas the intra-aggregate pores almost disappear when the compaction water content decreases to a relatively low value. Figure 4.2(b) shows the typical microstructural evolution of a compacted clayey soil with a bi-modal PSD subjected to saturation and drying. The essentially unaltered inter-aggregate pores domain and remarkable decrease in modal pore size for intra-aggregate pores were observed in the compacted specimen subjected to monotonic increase in suction (from about 200 kPa to 2160 kPa). In contrast, the expansion of clay aggregates as well as clay particles (with active clay mineral of interstratified illite-smectite) results in an increase in the modal size of intra-aggregate pores and decrease in that of inter-aggregate pores (i.e. occlusion of macropores) in the compacted specimen during soaking at a constant vertical stress of 2 kPa.

As for the type III of microfabric feature, the presence of clay particles acts as connectors between sand/silt grains or coats the surfaces of grains (Figure 4.1(c)). In comparison to the first two types, one more large pore mode (inter-grain pores) appears between the shielding skeleton. Figure 4.2(c) presents the difference in the microstructural evolution upon saturation between the compacted bentonite and sand-bentonite mixture specimens. For the compacted MX80 bentonite specimen, the aggregates expand and fuse together during saturation, which leads to the occlusion of inter-aggregate pores by the swelling aggregates. Due to this reason, the dominate peak corresponding to the inter-aggregate pores shifts towards

smaller pore size and merged to the other peak for intra-aggregate pores. The sand-bentonite mixture (80% uniform silica sand and 20% Kunigel V1 sodium bentonite on dry mass basis) preserves the two modes of the intra-aggregate pores and inter-aggregate pores and eliminates the inter-grain pores after saturation. This is a consequence of the occlusion of inter-grain pores due to the invasion of the highly swelling bentonite subjected to hydration (Romero et al. 2011). The type III of microfabric feature is beyond the scope of the thesis and hence is not discussed.

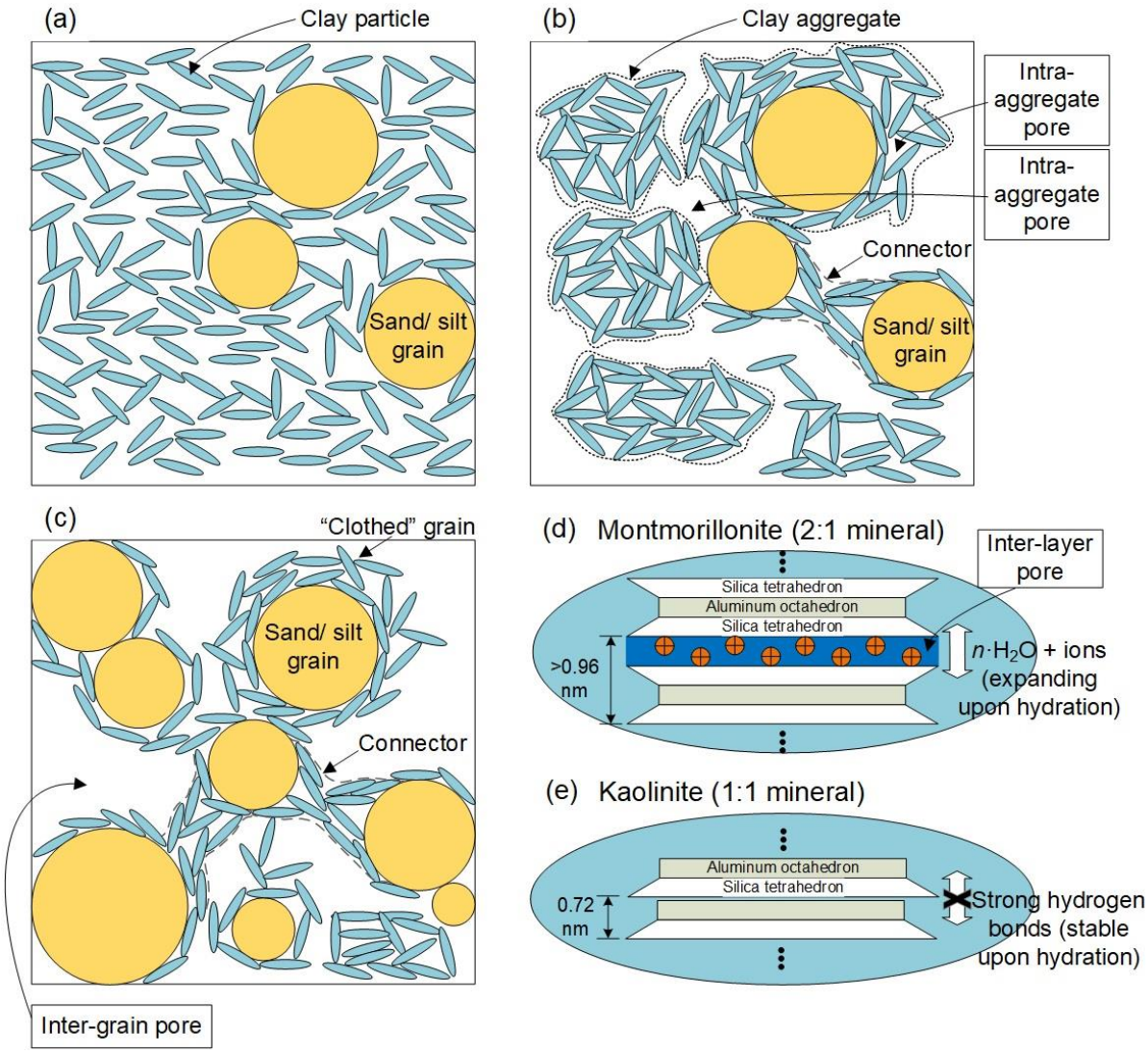

Figure 4.1 Typical microstructures of a compacted clayey soil with a few sand/silt grains (a) at wet side of optimum; and (b) that at dry side of optimum; and (c) a compacted soil with a coarse shielding skeleton (sand/silt grains) and clay connectors between individual grains; and elementary arrangement of clay particles containing (d) montmorillonite mineral and (e) kaolinite mineral.

Figures 4.1(d) and 4.1(e) represent the elementary arrangement of clay particles that contain various stacks of unit layers of montmorillonite and kaolinite, respectively. The inter-layer space among unit layers of montmorillonite will remarkably expand upon hydration, whereas no inter-layer swelling upon hydration

for kaolinite-based clay particles due to strong hydrogen bonds (Mitchell and Soga 2005). However, the inter-layer pores with size of less than 1 nm cannot be intruded by MIP technique due to the limited range of applied pressures. This is one of the technical obstacles using the MIP results. The MIP technique does not facilitate the direct and quantitative studies on the microstructural evolution of clayey soils containing active clay minerals at nano-scale level. Three peak modal sizes corresponding to inter-layer pores, intra-aggregate pores and inter-aggregate pores are expected for a dry-of-optimum compacted clayey soil with few skeleton silt/sand grains. The difference between the actual total void ratio (e_0) and the maximum cumulative void ratio intruded by MIP technique (e_{MIP}) is associated with the volume of inter-layer pores which was referred as "nanostructural void ratio" (e.g., Monroy et al. 2010; Seiphoori et al. 2014). It is worth noting that the microstructure of soil specimens is essentially the geometrical topology of the soil pores. The MIP results provide the information on the soil pore structure from one aspect, i.e. the intruded volume of the nonwetting phase versus the entrance pore size. The different populations of soil pores might overlap for a given compacted specimen in the PSD. Thus, to distinguish the different populations of soil pores based on MIP results could be somewhat subjective. As a first approximation, only the separation between inter-aggregate pores and intra-aggregate pores is considered, hereafter. The volume of inter-layer pores and intra-aggregate pores over the solid volume is referred as the "microstructural void ratio", which can be obtained by extracting the void ratio corresponding to inter-aggregate pores (e_M) from the actual total void ratio:

$$e_m = e_0 - e_M \tag{4.5}$$

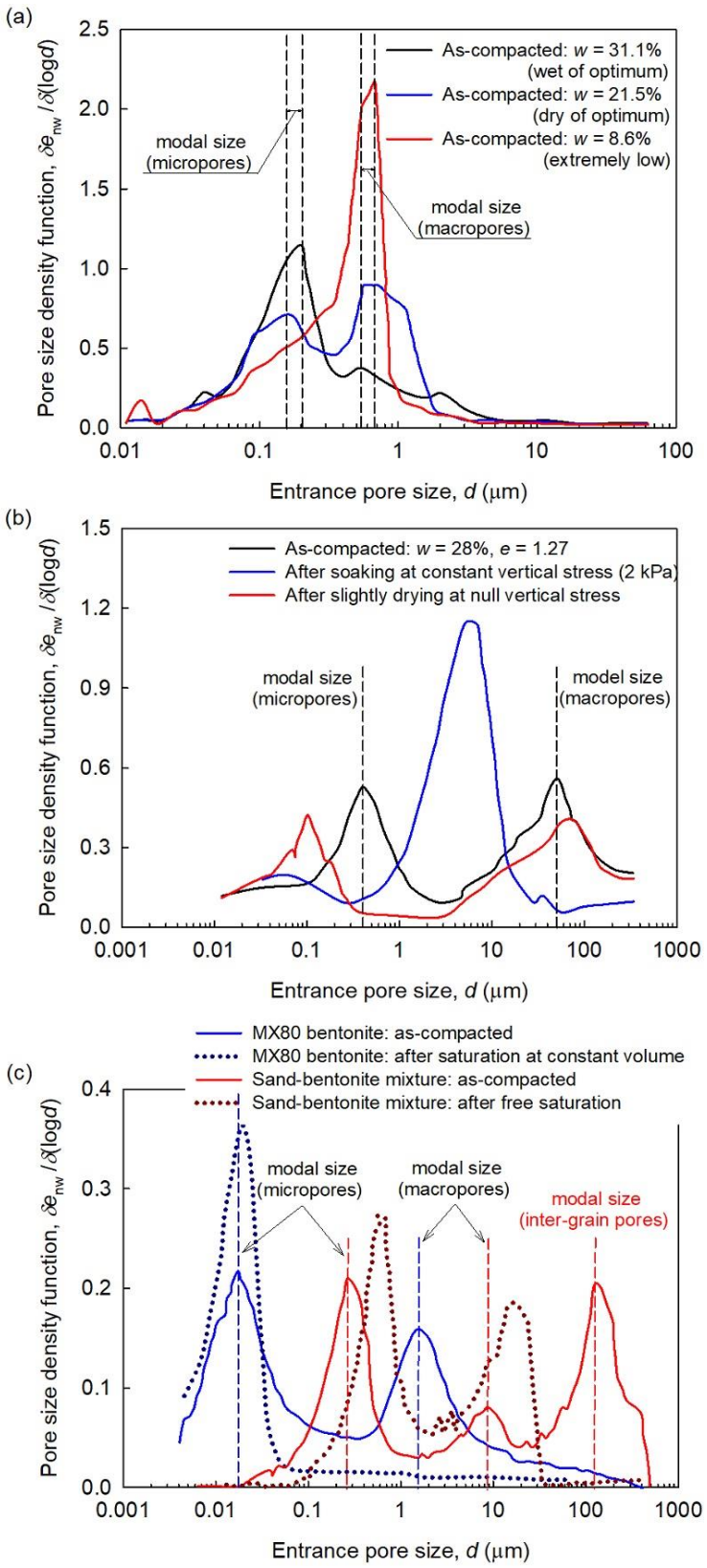

Figure 4.2 Pore size density function (PSD) of: (a) as-compacted Speswhite kaolin specimens at wet side of optimum, at dry side of optimum, and with a extremely low water content, respectively (Tarantino and De Col 2008); (b) the as-compacted Maryland clay undergoing soaking and slightly drying (Burton et al. 2015); (c) the change in PSD of a compacted MX80 bentonite (Seiphoori et al. 2014) and a compacted sand-bentonite mixture (Romero et al. 2011) upon saturation.

4.2.3 Criterion to distinguish inter-aggregate and intra-aggregate pores

The criteria proposed in the existing literature to discriminate the inter- and intra- aggregate pores based on the MIP results are summarized in Table 4.1. Figures 4.3 and 4.4 illustrate the approaches for determination of the delimiting pore size. If the cumulative intrusion-extrusion cycle is available, the criterion 1 proposed by Delage and Lefebvre (1984) might be the best choice to identify inter-aggregate pores (i.e. constricted pores) and intra-aggregate pores (i.e. non-constricted pores) (Figure 4.3(a)). According to Alonso et al. (2013), criterion 1 has two main advantages: (i) it results in a non-ambiguous procedure to discriminate the pore populations at two structural levels, and (ii) it is consistent with the reversible volumetric behavior of active clay particles due to the release of applied mercury pressure. In contrast, the identification procedure using criterion 2 or criterion 3 can be somewhat subjective due to the graphical procedures (see Figures 4.3(b) and 4.3(c)). Zhang et al. (2018) evaluated the performance of various criteria in terms of two aspects: (i) whether the microstructural void ratio changes with respect to water content; (ii) whether the criterion results in saturated intra-aggregate pores excluding oven-dried condition. The former is reasonable for the micropores, especially in active clays, as they are expected to swell/shrink subjected to wetting/drying. However, the drying process (e.g., air drying in the laboratory) induces high suction and contributes to the desaturation of intra-aggregate pores; thus, the latter aspect might be questionable.

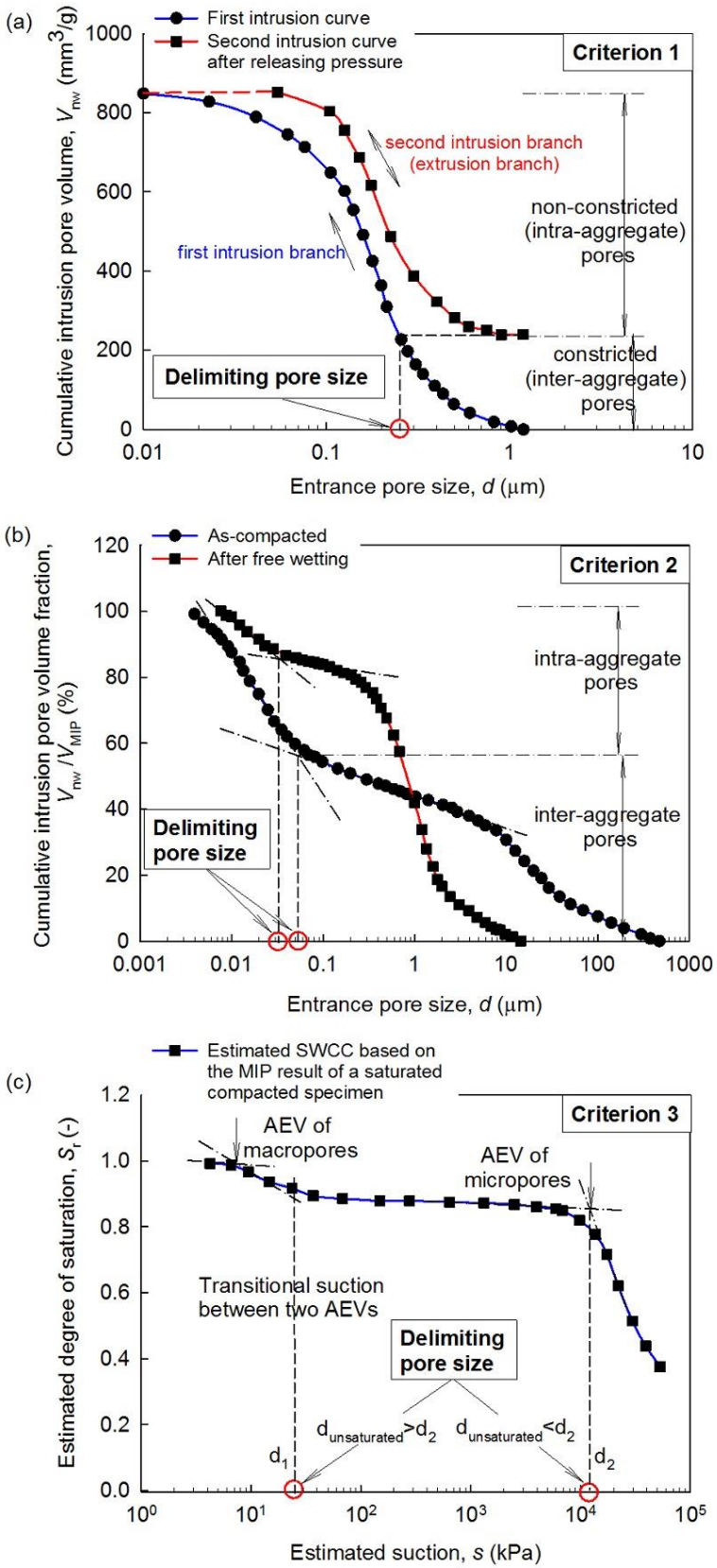

Figure 4.3 Different criteria to identify inter-aggregate pores and intra-aggregate pores based on the cumulative intrusion curves of MIP results: (a) Champlain sea clay (Delage and Lefebvre 1984); (b) 50/50 bentonite-sand mixture at as-compacted and after free wetting conditions (Samingan 2005); (c) estimated SWCC of the compacted MX80 bentonite after saturation at constant volume condition (Zhang et al. 2018).

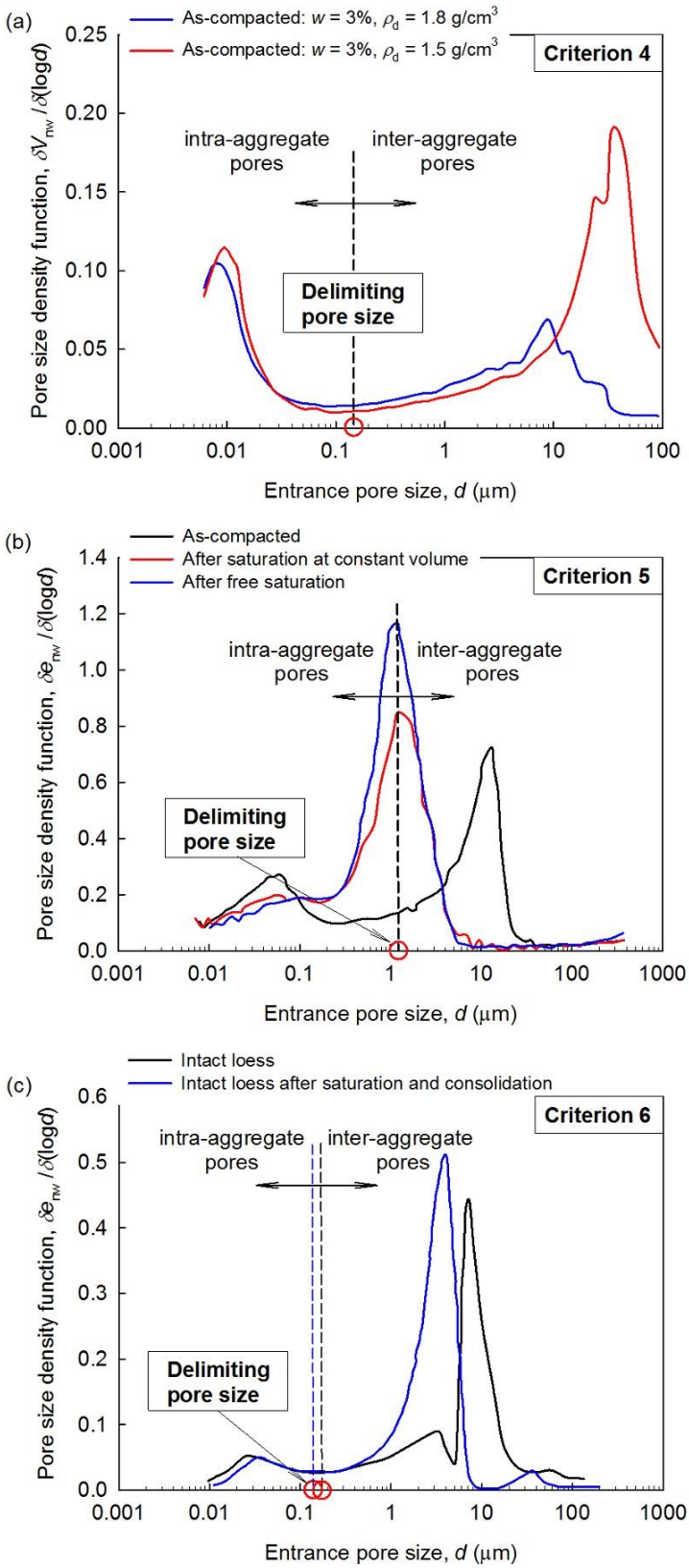

Figure 4.4 Different criteria to identify inter-aggregate pores and intra-aggregate pores based on pore size density function (PSD) of MIP results: (a) two compacted FEBEX bentonite specimens at different dry densities with a given water content (Lloret et al. 2003); (b) compacted Boom clay specimens after saturation at constant volume and after free saturation conditions (Romero et al. 2011); (c) loess specimens at intact condition and that after saturation and consolidation (Ng et al. 2016).

Table 4.1 Existing criteria in the literature to distinguish the intra-aggregate pores from inter-aggregate pores based on MIP results.

Criterion No.	Reference	Determination of delimiting pore size	Required information
Criterion 1 (Figure 4.3(a))	Delage and Lefebvre (1984)	The difference between the intruded and extruded volumes is equivalent to the inter-aggregate porosity, and that the pore inlet size corresponding to this percent on the intrusion curve marks the delimiting pore size between the constricted (inter-aggregate) and non-constricted intra-aggregate porosity.	Cumulative intrusion/extrusion cycle
Criterion 2 (Figure 4.3(b))	Samingan (2005)	The delimiting pore size coincides with the intersection point of the two tangent lines for the mercury intrusion curve.	Cumulative intrusion curve
Criterion 3 (Figure 4.3(c))	Zhang et al. (2018)	If $d_{unsaturated} < d_2$, then d_2 is the delimiting pore size; else if $d_{unsaturated} > d_2$, then d_1 is the delimiting pore size. Where $d_{unsaturated}$ is the equivalent pore size corresponding to the suction in the specimen; d_1 and d_2 are the pore sizes corresponding to the transitional suction between two AEVs (i.e. at the inflection) and to the AEV for the macropore population of the estimated SWCC, respectively.	Cumulative intrusion curve
Criterion 4 (Figure 4.4(a))	Lloret et al. (2003)	The boundary between the intra-aggregate and inter-aggregate pores corresponds to the pore size as pores smaller than which do not appear to be affected by the compaction load.	PSDs for two compacted specimens with the identical water content and different compactive efforts
Criterion 5 (Figure 4.4(b))	Romero et al. (2011)	The delimiting pore size is assumed to be the dominant peak of the pore size density (PSD) function of the as-compacted specimen after saturation.	PSD of a compacted specimen after saturation
Criterion 6 (Figure 4.4(c))	Ng et al. (2016)	The delimiting pore size is defined as the valley separating two dominant peaks, at which the derivative of PSD function becomes zero.	PSD of a compacted specimen

If only the cumulative intrusion curve is available, the PSD (original expression (Eq. (4.2)) or modified expressions (Eqs. (4.3) and (4.4)) can be adopted to identify different pore populations in a straightforward manner. It is important to recognize that both MIP tests and SEM observations are typically performed after mechanical unloading. It is well accepted that the mechanical loading-unloading does not result in irreversible deformation in intra-aggregate pores (e.g., Alonso et al. 2013; Romero 2013). Extending this observation, Lloret et al. (2003) defines the delimiting pore size such that the PSDs of specimens with the same water content is not affected by the compactive effort for the entrance pore size smaller than that border (i.e. criterion 4 in Figure 4.4(a)). This criterion is widely used due to its reasonable assumption that can be extended with confidence in engineering practice (e.g., Li et al. 2014; Sun et al. 2019). At least two

PSDs of two specimens with different compactive efforts (or, dry density) at a given water content are necessary for exploiting criterion 4. If only one PSD of a compacted specimen is available, a possible alternative is criterion 6. Criterion 6 proposed by Ng et al. (2016) defines the valley between two peaks in the PSD curve as the delimiting pore size (Figure 4.4(c)). However, it is difficult to adopt criterion 6 if the distinct bimodal shape is lost, such as a mono-modal PSD of a compacted clayey soil after saturation. Technically, criterion 6 applies to clayey soils compacted at the dry-of-optimum condition, where bi-modal PSDs typically appears. For the compacted clayey soils after saturation under constant volume or free saturation condition, the delimiting pore size is assumed to coincide with the dominate peak of the mono-modal PSD for criterion 5 (Figure 4.4(b)) which was proposed by Romero et al. (2011). Criterion 5 stems from the rational assumption that the size of the inter-aggregate pores is not less than that of intra-aggregate pores. In addition to the above criteria, several researchers selected a constant value as the delimiting pore size for both as-compacted specimens and wetted and dried specimens after compaction, e.g., 1 μm for sandy loam (Cuisinier and Laloui 2004), 1 μm for London clay (Monroy et al. 2010), and 0.3 μm for MX80 bentonite (Seiphoori et al. 2014). However, it is possible for the delimiting pore size to shift towards a larger or smaller value for a compacted clayey soil due to the swelling (shrinkage) of clay aggregates subjected to wetting (drying).

Trabelsi et al. (2018) combined the criteria 5 and 6 for obtaining the peak of the mono-modal PSD and valley of the bi-modal PSD as the delimiting pore size. However, this combined criterion does not consider the effect of hydromechanical loading paths after compaction into consideration. For example, the peak of the mono-modal PSD is not likely to coincide with the delimiting pore size of as-compacted clay specimen with relatively high or low moisture contents (e.g., Tarantino and De Col 2008, 2009). The suggested criterion is summarized in Table 4.2 considering the intrinsic as well as external factors into account. The microstructural evolution for the following two specific scenarios are investigated in this study: (i) the as-compacted specimens with different compaction moisture contents, and (ii) the as-compacted specimens subjected to the monotonic hydraulic loading paths (i.e. monotonic wetting or monotonic drying) under certain mechanical constraints. The influence of other loading paths on the microstructure of compacted clayey soils, e.g., cyclic wetting-drying, consolidation, and shearing is out of the scope of the present study.

With the aid of the determination of the delimiting pore size by the suggested criterion (Table 4.2), the microstructural void ratio can be estimated by Eq. (4.5) from the cumulative intrusion curve or by integrating the PSD:

$$(4.6)\quad e_{\mathrm{m}} = e_0 - e_{\mathrm{MIP}} \int_{d_{\mathrm{del}}}^{d_{\max}} \frac{\mathrm{PSD}(\tau)}{\tau \ln(10)} d\tau$$

where d_{del} is the delimiting pore size between intra-aggregate pores and inter-aggregate pores, $d_{\max}$ is the upper bound of entrance pore size in the PSD, and integral can be numerically calculated by the trapezoidal rule.

Table 4.2 Suggested criterion to identify micropores and macropores of compacted clayey soils in the present study.

Scenario No.	Hydromechanical loading history	Typical PSD shape	Delimiting pore size in PSD
Scenario 1	Compaction with mediate water content (e.g., dry of optimum)	Bi-modal	Valley between two dominate peaks
Scenario 2	Compaction with extremely low water content	Quasi- mono-modal	On the left-hand side of the dominate peak
Scenario 3	Compaction with high water content (e.g., wet of optimum)	Quasi- mono-modal	On the right-hand side of the dominate peak
Scenario 4	Slightly wetting or drying after compaction at dry of optimum	Bi-modal	Valley between two dominate peaks
Scenario 5	Saturation after compaction	Mono-modal	Dominate peak

4.3 Quantifying the evolution of microstructural void ratio of compacted clayey soils upon wetting and drying

Romero et al. (2011) proposed a bi-linear model for the evolution of microstructural void ratio which is influenced by compaction water content as well as subsequent wetting and drying paths:

$$(4.7)\quad e_{\mathrm{m}} = e_{\mathrm{m}}^{*} + \beta \left\langle e_{\mathrm{w}} - e_{\mathrm{m}}^{*} \right\rangle$$

where $\langle x \rangle = 0.5(x + |x|)$ designates the Macauley brackets. For $e_{\mathrm{w}} \le e_{\mathrm{m}}^{*}$, a critical microstructural void ratio $e_{\mathrm{m}} = e_{\mathrm{m}}^{*}$ results. At the water ratio of e_{m}^{*}, water will be enough to saturate the intra-aggregate pores (i.e. microstructural degree of saturation, $S_{\mathrm{r,m}} = 1$) but leaving the inter-aggregate pores empty. The microstructural degree of saturation is defined as the volume of water inside the intra-aggregate pores over the total volume of intra-aggregate pores:

$$(4.8)\quad S_{\mathrm{r,m}} = \begin{cases} e_{\mathrm{w}} / e_{\mathrm{m}}, & e_{\mathrm{w}} < e_{\mathrm{m}}^{*} \\ 1, & e_{\mathrm{w}} \ge e_{\mathrm{m}}^{*} \end{cases}$$

For $e_w > e_m^*$, the slope β in e_m: e_w indicates the swelling (shrinkage) of aggregates upon wetting (drying) paths. Revisiting the interpreted data in the space (e_m, e_w) of Boom clay (low-plasticity clay) and bentonites (high-plasticity clay) plotted by Romero et al. (2011), it is observed that for low water ratios (i.e. $e_w \leq e_m^*$), e_m increases at a relatively slow rate with increasing e_w for Boom clay; however, it increases at a faster rate in bentonites. In addition, the effect of mechanical constraints during the wetting paths, e.g., soaking at the condition of constant volume or of constant confining stress, on the swelling of the intra-aggregate pores and inter-layer pores (for the active clay minerals) might be significant especially for high-plasticity clays.

In this section, Romero et al. (2011) bi-linear model is modified in order to improve the model capability for high-plasticity clays. The microstructural evolution of compacted clayey soils depends on two factors: (i) the intrinsic factor, such as the initial microfabric feature and the clay mineralogy, and (ii) the external factor, e.g., the hydromechanical stress paths subjected by the soil. In the following subsections 4.3.1 and 4.3.2, the initial condition and the evolution upon wetting and drying of microstructural void ratio will be discussed, respectively. Table 4.3 lists the physical properties of all the examined soils (four high-plasticity clays, eight low-plasticity clays, and one coarse-grained soil with fines) in this study. Note that the glacial till (i.e. coarse-grained soil with some fines) is included with the aim of comparison.

4.3.1 Soil microstructure and soil-water characteristic curve (SWCC) of compacted cohesive soils

Figures 4.5(a) and 4.5(b) presents the variation of microstructural void ratio with compaction water ratio of three high-plasticity clays (soils 1, 2 and 4), three low-plasticity clays (soils 6, 7, and 8), and one coarse-grained soil (soil 9) by interpreting the MIP results with the suggested criterion (Table 4.2).

The compaction effort is assumed to have no influence on the microstructural void ratio for a given water ratio, which is consistent with the MIP results in several studies (e.g., Alonso et al. 2013; Romero 2013). Thus, the state surface in the space (e_m, e_w, p) for the as-compacted state can be simplified as a state line in the plane (e_m, e_w), which is referred as "as-compacted state line" (ACSL) of microstructure void ratio. An exponential Eq. for the ACSL is proposed:

$$e_m = e_{m,d} \exp\left[\frac{e_w}{e_m^*} \ln\left(\frac{e_m^*}{e_{m,d}}\right)\right] \quad (4.9)$$

where $e_{m,d}$ is the minimal microstructural void ratio corresponding to the as-compacted condition with the oven-dried soil powder.

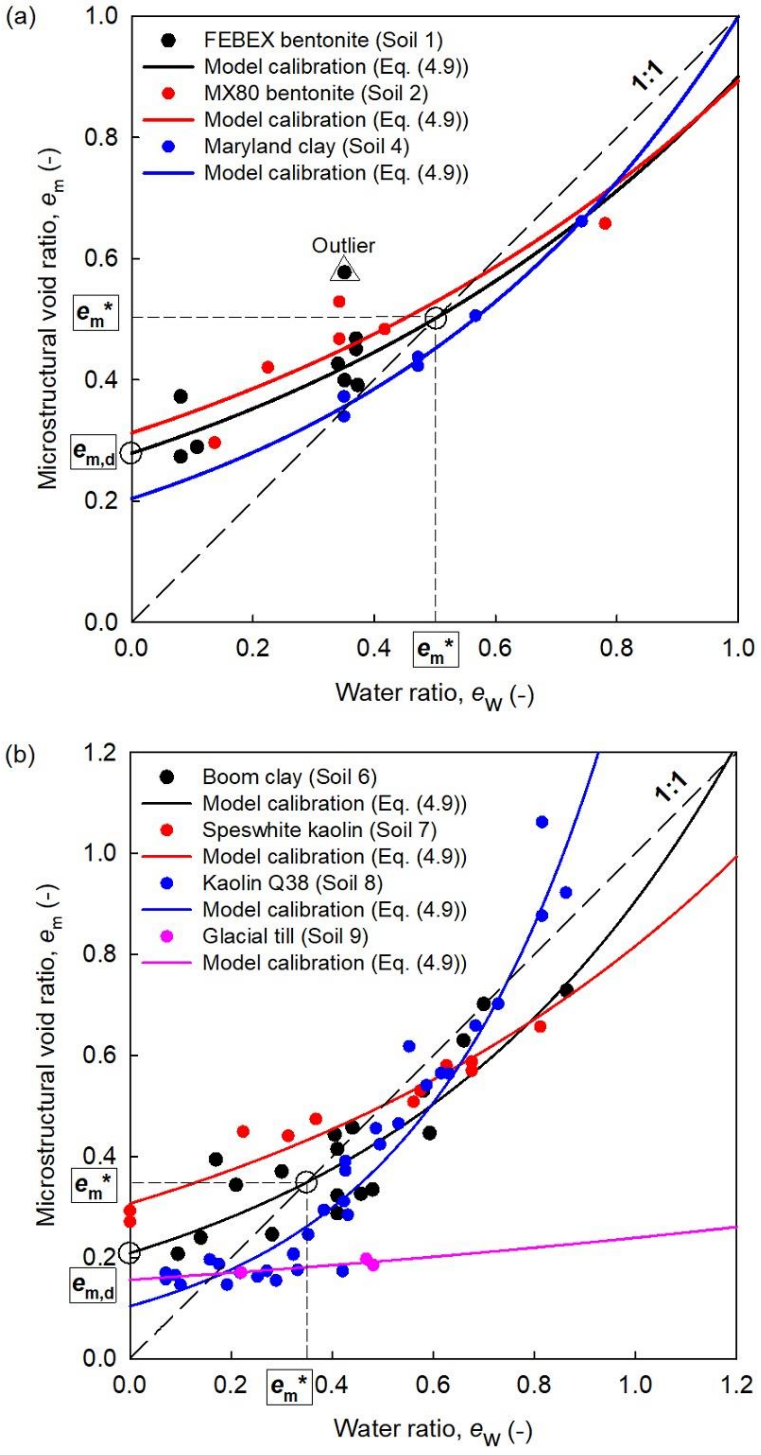

Figure 4.5 Comparison between measurements and prediction by the proposed model (Eq. (4.9)) for the microstructural void ratio of as-compacted specimens of examined soils 1, 2, 4, 5, 6, 7, 8, and 9.

The solid lines in Figure 4.5 demonstrate that the proposed ASCL (Eq. (9)) could track the evolution of microstructural void ratio at the entire range of compaction water ratio for high-plasticity clays (soils 1,

2, and 4) as well as low-plasticity clays (soils 6, 7, and 8). The outlier in Figure 4.5(a) corresponds to FEBEX bentonite (Lloret et al. 2005) compacted at a loose condition (i.e. dry density ρ_d = 1.4 g/cm^3). The existence of non-detectable pores (i.e. large pores) might result in the overestimation of microstructural void ratio using Eq. (6). There are three points with high water ratios of soil 8 (blue filled points in Figure 4.5(b)) above the 1:1 line, which indicates the aggregates become unsaturated when the compaction water ratio is high. In fact, as compaction water content is high (e.g., on the wet side of optimum), the aggregate size increases and the intra-aggregate pores are predominant (Tarantino and De Col 2008; Tarantino 2010). This tends to result in desaturated clay aggregates due to the unsaturated condition in the entire compacted specimen. Compared with low-plasticity clays, high-plasticity clays contain active clay minerals; for example, montmorillonite (Figure 4.1(d)), in which the inter-layer space is expected to expand significantly during hydration. The increase in inter-layer pores leads to the remarkable increase in the microstructural void ratio of high-plasticity clays with an increase in the compaction water ratio. On the other hand, the ACSL of the glacial till (soil 9) which contains 8% clay size fraction shows little or no swelling tendency with increasing compaction water ratio for the entire range. It is interesting to note that the microstructural void ratios of bentonites (soils 1 and 2) almost stay above the 1:1 line, which indicates unsaturated conditions in bentonite aggregates. This is perhaps a result of the underestimation of the water contents determined by the conventional laboratory procedure, in which the strongly adsorbed water in the inter-layer space cannot be removed completely in spite of subjecting it to oven-drying condition at 105°C. Table 4.4 presents the calibration results using the ACSL model for seven of the examined soils at as-compacted conditions.

Table 4.4 Model calibration details of Eqs. (4.9) and (4.16) for the microstructural void ratio of as-compacted specimens and that of as-compacted specimens after wetting and drying, respectively.

Soil No.	Soil name	Model calibration (Eq. (4.9))		Model calibration (Eq. (4.16))
		Minimal microstructural void ratio, $e_{m,d}$	Critical microstructural void ratio, e_m*	Parameter controlling the microstructural stiffness, κ_m
1	FEBEX bentonite	0.279	0.502	0.070
2	MX80 bentonite	0.313	0.567	0.096
3	London clay	------	------	0.037
4	Maryland clay	0.204	0.363	0.039
5	Barcelona clayey silt	------	------	0.074
6	Boom clay	0.209	0.349	0.064
7	Speswhite kaolin	0.307	0.502	0.022
8	Kaolin Q38	0.104	0.158	------
9	Glacial till	0.156	0.168	0.008

Table 4.3 Physical properties of all the examined soils for model calibration and validation in the present study.

Soil No.	Soil name	USCS[a]	Specific gravity, G_s	Grain size distribution (mass fraction)	Consistency limits	Dominate clay minerals	Total specific surface area, TSSA (m^2/g)	Standard Proctor compaction characteristics
1	FEBEX bentonite[1]	MH	2.70	Clay: 64-70% Silt: 26%; Sand: 7%	LL[b] = 102%; PL[c] = 53%; PI[d] = 49%; SL[e] = 20.2% (e_{SL}[f] = 0.545)	Montmorillonite (89-95%)	725	N/A[g]
2	MX80 bentonite[2]	CH	2.74	Clay: 80-85% Silt: 12%; Sand: 3%	LL = 420%; PL = 65%; PI = 355%; SL = 15.8% (e_{SL} = 0.433)	Na-Montmorillonite (82-85%)	523	OMC[h] = 6%; MDD[i] = 1790 kg/m^3 (Granular)
3	London clay[3]	CH	2.70	Clay: 58%; Silt: 40%; Sand: 2%	LL = 83%; PL = 29%; PI = 54%; SL = 21.5% (e_{SL} = 0.580)	Illite (52%); Montmorillonite (32%); Kaolinite (16%)	62	OMC = 23.5%; MDD = 1380 kg/m^3
4	Maryland clay[4]	CH	2.65	Clay: 56%; Silt: 27%; Sand: 17%	LL = 69%; PL = 26%; PI = 43%; SL = 16.0% (e_{SL} = 0.424)	Kaolinite (26.6%); Interstratified illite-smectite (10%)	95.2	OMC = 24.8%; MDD = 1500 kg/m^3
5	Barcelona clayey silt[5]	CL	2.71	Clay: 16% Silt: 44%; Sand: 40%	LL = 32%; PL = 16%; PI = 16%; SL = 14.8% (e_{SL} = 0.400)	Illite	12	OMC = 13.0%; MDD = 1890 kg/m^3
6	Boom clay[6]	CL	2.70	Clay: 50%; Silt: 47%; Sand: 3%	LL = 61.5%; PL = 34.5%; PI = 27%; SL = 15.9% (e_{SL} = 0.430)	Illite (20-30%); Kaolinite (20-30%); Smectite (10-20%)	42	OMC = 17.7%; MDD = 1760 kg/m^3
7	Speswhite kaolin[7]	CL	2.61	Clay: 80%; Silt: 20%	LL = 64%; PL = 32%; PI = 32%; SL = 31.4% (e_{SL} = 0.820)	Kaolinite (90%)	48	N/A
8	Kaolin Q38[8]	MH	2.63	Clay: 95%; Sand: 5%	LL = 51%; PL = 29%; PI = 22%; SL = N/A	Kaolinite (95%)	28	N/A

				(e_{SL} = 0.400[j])			
9	Glacial till[9]	GC	2.75	Clay: 8%; Silt: 14%; Sand: 18%; Gravel: 60%	LL = 27%; PL = 18%; PI = 9%; SL = 14.0% (e_{SL} = 0.385)	Illite; Chlorite	N/A	OMC = 13.7%; MDD = 1810 kg/m^3
10	Jossigny silt[10]	CL	2.77	Clay: 34% Silt: 56%; Sand: 10%	LL = 37%; PL = 19%; PI = 18%; SL = 12.0% (e_{SL} = 0.481)	Illite; Kaolinite; Interstratified illite-smectite	N/A	OMC = 18.3%; MDD = 1680 kg/m^3
11	Xiashu loess[11]	CL	2.73	Clay: 22% Silt: 76%; Sand: 2%	LL = 37%; PL = 20%; PI = 17%; SL = 10.5% (e_{SL} = 0.287)	Illite; Interstratified illite- montmorillonite	N/A	OMC = 16.5%; MDD = 1700 kg/m^3
12	Le Deffend clayey soil E1[12]	MH	2.60	Clay: 72%; Silt: 27%; Sand: 1%	LL = 86%; PL = 54%; PI = 32%; SL = 18.1% (e_{SL} = 0.470)	Smectite	N/A	OMC = 23.5%; MDD = 1380 kg/m^3
13	Xi'an clayey loess[13]	CL	2.70	Clay: 21%; Silt: 77%; Sand: 2%	LL = 36%; PL = 20%; PI = 16%; SL = N/A (e_{SL} = N/A)	Illite; Chlorite	N/A	OMC = 17.5%; MDD = 1680 kg/m^3

Note:
[1]Villar (2001), Lloret et al. (2003, 2005), Villar and Lloret (2018).
[2]Delage et al. (2006), Bag (2011), Seiphoori et al. (2014), Wang et al. (2014).
[3]Monroy et al. (2010), Zhang et al. (2017), Dewhurst et al. (1998).
[4]Burton et al. (2015), Burton (2016), Yuan et al. (2016), Liu et al. (2016).
[5]Barrera (2002), Romero (2013), Romero et al. (2011).
[6]Romero (1999), Romero et al. (1999, 2011), Merchán (2011), Romero (2013), Pérez Canals (2013), Della Vecchia et al. (2013), Dieudonné et al. (2014), Robinet et al. (1996).
[7]Tarantino and De Col (2008), Tripathy et al. (2010), Pedrotti (2016), Pedrotti et al. (2018).
[8]Nguyen et al. (2020).
[9]Simms and Yanful (2001).
[10]Delage et al. (1996), Sun and Cui (2018).
[11]Cheng et al. (2020a).
[12]Nowamooz and Masrouri (2010).
[13]Ge et al. (2019).
[a]Unified Soil Classification System (ASTM D2487-17, ASTM International 2017a); [b]liquid limit; [c]plasticity limit; [d]plasticity index; [e]shrinkage limit; [f]void ratio at shrinkage limit; [g]not available in the cited studies; [h]optimum moisture content; [i]maximum dry density; [j]estimated value.

4.3.2 Evolution of microstructural void ratio along wetting and drying paths with initial fabric generated by compaction

Following the studies on volumetric behavior of unsaturated soils (e.g., Alonso et al. 1990; Romero 1999; Airò Farulla et al. 2010), it is assumed that expansion (contraction) of clay aggregates subjected to wetting (drying) paths depends mainly on the initial microstructural void ratio as well as the stress acting on individual aggregates.

An individual clay aggregate is taken from the representative elementary volume (REV) of the compacted clayey soil (Figure 4.6(a)) for force equilibrium analysis. Following the procedure adopted by Mitchell and Soga (2005) and Lu and Likos (2006), the wavy surface through interparticle contacts of the REV is used to investigate the relationship among skeletal forces, interparticle forces and contact forces. In the past several decades, several researchers investigated different types of interparticle forces in clays (e.g., Ingles 1962; Hueckel 1992a; Lu and Likos 2006; Pedrotti and Tarantino 2018). The relatively sensitive microfabric feature of compacted clayey soils upon hydromechanical loading paths results in the changes in the interparticle forces among clay particles. Note that the externally applied stress tensor (σ_{ij}) on the REV induces both normal and shear forces at inter-aggregate contacts. It is widely accepted that the deformation of clay aggregates is volumetric (e.g., Alonso et al. 1999). In addition, the component of volumetric deformation induced by the shear force acting on the aggregates is ignored, hereafter. Thus, only the component of volumetric strain induced by normal force (σ_m) needs to be investigated. The relationship among different types of forces acting within and on the boundary of aggregates can be developed from the force equilibrium analysis of the vertical component. For the scenario of saturated aggregates (Figure 4.6(b)), readers can refer the derivation by Mitchell and Soga (2005); for the scenario of unsaturated aggregates (Figure 4.6(c)), the detailed derivation can be found in Appendix.

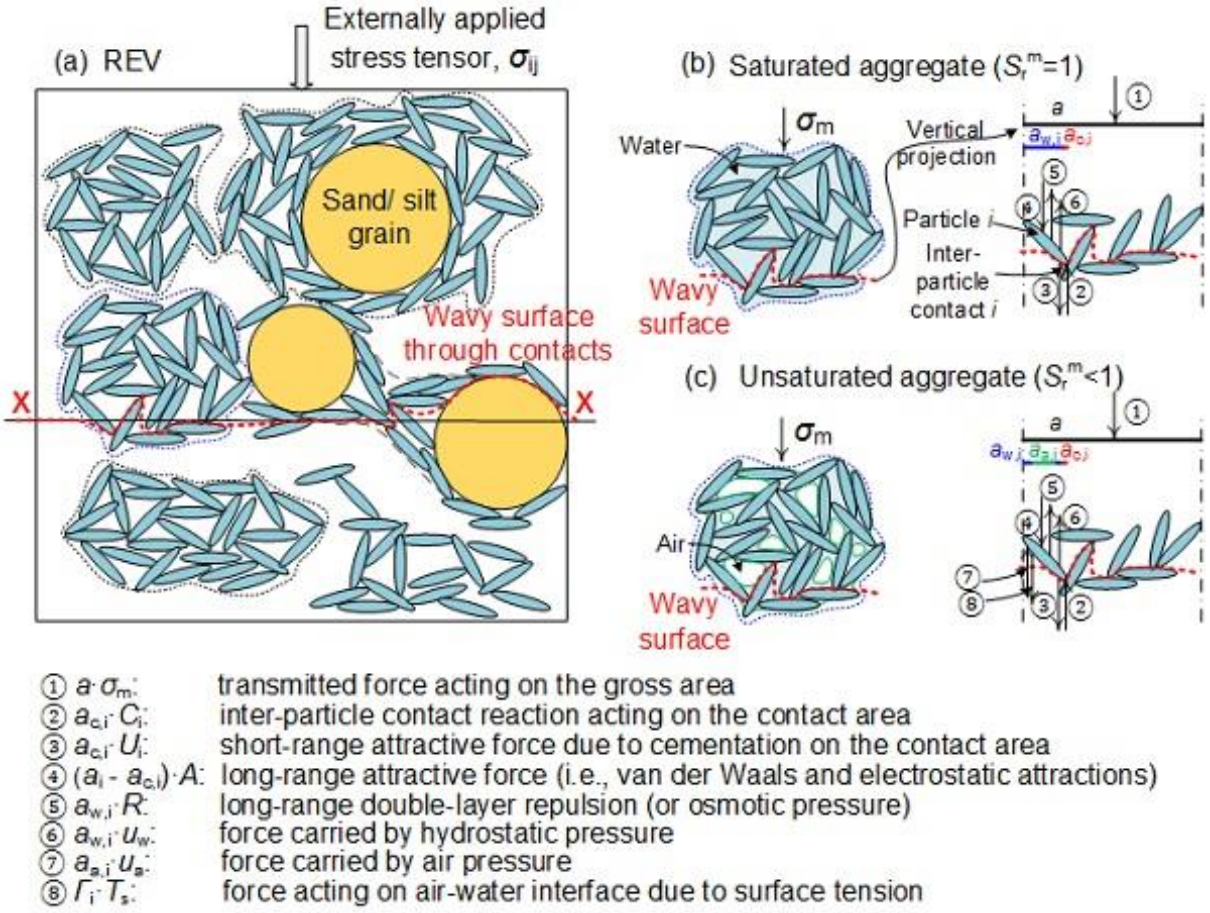

Figure 4.6 Schematic illustration of (a) multiphase air-water-solid representative elementary volume (REV) of a compacted clayey soil subjected to external applied stresses; (b) a saturated aggregate with the wavy surface and the forces acting on the interparticle contact *i*; (c) an unsaturated aggregate with the wavy surface and the forces acting on the interparticle contact *i*.

The "microstructural average skeleton stress" which is considered to control the volumetric deformation of clay aggregates can be simplified as

$$(4.10)\quad p_m'' = p_m^{net} + \frac{a_w}{a} s_m$$

where the net normal stress acting on the clay aggregates, $p_m^{net} = p_m - u_a$. It is reasonable to assume that $p_m^{net} = p_m$, if the cross-sectional area of aggregates is comparable to the total cross-sectional area (Mašín 2013). s_m is the suction within the clay aggregates, which is assumed to equal the global suction in the situation of thermodynamic equilibrium (i.e. $s_m = s$). The term a_w/a is the ratio of the vertically projected area occupied by water over the total projected area of the REV on the horizontal plane (Figure 4.6(c)). It is evident that this ratio is strongly correlated to the degree

of saturation in clay aggregates, $S_{r,m}$, based on the previous studies on unsaturated soils (e.g., Vanapalli et al. 1996; Lu and Likos 2006). The ratio a_w/a is approximated as the microstructural degree of saturation, $S_{r,m}$ to be consistent with Bishop's effective stress parameter (Bishop 1959) using the degree of saturation (e.g., Schrefler 1984).

(4.11) $$\frac{a_w}{a} = S_{r,m}$$

Therefore, the resulting formula of microstructural average skeleton stress can be written as

(4.12) $$p_m'' = p^{net} + sS_{r,m}$$

Following the proposal by Houlsby (1997), the work-conjugative strain rate with the above microstructural average skeleton stress is essentially the microstructural volumetric strain rate, $d\varepsilon_{vm}$. Based on the assumption that volume change in clay aggregates is reversible upon hydromechanical loading (e.g., Alonso et al. 1999; Sánchez et al. 2005), the following incremental linear elastic constitutive model is employed:

(4.13) $$d\varepsilon_{vm} = \frac{dp_m''}{K_m}$$

where $K_m = \frac{1+e_m}{\kappa_m} p_m''$ is the microstructural bulk modulus, κ_m is the parameter controlling the microstructural stiffness, the microstructural volumetric strain is defined as $d\varepsilon_{vm} = de_m / (1+e_m)$. Thus, Eq. (13) can be rearranged as

(4.14) $$de_m = \kappa_m \frac{dp_m''}{p_m''}$$

This model yields a linear relationship in the plane (e_m, $\ln(p_m'')$)

(4.15) $$e_m = C - \kappa_m \ln\left(p_m''\right)$$

The explicit formulation for predicting the evolution of microstructural void ratio for monotonic wetting and drying paths can be obtained from the initial microstructural void ratio, which can be estimated from the ASCL (i.e. Eq. (4.9)):

$$e_{\mathrm{m}} = e_{\mathrm{m}}^{\mathrm{AC}} - \kappa_{\mathrm{m}} \ln\left(\frac{p_{\mathrm{m}}''}{p_{\mathrm{m}}''^{\mathrm{AC}}}\right) \tag{4.16}$$

where $e_{\mathrm{m}}^{\mathrm{AC}}$ and $p_{\mathrm{m}}''^{\mathrm{AC}}$ are the microstructural void ratio and microstructural average skeleton stress in the initial condition (i.e. as-compacted state), respectively.

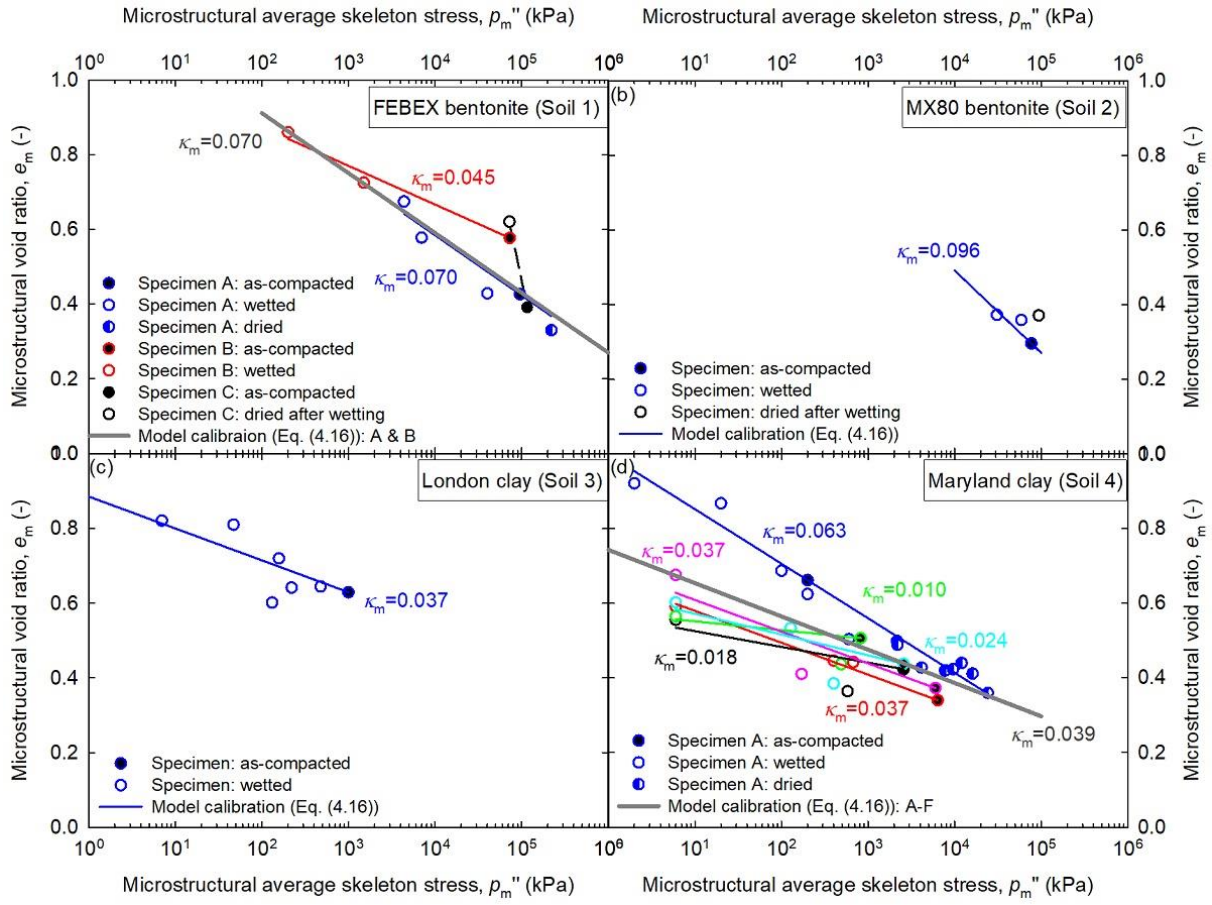

Figure 4.7 Comparison between measurements and prediction by the linear elastic model (Eq. (4.16)) for the microstructural void ratio of as-compacted specimens after wetting or drying of examined soils 1, 2, 3 and 4.

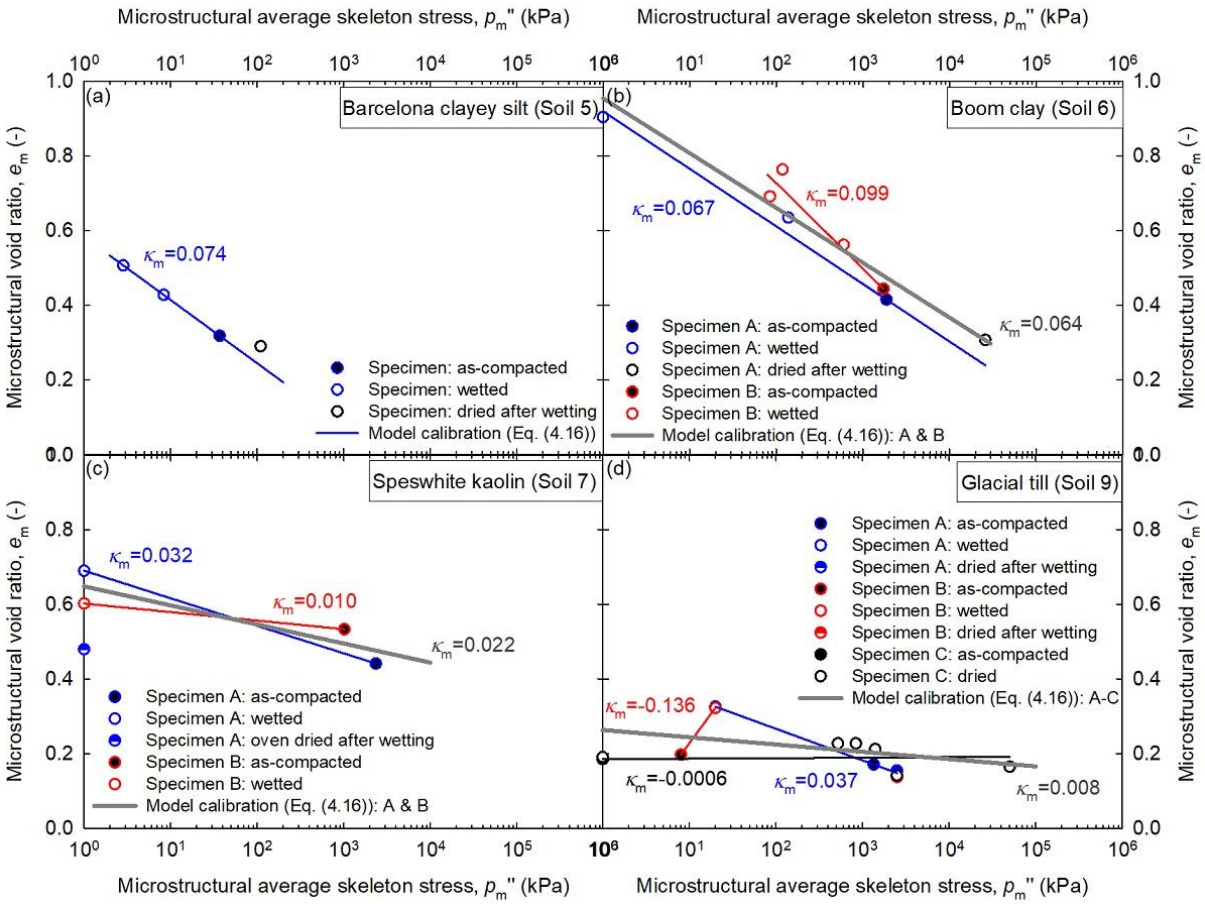

Figure 4.8 Comparison between measurements and prediction by the linear elastic model (Eq. (4.16)) for the microstructural void ratio of as-compacted specimens after wetting or drying of examined soils 5, 6, 7 and 9.

Figure 4.7 presents the variation of the interpreted microstructural void ratio, e_m based on the suggested criteria (Table 4.2) with respect to microstructural average skeleton stress, p_m'' after wetting or drying of four compacted high-plasticity clays (soils 1, 2, 3, and 4). Note that the microstructural volumetric deformation during mechanical unloading prior to MIP tests is assumed negligible. For soils 1 and 4 which have more than one set of test results, the linear regression using Eq. (16) is conducted for each set separately (lines with different colours in Figures 4.7(a) and (d)). Different slopes of the regression lines with different initial conditions indicate that the other factors might affect the volumetric behavior of clay aggregates, such as the interaction between microstructure and macrostructure levels in the double-porosity aggregated soils (e.g., Thom et al. 2007; Mašín 2013), the suction-induced additional bounding effect on the mechanical properties of unsaturated soils (e.g., Gallipoli et al. 2003). It is important to note that those factors are not specifically considered in the linear elastic constitutive model. In other words, the

parameter controlling the microstructural stiffness, κ_m is assumed constant. The grey line shows the calibration result using Eq. (16) with all the sets of test results, the slope of which is used as the average slope in case of multiple sets. It is worth noting that irreversible volumetric deformation occurs when the compacted specimen is subjected to drying after wetting path, e.g., specimen C of soil 1 (black open circle in Figure 4.7(a)) and soil 2 (black open circle in Figure 4.7(b)). However, this irreversibility in microstructural volumetric deformation seems less pronounced for the low-plasticity clays, e.g., soil 5 (black open circle in Figure 4.8(a)) and specimen A of soil 6 (black open circle in Figure 4.8(b)). The abnormal negative slope for specimen B of soil 9 upon wetting path (red open circle in Figure 4.8(d)) may be due to Eq. (16) that is not valid for soil 9 that has the initial microfabric of type III (i.e. Figure 4.1(c)). Table 4.4 presents calibration results by the linear elastic constitutive model (i.e. Eq. (4.16)) for eight of the examined soils.

4.3.3 Model parameters estimation

Figure 4.9 shows the variation of three model parameters, i.e. minimal microstructural void ratio ($e_{m,d}$), critical microstructural void ratio (e_m*) and parameter controlling the microstructural stiffness (κ_m) with physical properties of examined soils. Figure 4.9(a) plots $e_{m,d}$ as a function of the global void ratio at shrinkage limit, e_{SL} of seven of the examined soils. Note that the active clay mineral in bentonites (i.e. soils 1 and 2) has a large total specific surface area (e.g., 800 m^2/g for montmorillonite (Lambe and Whitman 1979)) and adsorbs a large amount of water in the inter-layer space as well as on the surface of clay particles. Essentially, the zero shrinkage zone, during which the decrease in water content does not induce any deduction in the void ratio, is not well developed in the soil shrinkage curve of bentonites (Chen and Lu 2018). The disagreement of soil 2 against the general trend of other soils (filled square in Figure 4.9(a)) may be attributed to the non-well defined “shrinkage limit” of bentonites. For other soils, the high correlation between $e_{m,d}$ and the global void ratio at shrinkage limit (R^2 = 0.88) can be represented as the following logarithmic form:

$$e_{m,d} = 0.363 + 0.194 \ln\left(e_{SL}\right) \quad (4.17)$$

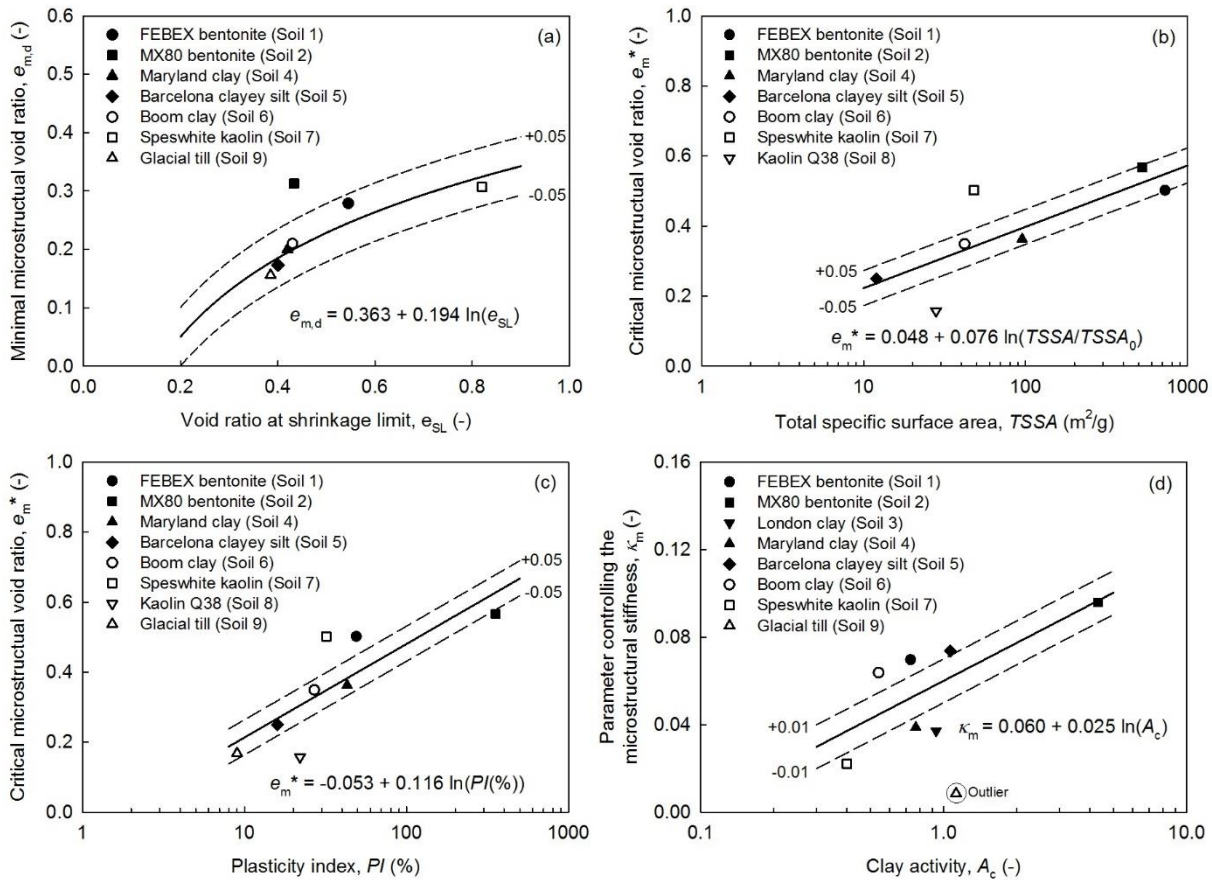

Figure 4.9 Correlation between model parameters and soil physical properties: (a) $e_{m,d}$ versus void ratio at shrinkage limit; (b) e_m* versus total specific surface area; (c) e_m* versus plasticity index; and (d) κ_m versus clay activity.

As suggested by Romero et al. (2011) and Romero et al. (2014), e_m* can be related to the total specific surface area (*TSSA*) or plasticity index (*PI*) of the clay. Good correlation between e_m* and those two soil physical properties can be (Figures 4.9(b) and (c)):

$$e_m^* = 0.048 + 0.076 \ln\left(\frac{TSSA}{TSSA_0}\right) \quad (4.18)$$

$$e_m^* = -0.053 + 0.116 \ln\left(PI(\%)\right) \quad (4.19)$$

where the parameter $TSSA_0$ = 1 m^2/g.

The parameter κ_m that controls the stiffness of clay aggregates subjected to monotonic wetting and drying paths is expected to be associated with the swelling (shrinkage) potential of the examined soils upon wetting (drying). Figure 4.9(d) indicates that κ_m increases with increase in the clay

activity (A_c) which is the index for identifying the soil swelling potential (i.e. A_c = *PI*/ clay size fraction). The following logarithmic form is used to fit the relationship between them:

(4.20) $\kappa_m = 0.060 + 0.025 \ln\left(A_c\right)$

The outlier corresponding to soil 9 (Glacial till) diverges from the fitted curve above (the open triangle with its apex upwards in Figure 4.9(d)) may be due to the overestimation of clay activity (A_c). Note that a large amount of coarse grains in soil 9 can be removed prior to performing the laboratory tests of the plasticity index according to ASTM D4318-17e1 (ASTM International 2017b).

4.4 Discussion

Figure 4.10 presents the comparison between the interpreted e_m based on MIP results and the predicted values using the proposed approach, i.e. the "as-compacted state line" (ACSL) (Eq. (4.9)) and the linear elastic constitutive model (Eq. (4.16)). Table 4.5 shows the empirical estimations of three model parameters, i.e. $e_{m,d}$, e_m^* and κ_m, using Eqs. (4.17), (4.19) and (4.20), respectively. The plot includes a total 150 data points of all the examined clayey soils (i.e. four high-plasticity clays, eight low-plasticity clays, and one coarse-grained soil with fines). In addition to the nine examined soils for developing the models in section 3, four more low-plasticity clays are added with a blind prediction (i.e. points in blue colour in Figure 4.10). Reasonably good predictions with an overall R^2 value of 0.88 are achieved except for one wetted specimen of soil 13 and the as-compacted specimens for soils 7 and 8 with high compaction water ratios. The overestimation of e_m for the wetted specimen of soil 13 may be attributed to the prolonged consolidation following saturation. The disagreements between measurements and the estimation by the ACSL (Eq. (4.9)) for high compaction water ratios can be explained as follows. The hypothesis underlying the proposed ACSL (Eq. (4.9)) is that the volumetric deformation of clay aggregates is reversible upon the compaction effort at a given compaction water ratio. In other words, the microstructural void ratio depends exclusively on the compaction water ratio for compacted clayey soils. This hypothesis is corroborated by soils with double-porosity structure which are typically compacted at the dry-of-optimum conditions (e.g., Miao et al. 2007; Alonso et al. 2013; Romero 2013). On the other hand, this assumption may not hold for soils compacted at

optimum and wet-of-optimum conditions. This is due to the possible breakage of clay aggregates and the plastic deformation of the clay paste without aggregated structures at the optimum and the wet-of-optimum conditions, respectively (Delage et al. 1996).

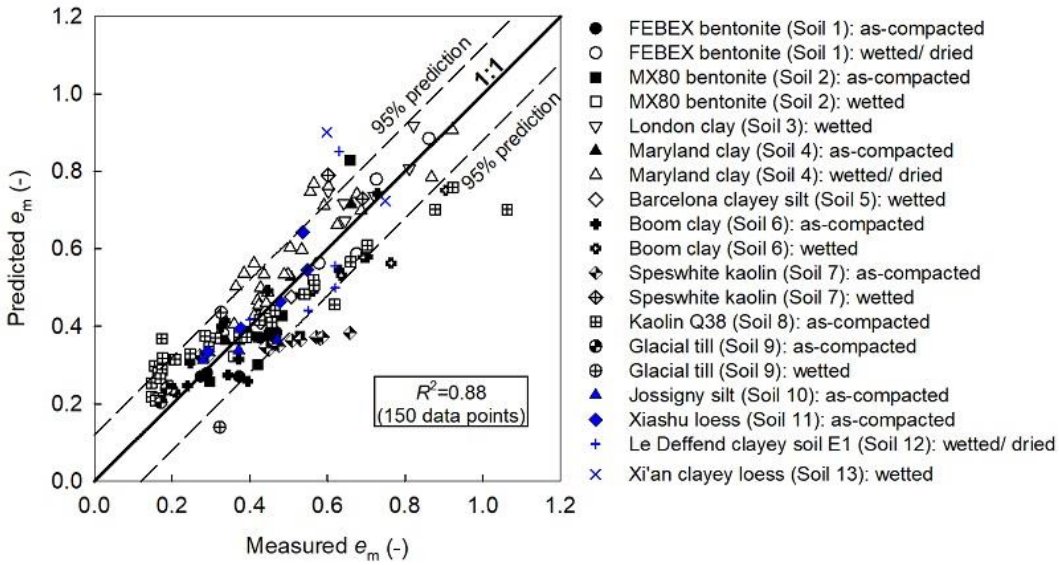

Figure 4.10 Comparison between measurements and prediction using Eqs. (4.9) and (4.16) of microstructural void ratio of as-compacted specimens and that of as-compacted specimens after wetting and drying, respectively, of all the examined soils that include a total of 150 data points.

Table 4.5 Model prediction by Eqs. (4.9) and (4.16) for the microstructural void ratio of as-compacted specimens and that of as-compacted specimens after wetting or drying paths, respectively for the examined soils.

Soil No.	Soil name	Model prediction (Eq. (4.9))		Model prediction (Eq. (4.16))
		Estimated minimal microstructural void ratio, $e_{m,d}$ (Eq. (4.17))	Estimated critical microstructural void ratio, e_m* (Eq. (4.19))	Estimated parameter controlling the microstructural stiffness, κ_m (Eq. (4.20))
1	FEBEX bentonite	0.245	0.398	0.052
2	MX80 bentonite	0.201	0.627	0.097
3	London clay	------	------	0.058
4	Maryland clay	0.197	0.383	0.053
5	Barcelona clayey silt	------	------	0.062
6	Boom clay	0.199	0.329	0.045
7	Speswhite kaolin	0.325	0.348	0.037
8	Kaolin Q38	0.185	0.305	------
9	Glacial till	0.178	0.201	0.063
10	Jossigny silt	0.221	0.279	------
11	Xiashu loess	0.121	0.273	------
12	Le Deffend clayey soil E1	------	------	0.039
13	Xi'an clayey loess	------	------	0.052

The linear elastic constitutive model (Eq. (4.16)) is examined against the interpreted MIP results of ten of the studied soils upon wetting and drying paths (Figures 4.7, 4.8, and 4.10). The discrepancy between the model predictions and the measurements of the change in microstructural void ratio (e.g., soils 7 and 8 in Figure 4.10) might be due to the following three reasons. Firstly, the derived expression of the "microstructural average skeleton stress" (Eq. (4.12)) is oversimplified. The derivation is based on the equilibrium condition of interparticle forces of double-porosity clayey soils (e.g., the dry-of-optimum as-compacted condition in Figure 4.6(a)). For the single-porosity clayey soils (e.g., the wet-of-optimum as-compacted condition), the contact states among clay particles might be different, e.g., face-to-face contacts instead of edge-to-edge or edge-to-face contacts (e.g., Hueckel 1992a). In the single-porosity clayey soils without aggregated structures, the constitutive stress relationship that is responsible for the volumetric deformation of clay particles might be different from the "microstructural average skeleton stress". Secondly, the collapse behavior (i.e. contraction in volume) of clay aggregates at loose packing state upon wetting cannot be modeled by the linear elastic constitutive model incorporating with the single constitutive stress, e.g., the reduction in e_m upon wetting of soils 3 and 4 (Figures 4.7(c) and (d)). This limitation can be partly due to the limitation of the single constitutive stress such as the one proposed in this study (i.e. Eq. (4.12)) for modelling the wetting-induced collapse behvior of unsaturated soils (e.g., Rojas et al. 2015). However, it is evident that the single constitutive stress works for most wetting paths of all the examined soils. This may be attributed to the relatively dense packing state of clay aggregates filled predominately with adsorbed water. Lastly, the effect on the volumetric deformation of clay aggregates of the macrostructural features (e.g., the relative openness of the inter-aggregate pores) is not considered. This effect can be introduced in the microstructural bulk modulus requires further investigation.

It should be pointed out that the linear elastic constitutive model (Eq. (4.16)) is only valid for the scenarios of monotonic wetting and drying paths, not including the conditions of cyclic suction loading. The irreversible volumetric deformation of clay aggregates upon suction cycles (e.g., wetting followed by drying) could be significant at least with respect to the microstructural average skeleton stress, especially for the high-plasticity clays (e.g., Figures 4.7(a) and (b)). Such a characteristic may be attributed to the irreversible modification in the microstructure upon wetting due to subdivision of clay particles containing active minerals (Seiphoori et al. 2014). This finding of irreversibility in the microstructural void ratio diverges several observations that microstructural

volume deformation is reversible (though hysteretic) after the wetting-drying cycle (e.g., Romero and Simms 2008; Romero et al. 2011).

4.5 Conclusions

The evolution of microstructural void ratio of compacted clayey soils upon drying and wetting paths is investigated by interpreting the MIP results of 13 soils, which include four high-plasticity clays, eight low-plasticity clays and one coarse-grained soil with fines. The proposed approach including the as-compacted state line (ACSL) (Eq. (4.9)) and the linear elastic constitutive model for clay aggregates (Eq. (4.16)), is capable to provide a reliable estimation of microstructure void ratio of compacted clayey soils upon monotonic wetting and drying paths (Figure 4.10). The key findings in this study are summarized below:

(1) A more reasonable criterion for identifying different pore populations of compacted clayey soils by interpreting the MIP results is suggested. Compared with the different criteria used in the literature, the suggested criterion in the present study requires the least information (i.e. the PSD or, cumulative intrusion curve) of clayey soil at a given state. The suggested criterion considers not only the PSD shape but also the influence of hydromechanical loading paths on the soil microstructure.

(2) Based on the assumption that compaction does not induce irreversible volumetric deformation of clay aggregates, the ACSL (Eq. (4.9)) of microstructural void ratio is proposed by interpreting the MIP results for seven of the examined soils. Good agreements between the predicted and measured values demonstrate that the proposed ACSL can reproduce the variation of microstructural void ratio with the compaction water ratio of both high-plasticity clays and low-plasticity clays.

(3) The constitutive stress that controls the volumetric deformation of a clay aggregate in an unsaturated condition is derived. The simplified expression (Eq. (4.12)) of the constitutive stress stems from the force equilibrium of interparticle force acting on the wavy surface through the interparticle contacts in an unsaturated clay aggregate. Thereafter, the linear elastic constitutive model (Eq. (4.16)) is examined for predicting the change in microstructural void ratio upon monotonic wetting and drying paths of eight of the examined compacted soils. The capability of

the proposed approach, (i.e. the predictive models, Eqs. (4.9) and (4.16)) together with the estimated model parameters (Eqs. (4.17), (4.19) and (4.20)) is confirmed by the high correlation (R^2 = 0.88) between the predicted and measured microstructural void ratios for all the examined soils using total 150 data points.

(4) The proposed novel approach is promising and can be used in modelling of the hydromechanical behavior of compacted clayey soils by incorporating explicitly the microstructural state variable (e.g., e_m/e_0). The estimation of microstructural evolution through the proposed models (i.e. Eqs. (4.9) and (4.16)) requires no additional microstructural studies.

4.6 Appendix

Compared with the fully saturated condition, there are two additional interparticle forces acting on unsaturated aggregates, i.e. air pressure and air-water interfacial tension (forces 7 and 8 in Figure 4.6(c)). Vertical equilibrium of interparticle forces leads to

(A.1)

$$\underset{1}{a\cdot\sigma_m}+\underbrace{\sum_{i=1}^{n}a_{c,i}\cdot U_i}_{3}+\underbrace{\sum_{i=1}^{n}a_{w,i}\cdot A}_{4}+\underbrace{T_s\cdot\sum_{i=1}^{n}\Gamma_i}_{8}=\underbrace{\sum_{i=1}^{n}a_{c,i}\cdot C_i}_{2}+\underbrace{\sum_{i=1}^{n}a_{w,i}\cdot R}_{5}+\underbrace{\sum_{i=1}^{n}a_{w,i}\cdot u_w}_{6}+\underbrace{\sum_{i=1}^{n}a_{a,i}\cdot u_a}_{7}$$

To divide all the terms by the vertical projection of the total gross area, a, Eq. (A.1) can be rewritten as

(A.2) $$\sigma_m+\frac{\sum_{i=1}^{n}a_{w,i}}{a}\cdot(A-R)+\frac{T_s\cdot\sum_{i=1}^{n}\Gamma_i}{a}=\frac{1}{a}\left(\sum_{i=1}^{n}a_{c,i}\cdot C_i-\sum_{i=1}^{n}a_{c,i}\cdot U_i\right)+\frac{\sum_{i=1}^{n}a_{w,i}}{a}\cdot u_w+\frac{\sum_{i=1}^{n}a_{a,i}}{a}\cdot u_a$$

The “skeleton stress” at microstructure level is defined as

(A.3) $$\sigma_m''=\frac{1}{a}\left(\sum_{i=1}^{n}a_{c,i}\cdot C_i-\sum_{i=1}^{n}a_{c,i}\cdot U_i\right)$$

It is evident that

(A.4) $$a = \sum_{i=1}^{n} a_{\mathrm{c,i}} + \sum_{i=1}^{n} a_{\mathrm{w,i}} + \sum_{i=1}^{n} a_{\mathrm{a,i}} = a_{\mathrm{c}} + a_{\mathrm{w}} + a_{\mathrm{a}}$$

Thus Eq. (A.2) can be rewritten as

(A.5) $$\sigma_{\mathrm{m}}'' = \sigma_{\mathrm{m}} + \frac{a_{\mathrm{w}}}{a} \cdot \left(A - R\right) - \frac{a_{\mathrm{w}}}{a} \cdot u_{\mathrm{w}} - \frac{a_{\mathrm{a}}}{a} \cdot u_{\mathrm{a}} + \frac{T_{\mathrm{s}} \cdot \sum_{i=1}^{n} \Gamma_{\mathrm{i}}}{a}$$

It is assumed that $a_{\mathrm{c}} \ll a$, which is hold true for edge-to-edge or edge-to-face contacts among clay particles. Thus, it results in $a \approx a_{\mathrm{w}} + a_{\mathrm{a}}$. The resulting expression for normal skeleton stress in clay aggregates can be simplified as

(A.6) $$\sigma_{\mathrm{m}}'' = \left(\sigma_{\mathrm{m}} - u_{a}\right) + \frac{a_{\mathrm{w}}}{a} \cdot \left(A - R\right) + \frac{a_{\mathrm{w}}}{a} \cdot \left(u_{\mathrm{a}} - u_{\mathrm{w}}\right) + \frac{T_{\mathrm{s}} \cdot \sum_{i=1}^{n} \Gamma_{\mathrm{i}}}{a}$$

Various quantitative models were proposed to evaluate the long-range attractive force (A), including van der Waals and electrostatic attraction (e.g., Ingles 1962; Anandarajah and Chen 1997). The long-range double-layer repulsion (R) is associated with the soil-water-chemical interaction (e.g., Gens and Alonso 1992; Hueckel 1992b). For coarse-grained soils, silts and low-plasticity clays, both long-range attractive force (A) and repulsive force (R) are small (Mitchell and Soga 2005), which results in (A-R) to be approximately null. For the high-plasticity clays with active clay minerals (e.g., montmorillonite), the double-layer repulsion might be remarkable at a relatively loose-packed condition. However, quantification of those two long-range interparticle forces based on macroscopic measurable quantities is beyond the present state-of-the-art knowledge. For the first approximation, the net long-range force among clay particles (A-R) is assumed zero for low-plasticity clays as well as high-plasticity clays.

The surface tension induced interparticle stress (i.e. the last term on the right-hand side of Eq. (A.6)) exists in unsaturated intra-aggregate pores. Although analytical approaches (e.g., Likos and Jaafar 2013) and empirical approaches (e.g., Yin and Vanapalli 2018) were proposed in the previous studies, the magnitude of surface tension in clay aggregates might be relatively small. Yin and Vanapalli (2018) argued that the surface tension depends on the degree of saturation and

is dominant in pendular regime (i.e. boundary effect zone). For all the examined soils, the clay aggregates are at large in capillary or funicular regime (i.e. microstructural degree of saturation, $S_{r,m} > 0.7$) except for the extremely dried specimen after compaction (e.g., after oven-drying). Therefore, the surface tension induced interparticle force is not considered hereafter.

Thus, Eq. (A.6) can be rewritten as

$$\sigma_m'' = \left(\sigma_m - u_a\right) + \frac{a_w}{a} \cdot \left(u_a - u_w\right) \quad \text{(A.7)}$$

Therefore, the constitutive stress that is regarded to control the volumetric deformation of clay aggregates can be referred as “microstructural average skeleton stress”,

$$p_m'' = \left(p_m - u_a\right) + \frac{a_w}{a} \cdot \left(u_a - u_w\right) \quad \text{(A.8)}$$

4.7 References

Airò Farulla, C., Ferrari, A. and Romero, E. 2010. Volume change behaviour of a compacted scaly clay during cyclic suction changes. Canadian Geotechnical Journal, 47(6): 688-703.

Alonso, E.E., Gens, A. and Hight, D.W. 1987. Groundwater effects in geotechnical engineering, General report. In Proceedings of the 9th European Conference on Soil Mechanics and Foundation Engineering, pp. 1087-1146.

Alonso, E.E., Gens, A. and Josa, A. 1990. A constitutive model for partially saturated soils. Géotechnique, 40(3): 405-430.

Alonso, E.E., Pereira, J.M., Vaunat, J. and Olivella, S. 2010. A microstructurally based effective stress for unsaturated soils. Géotechnique, 60(12): 913-925.

Alonso, E.E., Pinyol, N.M. and Gens, A. 2013. Compacted soil behaviour: Initial state, structure and constitutive modelling. Géotechnique, 63(6): 463-478.

Alonso, E.E., Vaunat, J. and Gens, A. 1999. Modelling the mechanical behaviour of expansive clays. Engineering geology, 54(1-2): 173-183.

Al-Mukhtar, M., Belanteur, N., Tessier, D. and Vanapalli, S.K. 1996. The fabric of a clay soil under controlled mechanical and hydraulic stress states. Applied Clay Science, 11(2-4): 99-115.

Anandarajah, A. and Chen, J. 1997. Van der Waals attractive force between clay particles in water and contaminants. Soils and Foundations, 37(2): 27-37.

ASTM International. 2017a. D2487-17 Standard Practice for Classification of Soils for Engineering Purposes (Unified Soil Classification System). West Conshohocken, PA.

ASTM International. 2017b. D4318-17e1 Standard Test Methods for Liquid Limit, Plastic Limit, and Plasticity Index of Soils. West Conshohocken, PA.

Azizi, A., Musso, G. and Jommi, C. 2020. Effects of repeated hydraulic loads on microstructure and hydraulic behaviour of a compacted clayey silt. Canadian Geotechnical Journal, 57(1): 100-114.

Bag, R. 2011. Coupled thermo-hydro-mechanical-chemical behaviour of MX80 bentonite in geotechnical applications. Doctoral dissertation, Cardiff University, UK.

Barrera, M. 2002. Estudio experimental del comportamiento hidro-mecánico de suelos colapsables. Doctoral dissertation, Universitat Politècnica de Catalunya, Spain. [in Spanish]

Bishop, A.W. 1959. The principle of effective stress. Teknisk ukeblad, 39: 859-863.

Burton, G.J. 2016. An experimental investigation of unsaturated clay: volume change and microstructural considerations. Doctoral dissertation, The University of Newcastle, Australia.

Burton, G.J., Pineda, J.A., Sheng, D. and Airey, D. 2015. Microstructural changes of an undisturbed, reconstituted and compacted high plasticity clay subjected to wetting and drying. Engineering Geology, 193: 363-373.

Chen, P. and Lu, N. 2018. Generalized Eq. for soil shrinkage curve. Journal of Geotechnical and Geoenvironmental Engineering, 144(8): p.04018046.

Cheng, Q., Tang, C.S., Zeng, H., Zhu, C., An, N. and Shi, B. 2020. Effects of microstructure on desiccation cracking of a compacted soil. Engineering Geology, 265: p.105418.

Collins, K.T. and McGown, A. 1974. The form and function of microfabric features in a variety of natural soils. Géotechnique, 24(2): 223-254.

Cuisinier, O. and Laloui, L. 2004. Fabric evolution during hydromechanical loading of a compacted silt. International Journal for Numerical and Analytical Methods in Geomechanics, 28(6): 483-499.

Delage, P., Audiguier, M., Cui, Y.J. and Howat, M.D. 1996. Microstructure of a compacted silt. Canadian Geotechnical Journal, 33(1): 150-158.

Delage, P. and Lefebvre, G. 1984. Study of the structure of a sensitive Champlain clay and of its evolution during consolidation. Canadian Geotechnical Journal, 21(1): 21-35.

Delage, P., Marcial, D., Cui, Y.J. and Ruiz, X. 2006. Ageing effects in a compacted bentonite: a microstructure approach. Géotechnique, 56(5): 291-304.

Delage, P. and Pellerin, F.M. 1984. Influence de la lyophilisation sur la structure d'une argile sensible du Québec. Clay minerals, 19(2): 151-160. [in French]

Della Vecchia, G., Dieudonné, A.C., Jommi, C. and Charlier, R. 2015. Accounting for evolving pore size distribution in water retention models for compacted clays. International Journal for Numerical and Analytical Methods in Geomechanics, 39(7): 702-723.

Della Vecchia, G., Jommi C. and Romero, E. 2013. A fully coupled elastic–plastic hydromechanical model for compacted soils accounting for clay activity. International Journal for Numerical and Analytical Methods in Geomechanics, 37(5): 503-535.

Dewhurst, D.N., Aplin, A.C., Sarda, J.P. and Yang, Y. 1998. Compaction-driven evolution of porosity and permeability in natural mudstones: An experimental study. Journal of Geophysical Research: Solid Earth, 103(B1): 651-661.

Di Sante, M., Fratalocchi, E., Mazzieri, F. and Pasqualini, E. 2014. Time of reactions in a lime treated clayey soil and influence of curing conditions on its microstructure and behaviour. Applied Clay Science, 99: 100-109.

Diamond, S. 1970. Pore size distributions in clays. Clays and Clay Minerals, 18(1): 7-23.

Dieudonné, A.C., Della Vecchia, G., Charlier, R. and Jommi, C. 2014. Influence of microfabric evolution on the retention behaviour of compacted clayey soils. In Proceedings of the 6th International Conference on Unsaturated Soils (eds. N. Khalili, A.R. Russell, and A. Khoshghalb), Sydney, Australia.

Gallipoli, D., Gens, A., Sharma, R. and Vaunat, J. 2003. An elasto-plastic model for unsaturated soil incorporating the effects of suction and degree of saturation on mechanical behaviour. Géotechnique, 53(1): 123-135.

Ge, M., Pineda, J.A., Sheng, D., Burton, G.J. and Li, N. 2019. Collapse behaviour of compacted loess: role of the stress level on soil microstructure. Japanese Geotechnical Society Special Publication, 7(2): 209-214.

Gens, A. 2010. Soil–environment interactions in geotechnical engineering. Géotechnique, 60(1): 3-74.

Gens, A. and Alonso, E.E. 1992. A framework for the behaviour of unsaturated expansive clays. Canadian Geotechnical Journal, 29(6): 1013-1032.

Houlsby, G.T. 1997. The work input to an unsaturated granular material. Géotechnique, 47(1): 193-196.

Hu, R., Chen, Y.F., Liu, H.H. and Zhou, C.B. 2013. A water retention curve and unsaturated hydraulic conductivity model for deformable soils: consideration of the change in pore-size distribution. Géotechnique, 63(16): 1389-1405.

Hueckel, T. 1992a. On effective stress concepts and deformation in clays subjected to environmental loads: Discussion. Canadian Geotechnical Journal, 29(6): 1120-1125.

Hueckel, T.A. 1992b. Water–mineral interaction in hygromechanics of clays exposed to environmental loads: a mixture-theory approach. Canadian Geotechnical Journal, 29(6): 1071-1086.

Ingles, O.G. 1962. A theory of tensile strength for stabilized and naturally coherent soils. In Proceedings of 1st Conference of the Australian Road Research Board, Vol. 1, pp. 1025-1047.

Juang, C.H. and Holtz, R.D. 1986. A probabilistic permeability model and the pore size density function. International Journal for Numerical and Analytical Methods in Geomechanics, 10(5): 543-553.

Koliji, A., Vulliet, L. and Laloui, L. 2010. Structural characterization of unsaturated aggregated soil. Canadian Geotechnical Journal, 47(3): 297-311.

Lambe, T.W. 1958. The engineering behavior of compacted clay. Journal of the Soil Mechanics and Foundations Div., 84(2): 1-35.

Lambe, T.W. and Whitman, R.V. 1979. Soil Mechanics, SI Version. John Wiley and Sons, New York.

Li, P., Shao, S. and Vanapalli, S.K. 2020. Characterizing and modeling the pore-size distribution evolution of a compacted loess during consolidation and shearing. Journal of Soils and Sediments, https://doi.org/10.1007/s11368-020-02621-3.

Li, X., Zhang, L.M. and Wu, L.Z. 2014. A framework for unifying soil fabric, suction, void ratio, and water content during the dehydration process. Soil Science Society of America Journal, 78(2): 387-399.

Likos, W.J. and Jaafar, R. 2013. Pore-scale model for water retention and fluid partitioning of partially saturated granular soil. Journal of Geotechnical and Geoenvironmental Engineering, 139(5): 724-737.

Liu, X., Buzzi, O., Yuan, S., Mendes, J. and Fityus, S. 2016. Multi-scale characterization of retention and shrinkage behaviour of four Australian clayey soils. Canadian Geotechnical Journal, 53(5): 854-870.

Lloret, A., Romero, E. and Villar, M.V. 2005. FEBEX II Project: Final report on thermo-hydro-mechanical laboratory tests (No. ENRESA--10/04). Centro De Investigaciones Energeticas.

Lloret, A., Villar, M.V., Sanchez, M., Gens, A., Pintado, X. and Alonso, E.E. 2003. Mechanical behaviour of heavily compacted bentonite under high suction changes. Géotechnique, 53(1): 27-40.

Lu, N. and Likos, W.J. 2006. Suction stress characteristic curve for unsaturated soil. Journal of Geotechnical and Geoenvironmental Engineering, 132(2): 131-142.

Mašín, D. 2013. Double structure hydromechanical coupling formalism and a model for unsaturated expansive clays. Engineering Geology, 165: 73-88.

Merchán, V. 2011. Small strain stiffness and residual strength of unsaturated Boom clay: a microstructural insight. Doctoral dissertation, Universitat Politècnica de Catalunya, Spain.

Miao, L., Houston, S.L., Cui, Y. and Yuan, J. 2007. Relationship between soil structure and mechanical behavior for an expansive unsaturated clay. Canadian Geotechnical Journal, 44(2): 126-137.

Mitchell, J.K., Hooper, D.R. and Campenella, R.G. 1965. Permeability of compacted clay. Journal of the Soil Mechanics and Foundations Div., 91(4): 41-66.

Mitchell, J.K. and Soga, K. 2005. Fundamentals of Soil Behavior (3rd edition). John Wiley and Sons, New York.

Monroy, R., Zdravkovic, L. and Ridley, A. 2010. Evolution of microstructure in compacted London Clay during wetting and loading. Géotechnique, 60(2): 105-119.

Ng, C.W.W., Sadeghi, H., Hossen, S.B., Chiu, C.F., Alonso, E.E. and Baghbanrezvan, S. 2016. Water retention and volumetric characteristics of intact and re-compacted loess. Canadian Geotechnical Journal, 53(8): 1258-1269.

Nguyen, V., Pineda J.A., Romero, E. and Sheng, D. 2020. Influence of soil microstructure on air permeability in compacted clay. Géotechnique, https://doi.org/10.1680/jgeot.18.P.186.

Nowamooz, H. and Masrouri, F. 2010. Relationships between soil fabric and suction cycles in compacted swelling soils. Engineering Geology, 114(3-4): 444-455.

Pedrotti, M. 2016. An experimental investigation on the micromechanics of non-active clays in saturated and partially saturated states. Doctoral dissertation, University of Strathclyde, UK.

Pedrotti, M. and Tarantino, A. 2018. An experimental investigation into the micromechanics of non-active clays. Géotechnique, 68(8): 666-683.

Penumadu, D. and Dean, J. 2000. Compressibility effect in evaluating the pore-size distribution of kaolin clay using mercury intrusion porosimetry. Canadian Geotechnical Journal, 37(2): 393-405.

Pérez Canals, M.C. 2013. Residual strength of compacted boom clay: dependency on stress, suction and microstructure. Master's thesis, Universitat Politècnica de Catalunya, Spain.

Qiao, Y., Xiao, Y., Laloui, L., Ding, W. and He, M. 2019. A double-structure hydromechanical constitutive model for compacted bentonite. Computers and Geotechnics, 115: p.103173.

Robinet, J.C., Rahbaoui, A., Plas, F. and Lebon, P. 1996. A constitutive thermomechanical model for saturated clays. Engineering Geology, 41(1-4): 145-169.

Rojas, E., Pérez-Rea, M.L., López-Lara, T., Hernández, J.B. and Horta, J. 2015. Use of effective stresses to model the collapse upon wetting in unsaturated soils. Journal of Geotechnical and Geoenvironmental Engineering, 141(5): p.04015007.

Romero, E. 1999. Characterisation and thermo-hydro-mechanical behaviour of unsaturated Boom clay: An experimental study. Doctoral dissertation. Universitat Politècnica de Catalunya, Spain.

Romero, E. 2013. A microstructural insight into compacted clayey soils and their hydraulic properties. Engineering Geology, 165: 3-19.

Romero, E., Della Vecchia, G. and Jommi, C. 2011. An insight into the water retention properties of compacted clayey soils. Géotechnique, 61(4): 313-328.

Romero, E., Gens, A. and Lloret, A. 1999. Water permeability, water retention and microstructure of unsaturated compacted Boom clay. Engineering Geology, 54(1-2): 117-127.

Romero, E. and Simms, P.H. 2008. Microstructure investigation in unsaturated soils: a review with special attention to contribution of mercury intrusion porosimetry and environmental scanning electron microscopy. Geotechnical and Geological Engineering, 26(6): 705-727.

Romero, E., Vaunat, J. and Merchán, V. 2014. Suction effects on the residual shear strength of clays. Journal of Geo-Engineering Sciences, 2(1-2): 17-37.

Samingan, A.S. 2005. An experimental study on hydro-mechanical characteristics of compacted bentonite-sand mixtures. Doctoral dissertation. Bauhaus-Universität Weimar, Germany.

Sánchez, M., Gens, A., do Nascimento Guimarães, L. and Olivella, S. 2005. A double structure generalized plasticity model for expansive materials. International Journal for Numerical and Analytical Methods in Geomechanics, 29(8): 751-787.

Schrefler B.A. 1984. The finite element method in soil consolidation: with application to surface subsidence. Doctoral dissertation, Swansea University, UK.

Seiphoori, A., Ferrari, A. and Laloui, L. 2014. Water retention behaviour and microstructural evolution of MX-80 bentonite during wetting and drying cycles. Géotechnique, 64(9): 721-734.

Simms, P.H. and Yanful, E.K. 2001. Measurement and estimation of pore shrinkage and pore distribution in a clayey till during soil-water characteristic curve tests. Canadian Geotechnical Journal, 38(4): 741-754.

Simms, P.H. and Yanful, E.K. 2005. A pore-network model for hydromechanical coupling in unsaturated compacted clayey soils. Canadian Geotechnical Journal, 42(2): 499-514.

Sun, H., Mašín, D., Najser, J., Neděla, V. and Navrátilová, E. 2019. Bentonite microstructure and saturation evolution in wetting–drying cycles evaluated using ESEM, MIP and WRC measurements. Géotechnique, 69(8): 713-726.

Sun, W.J. and Cui, Y.J. 2018. Investigating the microstructure changes for silty soil during drying. Géotechnique, 68(4): 370-373.

Tarantino, A. 2010. Unsaturated soils: Compacted versus reconstituted states. In Proceeding of the 5th International Conference on Unsaturated Soil (eds E.E. Alonso and A. Gens), pp. 113-136.

Tarantino, A. and De Col, E. 2008. Compaction behaviour of clay. Géotechnique, 58(3): 199-213.

Tarantino, A. and De Col, E. 2009. Compaction behaviour of clay: Authors' reply to discussion by P. Delage. Géotechnique, 59(1): 75-77.

Thom, R., Sivakumar, R., Sivakumar, V., Murray, E.J. and Mackinnon, P. 2007. Pore size distribution of unsaturated compacted kaolin: The initial states and final states following saturation. Géotechnique, 57(5): 469-474.

Trabelsi, H., Romero, E. and Jamei, M. 2018. Tensile strength during drying of remoulded and compacted clay: The role of fabric and water retention. Applied Clay Science, 162: 57-68.

Tripathy, S., Bag, R., Thomas, H.R., Alonso, E.E. and Gens, A. 2010. Desorption and consolidation behaviour of initially saturated clays. In Proceedings of the 5th International Conference on Unsaturated Soils (eds E.E. Alonso and A. Gens), Vol. 1, pp. 381-386.

Vanapalli, S.K., Fredlund, D.G., Pufahl, D.E. and Clifton, A.W. 1996. Model for the prediction of shear strength with respect to soil suction. Canadian Geotechnical Journal, 33(3): 379-392.

Villar, M. 2001. Caracterización termo-hidro-mecánica de una bentonita de Cabo de Gata. Doctoral dissertation, Universidad Complutense de Madrid, Spain. [in Spanish]

Villar, M.V., Campos, G., Gutiérrez-Nebot, L. and Arroyo, X. 2019. Effect of prolonged drying at high temperature on the water retention capacity of bentonite (FEBEX-DP samples). Applied Clay Science, https://doi.org/10.1016/j.clay.2019.105290.

Villar Galicia, M.V. and Lloret Morancho, A. 2018. Bentonite strain due to cyclic suction changes. In Proceedings of the 7th International Conference on Unsaturated Soils, Hong Kong, China, pp. 557-562.

Wang, Q., Cui, Y.J., Tang, A.M., Barnichon, J.D., Saba, S. and Ye, W.M. 2013. Hydraulic conductivity and microstructure changes of compacted bentonite/sand mixture during hydration. Engineering Geology, 164: 67-76.

Wang, Q., Cui, Y.J., Tang, A.M., Xiang-Ling, L. and Wei-Min, Y. 2014. Time-and density-dependent microstructure features of compacted bentonite. Soils and Foundations, 54(4): 657-666.

Washburn, E.W. 1921. Note on a method of determining the distribution of pore sizes in a porous material. In Proceedings of the National Academy of Sciences of the United States of America, 7(4): 115-116.

Xu, J., Ren, J., Wang, Z., Wang, S. and Yuan, J. 2018. Strength behaviors and meso-structural characters of loess after freeze-thaw. Cold Regions Science and Technology, 148: 104-120.

Yin, P. and Vanapalli, S.K. 2018. Model for predicting tensile strength of unsaturated cohesionless soils. Canadian Geotechnical Journal, 55(9): 1313-1333.

Yuan, S., Liu, X. and Buzzi, O. 2019. Technical aspects of mercury intrusion porosimetry for clays. Environmental Geotechnics, https://doi.org/10.1680/jenge.16.00039.

Yuan, S., Liu, X., Sloan, S.W. and Buzzi, O.P. 2016. Multi-scale characterization of swelling behaviour of compacted Maryland clay. Acta Geotechnica, 11(4): 789-804.

Zhang, F., Cui, Y.J. and Ye, W.M. 2018. Distinguishing macro-and micro-pores for materials with different pore populations. Géotechnique Letters, 8(2): 102-110.

Zhang, X., Mavroulidou, M. and Gunn, M.J. 2017. A study of the water retention curve of lime-treated London Clay. Acta Geotechnica, 12(1): 23-45.

Chapter 5. Geological and Geotechnical Characteristics of the Investigated Soil

5.1 Origin and composition of the studied soil

5.1.1 Geological origin and climate conditions

The soil used in the present study is Indian Head till (IHT) which is collected from Indian Head, Saskatchewan, Canada. Indian Head till has been extensively studied at the University of Saskatchewan and University of Ottawa (e.g., Lau 1987, Vanapalli 1994, Vanapalli et al. 1996, 1999, Infante Sedano 2006, Oh 2012, Han 2016, and Ren 2019).

The Quaternary period in southern Saskatchewan (Figure 5.1(a)) was associated with a series of glacial events that were responsible for erosion of the Cretaceous and Tertiary rocks and their subsequent deposition to form the indigenous glacial drift. All sediments between the bedrock surface and the present surface are termed “drift”, the thickness of which ranges from about 80 to 150 m in Indian Head region. The bedrock that directly underlies the drift is composed of thick, soft, gray noncalcareous silt and clay which was deposited in a shallow sea and has not been consolidated into solid “rock”. These shales belong to the Riding Mountain Formation (also referred to as the Pierre Shale) in the eastern part of the area and Bearpaw Shale in the western part (Staff, Saskatchewan Soil Survey 1986). The Judith River Formation, a thin silt unit, and the Lea Park and Upper Colorado Group occur beneath the Bearpaw Formation. The drift consists of the following three groups from older to younger (Staff, Saskatchewan Soil Survey 1986; Christiansen and Saure 2002): Empress group (gravel and sand), Sutherland group (till and stratified deposits), and Saskatoon group (till, gravel, sand, silt, and clay). Alternate scraping, deposition, overburdening, and reworking of materials by up to seven glacial advances and retreats resulted in extensive particle disintegration. The current surface soils in Saskatchewan formed during the last glaciation known as the Wisconsinan (i.e. 23,000 years before the present (B.P.) to 17,000 years B.P (Ito and Azam 2013)). The ice sheet started to retreat in the northeastward direction around 17,000 years B.P. The rate of ice meltdown was initially about 60 m/year and gradually increased to 275 m/year in the final stages, which was completed around 8,000 years B.P. when the essential feature of the present landform emerged including moraines (a raised ground covering of unsorted till) and eskers (a long winding ridge of sorted sands and gravel)

(Mollard et al. 1998). These ground features bounded the proglacial Regina Lake where fine-grained soils gradually settled at the basin floor during the Wisconsinan to develop a homogeneous clay deposit of up to 12 m depth. Subsequent wet-dry and freeze-thaw cycles, alluvial and fluvial transportation processes and the presence of salt-forming ions further modified the deposit during the postglacial period.

Figure 5.1 (b) shows the generalized geological maps of the Indian Head municipality. Indian Head town (50°32’ N, 103°40’ W) falls within the semi-arid climate zone. At Indian Head town, the daily temperature average -14.8 °C in January and 18.2 °C in July, according to the online data of Environment Canada. The annual average precipitation is 428.4 mm, most of which occurs from May to August. The seasonal variations in water availability (snow melt in spring and rainfall in summer) and water deficiency (low rainfall and freezing in fall and winter) result in periodic swelling and shrinkage of the glacio-lacustrine clay deposits in southern Saskatchewan.

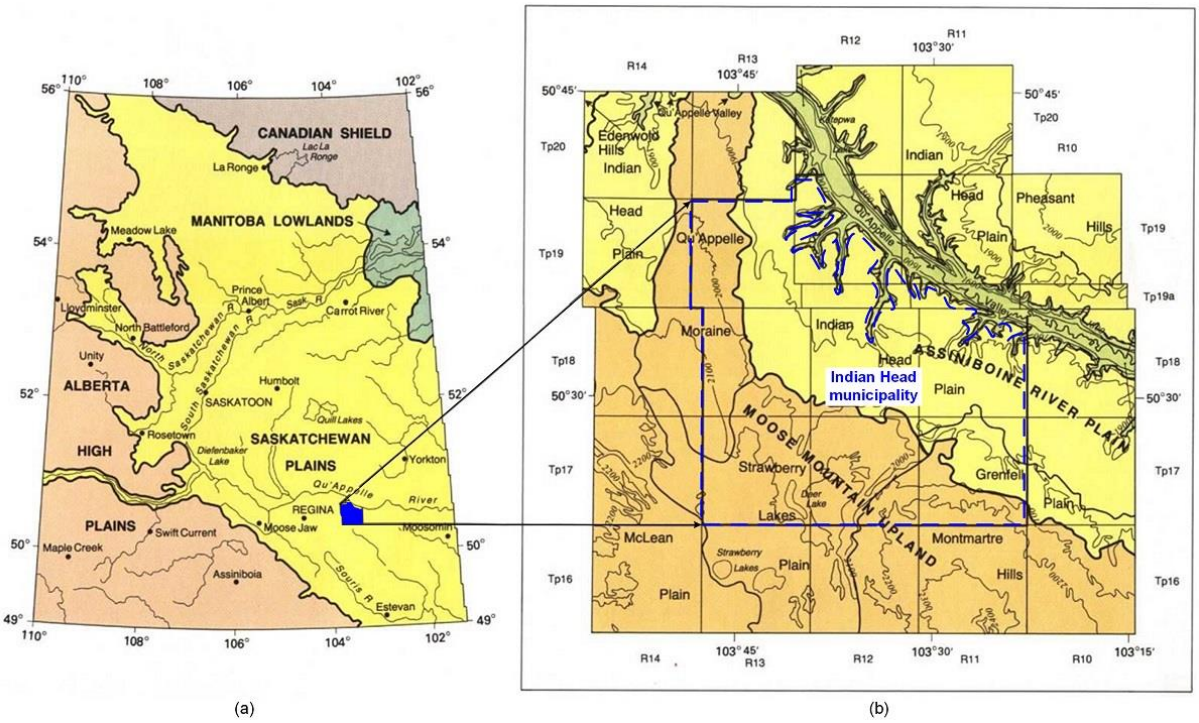

Figure 5.1 Illustration of (a) A physiographic map of southern Saskatchewan (adapted from Staff, Saskatchewan Soil Survey 1986); (b) the geological map of the Indian Head municipality (adapted from Staff, Saskatchewan Soil Survey 1986).

5.1.2 X-ray diffraction (XRD) and X-ray fluorescence (XRF)

The fundamental application of the X-ray diffraction (XRD) technique is for qualitative identification of mineralogical composition of a crystalline sample (e.g., Lakshmikantha 2009). Diffraction effects are observed when electro-magnetic radiation impinges on periodic structures with geometrical variations on the length scale of the wavelength of the radiation. The inter-atomic distances in crystals and molecules amounts to 0.15-0.4 nm which correspond to the electro-magnetic spectrum with the wavelength of X-ray having photon energies between 3 and 8 keV. The phenomenon such as the constructive and destructive interference should become observable when crystalline and molecular structures are exposed to X-rays. XRD is one of the most used methods for the identification of minerals in fine-grained soils (i.e. crystalline phase identification) which is performed by comparison of the diffraction pattern with that of a known substance or by search-match analysis using a database such as the International Center for Diffraction Database (ICDD).

The equipment used in the present study is the commercially available Rigaku Ultimate IV Diffractometer at X-ray Core Facility, University of Ottawa. For this diffractometer, a general-purpose theta-theta system with a cooper source and one diffraction beam monochromator that can be used with either focused beam or parallel beam geometries. The system is configured for use of either fixed or variable slit widths; the latter facilitating data measurement at low angles. A small-angle X-ray scattering (SAXS) attachment is used for determining particle/pore size of a nanomaterial (1-100 nm) in transmission mode. A micro area stage and microscope allow for x-y mapping of a sample by scanning various x-y positions with very small beam sizes using a specially designed selection slit. The *Cu K-*α radiation is used as the X-ray energy source with the energy of 8.04 keV which corresponds to an X-ray wavelength of 1.5406 Å. The 2θ measurement ranges from -3° to 162° with a minimum step size of 0.0001°. In the present study, the representative samples of collected Indian Head till and Regina clay are left to dry in air and sieved with No. 200 sieve (75 μm opening) and then pulverized for XRD testing. The X-ray scans with a starting value of $2\theta = 5°$ and ending up with 75°, with a step magnitude of 0.02°. The pulverized particles are randomly oriented in all directions assuring that at least some will be oriented with respect to the X-ray beams. A characteristic set of continuous reflection was produced at various values of θ (angle of the diffracted X-ray) corresponding to the basal spacing of the prominent

planes. According to Bragg's law (e.g., Meyers and Myers 1997), the spacing of basal planes (d) and the angle (θ) at which the diffraction occurs are correlated as

(5.1) $2d\sin\theta = n\lambda$

where n is a positive integer, and λ is the wavelength of the X-ray (i.e. 1.5406 Å in the present XRD tests). Hence, the angle θ can be used for the identification of the minerals, because every type of mineral has its specific spacing of basal planes (d). The resulting diffraction pattern is like a "finger print" of the crystalline components. Figure 5.2 shows the XRD results of Indian Head till. The mineralogical composition of Indian Head till consists predominantly of the following minerals; namely, Quartz, Dolomite, Iron magnesium catena-disilicate, Enstatite ferroan, Albite, and Serpentine (Lizardite, Chrysotile) (Table 5.1), which are confirmed with the help of the data files presented by the Joint Committee on Powder Diffraction Standards (JCPDS, 1994).

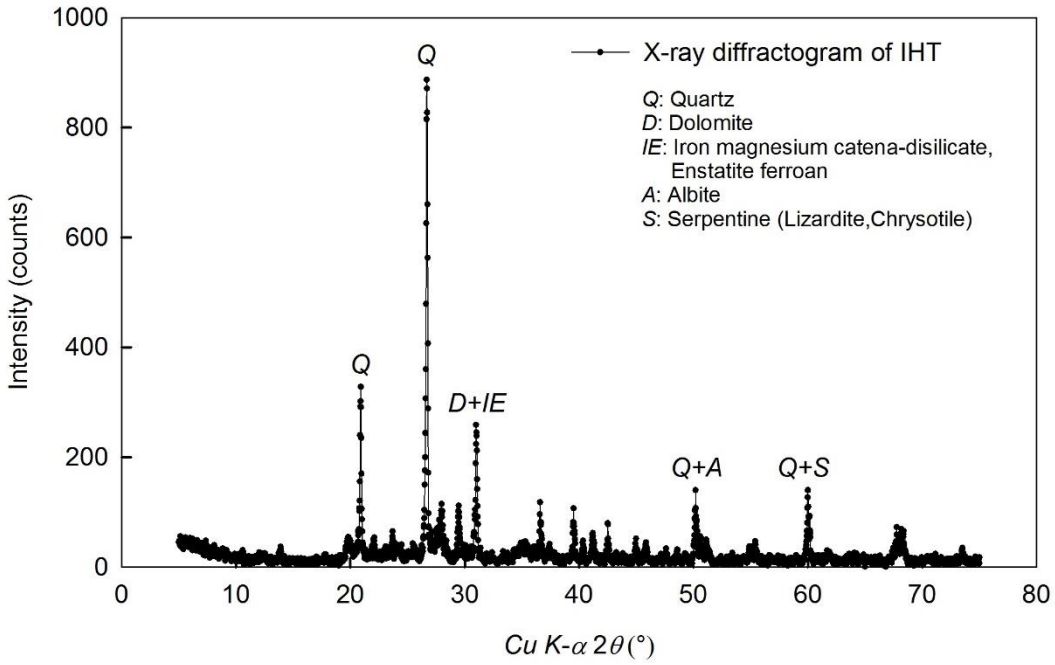

Figure 5.2 The X-ray diffraction result of Indian Head till.

X-ray fluorescence (XRF) is a non-destructive analytical technique used to identify and determine the elemental composition of materials. XRF analyzers determine the chemistry of a sample by measuring the fluorescent (or secondary) X-ray emitted from a sample when it is excited by a primary X-ray source. Each of the elements present in a sample produces a set of characteristic fluorescent X-rays that is unique for that specific element, which is why XRF spectroscopy is an

excellent technology for qualitative and quantitative analysis of material composition. It can measure elemental concentrations ranging from a few ppm to nearly 100%. Wavelength dispersive X-ray fluorescence (WDXRF) is extremely popular in the geological field and is often used for measuring raw minerals, and finished products composed of minerals. The samples analysis in the present study is performed on a Rigaku Supermini200 benchtop sequential wavelength-dispersive spectrometer at X-ray Core Facility, University of Ottawa, equipped with a 200 W Pd-anode X-ray tube. A combination of two analyzing crystals, and scintillation and flow proportional detectors permit analysis of all elements from Sodium (Na) to Uranium (U) in the periodic table. In the present study, the representative samples of collected Indian Head till and Regina clay are left to dry in air and then pulverized for XRF testing, without passing through the No. 200 sieve for sample preparation. The loss of ignition (LOI), which is assumed to mainly consist of adsorbed water, is determined under 1050 °C for one hour as well. Table 5.2 lists the chemical composition of Indian Head till determined by XRF.

Figure 5.3 Photos of Tescan Vega-II XMU (a) and JEOL JSM-6610LV (b), respectively.

Table 5.1 Details of XRD results of Indian Head till.

Phase No.	Phase 1	Phase 2	Phase 3	Phase 4	Phase 5	Phase 6	Phase 7	Phase 8
Phase Name	Quartz	Dolomite	Calcite	Albite	Muscovite	Iron magnesium catena-disilicate, Enstatite-ferroan	Polyhalite	Serpentine (Lizardite, Chrysotile)
Chemical Formula	SiO_2	$CaMg(CO_3)_2$	$CaCO_3$	$NaAlSi_3O_8$	$(K_{0.95}\,Na_{0.05})\,(Al_{0.76}\,Fe_{0.14}\,Mg_{0.10})_2\,(Si_{3.25}\,Al_{0.75})\,O_{10}\,((OH)_{1.96}\,F_{0.04})$	$(Fe_{0.084}\,Mg_{0.916})\,(Fe_{0.414}\,Mg_{0.586})\,Si_2O_6$	$K_2Ca_2Mg(SO_4)_4{\cdot}2H_2O$	$Mg_3Si_2O_5(OH)_4$
JCPDS File No.	00-033-1161	01-075-3686	01-086-2334	01-089-6427	01-074-2773	01-083-0667	00-021-0982	01-077-5040
SYMBOL (in Figure 5.2)	Q	D	C	A	M	IE	P	S

Table 5.2 Chemical composition (in percentage by weight) of the Indian Head till specimen.

Chemical composition	Indian Head till (IHT)
Na_2O (%)	1.291
MgO (%)	3.73
Al_2O_3 (%)	9.896
SiO_2 (%)	59.425
P_2O_5 (%)	0.088
K_2O (%)	1.827
CaO (%)	6.877
TiO_2 (%)	0.43
MnO (%)	0.077
Fe_2O_3 (%)	3.698
V (ppm*)	56
Cr (ppm)	42
Ni (ppm)	70†
Cu (ppm)	132†
Zn (ppm)	74
Rb (ppm)	73
Sr (ppm)	193
Zr (ppm)	226
Co (ppm)	9
Y (ppm)	19
Nb (ppm)	7
Ba (ppm)	1277
Ce (ppm)	0
Pb (ppm)	48†
Th (ppm)	27†
U (ppm)	10†
S (ppm)	609†
La (ppm)	26
LOI (loss of ignition, %)	11.11
Total percent (%)	98.74

Note: *1 ppm = 1×10^{-4}%; †approximate values.

5.1.3 Scanning Electron Microscope (SEM)

With the advent of modern microstructural testing techniques, such as Environmental Scanning Electron Microscopy (ESEM) and Mercury Intrusion Porosimetry (MIP), the microstructural characteristic of soils is gaining prominence. For example, the microstructural observation of compacted soils subjected to different hydro-mechanical paths (e.g., Delage and Lefebvre 1984; Delage et al. 1996; Simms and Yanful 2001; Koliji et al. 2010; Romero et al. 2011) has provided new insight into the link between hydraulic and mechanical behavior and the fabric in compacted soils and promoted the development of microstructure based constitutive models (e.g., Simms and Yanful 2005; Della Vecchia et al. 2013; Mašín 2013; Qiao et al. 2019). Scanning Electron

Microscope (SEM) uses a focused beam of high-energy electrons to generate a variety of signals at the surface of solid specimens. The signals that derive from electron-sample interactions directly reveal information about the sample including external morphology (texture), chemical composition, and crystalline structure and orientation of materials making up the sample. In most applications, data are collected over a selected area of the surface of the sample, and a two-dimensional image is generated that displays spatial variations in these properties. Areas ranging from approximately 10 mm to 5 μm in width can be imaged in a scanning mode using conventional SEM techniques (magnification ranging from 20X to approximately 30000X, spatial resolution of 50 to 100 nm). The historical developments for SEM along with its application to clay minerals and aggregates examination are available in McHardy and Birnie (1987). In the present study, the microstructural characteristics of Indian Head till and Regina clay at remoulded and compacted states are investigated by Scanning Electron Microscope (SEM) and Mercury Intrusion Porosimetry (MIP) techniques. The SEM facilities used are Tescan Vega-II XMU at Carleton University and JEOL JSM-6610LV at University of Ottawa. The photos and specifications of these two SEM facilities are illustrated in Figure 5.3 and Table 5.3.

Table 5.3 Specifications of the SEM facilities used in the present studies.

Specifications	Tescan Vega-II XMU	JEOL JSM-6610LV
Resolution	3 nm (30 kV, high vacuum mode); 3.5 nm (30 kV, low vacuum mode)	3 nm (30 kV, high vacuum mode); 4 nm (30 kV, low vacuum mode)
Magnification	3X – 500,000X	5X – 300,000X
Accelerating voltage	0.2 kV – 30 kV	0.3 kV – 30 kV
Electron gun	Tungsten heated cathode	Fully automated, manual override
Maximum specimen size	20 mm in diameter	200 mm in diameter
Elemental analysis	Oxford Inca Energy 250X EDS	Oxford Inca large area SDD EDS
Cold stage	Available	Not available

The SEM requires an evacuated sample chamber (e.g., 10 Pa for low vacuum, and 10^{-3} Pa for high vacuum), so wet soil specimens cannot be studied directly unless they are housed in a special chamber (Mitchell and Soga 2005). It is usually necessary to coat SEM sample surfaces with a conducting film to prevent surface charging and loss of resolution. Gold placed in a very thin layer (20 to 30 nm) in a vacuum evaporator is often used. The main difficulty in the SEM study of soil fabric is the preparation of sample surfaces, surface replicas, or ultra-thin sections that retain the undisturbed fabric of the original soil specimen. In general, the higher the water content and void ratio of the original soil specimen, the greater the likelihood of disturbance. Soil containing

expansive clay minerals may undergo changes in microfabric as a result of removal of interlayer water, or there may be shrinkage (Mitchell and Soga 2005). The dry-fracture-peel technique (e.g., Tovey and Yan 1973) and the freeze-fracture technique (e.g., Delage et al. 1982) are the best of the available methods for obtaining representative specimen surfaces. In order to minimize the disturbance to the microstructure of the original specimens during the preparation of the specimen surfaces, two methods are adopted: (i) freeze-fracture technique (FF) for Tescan Vega-II XMU due to the availability of cold stage, and (ii) freeze-dry-fracture-peel technique (FDFP) for JEOL JSM-6610LV. The difference in the phase change of soil water for these two preparation methods are demonstrated by Figure 5.4.

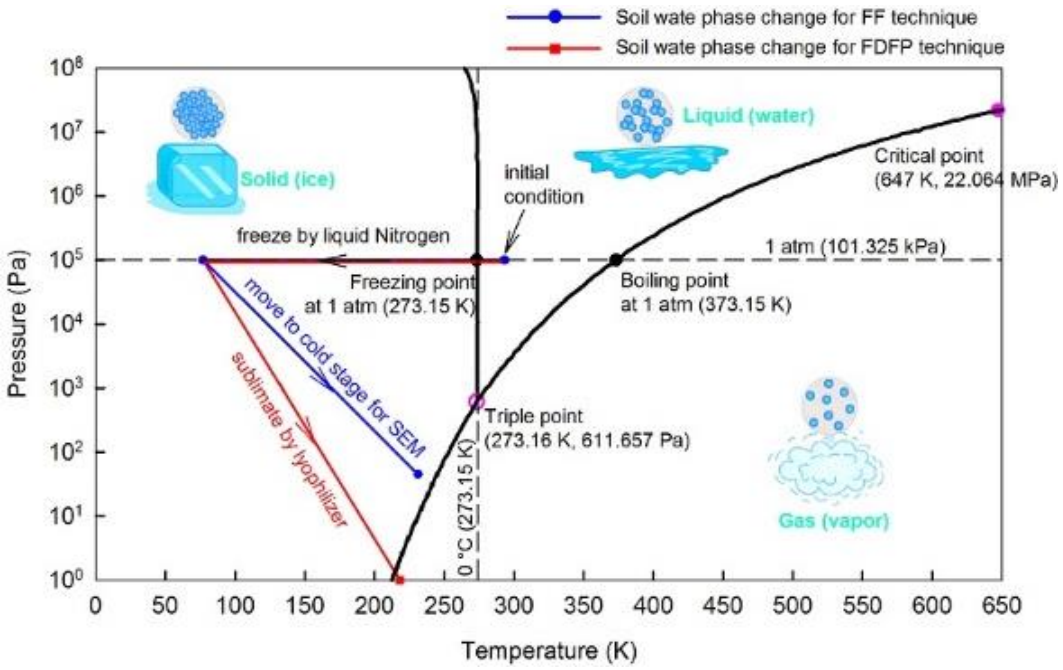

Figure 5.4 Illustration of the phase change of soil water on the water phase diagram (modified after Balmer 1990) for two different specimen preparation methods (i.e., FF technique, and FDFP technique).

According to intensive studies reported in the literature (e.g., Delage and Lefebvre 1984; Cui 1993; Vanapalli et al. 1999; Cuisinier and Laloui 2004; Monroy et al. 2010; Simms et al. 2017; Sun et al. 2019), soil microstructure is influenced by various factors, such as soil type (e.g., coarse-grained soil, fine-grained soil), preparation method (e.g., remoulded soil, or compacted soil), water content (e.g., dry of optimum, or wet of optimum), stress history (e.g., normal consolidated, or over-consolidated) and stress state (e.g., traction-free, or isotropic/ triaxial loading). In the present studies, the effects on the soil microstructure of soil type, preparation method, and water content

are investigated. Table 5.4 presents the initial states and specimen preparation methods of Indian Head till for SEM tests. For providing comparisons, the SEM images with different preparation methods are presented together (i.e. Figures 5.5, 5.6, 5.7, and 5.8).

Table 5.4 Soil initial states of Indian Head till for performing SEM tests.

Specimen ID	Original specimen formation	Compaction water content, dry density/ Water content, preconsolidation pressure (initial water content)	Preparation methods for SEM test	Figure No.
IHT-C-W	Compacted (static)	18.4%, $0.95\rho_{d,max}$	Freezing (i.e. FF technique); Freezing-dry (i.e. FDFP technique)	Figure 5.5
IHT-C-D	Compacted (static)	12.2%, $0.95\rho_{d,max}$	Freezing (i.e. FF technique); Freezing-dry (i.e. FDFP technique)	Figure 5.6
IHT-R-800	Reconstituted	17.4%, 800 kPa (35.1%)	Freezing (i.e. FF technique); Freezing-dry (i.e. FDFP technique)	Figure 5.7
IHT-R-800-O	Reconstituted	17.4%, 800 kPa (35.1%)	Oven-dry at 35 °C for seven days	Figure 5.8

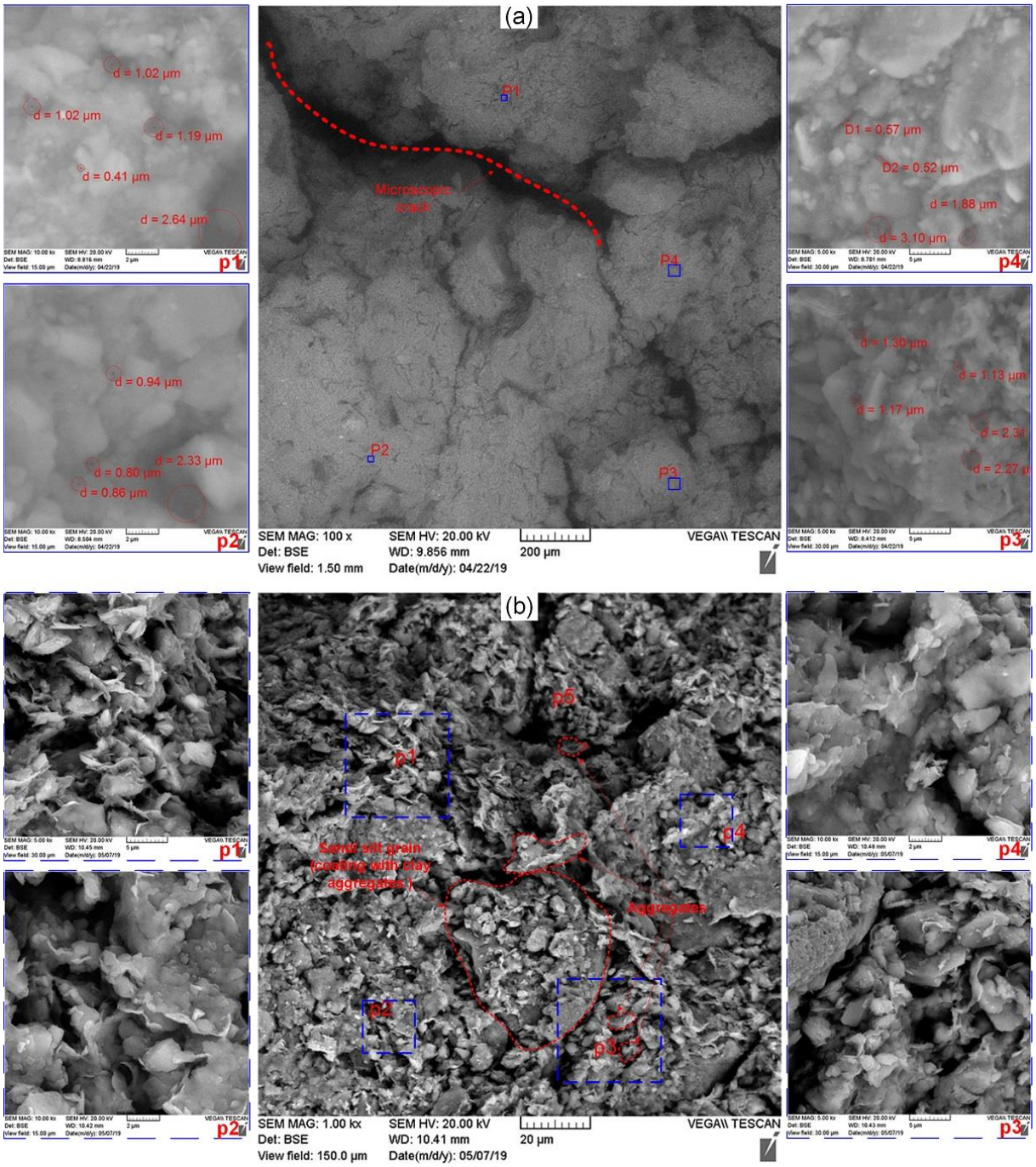

Figure 5.5 SEM images of IHT-C-W with different specimen preparation methods: (a) FF technique, and (b) FDFP technique.

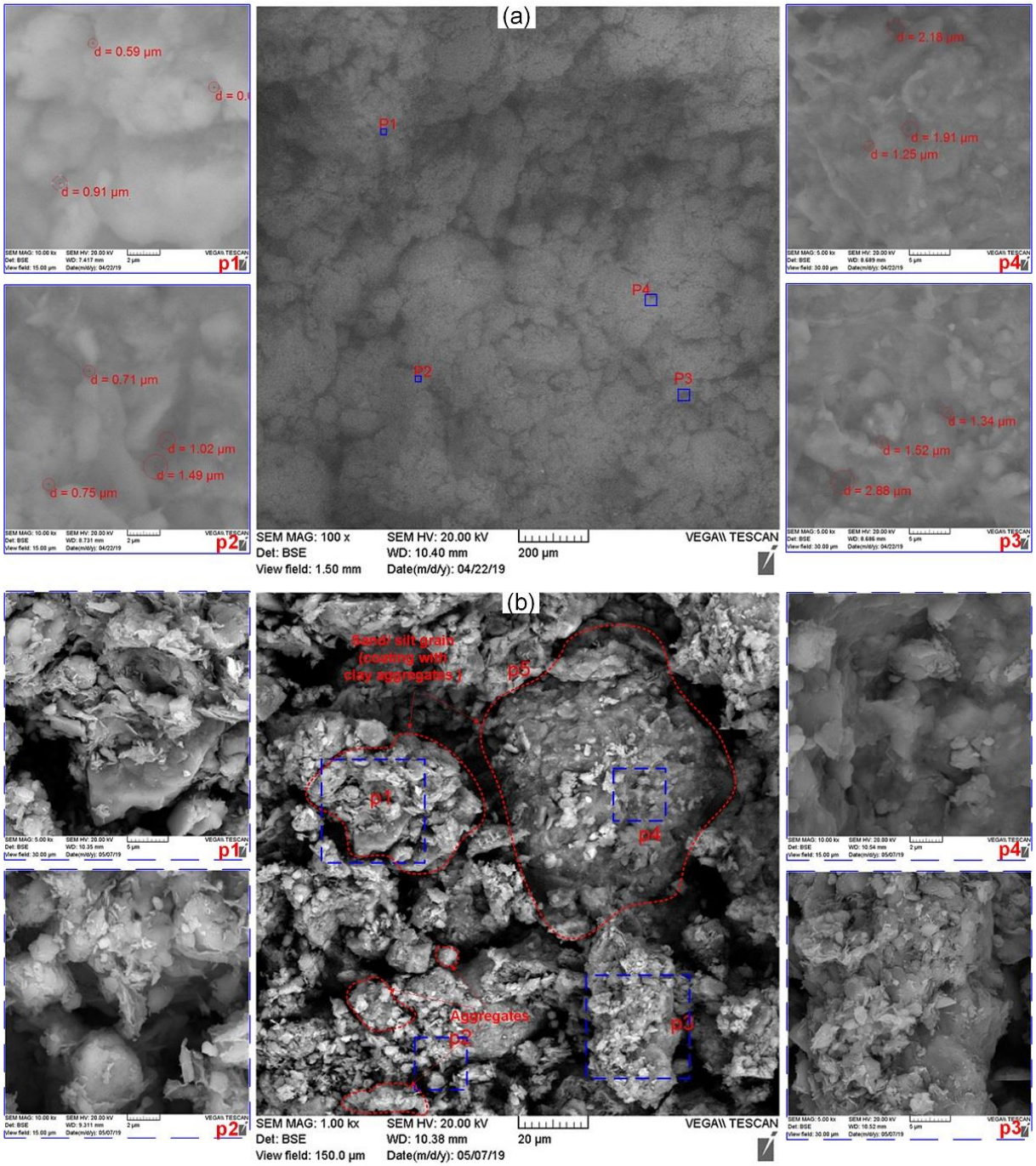

Figure 5.6 SEM images of IHT-C-D with different specimen preparation methods: (a) FF technique, and (b) FDFP technique.

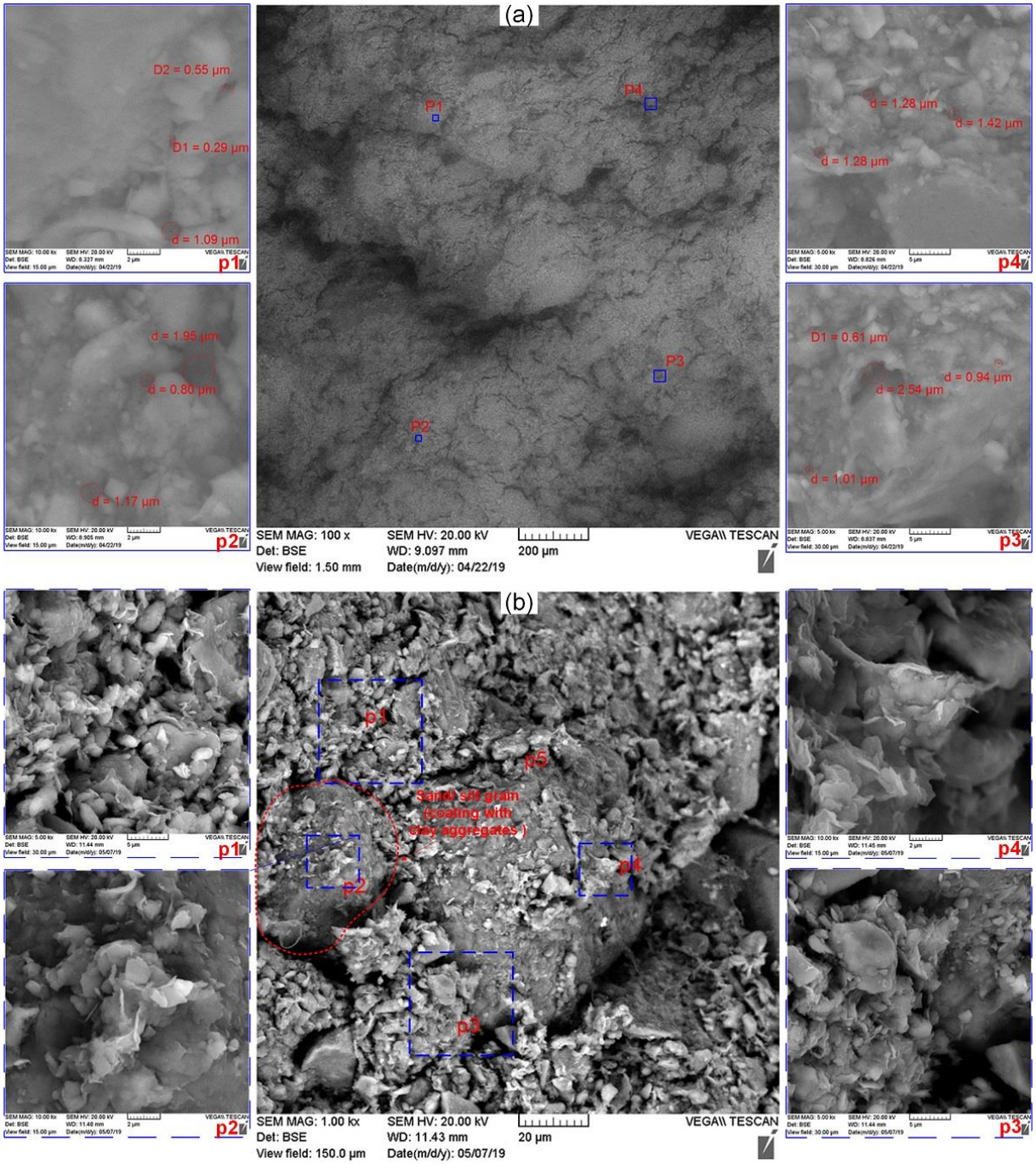

Figure 5.7 SEM images of IHT-R-800 with different specimen preparation methods: (a) FF technique, and (b) FDFP technique.

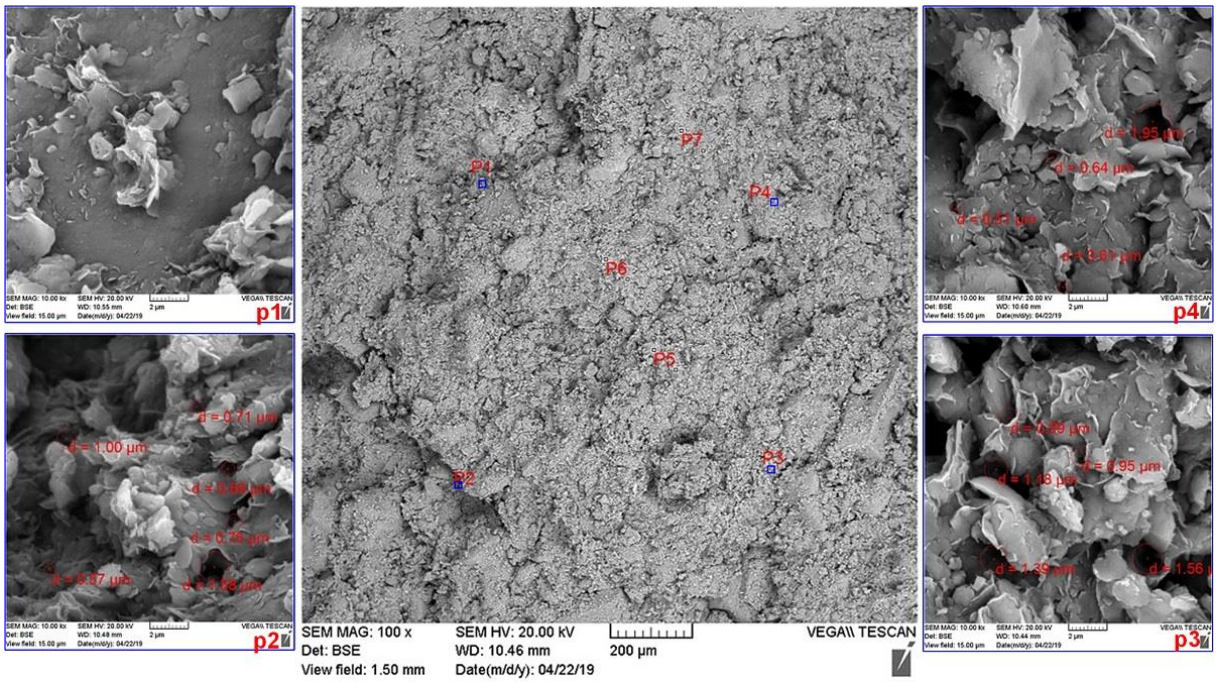

Figure 5.8 SEM images of IHT-R-800-O after oven-dried.

5.1.4 Mercury Intrusion Porosimetry (MIP)

The shape and distribution of voids are one of the three most important measures of fabric, along with contact distributions and particle orientations (Mitchell and Soga 2005). Pore information can be obtained by volumetric pore size distribution determinations and from image analysis of thin sections and SEM pictures. The pore size distribution (PSD) determined using forced intrusion of mercury, i.e. Mercury Intrusion Porosimetry (MIP), gives the essential elements to quantitively characterize the structure of soil specimens. The PSD is directly related to the key engineering properties of the soil, such as soil water retention capacity hydraulic conductivity (e.g., Romero et al. 2011; Hu et al. 2013; Zhai et al. 2018), stiffness (Li et al. 2014), shear strength (e.g., Miao et al. 2007; Ng et al. 2016; Satyanaga and Rahardjo 2019) and tensile strength (Trabelsi et al. 2018). The MIP is useful for measurement of pore sizes from about 0.01 µm to several tens or even hundreds of micrometers. Koliji et al. (2010) gave the general pore-size range examined by three different techniques as Figure 5.9. The basis of MIP is that the non-wetting fluid, e.g. mercury (fluid-to-solid contact angle >90°) will not enter pores without application of pressure. For pores of cylindrical shape, the Washbum's equation applies (e.g., Griffiths and Joshi 1989; Yuan et al. 2019), and

$$(5.2)\quad D = -\frac{4T_{Hg}\cos\theta_{Hg}}{P_{Hg}}$$

where D is the diameter of pore intruded, T_{Hg} is the surface tension of intruding mercury (i.e. 0.484 N/m at 25 °C (e.g., Diamond 1970)), θ_{Hg} is the contact angle between liquid mercury and the solid surface (i.e. 140° (e.g., Diamond 1970)), P is the applied pressure. The pores of soil specimens must be dry prior to MIP tests. In order to minimize the effect of volume change on drying, the freezing-drying procedure are followed to prepare the soil specimens. The initial states and specimen formation are as same as those for SEM tests (i.e. Table 5.4). The phase change of soil water in the freezing-drying process follows the "FDFP" path in Figure 5.4.

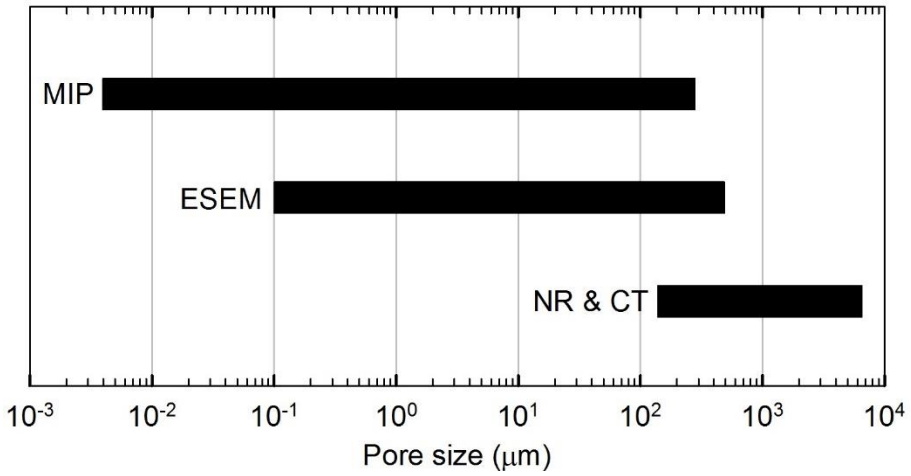

Figure 5.9 Pore size range examined by different techniques: MIP, Mercury Intrusion Porosimetry; ESEM, Environmental Scanning Electron Microscopy; NR, Neutron Radiography; CT, Computed Tomography (adapted from Koliji et al. 2010).

The MIP tests in the present studies are conducted by Micromeritics AutoPore IV 9500 (V1.07, Serial 689) pore size analyzer at Western University, Canada. The important characteristics and specifications of the equipment are summarized in Table 5.5. For this equipment, the restriction on the specimen volume is around 3000 mm^3, which depends on the volume of the penetrometer (i.e. 3.420 mL). The soil specimens are cut to a cubic shape with side length of 10 mm prior to the freezing-drying preparation procedure for MIP tests. The penetrated volume of mercury into the soil pores is measured as a function of applied pressure, P_{Hg}, which is converted to the pore diameter, D by Washburn Eq. (i.e. Eq. (5.2)). Figures 5.10(a) and 5.11(a) present all the mercury intrusion and extrusion curves of Indian Head till and Regina clay at different initial conditions, which addressed in Table 5.4. The successive extrusion curves are different from the intrusion

curves due to the entrapment of the liquid mercury in the constricted pores, i.e. the pores that are accessible only through smaller channels which will not be detected until the smaller channels are penetrated (e.g., Delage and Lefebvre 1984; Wang et al. 2020). A cycle of intrusion-extrusion provides important information on the pore structure of the studied soils. The mercury intrusion fills all the interconnected and accessible pores, which presents the entire pore size distribution. On the other hand, when intrusion pressure relieves, extrusion only takes place from the non-constricted pores. In Figure 5.11(a), the intrusion-extrusion curves for ITH-R-800-O seem unreasonable and wrong. After repeating and test on the identical specimen and confirming there are no operation mistakes, the strange curves may be attributed to the time duration (i.e. seven days) for oven-dry (35 °C) is not sufficient to totally dry the specimens, which leads to the soil pores non-accessible for the liquid mercury due to the presence of liquid water.

Table 5.5 Specifications of the Micromeritics used for MIP tests in the present studies.

	Characteristics	Specifications
Low pressure	Pressure range	1.4 kPa to 344.7 kPa
	Sensitivity	344.7 Pa
	Pore diameter	360 mm to 4 mm
	Maximum intrusion volume	0.010 mL/g
High pressure	Pressure range	up to 4.1×10^5 kPa
	Pore diameter	to 0.003 mm
	Maximum intrusion volume	0.010 mL/g
Intrusion and extrusion	Sensitivity	better than 0.1 μL
	Evacuation pressure	6.7 Pa

Figures 5.10(b) and 5.11(b) illustrate the pore size distribution curves of Indian Head till at different initial conditions which addressed in Table 5.4. According to Figure 5.10(b), single pore structure is predominated for compacted soils at wet of optimum; on the other hand, double pore structure is predominated for compacted soils at dry of optimum, which is also concluded by other researchers (e.g., Delage et al. 1996; Tarantino 2010). The effect of oven-dry and the induced shrinkage on the pore structure can be examined from Figure 5.11(b). Therefore, the freezing-drying procedure should be used in order to minimize the shrinkage due to drying.

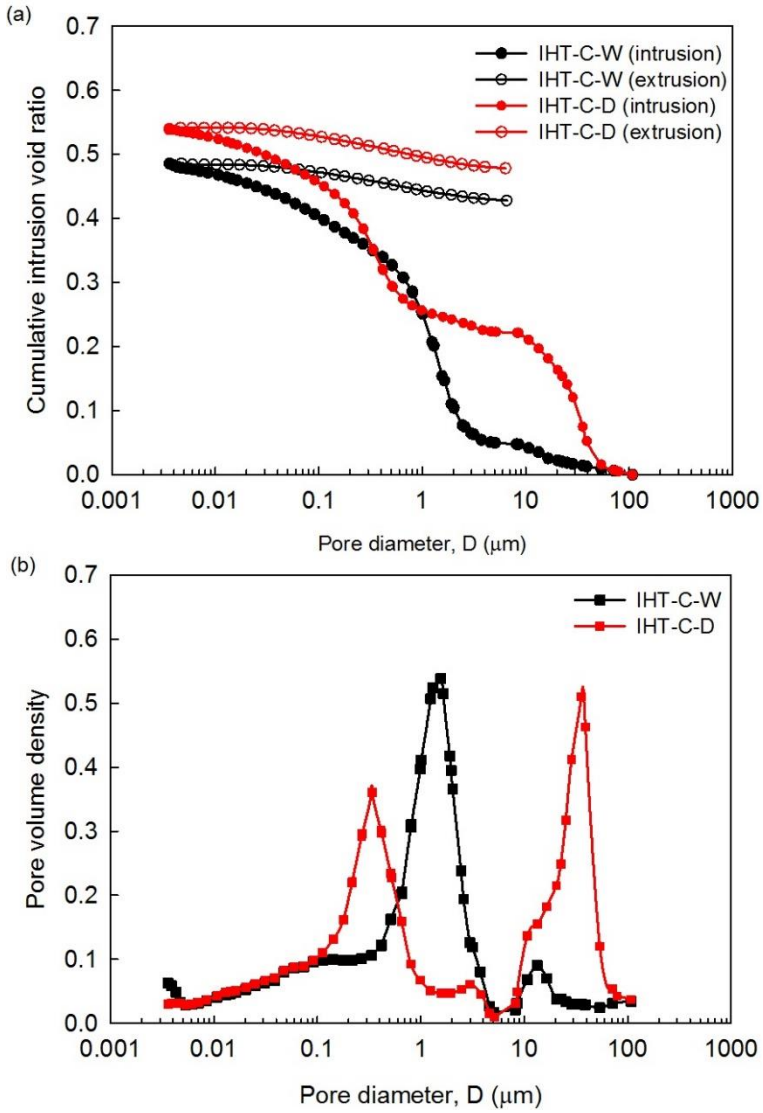

Figure 5.10 Illustration of (a) cumulative pore volume curves of IHT-C-W and IHT-C-D, and (b) pore volume density of IHT-C-W and IHT-C-D.

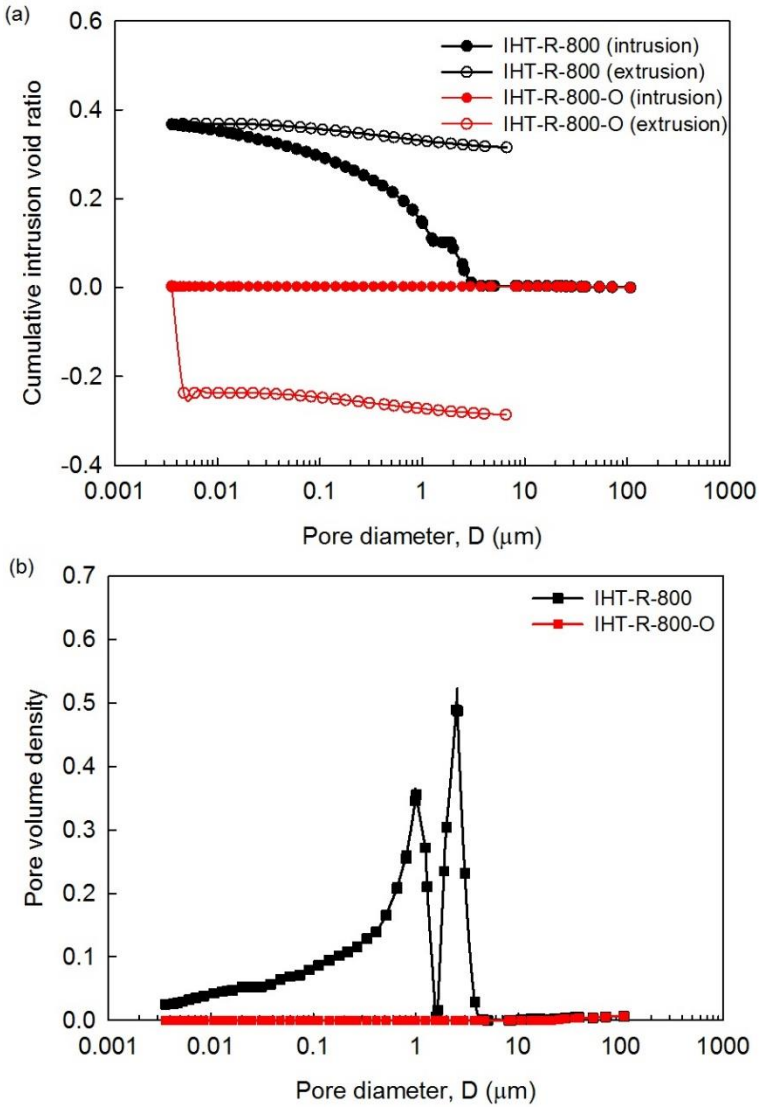

Figure 5.11 Illustration of (a) cumulative pore volume curves of IHT-R-800 and IHT-R-800-O, and (b) pore volume density of IHT-R-800 and IHT-R-800-O.

5.2 Geotechnical characteristics of studied soils

5.2.1 Grain size distribution

In order to determine the grain size distribution (GSD) curves of Indian Head till, two commonly used methods, namely mechanical sieving method (i.e. ASTM D6913/D6913M-17 (ASTM International 2017a)) for particle size greater than 0.075 mm, and sedimentation technique (i.e. ASTM D7928-17 (ASTM International 2017b)) for the fraction finer than 0.075 mm. Table 5.6 and Figure 5.12 show the complete grain size distribution characteristics of Indian Head till. The

specific gravity of the solid particles is determined by the water Pycnometer procedure (i.e. ASTM D854-14 (ASTM International 2014)) as shown in Table 5.6 as well.

Table 5.6 Grain size characteristics and Atterberg's limits of Indian Head till.

Soil Name	Indian Head till (IHT)
Sand size fraction (%)	20
Silt size fraction (%)	46
Clay size fraction (%)	34
Specific gravity, G_s	2.70
Liquid limit, LL (%)	35.0
Plastic limit, PL (%)	14.0
Plasticity index, PI (%)	21.0
*Shrinkage limit, SL (%)	14.0
USCS	CL

Note: *values obtained from Lau (1987).

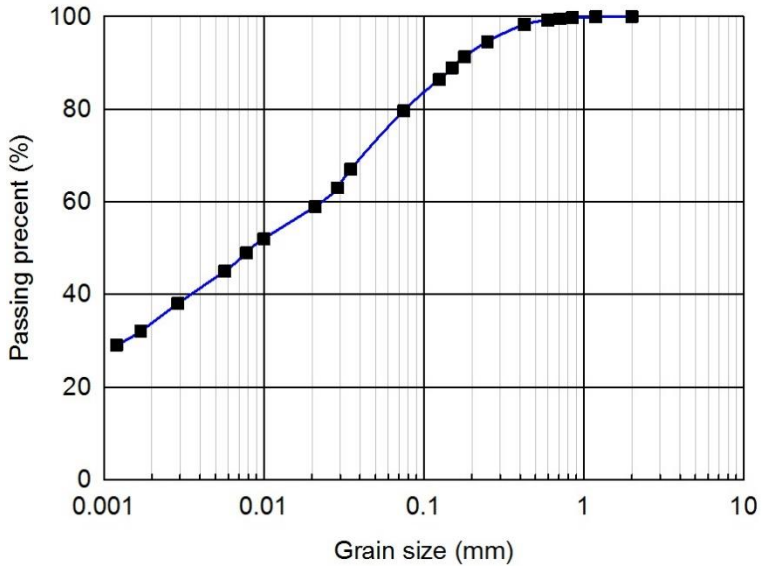

Figure 5.12 Grain size distribution curves of Indian Head till.

5.2.2 Atterberg's limits

Atterberg's limits (or consistency limits), namely, liquid limit and plastic limit are determined according to ASTM D4318-17e1 (ASTM International 2017c). Consistency limits provide the information on the soil states with respect to water content (Table 5.6); they can be regarded as the best empirical tool for a rapid assessment of the soil behavior (e.g., plasticity index). Based on the plasticity chart of Unified Soil Classification System (USCS, ASTM D2487-17 (ASTM International 2017d)), Indian Head till can be classified as a lean clay (CL).

5.2.3 Consolidation characteristics

The characteristics of one-dimensional consolidation is determined by means of the oedometer test (i.e. ASTM D2435/D2435M-11 (ASTM International 2011)). The dry soil powder is mixed with deaired water using a kitchen mixer which helps to make the paste uniform. The soil water mixture with the initial water content of 1.2 times liquid limit (i.e. 42%) is then shaken for five minutes in order to remove the air bubbles. The soil water mixture is covered and kept still overnight. Two cutting rings are used to take the reconstituted specimens from the upper and lower layer of the slurry, respectively (i.e. labeled "IHT-CON1" and "IHT-CON2"). The measured compression curves (e – log p) of the two reconstituted Indian Head till specimens are summarized in Figure 5.13. The compression index (C_c) and recompression index (C_r) of Indian Head till are 0.246 and 0.026, respectively.

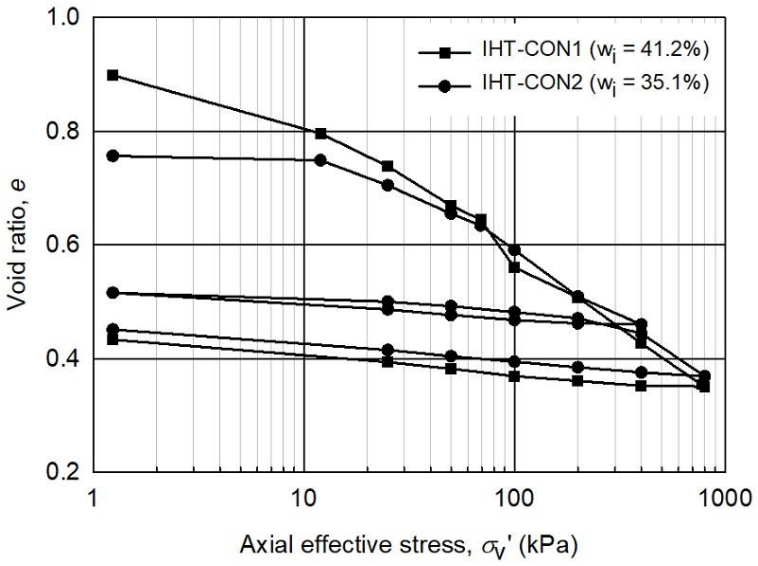

Figure 5.13 The compression curves (e – log p) of the reconstituted Indian Head till.

5.2.4 Compaction curve

Compaction is the process of increasing the density of a soil by packing the particles closer together with a reduction in the volume of air; there is no significant change in the volume of water in the soil (Knappett and Craig 2012). Compaction will remarkably change the soil microstructure and the key engineering properties, such as permeability, stiffness, and strength (including shear strength and tensile strength). In general, the higher the degree of compaction, the higher will be the shear strength and the stiffness, and the lower will be the permeability of the soil. The

procedure adopted to obtain the compaction curves of the studied soils follows the ASTM D698-12e2 (ASTM International 2012). The compaction curves using the standard Proctor of Indian Head till is presented in Figure 5.14. The optimum moisture content (w_{opt}) and maximum dry density ($\rho_{d,max}$) of Indian Head till are 15.3% and 1843 kg/m^3, respectively.

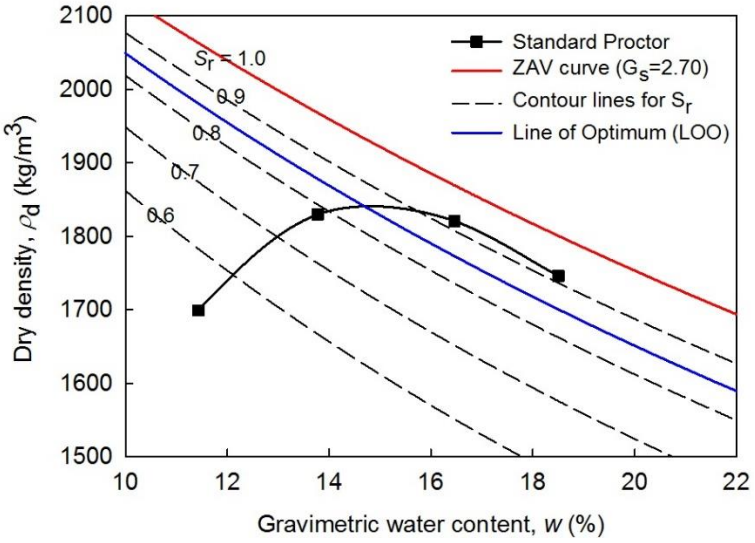

Figure 5.14 Compaction curves using standard Proctor of Indian Head till.

5.2.5 Soil-water Characteristic Curve (SWCC)

5.2.5.1 Pressure plate method

Pressure plate method uses overpressure to extract water out of the pore structure of soil specimen until equilibrium is achieved between the moisture content in the specimen and the applied overpressure. This technique is called "Axis Translation Technique (ATT)". Equilibrium can only be reached by desorption using the pressure plate extractor, so only the drying curve of the SWCC can be obtained. The setup of the pressure plate extractor used in the present study is shown in Figure 5.15. The maximum overpressure that can be applied to the soil specimen is limited by the air-entry value of the high-air-entry ceramic plate (HAECP). The reconstituted specimen "IHT-CON1" (Figure 5.13) is used after the consolidation test. The preconsolidation pressure is 800 kPa that produces the desired dry density (i.e. 1.954 g/cm^3) close to maximum dry density on the standard Proctor compaction curve (i.e. 1.843 g/cm^3) after unloading from the oedometer. Following the procedure in ASTM C1699-09(2015) (ASTM International 2016a), for each desired overpressure the equilibrium moisture content reaches when the change in the mass of the

specimen is less than 0.01g for 24 hours. After achieving equilibrium states corresponding to applied overpressure values, the soil specimen is removed from the pressure plate extractor and placed in the drying oven for determining the gravimetric water content.

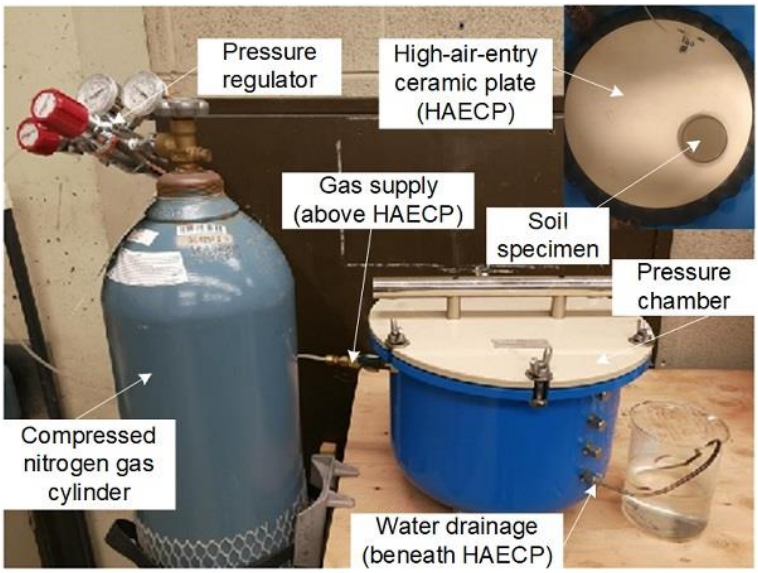

Figure 5.15 Setup of the pressure plate test apparatus.

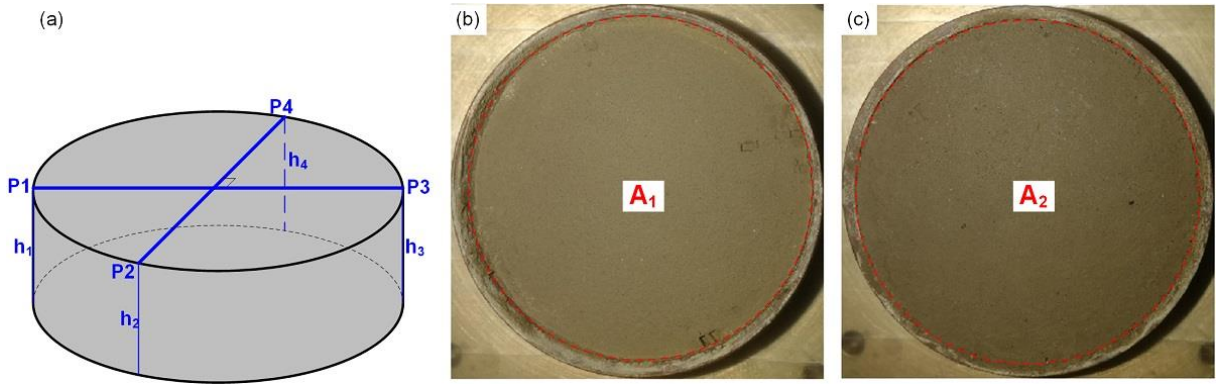

Figure 5.16 Schematic illustration of estimating the volume of the soil specimen during drying: (a) the height is measured by caliper; (b) top surface area of the soil specimen at matric suction of 200 kPa is estimated by digital image technique; (c) bottom surface of the soil specimen at matric suction of 200 kPa is estimated by digital image technique.

At each equilibrium state for a given overpressure, the volume of the soil specimen is estimated by the height and surface area. The height is measured by the caliper at four locations (i.e. P1, P2, P3, and P4) and taken as the average value (Figure 5.16(a)). When the overpressure is less than 150 kPa, the soil specimen doesn't detach from the wall of the cutting ring. The surface area equals the reference area (A_0) which is the section area of the cutting ring with a diameter of 63.5mm.

When the soil specimen detaches from the wall of the cutting ring, the surface area is estimated by digital image technique. The ratio between the surface area of the soil specimen (Figure 5.16(b) and 5.16(c)) and the section area of the cutting ring is estimated by those areas in pixels measured by the image processing and analysis program ImageJ (Ferreira and Rasband 2012). The estimated results of the volume and bulk density at different matric suctions are listed in Table 5.7.

Table 5.7 Estimated volume and bulk density of the soil specimen at different matric suctions.

Matric suction, $(u_a - u_w)$ (kPa)	Gravimetric water content, w	Average height, h (mm)	Reference surface area, A_0 (mm^2)	Surface area ratio, A/A_0	Surface area, A (mm^2)	Estimated volume, V (mm^3)	Mass of soil specimen, m (g)	Bulk density, ρ = m/V (g/cm^3)
0	16.4%	13.77	3166.9	1	3166.9	43608	99.204	2.275
25	16.0%	13.76	3166.9	1	3166.9	43577	98.898	2.269
50	15.7%	13.71	3166.9	1	3166.9	43418	98.646	2.272
75	15.5%	13.56	3166.9	1	3166.9	42943	98.455	2.293
100	15.3%	13.62	3166.9	1	3166.9	43133	98.260	2.278
125	15.1%	13.77	3166.9	1	3166.9	43608	98.084	2.249
150	14.9%	13.88	3166.9	0.9816	3108.6	43147	97.895	2.269
175	14.7%	13.88	3166.9	0.9788	3099.8	43025	97.772	2.272
200	14.6%	13.69	3166.9	0.9749	3087.4	42267	97.641	2.310

5.2.5.2 Filter paper method

Filter paper can be used as passive sensors to evaluate the soil matric or total suction, which is a measure of the free energy of the pore-water. In the present study, the water content of the filter paper which is in direct contact with the soil specimen is measured and the matric suction is evaluated. The soil specimens are prepared by static compaction (Figure 5.17(a)). The compaction water content and dry density are summarized in Table 5.8. The dimensions of the compacted specimens are 60 mm in diameter by 20 mm in height. The desired dry density is the maximum dry density. However, the dry density varies due to operation error during the compaction procedure. For the highest compaction water content of 18.3%, the maximum dry density cannot be obtained due to the degree of saturation of compacted specimens is typically less than unity. According to the compaction curve (Figure 5.14), 95% of the maximum dry density is therefore chosen for the IHT-18. The compacted soil specimens at desired water contents are sealed with plastic wrap for 24 hours prior to suction measurement. According to ASTM D5298-16 (ASTM International 2016b), three stacked ash-free Whatman No. 42 filter paper are placed between two

identical compacted soil specimens (Figure 5.17(b)). An aluminium container containing the specimens and filter papers is sealed with wrapping of plastic electrical tape. Then the aluminium container is placed and sealed in an insulated desiccator, which is placed in a room with temperature variation less than 1°C (i.e. 23±1°C) as shown in Figure 5.17(c). The water content of the filter papers in direct contact with the soil specimens is allowed to come to equilibrium for 14 days. Once the water content of the middle filter paper at the equilibrium status has been determined, the calibration curve for Whatman No. 42 filter paper suggested by ASTM D5298-16 (ASTM International 2016b) is used to evaluate the matric suction, s_{fp} (Table 5.8):

$$\log(s_{fp}) = \begin{cases} 5.327 - 0.0779 w_{fp}, & for\ w_{fp} < 45.3; \\ 2.412 - 0.0135 w_{fp}, & for\ w_{fp} \geq 45.3. \end{cases} \quad (5.3)$$

where, w_{fp} is the water content of the middle filter paper at equilibrium states, precent.

Table 5.8 Measurements of matric suction for different water contents using filter paper technique

Specimen No.	Gravimetric water content, w	Bulk density, ρ (g/cm^3)	Cold tare mass, T_c (g)	Mass of wet filter paper + Cold tare mass, M_1 (g)	Mass of dry filter paper + Hot tare mass, M_2 (g)	Hot tare mass, T_h (g)	Water content of filter paper, w_{fp} (%)	Matric suction, s_{fp} (kPa)
IHT-18	18.3%	2.075	30.6471	30.9208	30.8283	30.6475	51.38	52
IHT-17	17.2%	2.087	30.5207	30.7670	30.7018	30.5208	36.08	328
IHT-16	16.3%	2.098	30.6482	30.8765	30.8156	30.6448	33.67	506
IHT-15	15.3%	2.095	30.3908	30.6230	30.5664	30.3915	32.76	596
IHT-14	14.3%	2.050	30.6543	30.8904	30.8263	30.6447	30.01	975
IHT-12	12.3%	2.085	30.6487	30.8746	20.8267	30.6481	26.48	1836
IHT-10	10.3%	2.015	30.5658	30.7883	30.7044	30.5255	24.37	2682

5.2.5.3 Dew-point Water PotentiaMeter (WP4-T)

The dew-point WaterPotentiaMeter (from Decagon) at University of Ottawa is used for measuring total suction in the high suction range (Figure 5.18(a)). The WP4-T device can reduce the time and costs associated with suction measurements and provide reliable measurements in the high suction range (e.g., Ebrahimi-Birang and Fredlund 2016). The WP4-T device consists of a sealed chamber with a fan, a mirror, a photodetector cell, and a temperature sensor. After sealed in the closed chamber, the soil specimen is allowed to thermodynamically equilibrate with the chamber environment assisted by the small fan. The dew-point is detected by the photodetector cell once

the condensation first appears on the mirror. The dew-point is measured using a thermocouple. The temperature sensor is used to measure the temperature in the sealed chamber which is the temperature of the soil specimen under equilibrium conditions. The saturated vapor pressure and the vapor pressure above the soil specimen can be derived from the dew-point and specimen temperature, respectively. Kelvin's Eq. is then used to calculate the total suction of the soil specimen (Fredlund et al. 2012):

$$(5.4)\quad \psi = -\frac{RT_K \rho_w}{\omega_v} \ln\left(\frac{u_v}{u_{v0}}\right)$$

where ψ is the total suction, kPa; R is the universal (molar) gas constant (i.e. 8.31432 J/(mol·K)); T_K is the absolute temperature, K; ρ_w is the density of water, kg/m^3; ω_v is the molecular mass of water vapor (i.e. 18.016 kg/kmol); u_v is the partial pressure of pore-water vapor, kPa; u_{v0} is the saturated vapor pressure over a flat surface of pure water at the same temperature, kPa. The calculation of total suction based on Eq. (5.4) is automatically performed by the software internal to the WP4-T device.

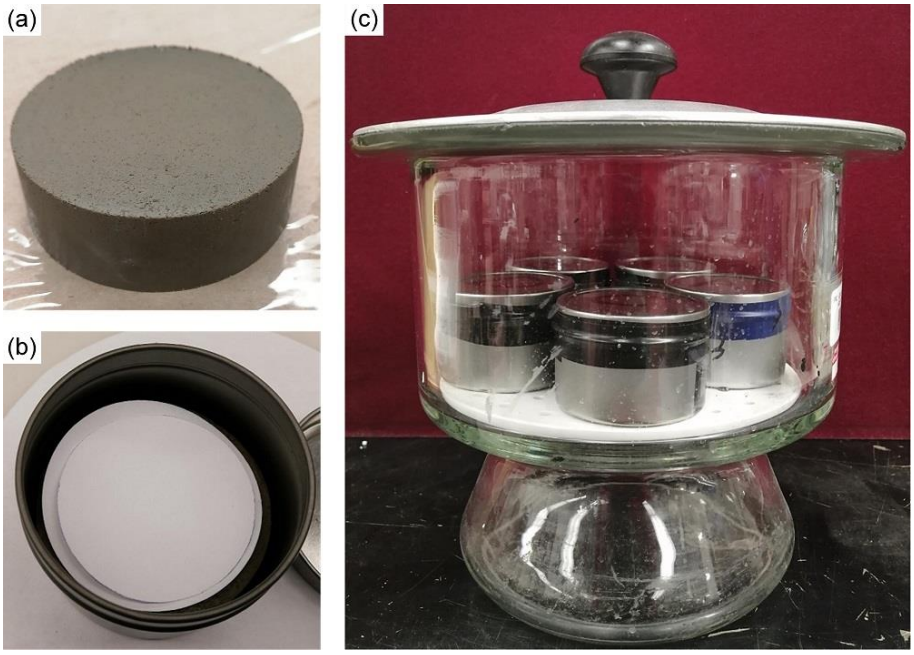

Figure 5.17 Matric suction measurement procedure by filter paper method: (a) as-compacted soil specimen at desired water content and dry density; (b) three stacked filter papers placed between two soil specimens; (c) sealed specimen container placed in an insulated desiccator.

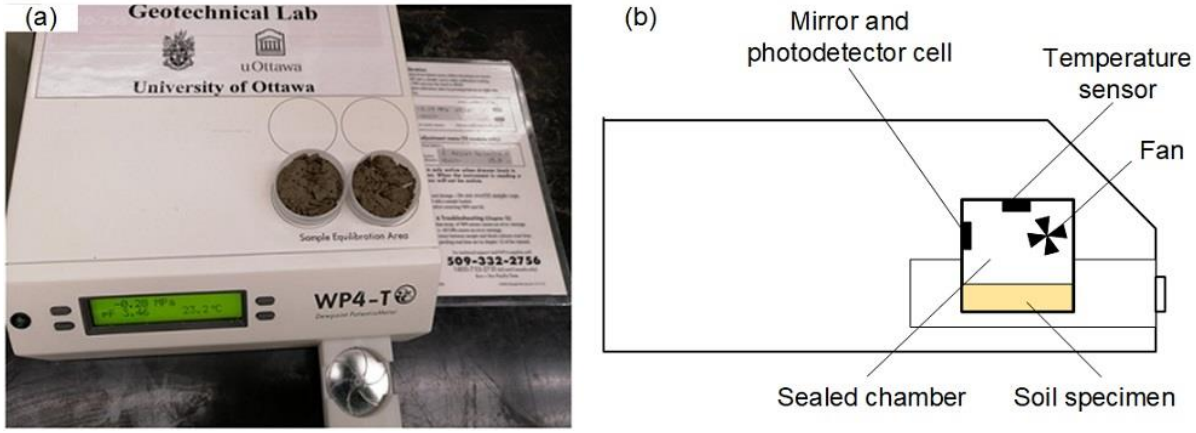

Figure 5.18 (a) Dew-point WP4-T (v3.52) device used in the present study; (b) Schematic diagram of the main components inside the WP4-T device (after Leong et al. 2003).

The soil specimens undergo desiccation cracking test under the laboratory environment prior to Brazilian split tests (which is discussed in chapter 6), so the specimens are extremely dry with high suction. After the Brazilian split tests, the soil specimen is divided into six small pieces. Two are oven-dried to determine the water content; two are submitted to the dew-point WP4-T device for measuring the total suction; the last two are used for estimating the specimen volume by wax immersion technique (i.e. ASTM C914-09 (ASTM International 2015)). The measurements of specimen water content, total suction, and volume are presented in Table 5.9. The setup for wax immersion method is shown in Figure 5.19.

Table 5.9 The test results of total suction, volume and bulk density of soil specimens.

*Specimen No.	Gravimetric water content, w	Total suction, ψ (MPa)	Moist specimen volume, V (cm^3)	Moist specimen mass, m (g)	Bulk density, $\rho = m/V$ (g/cm^3)
IHT-15-f	2.9%	75.68	1.128	2.380	2.111
	2.7%	75.96	1.164	2.396	2.059
IHT-15-LR	3.3%	79.28	1.508	3.178	2.108
	2.8%	83.11	2.856	5.889	2.062
IHT-15-HR	3.2%	69.81	2.520	5.257	2.086
	3.3%	70.61	2.776	5.722	2.061
IHT-12-f	2.9%	82.73	4.153	8.266	1.991
	3.0%	82.84	3.931	7.736	1.968
IHT-12-LR	3.0%	83.52	3.620	7.351	2.031
	3.1%	82.41	4.299	8.690	2.022
IHT-12-HR	2.3%	146.29	2.234	4.601	2.060
	2.4%	146.19	2.853	5.895	2.067

Note: * "15" stands for the initial water content prior to desiccation cracking test; "f", "LR", and "HR" represent the smooth, low-rough and high-rough base of the specimen container.

Figure 5.19 (a) Setup for wax immersion method for measuring the specimen volume; (b) Coated soil specimen with wax after dipping into the melted wax; (c) Suspended weight of the wax-coated specimen in kerosene determined by below balance weighing.

5.2.5.4 Synthesis of measurements of soil-water characteristic curve (SWCC)

All the measurements of gravimetric water content and the corresponding soil suction using different techniques are summarized in Table 5.10. With the known bulk density (ρ), the dry density (ρ_d), the void ratio (e) and the degree of saturation (S_r) can be calculated by the following the mass-volume relationships:

(5.5a) $$\rho_d = \frac{\rho}{1+w}$$

(5.5b) $$e = \frac{G_s}{\rho_d} - 1$$

(5.5c) $S_r = \frac{wG_s}{e}$

Table 5.10 Summary of the measurements of SWCC using different techniques

Measurement technique	Specimen No.	*Matric suction, (u_a - u_w) (kPa)	Gravimetric water content, w	Dry density, ρ_d (g/cm^3)	Void ratio, e	Degree of saturation, S_r
Pressure plate method (Axis-translation technique)	IHT-CON1	0	16.4%	1.954	0.443	1
		25	16.0%	1.956	0.442	0.979
		50	15.7%	1.964	0.440	0.965
		75	15.5%	1.985	0.436	0.961
		100	15.3%	1.976	0.438	0.943
		125	15.1%	1.954	0.442	0.920
		150	14.9%	1.975	0.438	0.916
		175	14.7%	1.981	0.437	0.910
		200	14.6%	2.016	0.429	0.917
Measurement technique	Specimen No.	Matric suction, s_{fp} (kPa)	Gravimetric water content, w	Dry density, ρ_d (g/cm^3)	Void ratio, e	Degree of saturation, S_r
Filter paper technique (contact)	IHT-18	52	18.3%	1.743	0.549	0.935
	IHT-17	328	17.2%	1.782	0.515	0.896
	IHT-16	506	16.3%	1.801	0.496	0.887
	IHT-15	596	15.3%	1.836	0.487	0.853
	IHT-14	975	14.3%	1.800	0.507	0.767
	IHT-12	1836	12.3%	1.848	0.459	0.747
	IHT-10	2682	10.3%	1.810	0.485	0.602
Measurement technique	Specimen No.	Total suction, ψ (MPa)	Gravimetric water content, w	Dry density, ρ_d (g/cm^3)	Void ratio, e	Degree of saturation, S_r
WP4-T (Chilled-mirror dew-point technique)	IHT-15-f	75.82	2.8%	2.028	0.332	0.229
	IHT-15-LR	81.20	3.0%	2.023	0.335	0.250
	IHT-15-HR	70.21	3.2%	2.008	0.344	0.258
	IHT-12-f	82.79	3.0%	1.923	0.404	0.199
	IHT-12-LR	82.97	3.0%	1.966	0.373	0.223
	IHT-12-HR	146.24	2.4%	2.016	0.339	0.187

Note: *In fact, (u_a - u_w) is the capillary component of the matric suction (Zhang and Lu 2019).

It should be noted that both the gravimetric water content (w) and the dry density (ρ_d) of soil specimens used for measuring soil suction by filter paper and WP4-T in Table 5.10 are the average values of two specimens. The variation of degree of saturation with respect to soil suction is plot in Figure 5.20. The mathematical model proposed by van Genuchten (i.e. Eq. (3.1)) is used for curve fitting based on the measurements. The air-entry value (i.e. AEV = 270 kPa) and the residual

degree of saturation (i.e. $S_{r,res}$ = 0.22) can be determined by graphical construction method (e.g., Vanapalli et al. 1999) as shown in Figure 5.20.

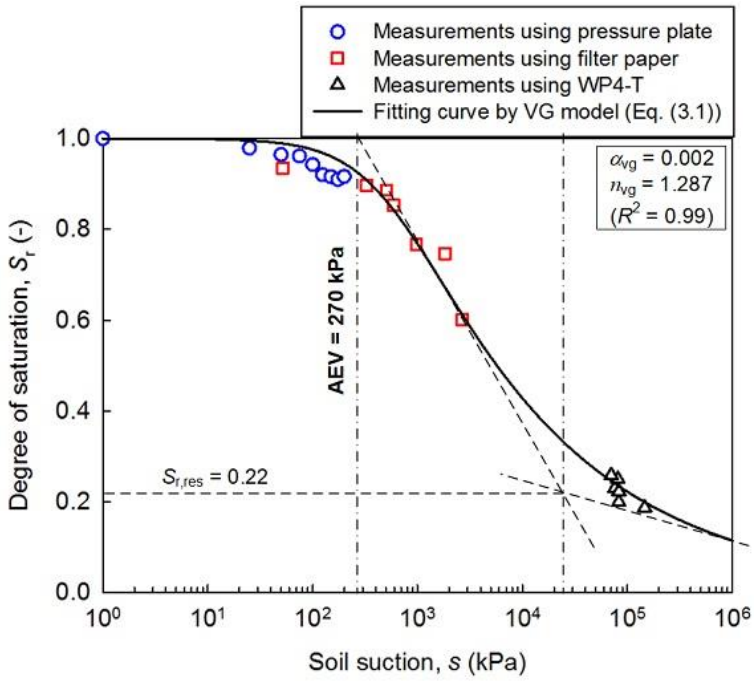

Figure 5.20 Soil-Water Characteristic Curve of Indian Head till.

5.3 References

ASTM International. 2011. D2435/D2435M-11 Standard Test Methods for One-Dimensional Consolidation Properties of Soils Using Incremental Loading. West Conshohocken, PA.

ASTM International. 2012. D698-12e2 Standard Test Methods for Laboratory Compaction Characteristics of Soil Using Standard Effort (12 400 ft·lbf/ft^3 (600 kN·m/m^3)). West Conshohocken, PA

ASTM International. 2014. D854-14 Standard Test Methods for Specific Gravity of Soil Solids by Water Pycnometer. West Conshohocken, PA.

ASTM International. 2015. C914-09(2015) Standard Test Method for Bulk Density and Volume of Solid Refractories by Wax Immersion, West Conshohocken, PA.

ASTM International. 2016a. ASTM C1699-09(2015), Standard Test Method for Moisture Retention Curves of Porous Building Materials Using Pressure Plates. West Conshohocken, PA. DOI: 10.1520/C1699-09R15.

ASTM International. 2016b. ASTM D5298-16, Standard Test Method for Measurement of Soil Potential (Suction) Using Filter Paper. West Conshohocken, PA. DOI: 10.1520/D5298-16.

ASTM International. 2017a. D6913/D6913M-17 Standard Test Methods for Particle-Size Distribution (Gradation) of Soils Using Sieve Analysis. West Conshohocken, PA.

ASTM International. 2017b. D7928-17 Standard Test Method for Particle-Size Distribution (Gradation) of Fine-Grained Soils Using the Sedimentation (Hydrometer) Analysis. West Conshohocken, PA.

ASTM International. 2017c. D4318-17e1 Standard Test Methods for Liquid Limit, Plastic Limit, and Plasticity Index of Soils. West Conshohocken, PA.

ASTM International. 2017d. D2487-17 Standard Practice for Classification of Soils for Engineering Purposes (Unified Soil Classification System). West Conshohocken, PA.

Balmer, R.T., 1990. Thermodynamics. West Publishing Co., St. Paul. MY.

Christiansen, E.A. and Saure, E.K. 2002. Stratigraphy and structure of Pleistocene collapse in the Regina low, Saskatchewan, Canada. Canadian Journal of Earth Sciences 39: 1411–1423.

Cui, Y.J. 1993. Etude du comportement d'un limon compacté non saturé et de sa modélisation dans un cadre élasto-plastique. Doctoral dissertation, École Nationale des Ponts et Chaussées, France. [in French]

Cuisinier, O. and Laloui, L. 2004. Fabric evolution during hydromechanical loading of a compacted silt. International Journal for Numerical and Analytical Methods in Geomechanics, 28(6): 483-499.

Delage, P., Audiguier, M., Cui, Y.J. and Howat, M.D. 1996. Microstructure of a compacted silt. Canadian Geotechnical Journal, 33(1): 150-158.

Delage, P. and Lefebvre, G. 1984. Study of the structure of a sensitive Champlain clay and of its evolution during consolidation. Canadian Geotechnical Journal, 21(1): 21-35.

Delage, P., Tessier, D. and Marcel-Audiguier, M. 1982. Use of the Cryoscan apparatus for observation of freeze-fractured planes of a sensitive Quebec clay in scanning electron microscopy. Canadian Geotechnical Journal, 19(1): 111-114.

Della Vecchia, G. and Romero, E., 2013. A fully coupled elastic–plastic hydromechanical model for compacted soils accounting for clay activity. International Journal for Numerical and Analytical Methods in Geomechanics, 37(5): 503-535.

Diamond, S. 1970. Pore size distributions in clays. Clays and Clay Minerals, 18(1): 7-23.

Ebrahimi-Birang, N. and Fredlund, D.G. 2016. Assessment of the WP4-T device for measuring total suction. Geotechnical Testing Journal, 39(3): 500-506.

Ferreira, T. and Rasband, W. 2012. ImageJ User Guide.

Fredlund, D. G., Rahardjo, H. and Fredlund M. D. 2012. Unsaturated Soil Mechanics in Engineering Practice. John Wiley and Sons, New York.

Griffiths, F.J. and Joshi, R.C. 1989. Change in pore size distribution due to consolidation of clays. Géotechnique, 39(1): 159-167.

Han, Z. 2016. Modelling stiffness and shear strength of compacted subgrade soils. Doctoral dissertation, University of Ottawa, Canada.

Hu, R., Chen, Y.F., Liu, H.H. and Zhou, C.B. 2013. A water retention curve and unsaturated hydraulic conductivity model for deformable soils: Consideration of the change in pore-size distribution. Géotechnique, 63(16): 1389-1405.

Infante Sedano, J.A. 2006. A modified ring shear test device for determining the hydro-mechanical behaviour of unsaturated soils. Doctoral dissertation, University of Ottawa, Canada.

Ito, M. and Azam, S. 2013. Engineering properties of a vertisolic expansive soil deposit. Engineering Geology, 152(1): 10-16.

JCPDS. 1994. Powder Diffraction File, 44, 7354-CD ROM (PDF 1-44), International Centre for Diffraction Data, Pennsylvania, USA.

Knappett, J. and Craig, R.F. 2012. Craig's soil mechanics. CRC press.

Koliji, A., Vulliet, L. and Laloui, L. 2010. Structural characterization of unsaturated aggregated soil. Canadian Geotechnical Journal, 47(3): 297-311.

Lakshmikantha, M.R. 2009. Experimental and theoretical analysis of cracking in drying soils. Doctoral dissertation, Universitat Politècnica de Catalunya, Spain.

Lau, J.T.K. 1987. Desiccation cracking of soils. Master's Dissertation, University of Saskatchewan, Canada.

Leong, E.C., Tripathy, S. and Rahardjo, H. 2003. Total suction measurement of unsaturated soils with a device using the Chilled-Mirror Dew-Point technique. Geotechnique, 35(2): 173–182.

Li, X., Zhang, L.M. and Wu, L.Z. 2014. A framework for unifying soil fabric, suction, void ratio, and water content during the dehydration process. Soil Science Society of America Journal, 78(2): 387-399.

Mašín, D. 2013. Double structure hydromechanical coupling formalism and a model for unsaturated expansive clays. Engineering Geology, 165: 73-88.

Meyers, H.P. and Myers, H.P. 1997. Introductory Solid State Physics. CRC press.

McHardy, W.J. and Birnie, A.C. 1987. Scanning electron microscopy. In: Wilson, M.J. (Eds.), A Handbook of Determinative Methods in Clay Mineralogy, pp. 174-208, London: Blackie.

Miao, L., Houston, S.L., Cui, Y. and Yuan, J., 2007. Relationship between soil structure and mechanical behavior for an expansive unsaturated clay. Canadian Geotechnical Journal, 44(2): 126-137.

Mitchell, J.K. and Soga, K. 2005. Fundamentals of Soil Behavior (3rd edition). John Wiley and Sons, Hoboken, NJ.

Mollard, J.D., Kozicki, P. and Adelman, T. 1998. Some geological, groundwater, geotechnical and geoenvironmental characteristics of the Regina area, Saskatchewan, Canada. In: Karrow, P.F., White, O.L. (Eds.), Urban Geology of Canadian Cities. Department of Earth science and Quaternary Sciences Institute, University of Waterloo, ON, Canada.

Monroy, R., Zdravkovic, L. and Ridley, A. 2010. Evolution of microstructure in compacted London Clay during wetting and loading. Géotechnique, 60(2): 105–119.

Ng, C.W.W., Mu, Q.Y. and Zhou, C. 2016. Effects of soil structure on the shear behaviour of an unsaturated loess at different suctions and temperatures. Canadian Geotechnical Journal, 54(2): 270-279.

Oh, W.T. 2012. Simple techniques for the implementation of the mechanics of unsaturated soils into engineering practice. Doctoral dissertation, University of Ottawa, Canada.

Qiao, Y., Xiao, Y., Laloui, L., Ding, W. and He, M. 2019. A double-structure hydromechanical constitutive model for compacted bentonite. Computers and Geotechnics, 115: p.103173.

Ren, J. 2019. Interpretation of the frozen soils behavior extending the mechanics of unsaturated soils. Doctoral dissertation, University of Ottawa, Canada.

Romero, E., Della Vecchia, G. and Jommi, C. 2011. An insight into the water retention properties of compacted clayey soils. Géotechnique, 61(4): p.313.

Satyanaga, A. and Rahardjo, H., 2019. Unsaturated shear strength of soil with bimodal soil-water characteristic curve. Géotechnique, 69(9): 828-832.

Simms, P., Soleimani, S., Mizani, S., Daliri, F., Dunmola, A., Rozina, E. and Innocent-Bernard, T., 2017. Cracking, salinity and evaporation in mesoscale experiments on three types of tailings. Environmental Geotechnics, 6(1): 3-17.

Simms, P.H. and Yanful, E.K., 2001. Measurement and estimation of pore shrinkage and pore distribution in a clayey till during soil-water characteristic curve tests. Canadian Geotechnical Journal, 38(4): 741-754.

Simms, P.H. and Yanful, E.K., 2005. A pore-network model for hydromechanical coupling in unsaturated compacted clayey soils. Canadian Geotechnical Journal, 42(2): 499-514.

Staff, Saskatchewan Soil Survey. 1986. The soils of Indian Head rural municipality No 156 Saskatchewan.

Sun, H., Mašín, D., Najser, J., Neděla, V. and Navrátilová, E. 2019. Bentonite microstructure and saturation evolution in wetting–drying cycles evaluated using ESEM, MIP and WRC measurements. Géotechnique, 69(8): 713-726.

Tarantino, A. 2010. Unsaturated soils: Compacted versus reconstituted states. In Proceedings of the 5th International Conference on Unsaturated Soil, Barcelona, Spain, pp. 113-136.

Tovey, N.K. and Yan, W.K. 1973. Preparation of soils and other geological materials for the SEM. In Proceedings of International Symposium on Soil Structure, Gothenburg, Sweden.

Trabelsi, H., Romero, E. and Jamei, M., 2018. Tensile strength during drying of remoulded and compacted clay: The role of fabric and water retention. Applied Clay Science, 162: 57-68.

Vanapalli, S.K. 1994. Simple test procedures and their interpretation in evaluating the shear strength of an unsaturated soil. Doctoral dissertation, University of Saskatchewan, Canada.

Vanapalli, S.K., Fredlund, D.G., Pufahl, D.E. and Clifton, A.W. 1996. Model for the prediction of shear strength with respect to soil suction. Canadian Geotechnical Journal, 33(3): 379-392.

Vanapalli, S.K., Fredlund, D.G. and Pufahl, D.E. 1999. The influence of soil structure and stress history on the soil water characteristics of a compacted till. Géotechnique, 49: 143–159.

Wang, J.D., Li, P., Ma, Y., Vanapalli, S.K. and Wang, X.G. 2020. Change in pore-size distribution of collapsible loess due to loading and inundating. Acta Geotechnica, 15: 1081–1094.

Yuan, S., Liu, X. and Buzzi, O. 2019. Technical aspects of mercury intrusion porosimetry for clays. Environmental Geotechnics, https://doi.org/10.1680/jenge.16.00039.

Zhai, Q., Rahardjo, H. and Satyanaga, A. 2018. A pore-size distribution function based method for estimation of hydraulic properties of sandy soils. Engineering Geology, 246: 288-292.

Zhang, C. and Lu, N. 2019. Unitary definition of matric suction. Journal of Geotechnical and Geoenvironmental Engineering, 145(2): p.02818004.

Chapter 6. Experimental Studies on Tensile Strength of Compacted Clayey Soil

6.1 Triaxial tensile test

6.1.1 Principle

The direct methods such as the triaxial tensile tests generate a homogeneous tensile force in the entire or a failure cross section of the compacted soil specimen and provide more reliable tensile stress and tensile strength information in comparison to the indirect methods (e.g., Brazilian split test and bending test). Direct tension tests are generally performed in a uniaxial stress state (i.e. uniaxial tensile test). Most uniaxial tensile tests are conducted via the following two approaches: (i) traction on the soil is generated by pulling apart a pair of specially designed moulds containing the soil specimen (e.g., Tschebotarioff et al. 1953; Mikulitsch and Gudehus 1995; Nahlawi et al. 2004; Tang et al. 2015; Cai et al. 2019); and (ii) traction on the soil is provided by the binding the soil specimens directly to the loading system using adhesive substances or a gripping system (e.g., Tang and Graham 2000; Wang et al. 2007; Zhang et al. 2015; Wang et al. 2019). However, unwanted stress field (e.g., friction between the traction system and the soil specimen) may develop and influence the tensile failure of the soil specimen (e.g., Zhang et al. 2010; Cai et al. 2020). Moreover, perfect adherence between the traction system and the soil specimen is not guaranteed (Tang and Graham 2000).

Bishop and Garga (1969) originally developed the testing technique using a triaxial shear strength apparatus for measuring triaxial tensile strength of the intact London clay specimens. In these tests, a necked central section was used to alleviate the drawbacks of the testing technique used in the uniaxial tensile tests. One of the key advantages of using the triaxial apparatus is that it facilitates in investigating the effect of confining pressure on the tensile strength. Following the same principle, Péron (2008) modified the conventional triaxial apparatus and conducted triaxial tensile test on saturated and unsaturated Bioley silt specimens with a reduced central section. The complete setup of the modified triaxial apparatus is shown in Figure 6.1.

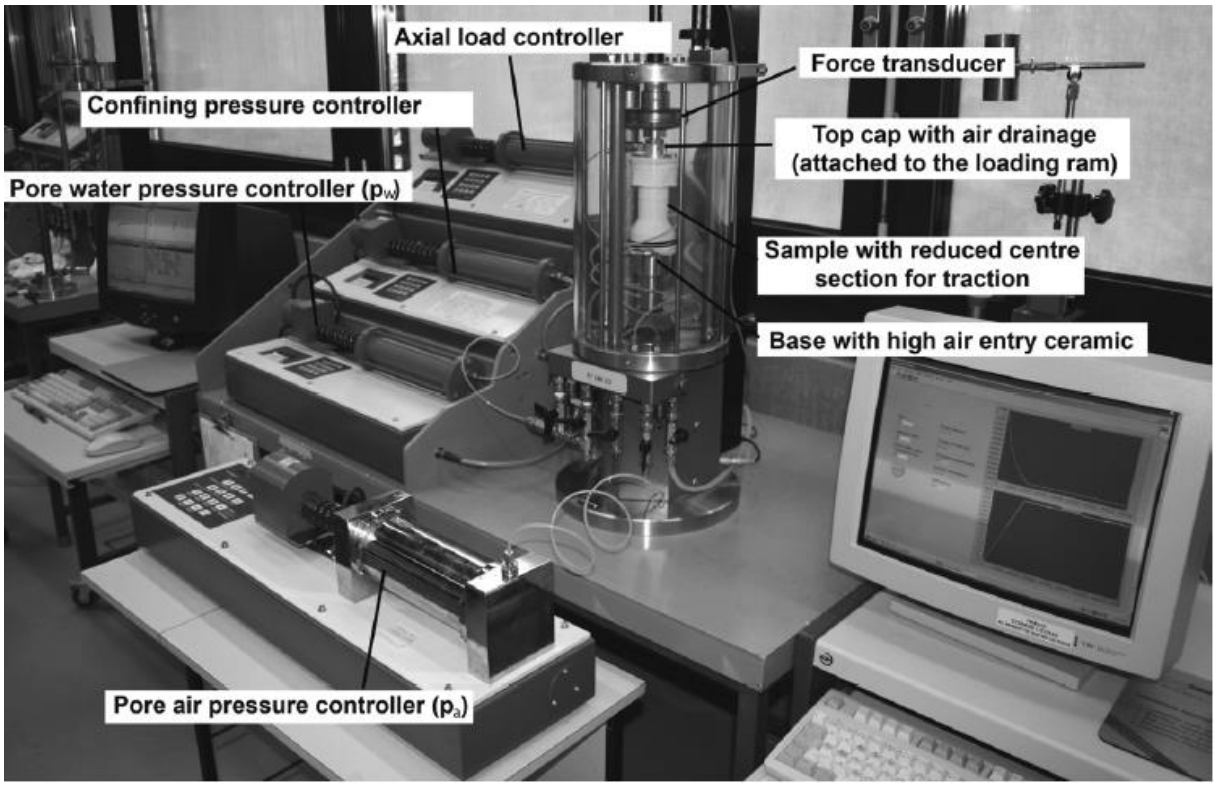

Figure 6.1 Modified triaxial apparatus for triaxial tensile tests on an unsaturated soil specimen (after Péron 2008).

The reconstituted cylindrical soil specimen that was initially subjected consolidation in the triaxial apparatus has been used for testing such that it attains sufficient stiffness and then cut to the desired shape. The geometry and loading of the specimen for triaxial tensile test are shown in Figure 6.2(a). Matric suction was applied to the soil specimen by either water sub-pressure technique or axis translation technique. The applied suction was lower than the air-entry value (AEV) of the studied soil, such that the degree of saturation would remain equal to unity. The stress paths experienced by the specimen during preparation and traction test are presented in Figure 6.2(b). The required confining pressure, pore air pressure and pore water pressure were applied such that the desired matric suction (i.e. the difference between pore air pressure and pore water pressure) and the net confining pressure (i.e. the difference between confining pressure and pore air pressure) could be achieved upon attaining the equilibrium condition (i.e. stress path OB in Figure 6.2(b)). Along with the subsequent reduced triaxial extension (RTE) path (i.e. stress path BC in Figure 6.2(b)), tensile stress develops in the central section of the specimen due to the special geometry. The axial effective stress at the extremity section *E* (σ_E') and the central section *M* (σ_M') during the RTE path

for the unsaturated soil test specimen with matric suction that is less than the air-entry value applied by axis translation technique are respectively, given below.

$$(6.1)\ \sigma_E' = \sigma_E^{net} + s = \left(\sigma_E - u_a\right) + \left(u_a - u_w\right) = \sigma_c - \frac{T}{A_E} - u_w$$

$$(6.2)\ \sigma_M' = \sigma_M^{net} + s = \left(\sigma_M - u_a\right) + \left(u_a - u_w\right) = \sigma_c - \frac{T}{A_M} - u_w$$

where, σ_E and σ_M are axial total stress at the extremity section and that at the central section, respectively; u_a and u_w are the pore air pressure and pore water pressure maintained during the RTE path, respectively; σ_c and T are the confining pressure and the tensile force recorded by the load cell during the RTE path, respectively; A_E and A_M are the area of the extremity and central section, respectively.

In Figure 6.2(b), the minimum axial stress in the central section generated during the RTE path ($\sigma_{M,min}$) could be determined at the moment of the detachment between the top cap and the specimen extremity section E (i.e. no force is transmitted to the specimen through the top cap). At the instant of the top cap detachment, the net axial stress at the extremity section would be zero and can be given by the relationship below.

$$(6.3)\ \sigma_{E,\min}^{net} = \sigma_{E,\min} - u_a = \sigma_c - \frac{T_{\max}}{A_E} - u_a = 0$$

Substituting Eq. (6.3) to Eqs. (6.1) and (6.2) yields

$$(6.4)\ \sigma_{M,\min}^{net} = \sigma_{M,\min} - u_a = \sigma_c - \frac{T_{\max}}{A_M} - u_a = -\left(\frac{A_E}{A_M} - 1\right)\left(\sigma_c - u_a\right)$$

The tensile force provided by the load cell reaches the maximum (T_{max}) when the top cap detaches from the specimen extremity section. In addition, for such a scenario, the axial stress in the central section equals the minimum ($\sigma_{M,min}$). After the top cap detachment, the tensile force cannot transmit via the top cap to the specimen and the test should be stopped. It is worth noting that the minimum axial stress in the central section is influenced by the section area ratio (A_E/A_M),

confining pressure (σ_c), and pore air pressure (u_a). Therefore, higher section area ratio and higher confining pressure would produce lower axial stress (or, higher axial tensile stress) in the central section. For a given specimen shape and the pore air pressure (i.e. atmospheric pressure), sufficient confining pressure is required to produce enough tensile stress to result in tensile failure in the central section.

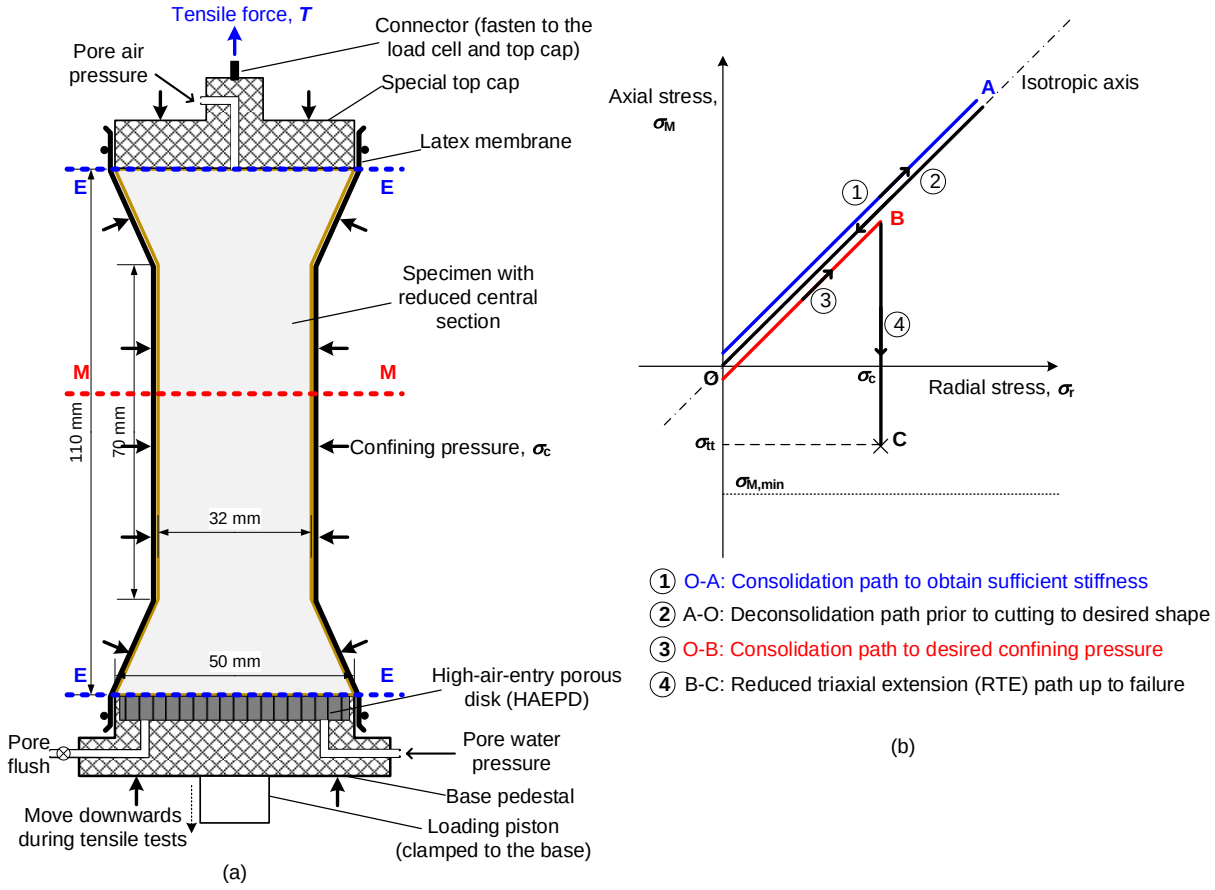

Figure 6.2 (a) Geometry and loading of the reconstituted specimen for triaxial tensile test performed by Péron (2008); (b) Stress paths in the central section of the specimen during preparation and tensile test (modified after Péron (2008)).

6.1.2 Equipment used and specimen preparation

The principle of triaxial tensile tests discussed in the earlier section is extended in the current study. Figure 6.3 shows the setup of the GDS Entry Level Dynamic triaxial testing system (ELDyn) which is used to investigate the influence of matric suction (or gravimetric water content) and confining pressure on the tensile strength of the studied clayey soil. The ELDyn system controls both the pore-air pressure (u_a) and pore-water pressure (u_w) and therefore the matric suction (u_a - u_w) using the axis-translation technique (Hilf 1956). The pore-water pressure is controlled by the

pore water/volume controller (i.e. 5 in Figure 6.3) and applied to the bottom of the specimen through a high air-entry value porous disk (air-entry value = 500 kPa) bonded in the base pedestal (i.e. 13 in Figure 6.3). The pore-air pressure and cell pressure (σ_c) are controlled by a two-channel pneumatic controller (i.e. 8 in Figure 6.3). An optical encoder is embedded inside the pneumatic actuator which is mounted on the beam (i.e. 1 in Figure 6.3) and is used to measure the axial displacement of the loading ram and therefore, the axial displacement of the soil specimen. The axial force acting on the soil specimen is measured by an internal load cell with the capacity of ±5 kN and accuracy of ±5 N (i.e. 3 in Figure 6.3) which measures force independent of cell pressure.

In comparison to the conventional triaxial compression tests, triaxial tensile tests take advantage of the GDS extension top cap with the air drainage, which is fastened to the load cell directly (i.e. 4 in Figure 6.3). The extension top cap is used to prevent cell pressure from acting vertically on the top cap resting on the soil specimen. A vylastic sleeve is used to seal the interface between the extension top cap and top cap, which guarantees the transmission of tensile force from the load cell and the top cap. Such a testing technique assures the reduction of axial stress acting vertically on the specimen below cell pressure during the tensile tests. In the present study, undrained tensile strength of the unsaturated Indian Head till specimens is investigated. Due to this reason, the pore water pressure/volume controller, pore-air pressure controller as well as the pedestal bonded with a high air-entry value porous disk are not used. The regular pedestal (13 in Figure 6.3) and coarse porous disc (12 in Figure 6.3) are used to connect to a valve to the atmosphere. The cell pressure is controlled by the pneumatic controller and connected to the triaxial cell chamber via the valve on the cell top (Figure 6.3).

Some preliminary tests were conducted to determine the feasible way to fabricate a specimen with a reduced central section (i.e. 10 in Figure 6.3). It was assumed that the specimen could be obtained by directly consolidating the prepared slurry in a tube with the same shape as the specimen. The soil slurry was prepared with a water content of 1.2 times liquid limit (i.e. 42%) by mixing dry soil powder and deaired water. A brass mould was fabricated with an internal profile which was same as the soil specimen and was placed in the cylindrical consolidation tube prior to pouring the slurry into the tube (Figure 6.4(a)). The consolidation test was performed on the slurry in the consolidation tube with the maximum preconsolidation pressure of 200 kPa (Figure 6.4(b)). However, this technique did not result in a homogeneous consolidation of the slurry in the mould

due to the irregular specimen shape. Due to this reason, the reconstituted specimen collapsed (i.e. failed) immediately after disassembling the mould (Figure 6.4(c)).

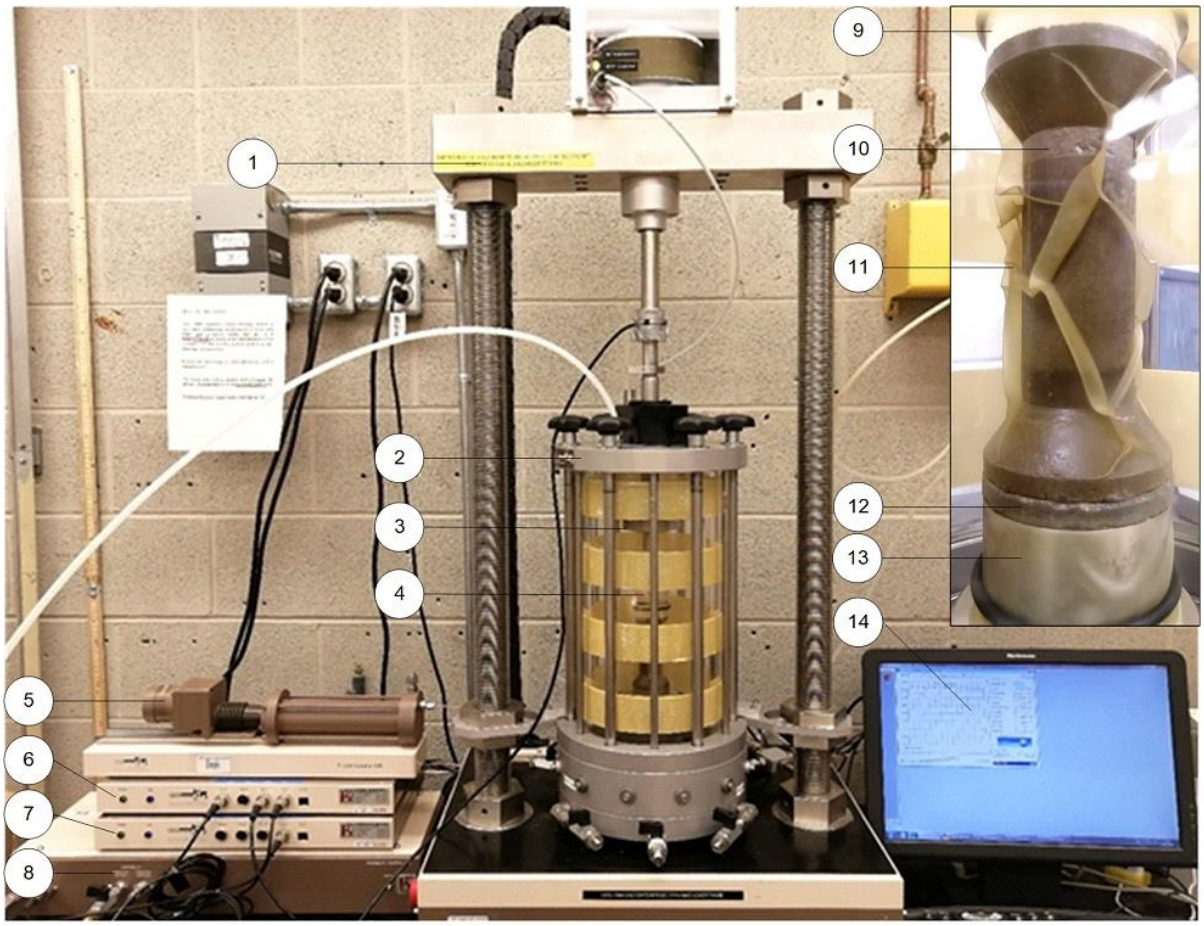

1 Load frame with a beam mounted electro-mechanical actuator
2 Triaxial cell chamber
3 Load cell
4 Extension top cap with connector to atmosphere (fastened to load cell)
5 Pore water pressure/volume controller
6 7 4 Channel dynamic control system (ELDCS)
8 Pneumatic controller (cell pressure and pore air pressure control)
9 Top cap (attached to extension top cap with vylastic sleeve)
10 Soil specimen with reduced central section
11 Latex membrane
12 Porous disc
13 Base pedestal
14 GDSLAB control and acquisition software

Figure 6.3 Setup of triaxial tensile test device at Depart of Civil Engineering, University of Ottawa.

Figure 6.4 The preparation procedure of a reconstituted specimen with the reduced central section by the consolidation test: (a) a cylindric consolidation tube and a disassemble brass mould; (b) the consolidation test conducted on the slurry; (c) the collapsed specimen after disassembling the mould.

Another option to prepare the soil specimen with a reduced central section to fabricate a cylindrical specimen and then to cut it to the desired shape. Péron (2008) used such an approach for preparing a reconstituted silty soil and Li et al. (2020) extended in preparing intact loess specimens. The specimen trimming operation needs to complete with the aid of specially designed devices; due to this reason, the specimen disturbance cannot be well controlled. Therefore, the disassemble brass mould is used in the current study for fabricating the soil specimens with the desired profile by static compaction, which was used in the previous studies (e.g., Lu and Fan 2014). It is found that the brass mould with three equivalent pieces as shown in Figure 6.5(c) would generate less disturbance to the specimen when disassembling in comparison to the mould with two pieces.

Oven-dried Indian Head till soil powder is thoroughly mixed with distilled water to achieve the desired water content, i.e. 17.2% (w_{opt} + 2%), 16.3% (w_{opt} + 1%), 15.3% (w_{opt}), 14.3% (w_{opt} - 1%), and 12.3% (w_{opt} - 3%). The moist soil aggregates are passed through the No. 10 sieve (2 mm) and sealed in a plastic bag for 24 hours. Figure 6.5(a) shows the dimensions of the desired specimen shape. The compaction is completed in four layers with the desired dry density (i.e. maximum dry density, $\rho_{d,max}$ = 1843 kg/m^3) and the identical thickness of 25 mm (Figure 6.5(b)). Figure 6.5(c) shows the as-compacted soil specimen after disassembling the brass mould. The compaction was performed in four layers of equal thickness to achieve uniform dry density in the entire test

specimen. However, the interface at the two compacted soil layers would be weaker in comparison to other sections of the soil specimen. The interfaces between layers act as defects which contribute to the stress heterogeneity while performing the triaxial tensile tests. This is the main error source of the measured tensile strength of compacted soil specimens, which is more significant at the dry-of-optimum side.

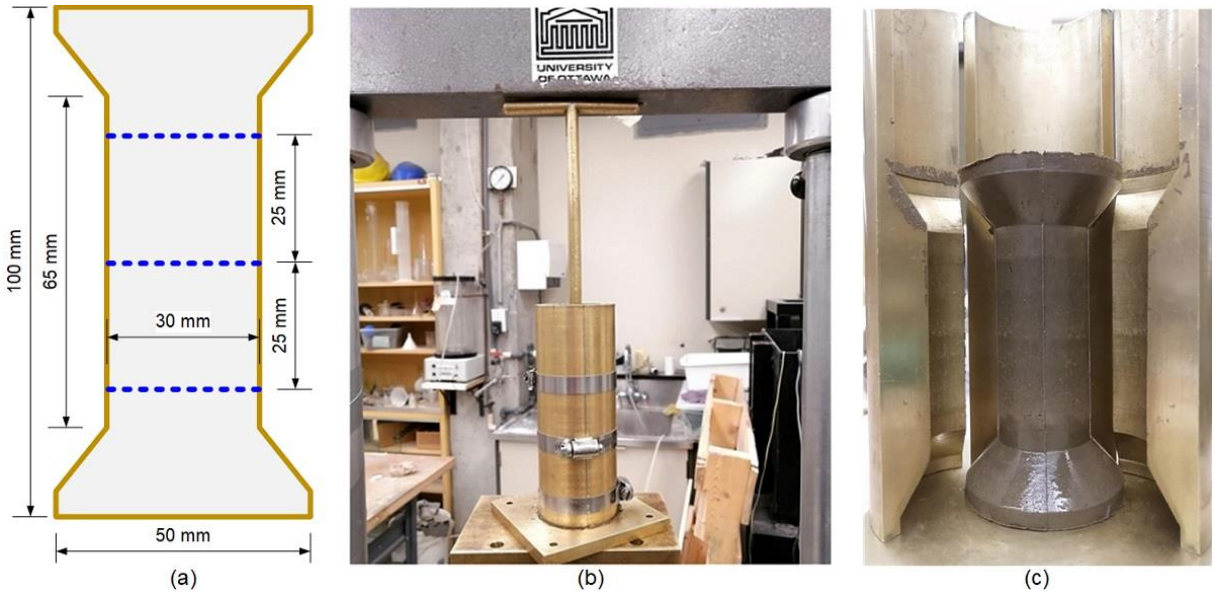

Figure 6.5 (a) Geometry of the compacted soil specimen with reduced central section; (b) Compaction mould with three pieces; (c) As-compacted soil specimen after removing the compaction mould.

6.1.3 Experimental program and test results

For each desired water content, six compacted soil specimens are fabricated and denoted as "IHT-17-TTT-1" through "IHT-17-TTT-6" for example for specimens with water content of 17.2%. Prior to triaxial tensile tests, the soil specimens are sealed using plastic wrap and stored for 24 hours for achieving uniform water content. The mass and dimensions of specimen are measured prior to performing the test. The setup of soil specimen, coarse porous disc and top cap are first assembled along with a latex membrane on the base pedestal as shown in Figure 6.6(a). The lax membrane used in the current study is as the same as that for regular cylindrical specimens. The thickness of the membrane (0.012 inches) is thinner than the usually used membrane in the lab (0.024 inches), to reduce its interaction with the soil specimen. A thin coating of silicone grease is applied to the inside surface of the vylastic sleeve. The flexible vylastic sleeve is then fitted onto the top cap such that the vertical part of vylastic sleeve matches the top cap tightly. Prior to assembling the triaxial cell chamber, the extension top cap is fastened to the load cell via a

connector. After placing the triaxial cell chamber, the reading of load cell is initialized to be zero which cancelled the influence of the extension top cap weight. Then load control (+0.002 kN) command is activated in the GDSLAB software in order to make the load ram lower until the extension top cap locates exactly in the vylastic sleeve. The seating load (+0.002 kN) (corresponding to 1 kPa acting on the upper end of the specimen) is maintained until the beginning of tensile tests to guarantee the good contact between extension top cap, top cap and the upper end of the soil specimen.

The confining pressure is applied first and maintained until the load cell reading recovers to the constant value of seating load (i.e. +0.002 kN). The confining pressures applied in the current experimental program are 25 kPa, 50 kPa, 75 kPa, 100 kPa, 150 kPa, and 200 kPa. During this period (less than 3 minutes), the pore air pressure is maintained to zero by opening the pore flush valve (Figure 6.6(a)). Prior to performing the tensile test, the pore flush valve is closed. The effectiveness of the vylastic sleeve is examined by checking whether the confining pressure is leaking through the air drainage valve connected to the interface between the extension top cap and the top cap (Figure 6.6(a)). It should be noted that compressive deformation of the specimen takes place after achieving the desired confining pressure. In the current study, however, the volumetric deformation of soil specimen is not measured. The experimental program of triaxial tensile tests on the compacted Indian Head till specimens as well as the axial compressive displacement prior to the RTE path is summarized in Table 6.1.

After the first stage of applying confining pressures, the undrained triaxial extension stress path is applied to soil specimen, in which a constant confining pressure is maintained and the axial compressive stress is reduced by moving the load ram upwards. Such a testing technique assures the tensile force provided by the load ram can be effectively transmitted and the compressive load acting on the upper end (section U in Figure 6.6(a)) can be reduced. This is because the top cap and the extension top cap are sealed by the vylastic sleeve and the extension top cap is fastened to the load cell. This stress path is also called as “Reduced Triaxial Extension (RTE)” path. As discussed earlier, the initial compressive stress acting in the central section can be reduced to tensile stress before the top cap detaches away from the upper end of the specimen. This can be attributed to the special profile with reduced central section in the specimen. Figure 6.6(b) presents the details of various stress paths that were subjected to by the soil specimen; starting from the

preparation by static compaction (O-A), then unloading by compaction mould removal (A-O), consolidation (with only pore-air drainage open) path by applying confining pressure (O-B), and finally the reduced triaxial extension (RTE) path under undrained conditions (B-C) until failure. Because the duration required to fully dissipate the excess pore-pressure in clayey soils is rather long compared with the typical construction activities related to earth structures (e.g., earth dams), the undrained condition is imposed to soil specimens while performing the tensile strength tests. The displacement control is used for the RTE path with a displacement rate of -0.01 mm/min (tension as negative and compression as positive in the thesis). The comparative investigation for the displacement rate is conducted using -0.1 mm/min, -0.05 mm/min, and -0.01 mm/min. It is found that both -0.1 mm/min and -0.05 mm/min are not slow enough to assure a good contact condition between the top cap and the upper end of the soil specimen prior to failure. Therefore, the slowest displacement rate of -0.01 mm/min is chosen for the RTE path. The test duration for the RTE path is 325 minutes, which corresponds to the axial tensile displacement of -3.25 mm and axial tensile strain of -5% for the central part with reduced section area of the specimen (initial length is 65 mm).

Table 6.1 Summary of the experimental program of triaxial tensile tests.

Specimen No.	Initial water content, w_i	Initial dry density, $\rho_{d,i}$ (kg/m^3) (initial void ratio, e_i)	*Initial matric suction, s_i (kPa)	Confining pressure, σ_c (kPa)
IHT-17-TTT-1	17.2%	1843 (0.456)	328	25
IHT-17-TTT-2				50
IHT-17-TTT-3				75
IHT-17-TTT-4				100
IHT-17-TTT-5				150
IHT-17-TTT-6				200
IHT-16-TTT-1	16.3%	1843 (0.456)	506	25
IHT-16-TTT-2				50
IHT-16-TTT-3				75
IHT-16-TTT-4				100
IHT-16-TTT-5				150
IHT-16-TTT-6				200
IHT-15-TTT-1	15.3%	1843 (0.456)	596	25
IHT-15-TTT-2				50
IHT-15-TTT-3				75
IHT-15-TTT-4				100
IHT-15-TTT-5				150
IHT-15-TTT-6				200
IHT-14-TTT-1	14.3%	1843	975	25

IHT-14-TTT-2		(0.456)		50
IHT-14-TTT-3				75
IHT-14-TTT-4				100
IHT-14-TTT-5				150
IHT-14-TTT-6				200
IHT-12-TTT-1				25
IHT-12-TTT-2				50
IHT-12-TTT-3	12.3%	1843 (0.456)	1836	75
IHT-12-TTT-4				100
IHT-12-TTT-5				150
IHT-12-TTT-6				200

Note: *Values are measured by filter paper technique using other two identical soil cakes with given water contents and dry density (Table 5.8).

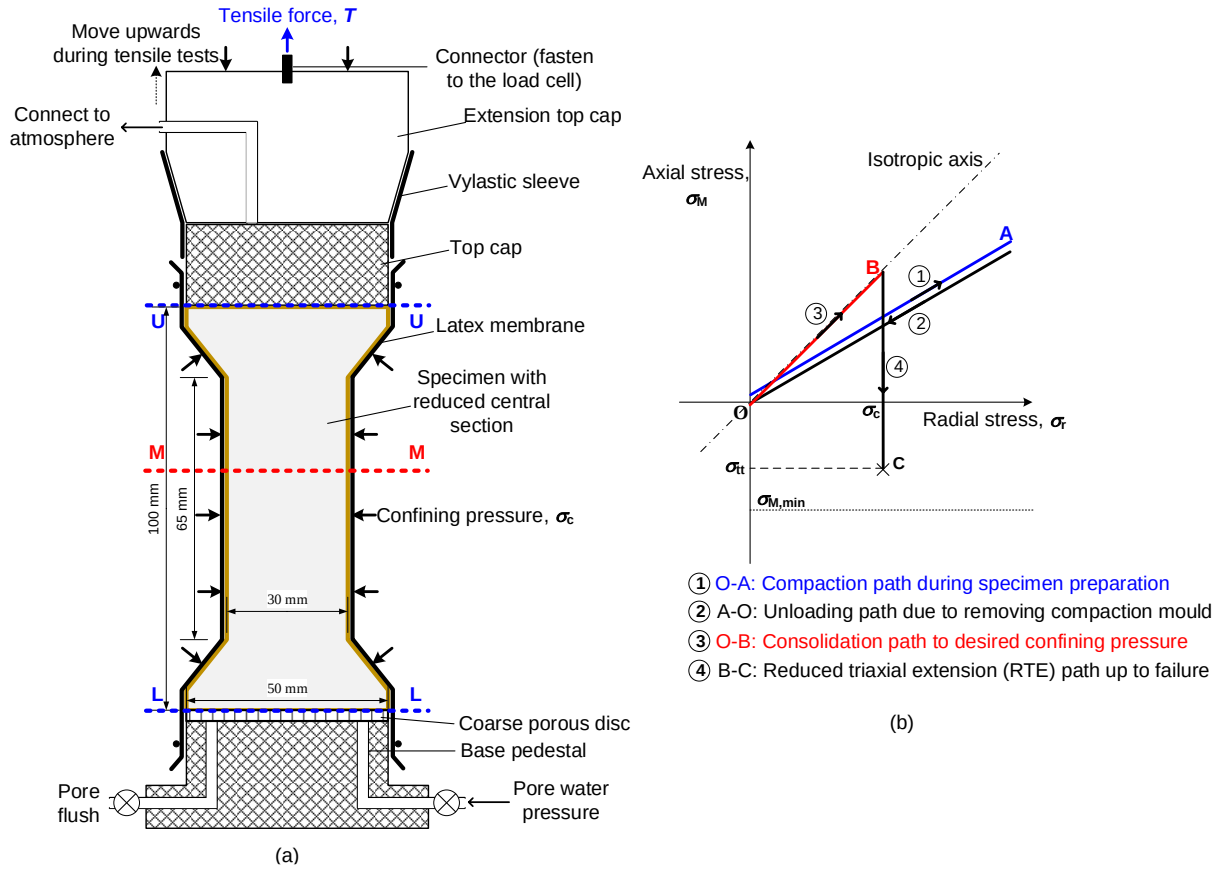

Figure 6.6 (a) Geometry and loading of the reconstituted specimen for triaxial tensile test performed in the current study; (b) Stress paths in the central section of the specimen during preparation and tensile test.

Figure 6.7 shows the typical test results of axial tensile force measured by load cell versus the axial tensile displacement measured by the optical encoder embedded inside the pneumatic actuator. At the beginning of the triaxial tensile test, the membrane shrinks to match the profile of the specimen due to the confining pressure. The load cell reading starts from the seating load (+0.002 kN) and

decreases rapidly to negative values, which means tensile force is provided as the top cap is pulled upwards. The axial force acting on the central section of the soil specimen is calculated based on the free body diagram shown in Figure 6.8. In the diagram, all the components above the potential rupture section (i.e. section *M*) of the specimen in the triaxial cell chamber are considered. The external forces acting on the free body diagram are tensile force provided by the moving upwards load ram (T_1), the confining pressure entering the cell via the valve on the cell top (σ_c), the membrane interaction force (f), and the gravity of all the components. From the free body diagram of the load ram and the load cell, the force equilibrium of the vertical component can be derived:

$$T + \sigma_c \left(A_2 - A_3\right) = G_1 + G_2 + \sigma_c \left(A_2 - A_1\right) + T_1 \tag{6.5}$$

in which T_1 and T are the tensile force provided by the load ram and that measured by the load cell, respectively; A_1, A_2 and A_3 are the section area of the load ram, load cell and connector, respectively; G_1 and G_2 are the gravity of the load ram and the load cell, respectively. From the free body diagram of all the components above the section *M* of the specimen, the force equilibrium of the vertical component can be derived:

$$\begin{aligned} &T_1 + G_1 + G_2 + G_3 + G_4 + G_{tc} + G_{vs} + G + G_m + \sigma_c \left(A_2 - A_1\right) + \sigma_c \left(A_4 - A_3\right) \\ &= \sigma_c \left(A_2 - A_3\right) + \sigma_c \left(A_4 - A_E\right) + \sigma_c \left(A_E - A_M\right) + f + \sigma_M A_M \end{aligned} \tag{6.6}$$

in which, A_4, A_E and A_M are the section area of the extension top cap, the end section and the central section of the specimen, respectively; G_3, G_4, G_{tc}, G_{vs}, G, and G_m are the gravity of the connector, extension top cap, the top cap, the vylastic sleeve, the soil specimen above section *M* and the latex membrane above the section *M*, respectively; f is the membrane interaction force; σ_M is the axial stress acting on the section *M* of the specimen.

It should be noted that the tensile forces T_1 and T in Eqs. (6.5) and (6.6) are considered to point downwards but with negative values, which follows the sign convention of positive values for compression and negative values for tension consistent with the terminology used in soil mechanics. In addition, by initializing the load cell reading at the beginning of the test, the gravities of load cell and extension top cap have been already cancelled in the load cell reading, i.e. G_3 +

$G_4 = 0$. Substituting T instead of T_1 into Eq. (6.6) using the relationship in Eq. (6.5) gives the axial stress acting on the potential rupture section,

$$(6.7)\ \sigma_M = \frac{T}{A_M} + \sigma_c\left(1 - \frac{A_3}{A_M}\right) + \frac{\left(G_{tc} + G_{vs} + G + G_m\right) - f}{A_M}$$

From the above relationship, the maximum tensile stress (or minimum stress) acting on the rupture section M at the moment of failure which is the triaxial tensile strength (σ_{tt}) can be derived from the test results (i.e. Figure 6.7) as

$$(6.8)\ \sigma_{tt} = \frac{T_m}{A_M} + \sigma_c\left(1 - \frac{A_3}{A_M}\right) + \frac{\left(G_{tc} + G_{vs} + G + G_m\right) - f_1}{A_M}$$

in which, T_m is the maximum tensile force (or minimum force) measured by the load cell, and f_1 is the membrane interaction force at failure. After the rupture of the specimen, the tensile force drops down abruptly to the tensile force, T_0 (Figure 6.7) can be estimated according to Eq. (6.7):

$$(6.9)\ \sigma_M = 0 \quad \Rightarrow T_0 = -A_M\left[\sigma_c\left(1 - \frac{A_3}{A_M}\right) + \frac{\left(G_{tc} + G_{vs} + G + G_m\right) - f_1}{A_M}\right]$$

The triaxial tensile strength of the soil specimen can be calculated by substituting Eq. (6.9) into Eq. (6.8):

$$(6.10)\ \sigma_{tt} = \frac{1}{A_M}\left(T_m - T_0\right)$$

It should be noted that the membrane tension (f_1) after failure in Eq. (6.9) is assumed to be as the same as that at the moment of failure in Eq. (6.8). This assumption is reasonable because of the negligible axial displacement (less than 0.5 mm for most tests) and consequently membrane extension occurs during the abrupt drop in tensile force from T_m to T_0 in Figure 6.7.

After the failure of the specimen, the tensile force measured by the load cell increase slightly after the point with stress T_0 in Figure 6.7. This is due to the extension of the membrane surrounding the rupture section of the specimen. The tensile force then decreases gradually until the test ends

due to the release of the initially folded membrane surrounding the soil specimen away from the rupture section. It is worth noting that the stress distribution in the membrane is not uniform because the membrane is not consistent with the exact shape of the specimen profile. Hence, the increase in tensile force measured by the load cell might be negligible or in certain cases significant after the specimen failure due to complicated stress distribution in the latex membrane. However, the tensile force measured by the load cell will eventually drop gradually due to the relaxation of the membrane when the folded part is activated. The test results for all the specimens tested are summarized in Table 6.2. The photos of the specimen in the green, red and blue boxes correspond to the moments at the beginning of RTE path starts, at tensile failure and at the end, respectively. The red box is located after the peak because the peak is difficult to be detected visually due to the limitation in resolution of the digital camera. It is worth noting that no failure is observed in the specimen IHT-12-TTT-1 after the test. This is because the maximum tensile stress (or the minimum stress) generated in the central section in the triaxial tensile test is bounded by the condition of Eq. (6.4). Due to the low confining pressure (i.e. 25 kPa), the maximum tensile stress acting on the central section is less than the tensile strength of specimen IHT-12-TTT-1 prior to the detachment of top cap. Additionally, the rupture is not observed in specimen IHT-16-TTT-6 after the tests, which is subjected to high confining pressure of 200 kPa. This phenomenon may be associated with failure modes which is significantly influenced by the confining pressure.

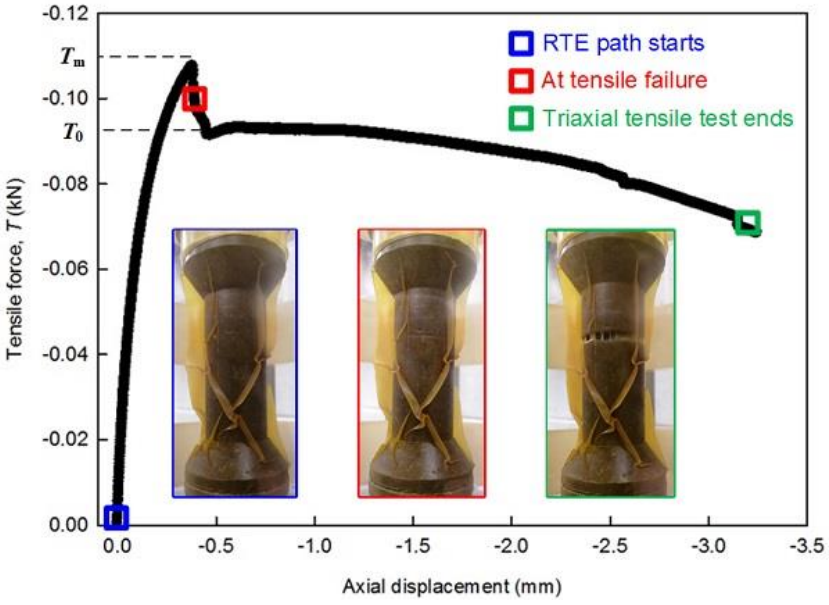

Figure 6.7 Typical triaxial tensile test result of the tensile force versus axial displacement.

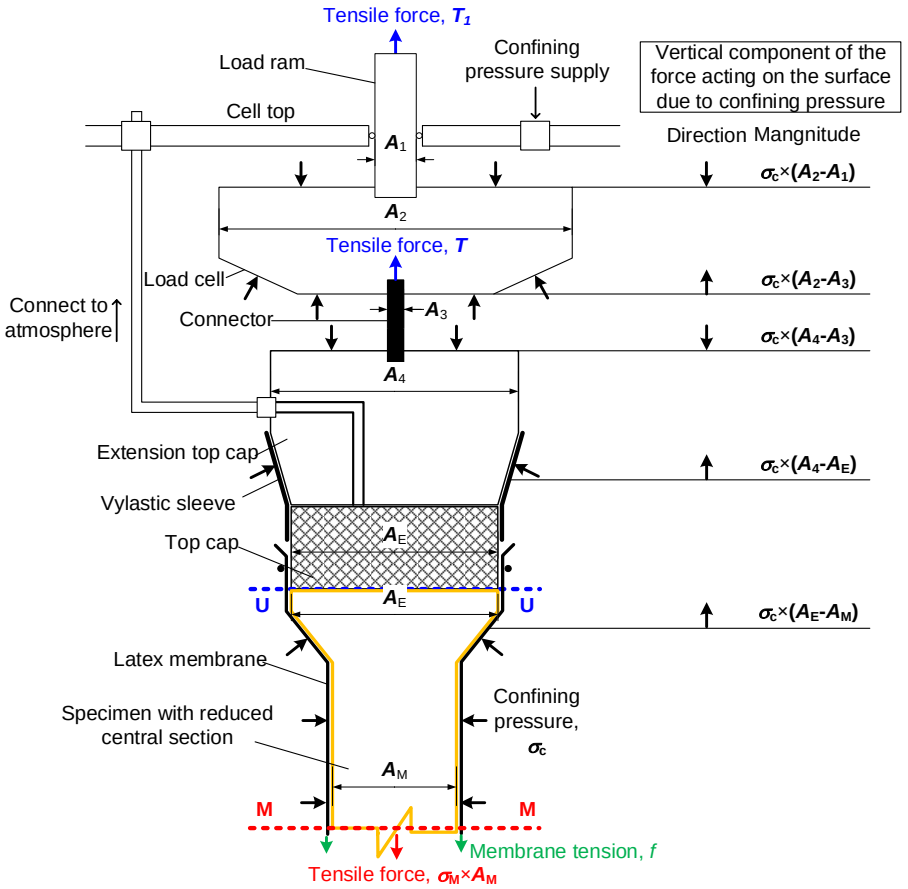

Figure 6.8 Free body diagram above the potential rupture section of the soil specimen during the RTE path.

Table 6.2 The estimation of the triaxial tensile strength of all the specimens.

Specimen No.	Confining pressure, σ_c (kPa)	Maximum tensile force, T_m (kN)	Tensile force after failure, T_0 (kN)	*Tensile strength, σ_{tt} (kPa)
IHT-17-TTT-1	25	-0.029	-0.024	-7.07
IHT-17-TTT-2	50	-0.018	-0.005	-18.39
IHT-17-TTT-3	75	-0.045	-0.042	-4.24
IHT-17-TTT-4	100	-0.040	-0.036	-5.66
IHT-17-TTT-5	150	-0.040	-0.038	-2.83
IHT-17-TTT-6	200	-0.027	-0.026	-1.41
IHT-16-TTT-1	25	-0.044	-0.025	-26.88
IHT-16-TTT-2	50	-0.054	-0.040	-19.81
IHT-16-TTT-3	75	-0.049	-0.035	-19.81
IHT-16-TTT-4	100	-0.064	-0.058	-8.49
IHT-16-TTT-5	150	-0.077	-0.066	-15.56
IHT-16-TTT-6	200	-0.027	-0.008	**No Failure**
IHT-15-TTT-1	25	-0.040	-0.025	-21.22
IHT-15-TTT-2	50	-0.047	-0.041	-8.49
IHT-15-TTT-3	75	-0.065	-0.053	-16.98
IHT-15-TTT-4	100	-0.048	-0.031	-24.05
IHT-15-TTT-5	150	-0.072	-0.037	-49.51
IHT-15-TTT-6	200	-0.075	-0.068	-9.90

IHT-14-TTT-1	25	-0.019	-0.010	-12.73
IHT-14-TTT-2	50	-0.044	-0.042	-2.83
IHT-14-TTT-3	75	-0.058	-0.037	-29.71
IHT-14-TTT-4	100	-0.085	-0.071	-19.81
IHT-14-TTT-5	150	-0.101	-0.090	-15.56
IHT-14-TTT-6	200	-0.129	-0.125	-5.66
IHT-12-TTT-1	25			**Top cap detaches**
IHT-12-TTT-2	50	-0.091	-0.046	-63.66
IHT-12-TTT-3	75	-0.085	-0.048	-52.34
IHT-12-TTT-4	100	-0.079	-0.065	-19.81
IHT-12-TTT-5	150	-0.123	-0.097	-36.78
IHT-12-TTT-6	200	-0.167	-0.155	-16.98

Note: *Tensile strength is calculated based on Eq. (6.10), in which $A_M = \pi \bullet (0.03)^2/4$ m^2.

After the test ends, the extension top cap is forced to detach from the top cap by providing sufficient air pressure via the valve connecting to the air drainage pipe of the extension top cap. Then the triaxial cell chamber is disassembled. The gravimetric water contents and void ratios of the upper end, rupture zone, and lower end of the specimen are measured by oven-drying and wax immersion technique (procedures are described in Chapter 5), respectively. The measurements of water contents and void ratios after tests are summarized in Table 6.3. Both water contents and void ratios in Table 6.3 are the average values derived from two pieces of the different sections in test specimens after failure. Based on the measurements of water contents in the rupture zone, the decrease in average water content after tests are 0.2%, 0.4%, 0.4%, 0.0%, and 0.9%, respectively for the specimens with initial water contents for IHT-17 (w_i = 17.2%), IHT-16 (w_i = 16.3%), IHT-15 (w_i = 15.3%), IHT-14 (w_i = 14.3%), and IHT-12 (w_i = 12.3%). The moisture loss in the central section may be associated with evaporation during the setup of membrane and top cap at the beginning to the test and evaporation during taking photos of rupture zone prior to measuring the water contents. The latter source might be dominant, because the rupture section of the intact specimen is not open to the atmosphere at the beginning and operation of setup is usually completed quickly (i.e. in one minute). Therefore, it is reasonable to assume that the water content of soil specimen at failure is close to the corresponding initial water content. As for IHT-17-TTT, IHT-16-TTT, IHT-15-TTT, IHT-14-TTT, and IHT-12-TTT, the sample standard derivation of the void ratios taken from three different sections are 0.01, 0.01, 0.04, 0.06, and 0.08, respectively. The uniformity of soil specimens could be examined based on the measured void ratios after the test. Rather large variations in void ratios are observed for some specimens, which include IHT-15-TTT-2, IHT-14-TTT-1, IHT-14-TTT-2, and all the IHT-12 specimens. The nonuniformity of those specimens might be mainly induced by the specimen fabrication using the static compaction

approach. It is difficult to produce uniform soil specimens by compacting them in four sublayers on the dry-of-optimum, compared with those on the wet-of-optimum side. More sublayers are recommended for the specimen fabrication by compaction, especially for specimens at the dry-of-optimum side.

Table 6.3 Summary of the water content and void ratio of soil specimens after the test.

Specimen No.	Gravimetric water content, w_f			Void ratio, e_f		
	Upper end	Rupture zone	Lower end	Upper end	Rupture zone	Lower end
IHT-17-TTT-1	16.5%	17.3%	16.9%	0.377	0.383	0.403
IHT-17-TTT-2	16.3%	16.9%	16.5%	0.374	0.384	0.390
IHT-17-TTT-3	16.7%	17.0%	17.3%	0.392	0.361	0.380
IHT-17-TTT-4	16.1%	16.4%	16.5%	0.378	0.371	0.373
IHT-17-TTT-5	15.8%	17.2%	16.2%	0.400	0.402	0.368
IHT-17-TTT-6	16.9%	17.2%	16.2%	0.396	0.407	0.373
IHT-16-TTT-1	15.4%	16.1%	15.4%	0.359	0.366	0.354
IHT-16-TTT-2	15.1%	15.9%	15.3%	0.350	0.384	0.339
IHT-16-TTT-3	15.5%	16.1%	15.6%	0.391	0.427	0.363
IHT-16-TTT-4	15.5%	15.9%	15.4%	0.344	0.344	0.340
IHT-16-TTT-5	15.6%	15.7%	15.6%	0.347	0.353	0.324
IHT-16-TTT-6	**No Failure**					
IHT-15-TTT-1	14.7%	15.0%	14.8%	0.353	0.386	0.408
IHT-15-TTT-2	13.8%	13.5%	13.8%	0.471	0.651	0.405
IHT-15-TTT-3	15.0%	15.1%	14.8%	0.354	0.356	0.362
IHT-15-TTT-4	14.7%	15.1%	15.4%	0.496	0.509	0.478
IHT-15-TTT-5	15.2%	15.1%	14.7%	0.386	0.360	0.375
IHT-15-TTT-6	14.8%	15.3%	14.9%	0.330	0.340	0.349
IHT-14-TTT-1	14.6%	14.2%	14.0%	0.335	0.516	0.564
IHT-14-TTT-2	13.6%	13.7%	13.6%	0.392	0.578	0.531
IHT-14-TTT-3	13.9%	14.8%	13.7%	0.338	0.329	0.375
IHT-14-TTT-4	14.3%	14.8%	14.0%	0.358	0.391	0.459
IHT-14-TTT-5	14.2%	14.7%	14.2%	0.354	0.335	0.356
IHT-14-TTT-6	13.2%	13.7%	13.8%	0.320	0.314	0.368
IHT-12-TTT-1	**Top cap detaches**					
IHT-12-TTT-2	11.7%	11.2%	11.6%	0.373	0.557	0.383
IHT-12-TTT-3	11.4%	11.4%	11.6%	0.316	0.341	0.459
IHT-12-TTT-4	11.6%	11.5%	11.4%	0.462	0.366	0.436
IHT-12-TTT-5	11.4%	11.6%	11.2%	0.368	0.315	0.462
IHT-12-TTT-6	11.2%	11.5%	11.4%	0.300	0.315	0.431

6.1.4 Interpretation of triaxial tensile test results

6.1.4.1 Variation of triaxial tensile strength with matric suction and confining pressure

The tensile strength of compacted clayey soils is dependent on several factors such as the water content (or soil suction), dry density, soil microstructure (e.g., Nahlawi et al. 2004; Lakshmikantha

et al. 2012; Tang et al. 2015; Trabelsi et al. 2018). In addition to those internal factors, tensile strength of compacted clayey soils is found to be influenced by external factors, such as test method (direct or indirect methods), loading rate (e.g., Stirling et al. 2015; Zhang et al. 2015; Tollenaar et al. 2017; Li 2018). Comparative studies on the tensile strength of compacted clayey soil using both direct and indirect methods have been conducted (e.g., Stirling et al. 2015; Li 2018). The difference in the measured tensile strengths on the identical compacted specimen by direct and indirect methods might stem from two reasons (Yin and Vanapalli 2018): (i) the assumptions for estimating tensile stress by indirect methods are questionable, for example, the need for brittle failure in Brazilian split test cannot be satisfied for soft compacted clayey specimens (e.g., at wet-of-optimum side); (ii) the tensile strength is stress-state dependent. Based on the comprehensive review in Chapter 2, it is found that the studies on the tensile strength of unsaturated soils in geotechnical and geoenvironmental engineering community focus on the influence of internal influence factors. There is limited attention that has been paid to by the researchers towards understanding the influence of external stress state.

Figure 6.9 presents the 3D plot of the variation of triaxial tensile strength with matric suction and confining pressure. Kodikara (2012) proposed the "tensile failure surface" to describe the relationship among the void ratio, water content and external stresses at tensile failure. The terminology "tensile failure surface" is not used here due to the possible combined tensile-shear failure under high confining pressures. It is obvious that triaxial tensile strength is not a monotonic function of matric suction or the net confining pressure. Due to this reason, the 2D plots provide a better visualization of the triaxial tensile strength with respect to the matric suction and net confining pressure as shown in Figure 6.10 and Figure 6.12, respectively.

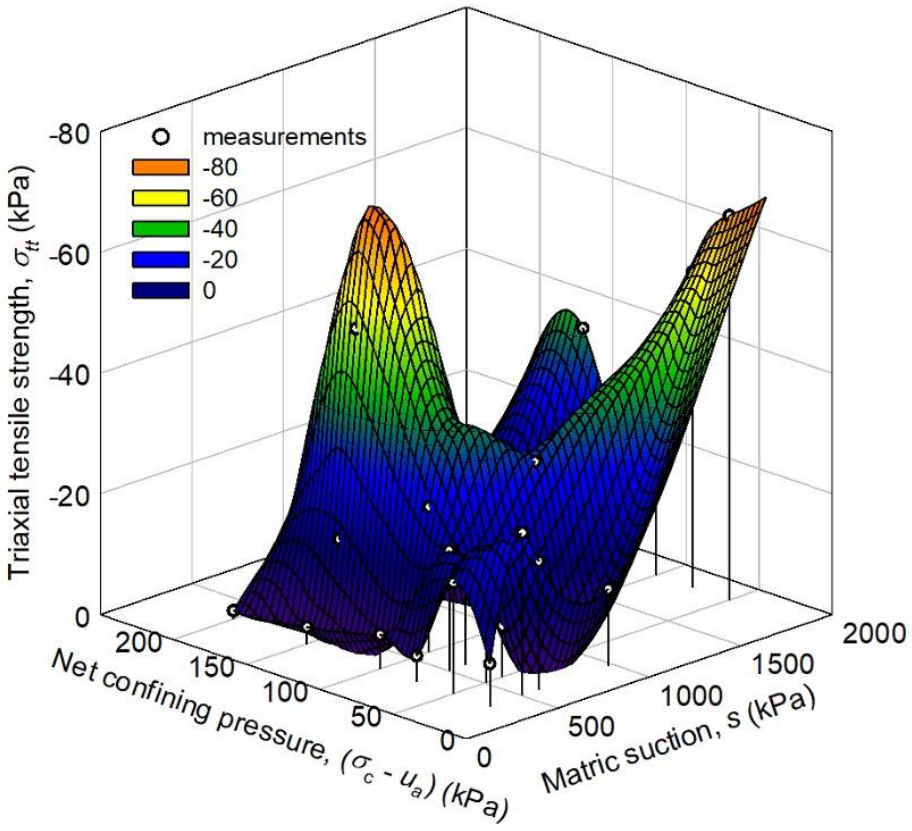

Figure 6.9 3D plot of triaxial tensile strength versus net confining pressure and matric suction.

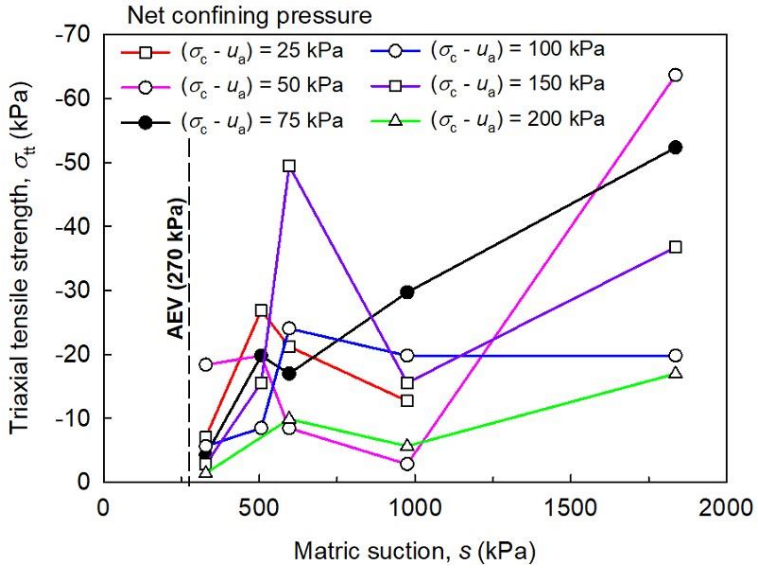

Figure 6.10 Variation of tensile strength with matric suction at different confining pressure.

For all the net confining pressures in Figure 6.10, the tensile strength increases firstly from matric suction of 328 kPa to the peak at matric suction of 506 kPa (i.e. confining pressures of 25 kPa, 50 kPa and 75 kPa) or 596 kPa (i.e. confining pressure of 100 kPa, 150 kPa, and 200 kPa). After the

peak, the tensile strength decreases and then increases, except for those under the confining pressures of 25 kPa. For that level of confining pressure, some test results are missing due to the limitations associated with the testing technique. The variation of tensile strength with matric suction (or degree of saturation) can be explained by the concept of "suction stress" in unsaturated soils proposed by Lu and Likos (2006) incorporating with the change in microstructure of compacted clayey soils (e.g., Tang et al. 2015; Trabelsi et al. 2018).

In order to exploit the relationship between the tensile strength and soil suction, the tensile strength characteristic curve (TSCC) as well as the soil-water characteristic curve (SWCC) are presented in Figure 6.11. The tensile strength under the confining pressures of 25 kPa (i.e. $\sigma_{tt,25}$) for specimens with a given initial water content and degree of saturation is shown in Table 6.4. Due to the possible different failure mode under high confining pressures (e.g., Guan 1983; Zhou 1984), only the triaxial tensile strength under low confining pressures are considered as the "true" tensile strength. In addition, due to the limited range of compaction water contents, the tensile strength of compacted Indian Head till at low degree of saturation is not investigated in the present study. The possible variation of TSCC is speculated by the blue dash line in Figure 6.11 based on the observations on the compacted clayey soil in previous studies, which demonstrated that the tensile strength reaches the maximum value lower than the optimum condition (e.g., Lakshmikantha et al. 2012; Tang et al. 2015; Trabelsi et al. 2018). As suggested in Vanapalli et al. (1999), three distinct zones are identified on the SWCC plot in the entire suction range, i.e. residual zone (zone I), transition zone (zone II) and boundary effect zone (zone III). For compacted clayey soils, dispersed structure and flocculated (or aggregated) structure develope in the specimen at the wet-of-optimum side and that at the dry-of-optimum side, respectively. For aggregated soil specimens, two different levels of pores, i.e. inter-aggregate pores and intra-aggregate pores are observed (Alonso et al. 1987; Alonso et al. 2010).

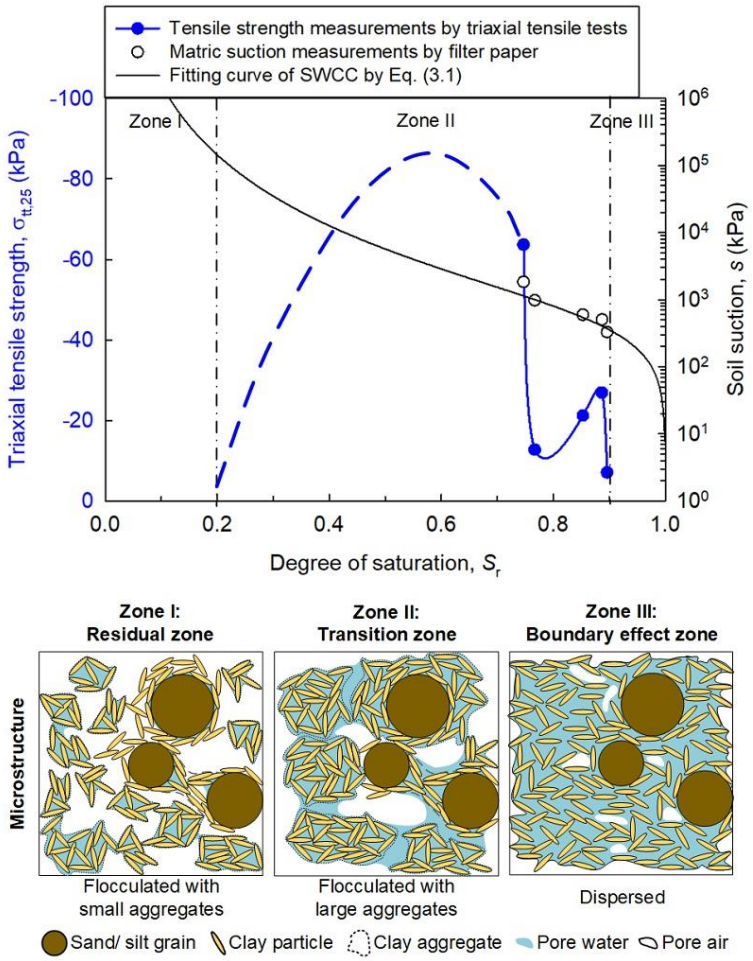

Figure 6.11 Tensile strength characteristic curve and the corresponding microstructure features in three different zones.

In zone I (residual zone), the degree of saturation is extremely low (e.g., $S_r < 0.2$) and the small clay aggregates form with sprayed water entrapped within the intra-aggregate pores. The sprayed water would firstly saturate the intra-aggregate pores and then the inter-aggregate pores for the commonly used preparation procedure for compacted clayey specimens (i.e. to mix the dry soil with water and then to compact the soil-water mixture to the desired state). Therefore, the preparation of specimen for tensile tests is difficult for the compacted specimen with extremely low water content, for example for the triaxial tensile test in the current study. The tensile strength of compacted clayey soil with extremely low water content might only be conducted with the specimen which is directly compacted in the tensile test apparatus (e.g., Xu et al. 2018). It is found that the tensile strength of compacted specimen with water content in the residual zone is rather low compared to the maximum tensile strength. Such a behavior may be explained as follows. It is well accepted that the capillary bonding force among aggregates contributes to the tensile

strength of compacted clayey specimen at the dry-of-optimum side (e.g., Aluko and Koolen 2000). In other words, the aggregates at saturated or unsaturated conditions in zone I would not rupture due to the tensile force acting on the whole specimen. Therefore, the clay aggregates would act like sand grains and the water bridges among aggregates contribute to the capillary bonding force and tensile strength of the compacted specimen (Tang et al. 2015). However, the amount of water bridges is limited because most water is adsorbed with clay aggregates. Therefore, the high suction in zone I, which mainly stems from the intra-aggregate adsorbed water, has a limited contribution to the capillary bonding force between aggregates. Due to the above explained mechanism and the limited experimental measurements in zone I, the tensile strength at zone I is assumed to be negligible, which is a reasonable approximation.

Table 6.4 Summary of the triaxial tensile strength at low confining pressure (e.g., σ_c = 25 kPa) and the corresponding degree of saturation and soil suction.

Specimen No. (initial water content)	Confining pressure, σ_c (kPa)	Triaxial tensile strength, $\sigma_{tt,25}$ (kPa)	Degree of saturation, S_r	Soil suction (kPa)
IHT-17 (w_i = 17.2%)	25	-7.07	0.896	328
IHT-16 (w_i = 16.3%)	25	-26.88	0.887	506
IHT-15 (w_i = 15.3%)	25	-21.22	0.853	596
IHT-14 (w_i = 14.3%)	25	-12.73	0.767	975
IHT-12 (w_i = 12.3%)	50*	-63.66	0.747	1836

Note: *Tensile strength of IHT-12 at confining pressure of 25 kPa is missing due to the detachment of top cap. Thus, the tensile strength at confining pressure of 50 kPa is used to represent the value under low confining pressure.

In zone II (transition zone) where the degree of saturation is in the middle range (e.g., .0.2 < S_r < 0.9), with the increase in the compaction water content, more water bridges form and the capillary bonding force between clay aggregates increases (Fisher 1926; Yin and Vanapalli 2018). The suction decreases with an increase in the degree of saturation, so the combined effect of the increase in number of water bridges and the decrease in suction in the inter-aggregated pores results in an up-and-down in the variation of capillary bonding force between clay aggregates. It should be noted that the tensile strength drops gradually to a low value and then recovers marginally at the optimum condition (i.e. S_r =0.8 in Figure 6.11). This phenomenon may be attributed to the filling of inter-aggregate pores of a particular size class by the water bridges after

compaction. The degree of saturation in inter-aggregate pores increases remarkably with a limited decrease in soil suction. The filling of part inter-aggregate pores brings about another type of capillary bonding force, i.e. negative pore water pressure (Lu et al. 2007) exerting within the saturated inter-aggregate pores. Therefore, the negative pore water pressure in the saturated inter-aggregate pores and the force exerting through the water bridges in unsaturated inter-aggregate pores contribute together to the capillary bonding force and tensile strength among clay aggregates.

In zone III (boundary effect zone), the degree of saturation is typically close to unity (i.e. $S_r > 0.9$) with disconnected air bubbles entrapped in the specimen. As the compaction water content is greater than the optimum water content, the microstructure would change from flocculated structure to dispersed structure (Figure 6.11). This is because the water entrapped with clay aggregated is forced to escape due to excess intra-aggregate pore water pressure during compaction. The clay particles would be rearranged from aggregated assembly to individual dispersed structure (edge-to-edge, or edge-to-face, or face-to-face). The capillary bonding force among clay particles is the main source of tensile strength of compacted clayey soils in zone III. Due to the limited increase in the degree of saturation, the reduction in the soil suction results in the decrease in tensile strength of compacted clayey soils.

Figure 6.12 shows the variation of tensile strength with net confining pressure for all the compacted Indian Head till specimens with different matric suctions. A common variation trend for the specimens with different water content (or matric suction) presented is the double-peak behavior. The double-peak behavior is more pronounced for the specimens with high matric suction (e.g., in boundary effect zone) than those with low matric suction (e.g., in transition zone). When the value of confining pressure is low, tensile strength decreases with an increase in the confining pressures. After a certain value of confining pressure, the tensile strength increases and then decreases again until a relatively high confining pressure (e.g., 150 kPa). The non-monotonic variation with respect to the confining pressure is a result of the following two competing factors: (i) the volumetric deformation under different levels of confining pressures prior to specimen failure which gives different values of dry density at failure; and (ii) the transition of failure modes from tensile failure to shear failure as the confining pressure increases.

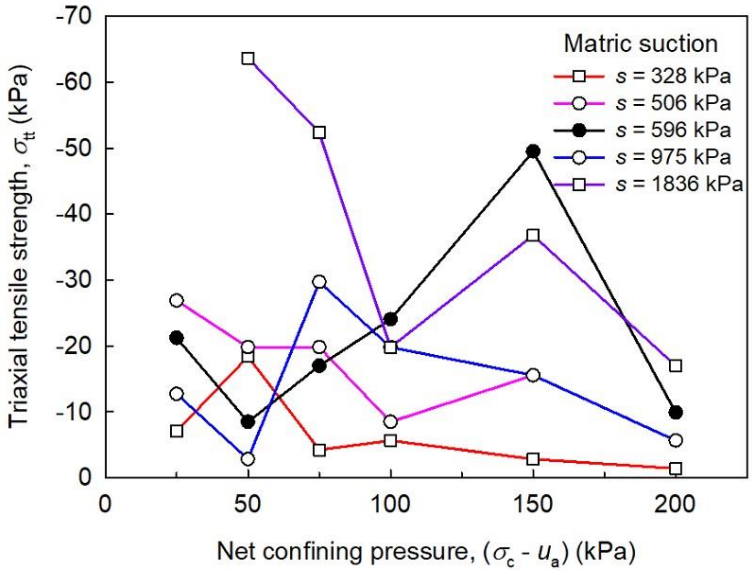

Figure 6.12 Variation of tensile strength with confining pressure at different matric suction.

The first influencing factor is the volumetric deformation which may contribute to different unsaturated states at failure even for the specimens with initial identical conditions (i.e. water content and dry density). Table 6.5 summarizes the axial displacement of all the specimens at failure, which includes the axial compressive displacement prior to RTE path as well as the subsequent axial tensile displacement at failure. It is found that the tensile displacement at failure under high confining pressures (i.e. 150 kPa and 200 kPa) is significantly greater than that under low confining pressures (i.e. 25 kPa and 50 kPa). Based on the measurements of void ratio after test in Table 6.3, the variation of void ratio after test with respect to the confining pressure is shown in Figure 6.13. It is found that the dependency on void ratio (or dry density) is more pronounced for the specimen with initial water content less than the optimum condition. This phenomenon has been explained by Tang et al. (2015). At the dry-of-optimum condition, the decrease in void ratio (or increase in dry density) would result in the increase in inter-aggregate degree of saturation (or macroscopic degree of saturation) and a slight decrease in soil suction. Consequently, the capillary bonding force exerted by the water bridges on the clay aggregates would increase. Therefore, the maximum tensile strength of IHT-15-TTT (i.e. suction is 596 kPa) and IHT-14-TTT (i.e. suction is 975 kPa) which are reached at the confining pressure of 150 kPa and 75 kPa, respectively, are due to the decrease in void ratio at failure. At the wet-of-optimum side, on the other hand, the decrease in void ratio would lead to increase in the degree of saturation as well as remarkable reduction in the soil suction, which counterbalance part of contribution to tensile strength from the

increase in the degree of saturation. Therefore, the first factor is not so pronounced for the wet-of-optimum specimens in comparison to the dry-of-optimum specimens. It is found that the tensile strength of IHT-17-TTT and IHT-16-TTT decreases as the confining pressure increases, which is similar to the drained triaxial tensile test results on intact London clay obtained by Bishop and Garga (1969). The London clay specimens might have the uniform microstructure due to the saturation ("saturation" here means the degree of saturation of the intact specimen increases to one) and consolidation procedure prior to the reduced triaxial extension path.

Table 6.5 Summary of the axial displacement during the triaxial tensile tests.

Specimen No.	Initial state		Confining pressure, σ_c (kPa)	Axial compressive displacement prior to RTE path, $\Delta\delta_c$ (mm)	Axial tensile displacement at failure, $\Delta\delta_t$ (mm)
	Initial water content, w_i	Initial dry density, $\rho_{d,i}$ (kg/m^3)			
IHT-17-TTT-1	17.2%	1843	25	+0.535	-0.337
IHT-17-TTT-2			50	N/A	-0.176
IHT-17-TTT-3			75	+0.404	-1.453
IHT-17-TTT-4			100	N/A	-0.380
IHT-17-TTT-5			150	N/A	-0.350
IHT-17-TTT-6			200	N/A	-0.163
IHT-16-TTT-1	16.3%	1843	25	N/A	-0.205
IHT-16-TTT-2			50	N/A	-0.336
IHT-16-TTT-3			75	N/A	-0.281
IHT-16-TTT-4			100	N/A	-0.898
IHT-16-TTT-5			150	+1.013	-1.383
IHT-16-TTT-6			200	N/A	**No failure**
IHT-15-TTT-1	15.3%	1843	25	+0.323	-0.161
IHT-15-TTT-2			50	+0.639	-0.295
IHT-15-TTT-3			75	+0.765	-0.812
IHT-15-TTT-4			100	+0.169	-0.341
IHT-15-TTT-5			150	N/A	-0.882
IHT-15-TTT-6			200	N/A	-0.693
IHT-14-TTT-1	14.3%	1843	25	+0.343	-0.113
IHT-14-TTT-2			50	+0.573	-0.295
IHT-14-TTT-3			75	+0.521	-0.273
IHT-14-TTT-4			100	+1.380	-0.736
IHT-14-TTT-5			150	N/A	-0.913
IHT-14-TTT-6			200	N/A	-2.524
IHT-12-TTT-1	12.3%	1843	25	N/A	**Top cap detaches**
IHT-12-TTT-2			50	N/A	-0.237
IHT-12-TTT-3			75	N/A	-0.193
IHT-12-TTT-4			100	N/A	-0.218
IHT-12-TTT-5			150	N/A	-0.388
IHT-12-TTT-6			200	N/A	-0.515

Note: N/A: not available due to missing data.

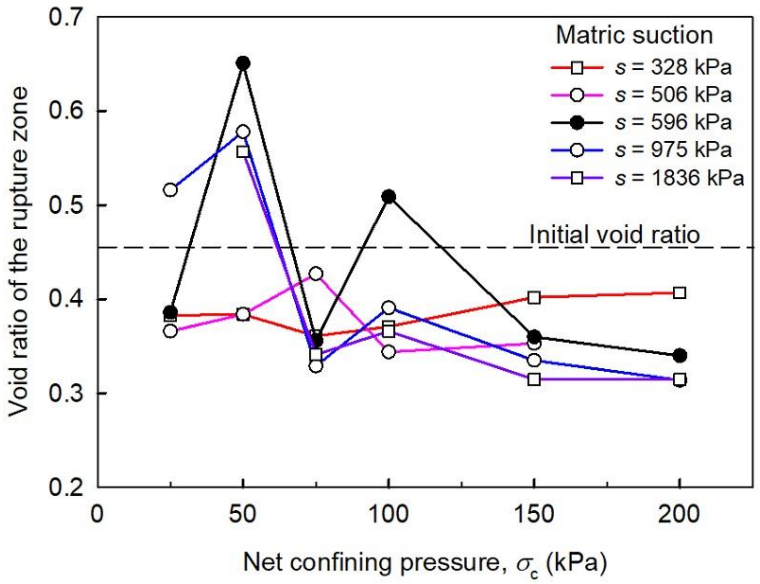

Figure 6.13 The void ratio of the rupture zone measured after the test.

The second influencing factor is the failure mode which is dependent on the confining pressure. The failure mode of soil specimens is found to transfer from pure tensile failure under low confining pressures to combined tensile-shear failure and pure shear failure under high confining pressures (Wong et al. 2017). Zhou (1984) proposed an analytical expression to predict the transition point of confining pressure, σ_{cI} from pure tensile failure to combined tensile-shear failure as follows:

(6.11) $\sigma_{cI} = c\tan(45° + \phi/2)$

where, c and ϕ are the cohesion and internal friction angle of the studied soil, respectively. For the unsaturated compacted clayey soil, internal friction angle in saturated condition (ϕ') is used as a first approximation. The cohesion could be the "apparent cohesion" (c_{app}) taking the contribution of soil suction into consideration (Fredlund and Rahardjo 1993), which essentially reflects the shear strength without confinement:

(6.12) $c_{app} = c' + s\tan\phi^b$

where, ϕ^b is the friction angle with respect to soil suction, c' is the cohesion in saturation condition. Vanapalli et al. (1996) proposed the predictive model to describe the nonlinear behavior of shear strength in unsaturated soils using the SWCC as a tool:

(6.13) $\tau_{ff} = c' + sS_r^{\kappa} \tan\phi' + (\sigma - u_a)\tan\phi'$

where, κ is the fitting parameter which reflects the scaling effect of the contribution to shear strength for the degree of saturation, and (σ - u_a) is the net normal stress. Hence, the "apparent cohesion" could be estimated as

(6.14) $c_{app} = c' + sS_r^{\kappa} \tan\phi'$

Therefore, the confining pressure corresponding to the transition from pure tensile failure to combined tensile-shear failure for the unsaturated compacted clay could be estimated as follows:

(6.15) $\sigma_{cI} = c_{app} \tan(45° + \phi'/2) = \left(c' + sS_r^{\kappa} \tan\phi'\right)\tan(45° + \phi'/2)$

Infante Sedano (2006) conducted ring shear tests on unsaturated Indian Head till and determined the parameters, i.e. c', ϕ' and κ associated with peak shear strength. The confining pressure corresponding to the failure mode transition for the compacted specimens are estimated and summarized in Table 6.6. The observations of the rupture zone after test confirmed the transition of the failure mode. For example, Figure 6.14 shows the decrease of the tension area (i.e. the red dash circle) on the rupture section and the appearance of the increasing shear band (the area outside the red dash circle) towards inner side as the confining pressure increases from 75 kPa to 100 kPa and then to 150 kPa in specimens IHT-14-TTT. The estimated confining pressures corresponding to the failure mode transition in Table 6.6 overestimate the real transition confining pressures (e.g., less than 100 kPa for IHT-14-TTT). The discrepancy might be induced by the inappropriate approximation of linear Mohr-Coulomb failure envelope for the range of low compressive and tensile normal stresses (i.e. Figure 2.18).

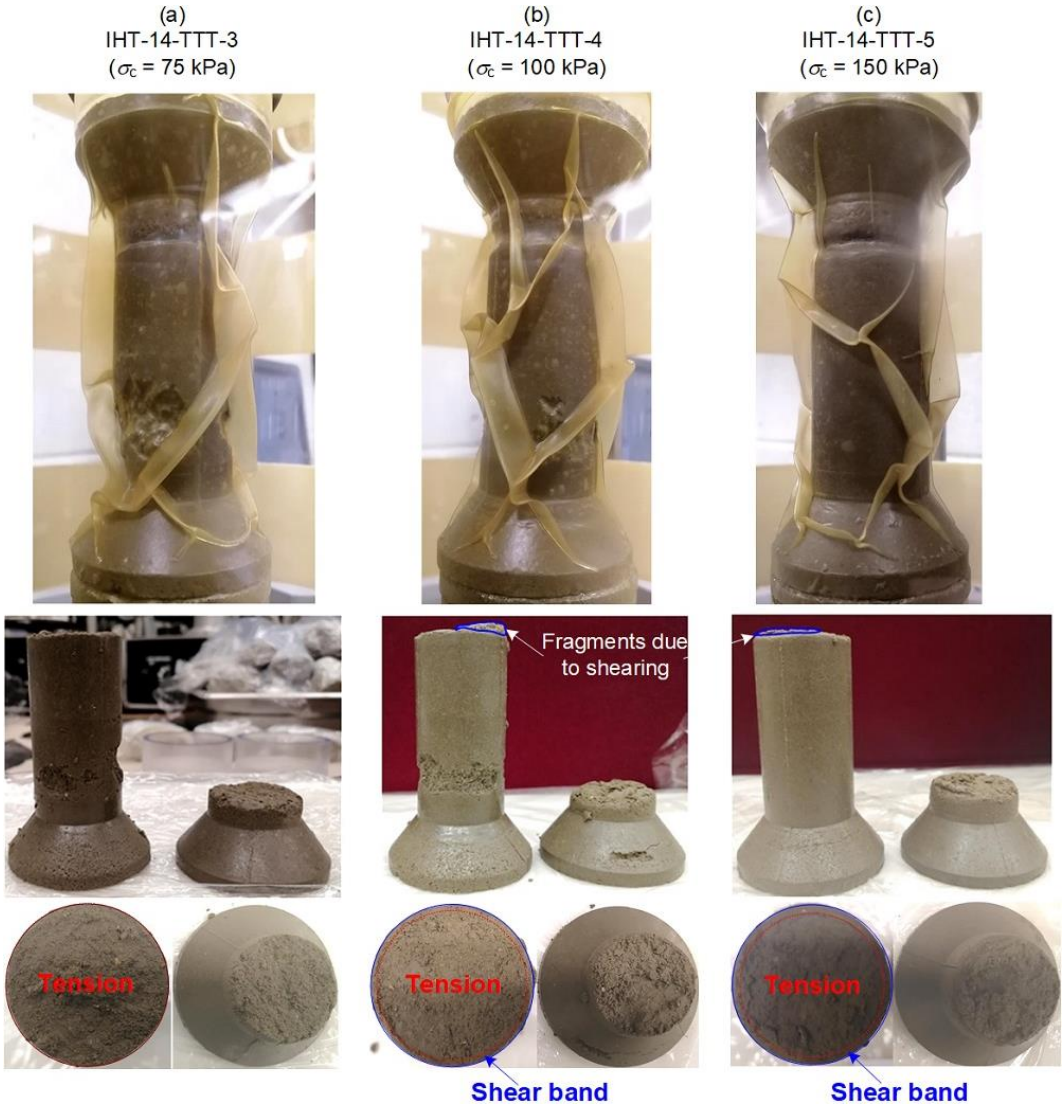

Figure 6.14 Photos of the rupture zone of compacted specimens after the triaxial tensile test: (a) IHT-14-TTT-3, (b) IHT-14-TTT-4, and (c) IHT-14-TTT-5.

Table 6.6 Estimation of the confining pressure corresponding to the transition of failure mode.

Specimen No.	*Cohesion, c' (kPa)	*Internal friction angle, ϕ' (°)	Soil suction, s (kPa)	Degree of saturation, S_r	*Fitting parameter, κ	Confining pressure corresponding to transition, σ_{cI}, (kPa)
IHT-17-TTT	10.61	26.3	328	0.896	2.20	432
IHT-16-TTT	10.61	26.3	506	0.887	2.20	642
IHT-15-TTT	10.61	26.3	596	0.853	2.20	693
IHT-14-TTT	10.61	26.3	975	0.767	2.20	894
IHT-12-TTT	10.61	26.3	1836	0.747	2.20	1571

Note: *values are derived from Infante Sedano (2006).

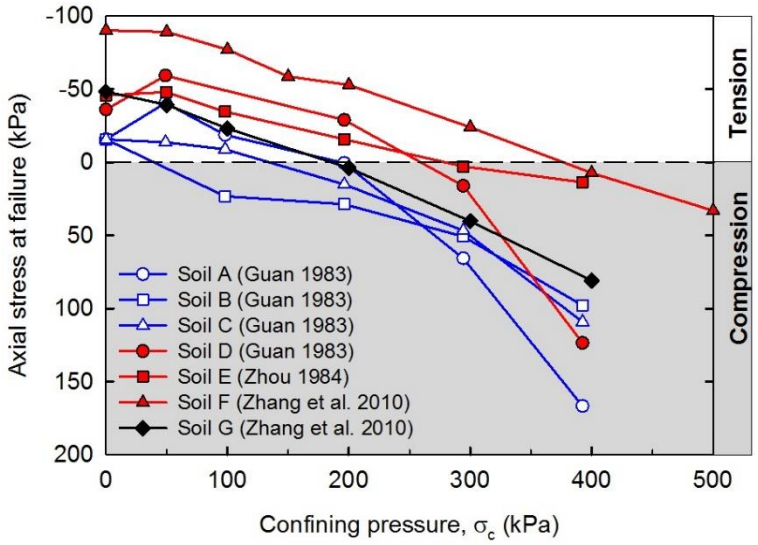

Figure 6.15 Variation of axial stress at failure with confining pressure for different compacted clayey soils investigated in the literature.

Figure 6.15 provides comparisons between the triaxial tensile test results with different levels of confining pressure on compacted clayey soils in the literature. The properties of the studied compacted clayey soils are summarized in Table 6.7. It is found that the tensile strength in the upper tension zone decreases as the confining pressure increases as predicted by several classic theories of rupture, such as the Griffith theory of rupture (Griffith 1921), Mohr-Coulomb failure criterion. The sudden increase in tensile strength were observed for compacted clayey soil A and soil D at confining pressure of 50 kPa (Figure 6.15). In those investigations, the compacted clayey soils are proposed to construct the core of earth dam with a height of tens of meter. Therefore, the confining pressure varies at a relatively board range, e.g., from 0 to 500 kPa. Three types of failure modes are identified by Zhang et al. (2010a), i.e. pure tensile failure at low confining pressures (e.g., 0 - 200 kPa for soil F), combined tensile-shear failure at mediate confining pressures (e.g., 300 kPa for soil F), and pure shear failure at high confining pressure (e.g., 400 - 500 kPa for soil F). The identification is confirmed by the features of the rupture sections of the compacted clayey soil F after tests as shown in Figure 6.16. Several researchers have proposed theoretical models to predict the transition behavior of failure modes with the dependency on the confining pressure in soils (e.g., Guan 1983; Zhang and Chen 1987; Lu et al. 2009; Kong et al. 2016; Wong et al. 2017). For example, Guan (1983) proposed the combined Griffith-Mohr theory of rupture following the concept of “crack closure stress” (McClintock and Walsh 1962) to explain the fundamental mechanism of the transition of failure modes from tensile failure to shear failure as the confining

pressure increases. Because the information of uniaxial tensile strength and the triaxial extension test results corresponding to shear failure mode is unavailable in the current study, the discussion on the theoretical models is not covered in detail.

Table 6.7 Summary of the basic properties of compacted clayey soils investigated by triaxial tensile tests in the literature.

No.	Initial water content, w_i	Initial dry density, $\rho_{d,i}$ (g/cm^3)	Specific gravity, G_s	*Grain size distribution			Atterberg's limits		Reference
				Sand size fraction	Silt size fraction	Clay size fraction	Liquid limit (%)	Plastic limit (%)	
Soil A	N/A	N/A	N/A	N/A	N/A	N/A	N/A	N/A	Guan (1983)
Soil B	N/A	N/A	N/A	N/A	N/A	N/A	N/A	N/A	Guan (1983)
Soil C	20%	1.65	N/A	N/A	N/A	N/A	N/A	N/A	Guan (1983)
Soil D	N/A	N/A	N/A	N/A	N/A	N/A	N/A	N/A	Guan (1983)
Soil E	20.1% - 21.7%	1.60 - 1.71	N/A	13.3%	51.0%	35.7%	43	22	Zhou (1984)
Soil F	22.0	1.63	2.73	N/A	N/A	40% - 49%	42.3	22.5	Zhang et al. (2010a)
Soil G	15.8	1.65	2.71	N/A	N/A	23.3%	33.4	19.6	Zhang et al. (2010a)

Note: *Clay size fraction is the mass fraction of soil grains with the size less than 0.005mm in the Chinese code, such as GB/T 50145-2007 (Ministry of Housing and Urban-Rural Development, People's Republic of China, 2008). N/A: Not available in the cited studies.

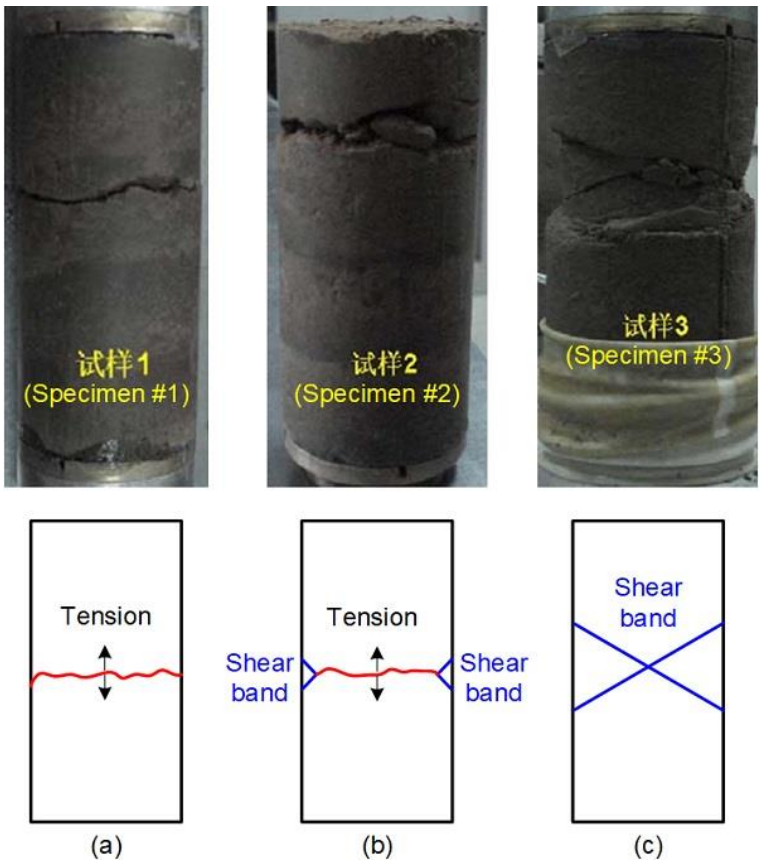

Figure 6.16 The photo and schematic illustration of the feature of rupture sections corresponding to three different failure modes after triaxial tensile tests on the compacted clayey soil conducted by Zhang et al. (2010b): (a) pure tensile failure under low confining pressures; (b) combined tensile-shear failure under mediate confining pressures; and (c) pure shear failure under high confining pressures.

6.1.4.2 Tensile stress- tensile displacement curves

Due to the membrane tension, some assumptions should be made prior to calculating the stress in the central section (i.e. section *M* in Figure 6.8): (i) the membrane is free of force at the beginning of the RTE path and reaches the interaction force of f_1; (ii) the membrane is a linearly elastic material; and (iii) the weight of membrane above the central section is negligible (i.e. $G_m = 0$ in Eq. (6.9)). Hence, according to Eq. (6.9), the membrane interaction force at failure reads as

$$f_1 = T_0 + \sigma_c \left(A_M - A_3 \right) + \left(G_{tc} + G_{vs} + G \right) \tag{6.16}$$

where the diameters of the central section (A_M) and the connector (A_3) are 30 mm and 10 mm, respectively. The calculation based on Eq. (6.16) for all the specimens are presented in Table 6.8. Hence, the membrane interaction force (f) in Eq. (6.7) could be estimated by the linear interpolation

from 0 to f_1 as the axial tensile displacement increases. The membrane interaction force at failure (f_1) has negative values that are relatively small in magnitude for some specimens. The test results were calculated extending simplified assumption related to the stress sustained by the membrane during the test. Thus, the axial stress acting in the central section could be estimated by Eq. (6.7) given all the known terms on the right-hand side. Figures 6.17, 6.18, 6.19, 6.20, 6.21 show the axial load measured by the load cell and the axial stress in the central section during the RTE path for all the triaxial tensile tests.

Table 6.8 Summary of the membrane tension at failure for all the specimens.

Specimen No.	Confining pressure, σ_c (kPa)	Tensile force after failure, T_0 (kN)	Mass of top cap and vylastic sleeve, (G_{tc} + G_{vs}) (g)	Mass of specimen above the rupture section, G (g)	Membrane interaction force at failure, f_1 (kN)
IHT-17-TTT-1	25	-0.024	90.027	59.693	-0.007
IHT-17-TTT-2	50	-0.005	90.007	65.112	0.028
IHT-17-TTT-3	75	-0.042	90.035	79.132	0.007
IHT-17-TTT-4	100	-0.036	90.066	119.002	0.029
IHT-17-TTT-5	150	-0.038	90.021	65.597	0.058
IHT-17-TTT-6	200	-0.026	90.087	66.315	0.101
IHT-16-TTT-1	25	-0.025	90.083	66.128	-0.008
IHT-16-TTT-2	50	-0.040	90.066	104.43	-0.007
IHT-16-TTT-3	75	-0.035	90.179	66.727	0.014
IHT-16-TTT-4	100	-0.058	90.035	67.699	0.006
IHT-16-TTT-5	150	-0.066	90.061	83.346	0.030
IHT-16-TTT-6	200				
IHT-15-TTT-1	25	-0.025	90.141	75.005	-0.008
IHT-15-TTT-2	50	-0.041	91.871	73.617	-0.008
IHT-15-TTT-3	75	-0.053	90.141	75.208	-0.004
IHT-15-TTT-4	100	-0.031	90.157	74.096	0.033
IHT-15-TTT-5	150	-0.037	90.103	53.171	0.059
IHT-15-TTT-6	200	-0.068	90.045	66.480	0.059
IHT-14-TTT-1	25	-0.010	90.128	75.503	0.007
IHT-14-TTT-2	50	-0.042	90.173	60.610	-0.009
IHT-14-TTT-3	75	-0.037	90.099	65.896	0.012
IHT-14-TTT-4	100	-0.071	90.071	64.244	-0.007
IHT-14-TTT-5	150	-0.090	90.068	66.160	0.006
IHT-14-TTT-6	200	-0.125	90.070	83.200	0.002
IHT-12-TTT-1	25				
IHT-12-TTT-2	50	-0.046	90.193	132.559	-0.012
IHT-12-TTT-3	75	-0.048	90.091	63.630	0.001
IHT-12-TTT-4	100	-0.065	90.090	42.565	-0.001
IHT-12-TTT-5	150	-0.097	90.093	63.374	-0.001
IHT-12-TTT-6	200	-0.155	90.046	63.613	-0.028

The test results trends of some specimens are different from typical results shown in Figure 3.7.For example, the axial force drops after tensile failure and increases again when the tensile displacement increases (e.g., Figures 6.17(a) and 6.18(a)). The unexpected increase in axial force measured by load cell after tensile failure may be attributed to the considerable tension sustained by the latex membrane. This phenomenon is more pronounced for wet specimens which have lower sustainable tensile stress at failure. It should be pointed out that no attempt has been made to measure the tensile strain in this study. This is because of the distribution of tensile strain is not uniform along the height of the specimen due to the irregular shape and non-uniform stress distribution. The measurements of the local tensile displacement in the central part with reduced section area, especially for the rupture zone is recommended in future investigations.

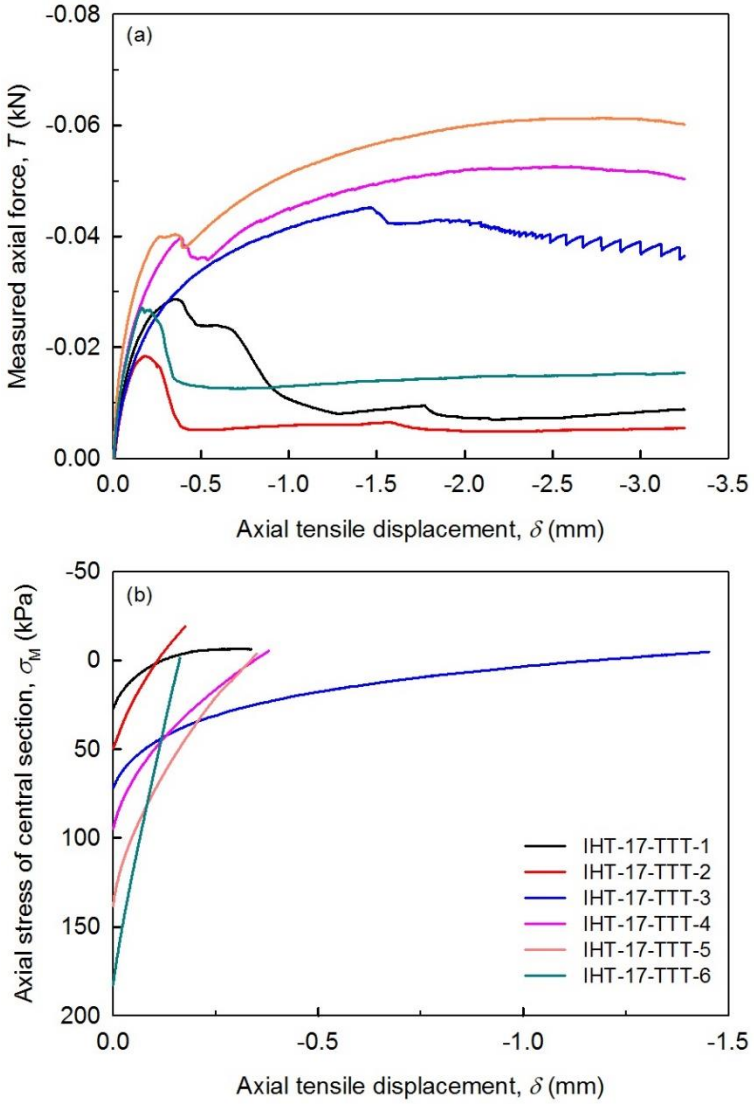

Figure 6.17 IHT-17-TTT: (a) the axial force measured by the load cell during the RTE path; (b) the estimated axial stress of the central section from the beginning of RTE path to rupture.

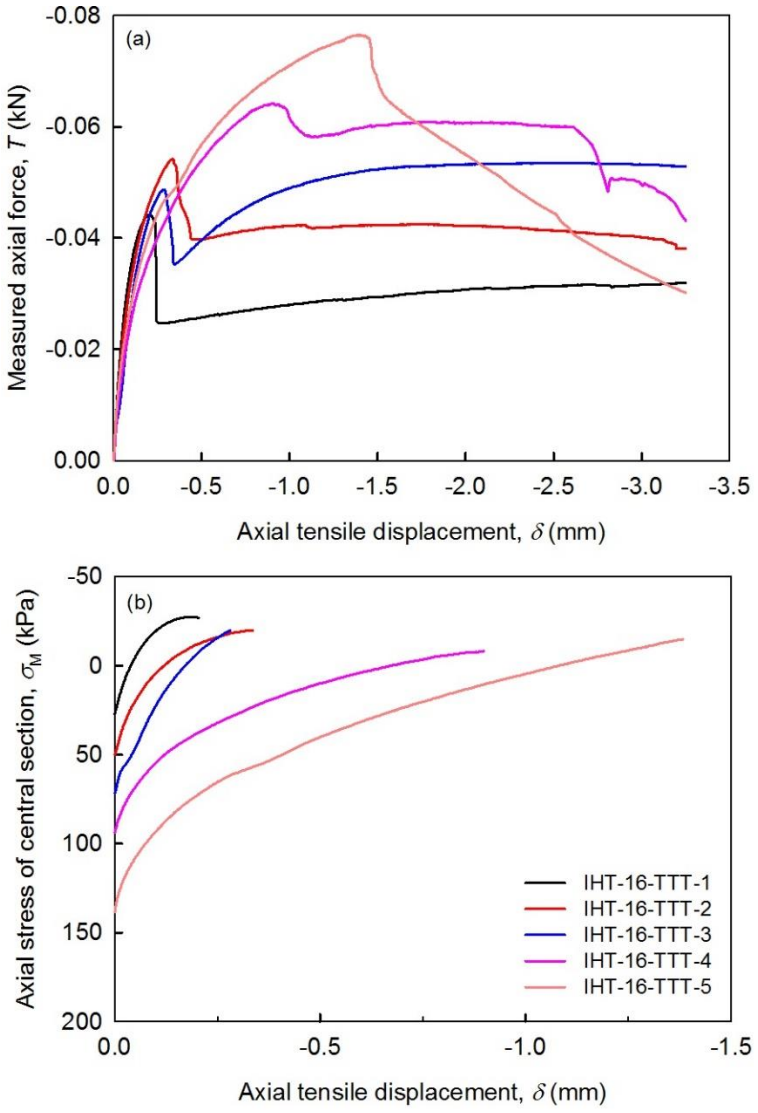

Figure 6.18 IHT-16-TTT: (a) the axial force measured by the load cell during the RTE path; (b) the estimated axial stress of the central section from the beginning of RTE path to rupture.

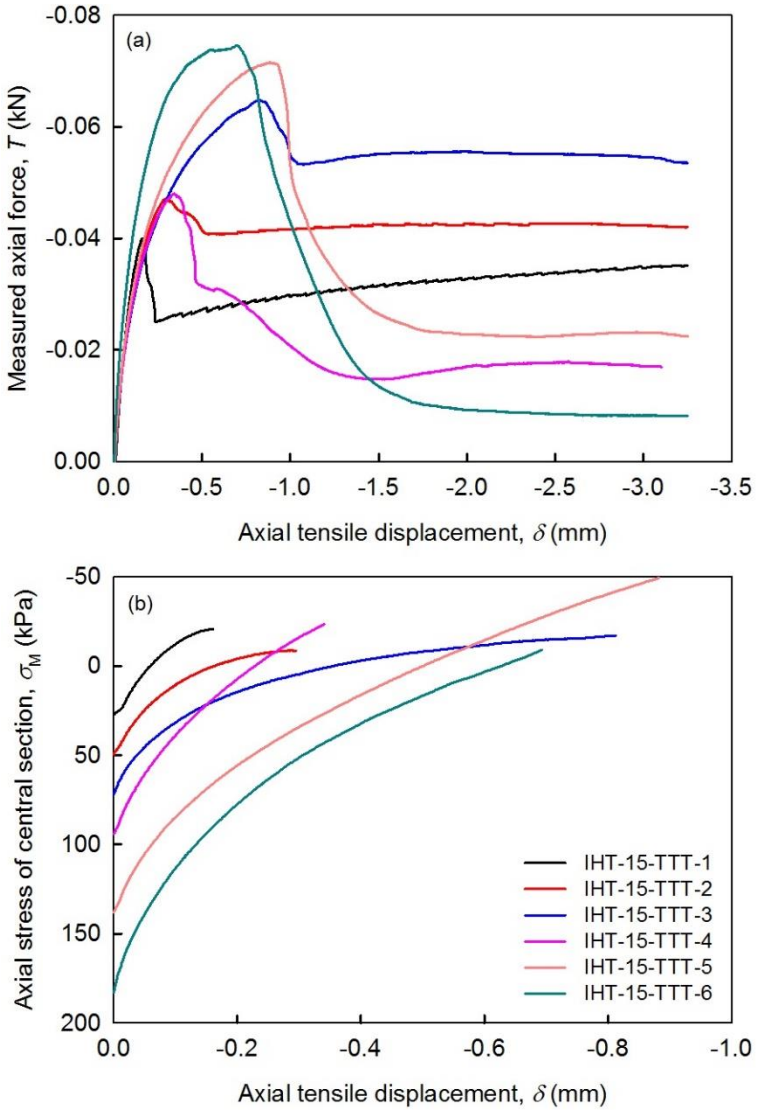

Figure 6.19 IHT-15-TTT: (a) the axial force measured by the load cell during the RTE path; (b) the estimated axial stress of the central section from the beginning of RTE path to rupture.

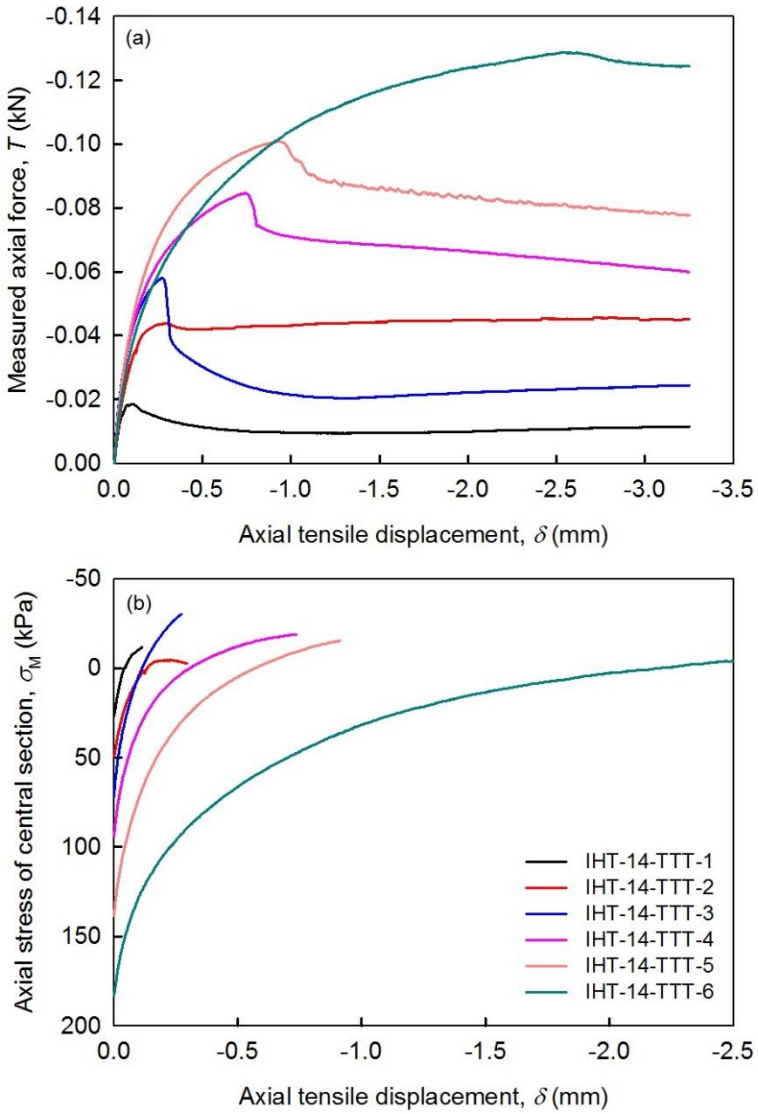

Figure 6.20 IHT-14-TTT: (a) the axial force measured by the load cell during the RTE path; (b) the estimated axial stress of the central section from the beginning of RTE path to rupture.

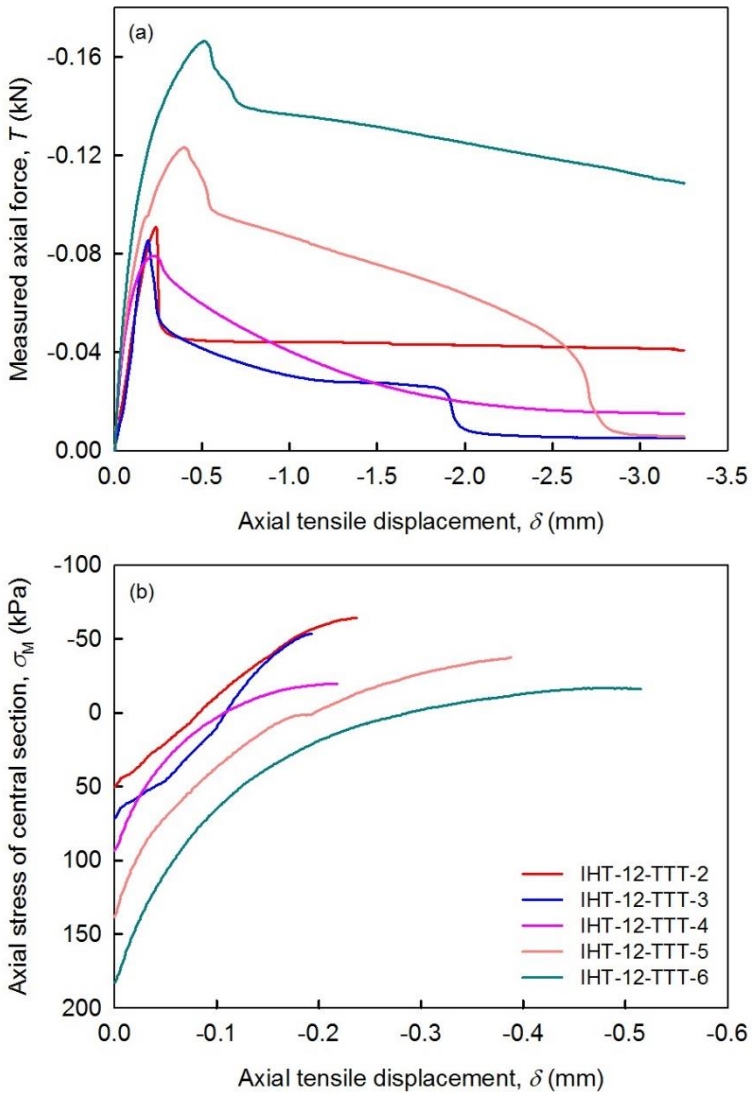

Figure 6.21 IHT-12-TTT: (a) the axial force measured by the load cell during the RTE path; (b) the estimated axial stress of the central section from the beginning of RTE path to rupture.

6.2 Brazilian split test

6.2.1 Principle

Carneiro (1943) and Akazawa (1943) originally proposed the Brazilian split test, which is an indirect method to determine the tensile strength of brittle materials (i.e. concrete). This type of test is performed by loading a disk specimen along its vertical axis to develop tensile stresses perpendicular to the vertical diameter. Brazilian split test is recommended to determine the indirect tensile strength of intact rock core specimens by the ISRM (ISRM 1977) and ASTM D3967-16 (ASTM International, 2016). Due to the simple procedure for specimen preparation and the wide

availability of the equipment in geotechnical labs, the Brazilian split test has been used in the past 50 years to determine the indirect tensile strength of various types of geomaterials, such as rocks (e.g., Mellor and Hawkes 1971), stabilized soils (e.g., Bofinger 1970), and soils (e.g., Frydman 1964; Krishnayya and Eisenstein 1973).

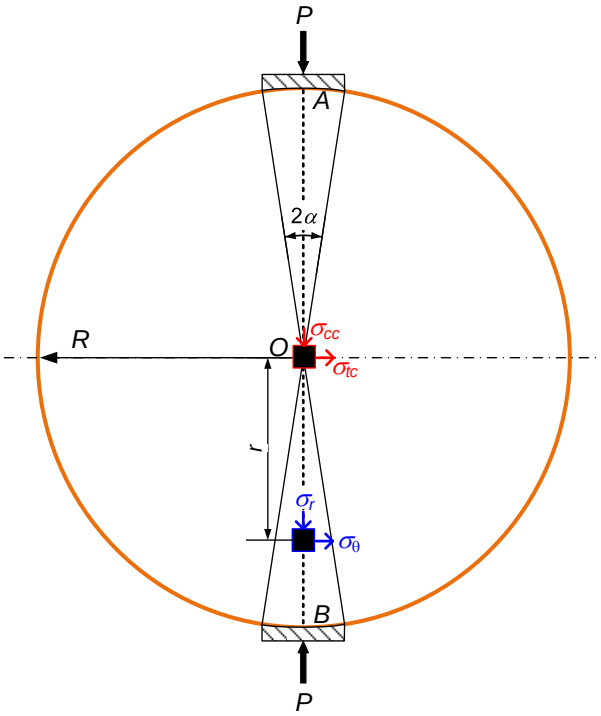

Figure 6.22 Sketch of the Brazilian split test under a uniformly distributed load over finite arcs (modified after Li and Wong 2013).

Figure 6.22 illustrates a soil disk subjected to the vertical load along the diameter. The vertical load is uniformly distributed over finite arcs (i.e. 2α). Hondros (1959) developed the complete stress solution along the load diameter (i.e. AB in Figure 6.22) in which the material is assumed as homogeneous, isotropic and linearly elastic (tensile stress is taken as negative):

$$(6.17a)\quad \sigma_\theta = -\frac{P}{\pi R t \alpha}\left\{\frac{\left[1-\left(\frac{r}{R}\right)^2\right]\sin 2\alpha}{1-2\left(\frac{r}{R}\right)^2\cos 2\alpha+\left(\frac{r}{R}\right)^4}-\tan^{-1}\left[\frac{1+\left(\frac{r}{R}\right)^2}{1-\left(\frac{r}{R}\right)^2}\tan\alpha\right]\right\}$$

$$(6.17b)\quad \sigma_r = +\frac{P}{\pi R t \alpha}\left\{\frac{\left[1-\left(\frac{r}{R}\right)^2\right]\sin 2\alpha}{1-2\left(\frac{r}{R}\right)^2\cos 2\alpha+\left(\frac{r}{R}\right)^4}+\tan^{-1}\left[\frac{1+\left(\frac{r}{R}\right)^2}{1-\left(\frac{r}{R}\right)^2}\tan\alpha\right]\right\}$$

where P is the applied load, R is the disk radius, t is the disk thickness, 2α is the angular distance over which P is assumed to be distributed radially (usually $2\alpha \leq 15°$), and r is the distance from the center of the disk. Thus, the horizontal tensile stress and vertical compressive stress at the center of the disk are

$$(6.18)\quad \sigma_{tc} = -\frac{P}{\pi R t}\left(\frac{\sin 2\alpha}{\alpha}-1\right); \qquad \sigma_{cc} = +\frac{P}{\pi R t}\left(\frac{\sin 2\alpha}{\alpha}+1\right)$$

According to Griffith's theory of rupture (Griffith 1921), the exact center of the disk is the only crack initiation point at which the conditions for tensile failure at a value equal to the uniaxial strength are met. However, in some Brazilian split tests performed on rock specimens, Li and Wong (2013) argued that (i) the crack initiation points have been observed to be located away from the center of the disk; and (ii) the stress concentration near the loading platen occasionally leads to an early shear failure in the rock specimens. The above two limitations are observed in the Brazilian split tests on soil specimens as well. In addition, the material properties of soils, such as anisotropy and ductility would put the stress solution given by Hondros (1959) into questionable (e.g., Das et al. 1995; Gaspar and Jacobsz 2021). Those limitations will be discussed in greater details in later sections.

6.2.2 Equipment used and experimental program

The Brazilian split tests are conducted following the general procedures described in ASTM D3967-16 (ASTM International, 2016). Figure 6.23 shows the setup for Brazilian split test using the loading frame with the capacity of 50 kN (1 in Figure 6.23) for applying the compressive force to the disk specimen at a constant displacement rate. Displacement rate of 0.5 mm/min is used here, because the displacement rate with the range between 0.1 mm/min and 1.0 mm/min has been found to induce no considerable change in the measured Brazilian tensile strength (e.g., Akin and Likos 2017). Applied compressive force and vertical compressive displacement are continuously

recorded with a S-type load cell having 100 lbs (445 N) capacity and the linear variable differential transformer (LVDT) (2 and 6 in Figure 6.23). The rubber strips and steel rods are placed on the upper and bottom loading platens for a proper distribution of the applied load (8 and 9 in Figure 6.23). Hence, the arc of contact between the loading strips and the disk specimen is limited and negligible. Following Eq. (6.18), the horizontal compressive stress and vertical tensile stress can be approximated as

$$\text{(6.19a)}\quad \sigma_{tc} = \lim_{2\alpha \to 0}\left[-\frac{P}{\pi R t}\left(\frac{\sin 2\alpha}{\alpha} - 1\right)\right] = -\frac{P}{\pi R t}$$

$$\text{(6.19b)}\quad \sigma_{cc} = \lim_{2\alpha \to 0}\left[+\frac{P}{\pi R t}\left(\frac{\sin 2\alpha}{\alpha} + 1\right)\right] = +\frac{3P}{\pi R t}$$

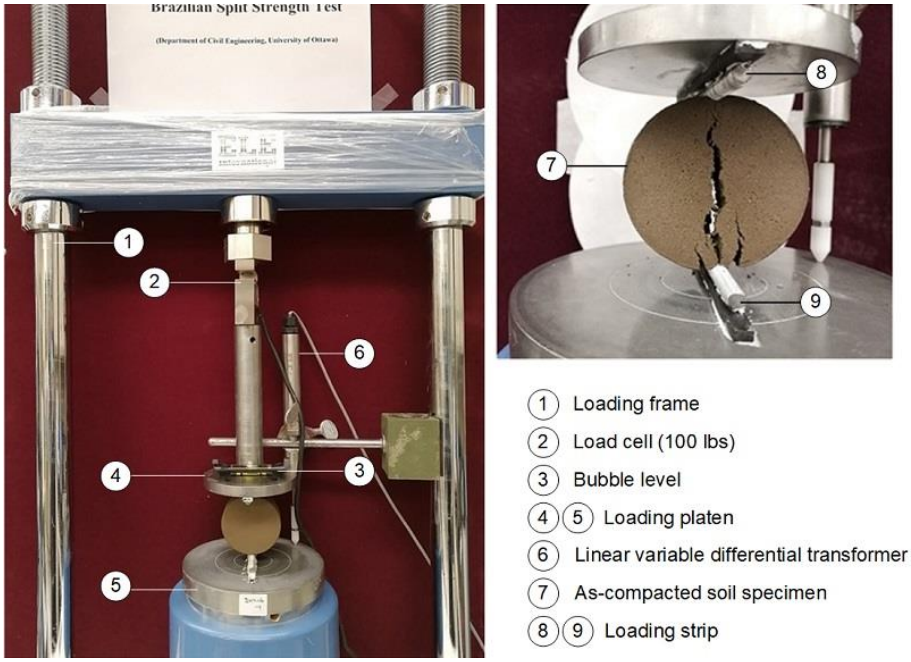

Figure 6.23 Setup of the Brazilian split test at Department of Civil Engineering, University of Ottawa.

As can be seen from Eq. (6.19), the vertical compression stress is three times the horizontal tension stress prior to failure for Brazilian split tests. It should be noted that the tensile strength derived from Brazilian split tests is different from the value measured by uniaxial tensile tests. The former is confined tensile strength; on the contrary, the latter is unconfined tensile strength (or uniaxial tensile strength).

The procedure for specimen preparation is the same as that used for filter paper test (see Chapter 5). According to ASTM D3967-16 (ASTM International, 2016), the thickness-to-diameter ratio (t/2R) of the circular disk should range between 0.20 and 0.75 and the diameter of the disk specimen should be at least 10 times greater than the largest mineral grain constituent. The as-compacted Indian Head till specimens has the diameter ($2R$) of 60 mm and the height (t) of 20 mm, such that the thickness-to-diameter ratio ($t/2R$) equals 0.33. Based on the investigation by Akin and Likos (2017), the measured Brazilian tensile strength of compacted clay specimens generally decreases with increasing thickness-to-diameter ratio and the tensile strength for ($t/2R$) >0.42 is approximately 77.5% of that for ($t/2R$) =0.25. Three parallel specimens are prepared for each desired water content (i.e. w_i = 17.2%, 16.3%, 15.3%, 14.3%, 12.3%, and 10.3%) and dry density (i.e. $\rho_{d,i} = \rho_{d,max}$ = 1843 kg/m^3) in order to check the repeatability of the test results. The as-compacted specimens are wrapped with two layers of plastic film and stored in a plastic box for 24 hours prior to Brazilian split tests. The dimensions and mass of the disk specimens are measured prior to perfroming the tests. Table 6.9 summarizes the initial state of all the compacted specimens prior to Brazilian split tests.

Table 6.9 Summary of the initial states for the as-compacted specimens.

Specimen No.	Initial water content, w_i	Initial dry density, $\rho_{d,i}$ (kg/m^3)	*Initial matric suction, s (kPa)	Initial void ratio, e	Initial degree of saturation, S_r
IHT-17-BST-1				0.491	0.946
IHT-17-BST-2	17.2	1843	328	0.506	0.917
IHT-17-BST-3				0.505	0.919
IHT-16-BST-1				0.490	0.897
IHT-16-BST-2	16.3	1843	506	0.504	0.874
IHT-16-BST-3				0.484	0.910
IHT-15-BST-1				0.491	0.841
IHT-15-BST-2	15.3	1843	596	0.481	0.858
IHT-15-BST-3				0.481	0.858
IHT-14-BST-1				0.506	0.764
IHT-14-BST-2	14.3	1843	975	0.484	0.798
IHT-14-BST-3				0.488	0.791
IHT-12-BST-1				0.496	0.669
IHT-12-BST-2	12.3	1843	1836	0.500	0.664
IHT-12-BST-3				0.507	0.655
IHT-10-BST-1				0.474	0.587
IHT-10-BST-2	10.3	1843	2682	0.503	0.553
IHT-10-BST-3				0.480	0.579

Note: *Values are measured by filter paper technique using other two identical soil cakes with given water contents and dry density (Table 5.8).

6.2.3 Test results and results interpretation

Table 6.10 summarizes the calculated Brazilian tensile strength (BTS) of all the as-compacted specimens as well as the measured water contents after test. The limited standard deviation of the Brazilian tensile strength for three parallel specimens with the desired water content indicates good consistency of specimen preparation and test procedures. The water contents in the center and on the sides of the disk specimen are measured immediately after the test. Compared with the initial water contents, the reduction in water content during the test due to evaporation is less than 0.5% except for the extremely wet specimens (i.e. IHT-17-BST and IHT-16-BST). For the water content close to the saturated water content, the degree of saturation is close to unity. Thus, the reduction in water content of 1% might not result in the remarkable increase in the matric suction according to the SWCC of Indian Head till (i.e. Figure 5.20 in Chapter 5). Therefore, the reduction in water content after test could be assumed to have insignificant influence in the degree of saturation as well as the matric suction.

Table 6.10 Summary of the test results of Brazilian split tests on the as-compacted specimens.

Specimen No.	Vertical compressive displacement at failure, v_f (mm)	Brazilian tensile strength			Water content after test	
		$BTS = -P_{max}/\pi Rt$ (kPa)	Mean	Standard deviation	Center	Sides
IHT-17-BST-1	4.00	28.51			16.1%	16.1%
IHT-17-BST-2	3.66	25.96	25.86	2.21	16.1%	16.5%
IHT-17-BST-3	3.43	23.11			16.6%	16.7%
IHT-16-BST-1	3.51	27.68			15.6%	15.8%
IHT-16-BST-2	3.35	25.96	27.53	1.23	15.6%	15.7%
IHT-16-BST-3	3.52	28.95			15.6%	15.5%
IHT-15-BST-1	3.61	27.49			15.0%	15.0%
IHT-15-BST-2	3.54	27.52	27.68	0.25	15.3%	15.2%
IHT-15-BST-3	4.00	28.04			15.2%	15.1%
IHT-14-BST-1	3.16	29.08			14.0%	13.9%
IHT-14-BST-2	2.81	29.37	29.65	0.61	14.1%	14.0%
IHT-14-BST-3	2.81	30.49			13.9%	13.8%
IHT-12-BST-1	2.48	38.89			11.9%	12.0%
IHT-12-BST-2	2.73	39.97	38.14	1.87	12.2%	12.2%
IHT-12-BST-3	2.43	35.57			11.9%	11.9%
IHT-10-BST-1	2.15	62.13			10.0%	9.9%
IHT-10-BST-2	2.56	60.32	60.36	1.43	10.0%	9.8%
IHT-10-BST-3	2.07	58.62			9.9%	9.9%

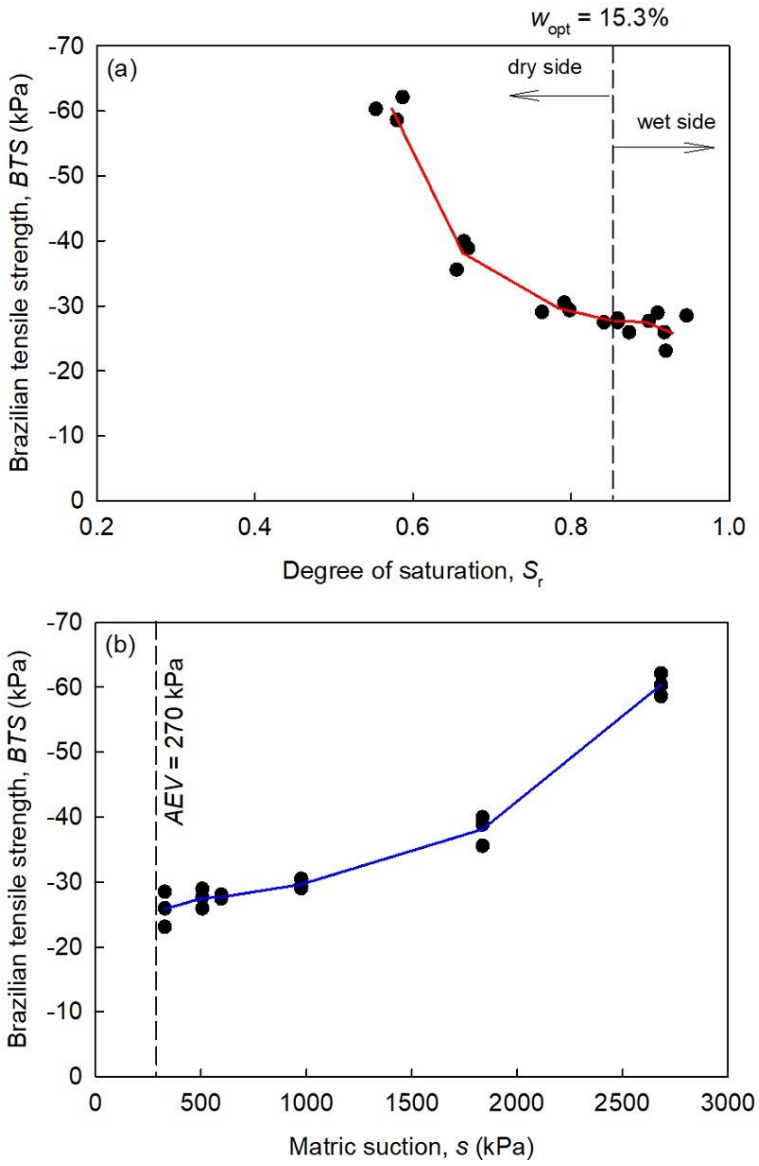

Figure 6.24 Variation of Brazilian split strength with (a) degree of saturation; and (b) matric suction.

Figure 6.24 shows the variation of Brazilian tensile strength with the degree of saturation and with the matric suction. It is found that the Brazilian tensile strength increases as the degree of saturation decreases and the matric suction increases. Such a behavior may be attributed to the variation of the inter-aggregate capillary bonding force as well as the change in microstructure of the as-compacted soils as the compaction water content decreases (i.e. Figure 6.11). Figure 6.25 presents the variation of tensile stress in the center of the disk versus the vertical compressive displacement until failure is observed. It is found that brittle failure occurs for the as-compacted specimens when the compaction water content is less than plastic limit (i.e. PL = 14%), in which crack initiation leads to complete failure rapidly (in a few seconds) and the tensile stress drops abruptly to zero

once the maximum tensile stress reaches (see Figures 6.25 (e) and (f)). In contrast, the ductile failure of the as-compacted specimens with compaction water content greater than the plastic limit (i.e. Figures 6.25 (a), (b), (c), and (d)) involves considerable plastic deformation as the crack propagates. The difference in specimen deformation could be reflected by the vertical compressive displacement before failure summarized in Table 6.10. The brittle failure is the ideal condition to use the theoretical solution to interpret the test results (Eq. (6.17)). On the other hand, the considerable plastic deformation associated with the ductile failure may result in the discrepancy between the theoretical solution and the real stress state of the ductile soil specimen at failure. For ductile failure of unsaturated soil specimens, Gaspar and Jacobsz (2021) proposed a novel technique to interpret the results of Brazilian tensile tests, in which the tensile stress corresponding to the end of the approximate linear stage was interpreted as the Brazilian tensile strength. Beyond the linear stage in the tensile stress- compressive displacement curve, the tensile strain (or transverse strain) in the center of the disk specimen increases rapidly as the microcracks initiate; and the vertical compressive load is supported not only by the tensile strength but also by the specimen compression. In the present study, the division of the multiple stages in the tensile stress-compressive displacement curve is not straightforward because the approximately linear stage is not well developed (see Figure 6.25 (a), (b), (c), and (d)). The measurement of tensile strain by strain gauge or digital image correlation (DIC) technique is recommended in the further studies, which could make the division of the multiple stages easier and give new insight to the failure mechanism of the disk specimen subjected to the vertical compressive load. Thus, Eq. (6.19) based on the theoretical solution is used to estimate the Brazilian tensile strength of the as-compacted specimens associated with ductile failure.

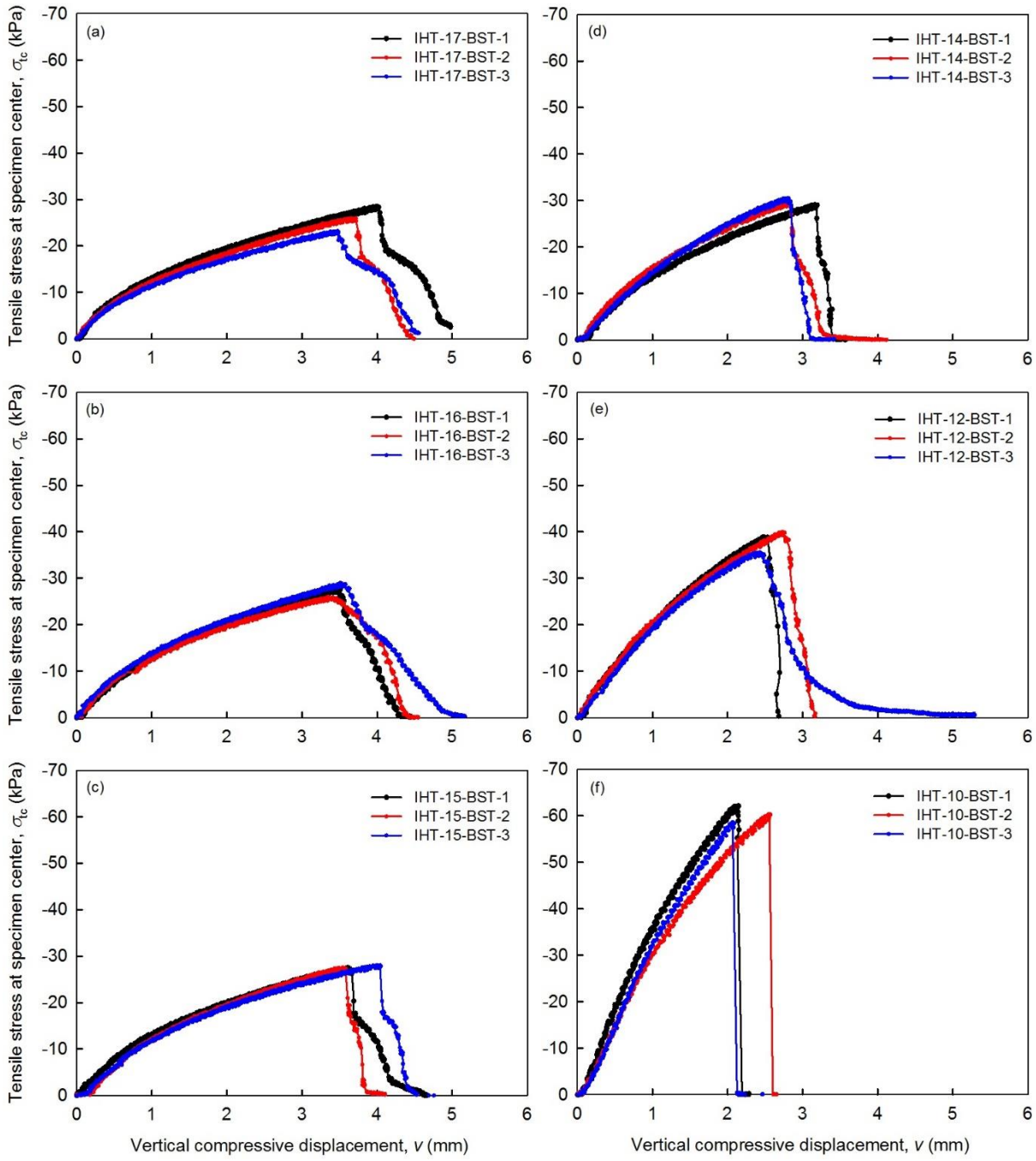

Figure 6.25 Calculated tensile stress at the center of the three identical specimens versus the vertical compression during the Brazilian split tests: (a) IHT-17-BST; (b) IHT-16-BST; (c) IHT-15-BST; (d) IHT-14-BST; (e) IHT-12-BST; and (f) IHT-10-BST.

Based on the theoretical solution (Eq. (6.17)) and the Griffith theory of rupture, the crack initiation point should be located at the center of the disk. However, crack initiation points for most disk specimens are away from the center and near the loading points as the arrows shown on the fractured specimens after test in Figure 6.26. This observation is consistent with the findings in

Brazilian split tests on disk rock specimens (e.g., Fairhurst 1964; Hudson et al. 1972; Swab et al. 2011). The discrepancy between the theoretical prediction and the laboratory observation might be attributed to the property of the real soil specimens which is heterogeneous, anisotropic, nonlinear. In addition, the stress concentration near the loading points might lead to an early shear failure prior to the tensile failure in the center of the disk (e.g., Figure 6.26 (a) and (b)). Li and Wong (2013) investigated the failure behavior of the rock disk specimen subjected to the vertical compressive load by numerical simulation and found that both the tensile strain and tensile stress reach the maximum value near the loading points instead of at the center of the disk. The crack initiation occurs near the loading points could be explained by the critical extension strain criterion (Stacey 1981) instead of the maximum tensile stress criterion.

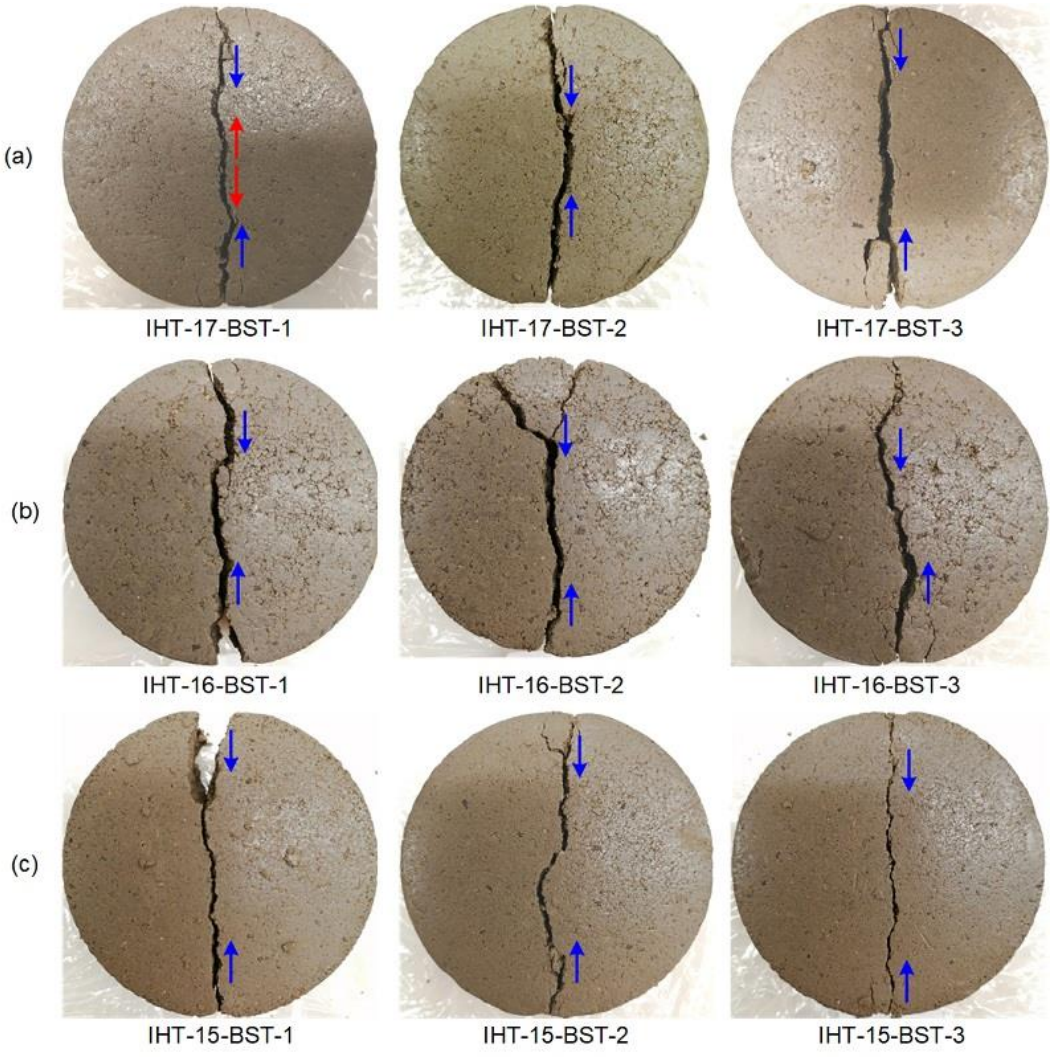

Figure 6.26 The photos of fractured specimens after Brazilian split tests: (a) IHT-17-BST; (b) IHT-16-BST; and (c) IHT-15-BST.

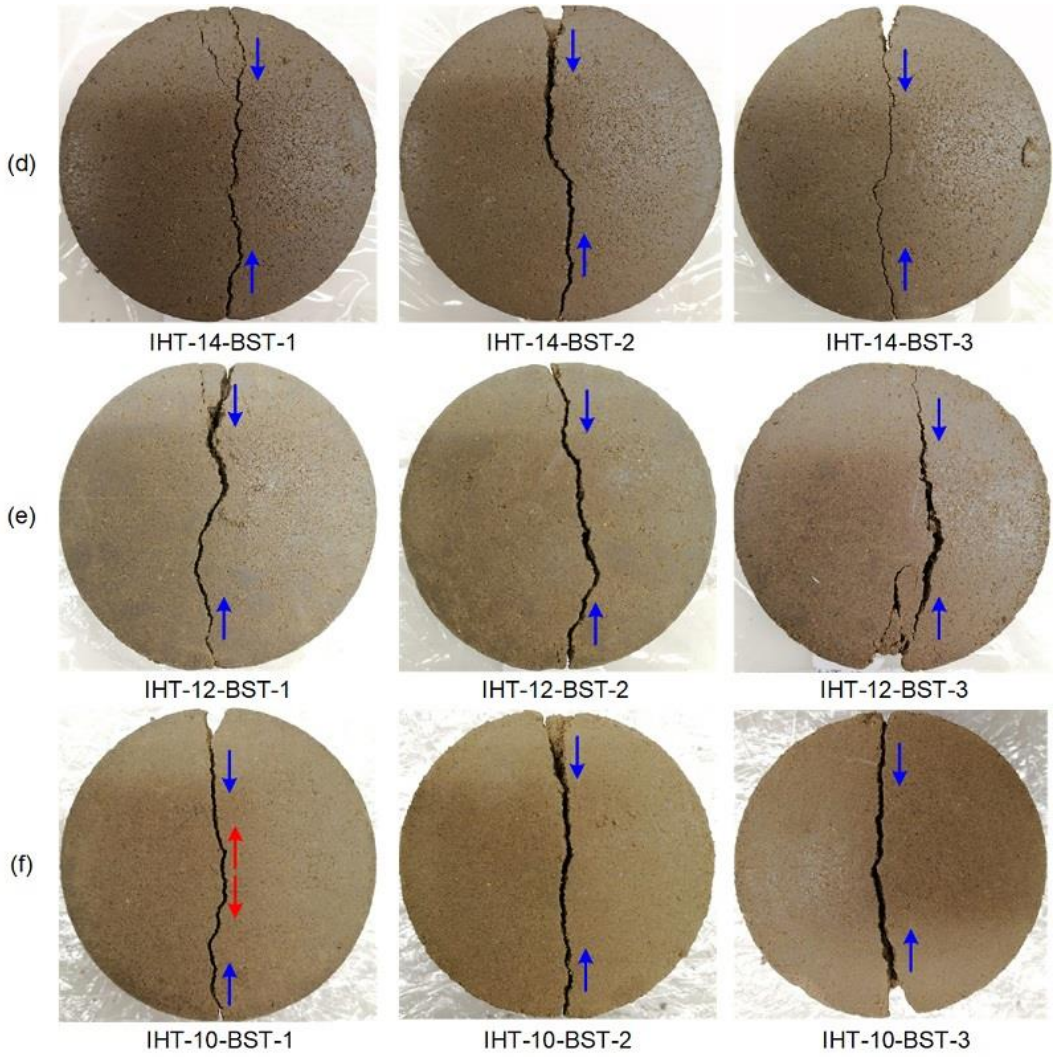

Figure 6.26 (Cont.) The photos of fractured specimens after Brazilian split tests: (a) IHT-14-BST; (b) IHT-12-BST; and (c) IHT-10-BST.

Figure 6.27 summarizes the triaxial tensile strength (σ_{tt}) under different confining pressures as well as the Brazilian tensile strength (BTS) in the stress space (τ, σ). It is found that the Brazilian tensile strength (i.e. black circles) is greater than the tensile strength for the wet specimens which have the compaction water content greater than the plastic limit (i.e. Figure 6.27 (a), (b), (c) and (d)) except for the outlier of IHT-15-TTT-5. This is because the calculated Brazilian tensile strength overestimates the true tensile strength when ductile failure occurs for wet specimens. On the other hand, the Brazilian tensile strength of IHT-12 provides the reasonable estimation of the true tensile strength when the effect of confining pressure is considered (Figure 6.27 (e)). In addition, the internal friction angle which can be determined from the Mohr envelopes based on shown in Figure 6.27 for the specimens with one tensile principal stress and one compressive

principal stress is remarkably greater than that for the specimens with all compressive principal stresses (i.e. 26.3°). This is consistent with the observation on unsaturated sands at low confining pressures by Lu et al. (2009).

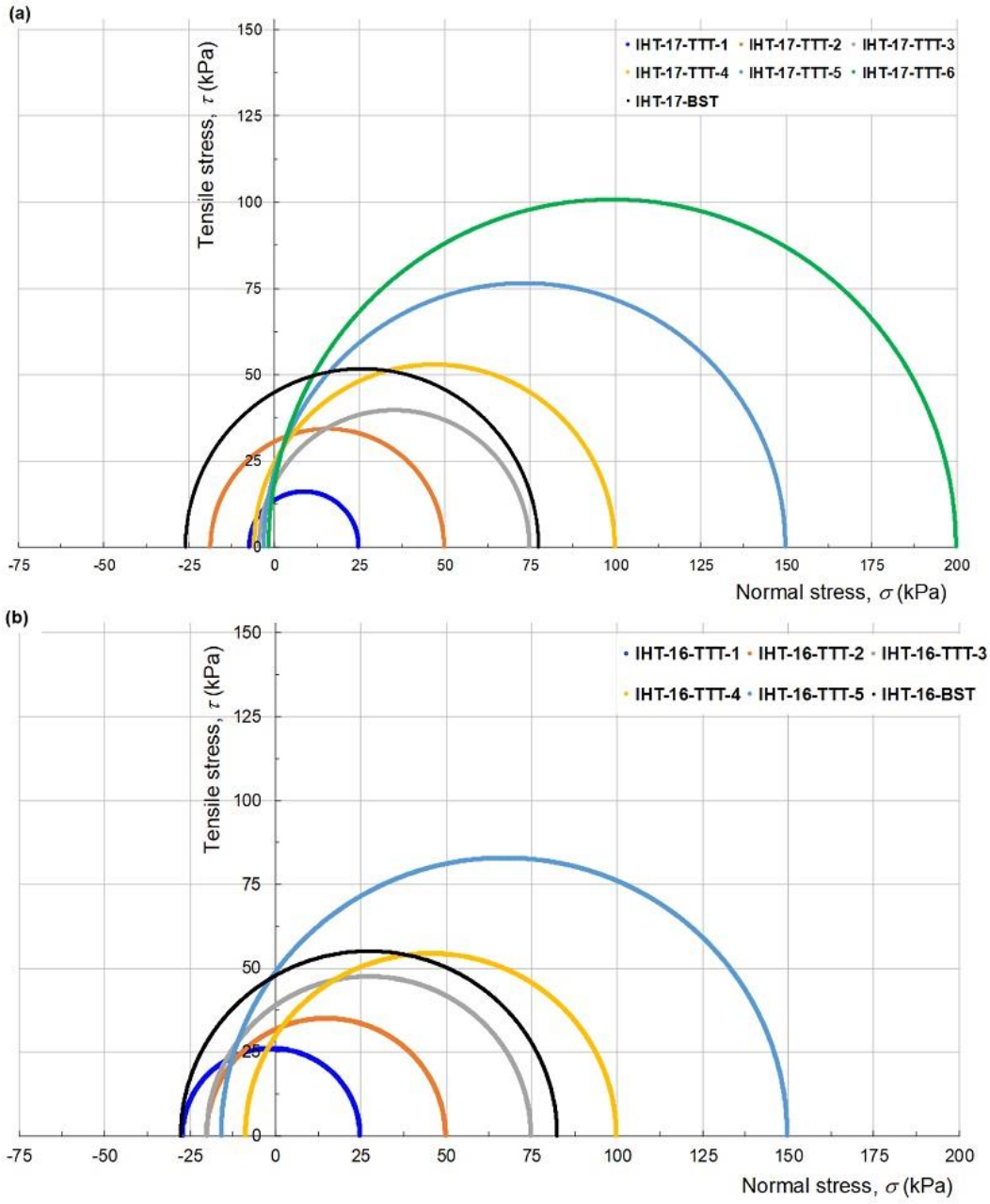

Figure 6.27 The plots of Mohr circles corresponding to triaxial tensile strength (circles in color) and Brazilian tensile strength (circle in black): (a) IHT-17; (b) IHT-16.

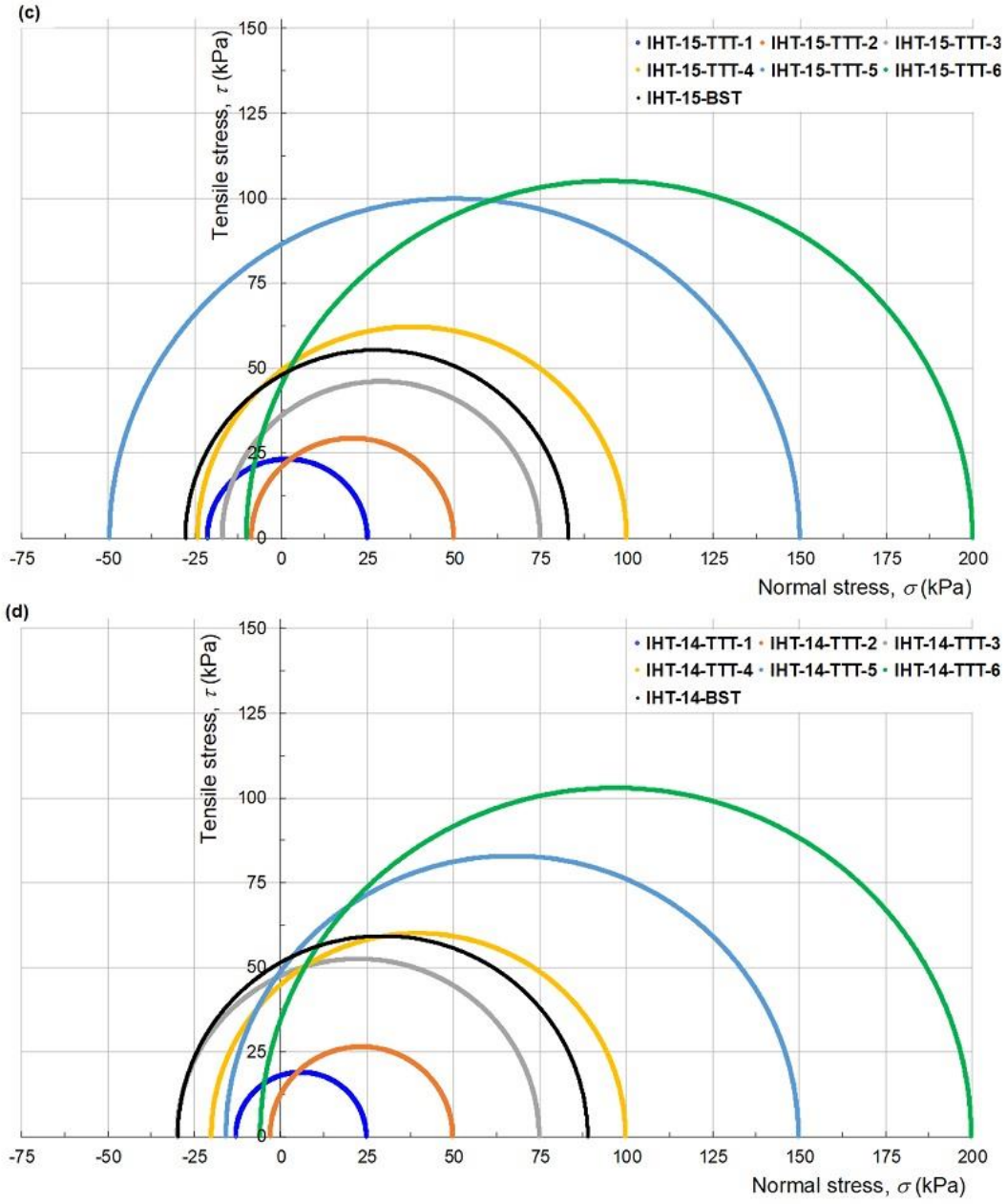

Figure 6.27 (Cont.) The plots of Mohr circles corresponding to triaxial tensile strength (circles in color) and Brazilian tensile strength (circle in black): (c) IHT-15; (d) IHT-14.

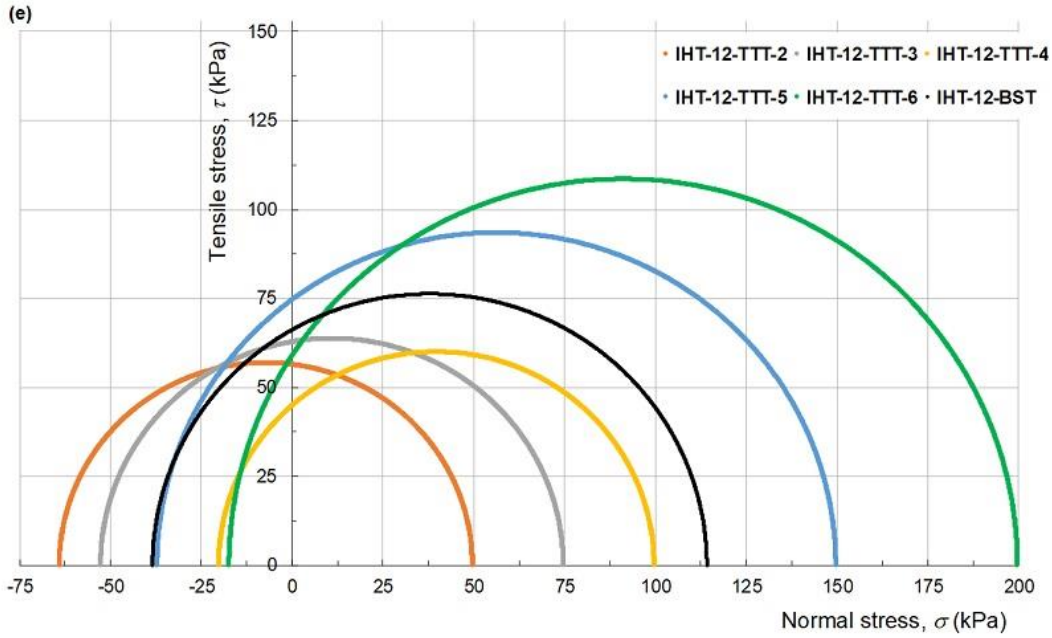

Figure 6.27 (Cont.) The plots of Mohr circles corresponding to triaxial tensile strength (circles in color) and Brazilian tensile strength (circle in black): (e) IHT-12.

6.3 Summary

In this chapter, the influence of matric suction as well as confining pressure on the tensile strength of compacted Indian Head till are investigated by triaxial tensile tests and Brazilian split tests. The main findings are summarized as follows:

(i) The tensile strength increases as the matric suction of the as-compacted clay specimens increases within the investigated range from an overall trend of view. This phenomenon could be explained by the variation of inter-aggregate capillary bonding force as the compaction water content decreases from the capillary boundary effect zone (zone III) to the transition zone (zone II). The change in microstructure from the dispersed structure in zone III to the flocculated structure in zone II influences the stress transmission among clay aggregates or clay particles.

(ii) The tensile strength decreases as the confining pressure increases for as-compacted clay specimens with the given compaction water content from an overall trend of view. The initial increase followed with decrease trend for the specimens IHT-15 and IHT-14 might be attributed to the remarkable increase in the dry density. As the confining pressure increases, the failure mode transit from pure tensile failure to combined tensile-shear failure in which shear failure occurs first at the weak section and then the tensile failure takes place at the central part of the weak section.

The shear failure under tensile normal stress on the shear plane is not fully developed prior to the failure of the specimen. The reduction of the section area which provides the tensile resistance results in the reduction in tensile strength which is calculated for the entire section area.

(iii) In spite of limitations in the technique, Brazilian split test is commonly used to determine the tensile strength of brittle materials, such as concrete and rock due to the simple procedure of specimen preparation and the wide availability of the test equipment. Brazilian split test was introduced to determine the tensile strength of unsaturated compacted soils as well. It is found that the theoretical solution of the Brazilian disk is suitable for the compacted clayey specimens with water content less than the plastic limit. In contrast, the calculated Brazilian tensile strength based on the theoretical solution might significantly overestimate the true tensile strength for those compacted specimens with water content higher than the plastic limit. Ductile failure instead of brittle failure occurs for those specimens with high water contents subjected to the diametral compressive load. The considerable plastic deformation accomplished with the ductile failure leads to the discrepancy between the theoretical solution and actual tensile strength.

(iv) The plot of Mohr circles corresponding to the tensile failure indicates that the internal frictional angle is remarkably greater than that corresponding to the shear failure under compressive normal stress. This observation provides clear evidence of the nonlinearity of the failure criterion, such as the nonlinear failure criteria proposed by Zhang and Chen (1987) and Lu et al. (2009). However, the uniaxial tensile strength is not measured in the current study. The investigation of the dependency of failure mechanism on the confining pressure for unsaturated soils deserves more experimental studies as well as theoretical investigations.

6.4 References

Akazawa, T. 1943. New test method for evaluating internal stress due to compression of concrete: the splitting tension test. Journal of Japan Society of Civil Engineers, 29: 777-787.

Akin, I.D. and Likos, W.J. 2017. Brazilian tensile strength testing of compacted clay. Geotechnical Testing Journal, 40(4): 608-617.

Alonso, E.E., Gens, A. and Hight, D.W. 1987. Groundwater effects in geotechnical engineering, General report. In Proceedings of the 9th European Conference on Soil Mechanics and Foundation Engineering, pp. 1087-1146.

Alonso, E.E., Pereira, J.M., Vaunat, J. and Olivella, S. 2010. A microstructurally based effective stress for unsaturated soils. Géotechnique, 60(12): 913-925.

Aluko, O.B. and Koolen, A.J. 2000. The essential mechanics of capillary crumbling of structured agricultural soils. Soil and Tillage Research, 55(3-4): 117-126.

ASTM International. 2016. ASTM D3967-16 Standard Test Method for Splitting Tensile Strength of Intact Rock Core Specimens. West Conshohocken, PA.

Bishop, A.W. and Garga, V.K. 1969. Drained tension tests on London clay. Géotechnique, 19(2): 309-313.

Bofinger, H.E. 1970. The measurement of the tensile properties of soil-cement. Rep. LR365., Minist. Transp., Road Research Lab, Crownthorne, Berks, Engl.

Cai, G., Shi, P., Kong, X., Zhao, C. and Likos, W.J. 2020. Experimental study on tensile strength of unsaturated fine sands. Acta Geotechnica, 15: 1057–1065.

Carneiro, F.L.L.B. 1943. A new method to determine the tensile strength of concrete. In Proceedings of the 5th Meeting of the Brazilian Association for Technical Rules, Vol. 3, No. 16, pp. 126-129.

Das, B.M., Yen, S.C. and Dass, R.N. 1995. Brazilian tensile strength test of lightly cemented sand. Canadian Geotechnical Journal, 32(1): 166-171.

Fairhurst, C. 1964. On the validity of the 'Brazilian' test for brittle materials. In International Journal of Rock Mechanics and Mining Sciences & Geomechanics Abstracts (Vol. 1, No. 4, pp. 535-546). Pergamon.

Fisher, R.A. 1926. On the capillary forces in an ideal soil; correction of formulae given by WB Haines. The Journal of Agricultural Science, 16(03): 492–505.

Fredlund, D.G. and Rahardjo, H. 1993. Soil Mechanics for Unsaturated Soils. John Wiley and Sons, New York.

Frydman, S. 1964. Applicability of the Brazilian (indirect tension) test to soils. Australian Journal of Applied Science, 15(4): 335-343.

Gaspar, T.A.V. and Jacobsz, S.W. 2021. Brazilian Tensile Strength Test Conducted on Ductile Unsaturated Soil Samples. Geotechnical Testing Journal, 44. https://doi.org/10.1520/GTJ20190078.

Griffith, A.A. 1921. VI. The phenomena of rupture and flow in solids. Philosophical Transactions of the Royal Society of London. Series A, containing papers of a mathematical or physical character, 221(582-593): 163-198.

Guan, D. 1983. Combined Griffith-Mohr strength theory of rupture in soils. In Proceedings of the 4th Academic Conference of China Civil Engineering Society for Soil Mechanics and Foundation Engineering, Beijing, China, pp. 131-124. [in Chinese]

Hilf, J.W. 1956. An investigation of pore water pressure in compacted cohesive soils. Technical Memorandum 654. United State Department of the Interior. Bureau of Reclamation, Denver Colorado.

Hudson, J.A., Brown, E.T. and Rummel, F. 1972. The controlled failure of rock discs and rings loaded in diametral compression. In International Journal of Rock Mechanics and Mining Sciences & Geomechanics Abstracts (Vol. 9, No. 2, pp. 241-248). Pergamon.

Infante Sedano, J.A. 2006. A modified ring shear test device for determining the hydro-mechanical behaviour of unsaturated soils. Doctoral dissertation, University of Ottawa, Canada.

ISRM (International Society for Rock Mechanics). 1977. Suggested methods for determining tensile strength of rock materials.

Kodikara, J. 2012. New framework for volumetric constitutive behaviour of compacted unsaturated soils. Canadian Geotechnical Journal, 49(11): 1227-1243.

Kong, X.A., Cai G.Q. and Zhao C.G. 2016. Study on tenso-shear coupling strength of clays. Chinese Journal of Rock and Soil Mechanics, 37(8): 2285-2293. [in Chinese]

Krishnayya, A.V.G. and Eisenstein, Z. 1974. Brazilian tensile test for soils. Canadian Geotechnical Journal, 11(4): 632-642.

Lakshmikantha, M.R., Prat, P.C. and Ledesma, A. 2012. Experimental evidence of size effect in soil cracking. Canadian Geotechnical Journal, 49(3): 264-284.

Li, D. and Wong, L.N.Y. 2013. The Brazilian disc test for rock mechanics applications: Review and new insights. Rock Mechanics and Rock Engineering, 46(2): 269-287.

Li, Y. 2018. A review of shear and tensile strengths of the Malan Loess in China. Engineering Geology, 236: 4-10.

Li, Y., Mo, P., Wang, Y., Zhang, T. and Zhang, H., 2020. Strength anisotropy of Malan loess and the implications for the formation of loess walls and columns. CATENA, 194: p.104809.

Lu, L. and Fan, H. 2014. Development on instrument of uniaxial tensile strength of soil. Yellow River, 36(9): 113-115. [in Chinese]

Lu, N. and Likos, W.J. 2006. Suction stress characteristic curve for unsaturated soil. Journal of Geotechnical and Geoenvironmental Engineering, 132(2): 131–142.

Lu, N., Kim, T.H., Sture, S. and Likos, W.J. 2009. Tensile strength of unsaturated sand. Journal of Engineering Mechanics, 135(12): 1410–1419.

Lu, N., Wu, B. and Tan, C. P. 2007. Tensile strength characteristics of unsaturated sands. Journal of Geotechnical and Geoenvironmental Engineering, 133(2): 144–154.

McClintock, F.A. and Walsh, J.B. 1962. Friction on Griffith cracks in rock under pressure. In Proceedings of the 4th US National Congress on Applied Mechanics, New York, NY, USA, Vol. 2, pp. 1015-1021.

Mellor, M. and Hawkes, I. 1971. Measurement of tensile strength by diametral compression of discs and annuli. Engineering Geology, 5(3): 173-225.

Mikulitsch, W.A. and Gudehus, G. 1995. Uniaxial tension, biaxial loading and wetting tests on loess. In Proceedings of the 1st International Conference on Unsaturated Soils, Paris, France, Vol. 1.

Ministry of Housing and Urban-Rural Development, People's Republic of China. 2008. GB/T 50145-2007 Standard for engineering classification of soil. China Planning Press, Beijing.

Nahlawi, H., Chakrabarti, S. and Kodikara, J. 2004. A Direct Tensile Strength Testing Method for Unsaturated Geomaterials. Geotechnical Testing Journal, 27(4): 1-6.

Péron H. 2008. Desiccation cracking of soils. Doctoral dissertation, École polytechnique fédérale de Lausanne, Switzerland.

Stacey, T.R. 1981. A simple extension strain criterion for fracture of brittle rock. In International Journal of Rock Mechanics and Mining Sciences & Geomechanics Abstracts (Vol. 18, No. 6, pp. 469-474). Pergamon.

Stirling, R. A., Hughes, P., Davie, C. T. and Glendinning, S. 2015. Tensile behaviour of unsaturated compacted clay soils - A direct assessment method. Applied Clay Science, 112–113: 123–133.

Swab, J.J., Yu, J., Gamble, R. and Kilczewski, S. 2011. Analysis of the diametral compression method for determining the tensile strength of transparent magnesium aluminate spinel. International Journal of Fracture, 172(2): 187-192.

Tang, G. X. and Graham, J. 2000. A method for testing tensile strength in unsaturated soils. Geotechnical Testing Journal, 23(3): 377–382.

Tang, C.S., Pei, X.-J., Wang, D.-Y., Shi, B. and Li, J. 2015. Tensile strength of compacted clayey soil. Journal of Geotechnical and Geoenvironmental Engineering, 141(4): 04014122.

Trabelsi, H., Romero, E. and Jamei, M. 2018. Tensile strength during drying of remoulded and compacted clay: The role of fabric and water retention. Applied Clay Science, 162: 57–68.

Tollenaar, R.N., van Paassen, L.A. and Jommi, C., 2017. Experimental evaluation of the effects of pull rate on the tensile behavior of a clay. Applied Clay Science, 144: 131-140.

Tschebatorioff, F.P. 1953. The tensile strength of disturbed and recompacted soils. In Proceedings of the 3rd International Conference on Soil Mechanics and Foundation Engineering, Vol. 1, pp. 207-210.

Vanapalli, S.K., Fredlund, D.G., Pufahl, D.E. and Clifton, A.W. 1996. Model for the prediction of shear strength with respect to soil suction. Canadian Geotechnical Journal 33(3): 379-392.

Vanapalli, S.K., Fredlund, D.G. and Pufahl, D.E. 1999. The influence of soil structure and stress history on the soil water characteristics of a compacted till. Géotechnique, 49: 143–159.

Wang, J., Li, P., Gu, Q., Xu, Y. and Gu, T. 2019. Changes in tensile strength and microstructure of loess due to vibration. Journal of Asian Earth Sciences, 169: 298-307.

Wang, J.J., Zhu, J.G., Chiu, C.F. and Zhang, H. 2007. Experimental study on fracture toughness and tensile strength of a clay. Engineering Geology, 94(1–2): 65–75.

Wong, C.K., Wan, R.G. and Wong, R.C., 2020. Tensile and shear failure behaviour of compacted clay–hybrid failure mode. International Journal of Geotechnical Engineering, 14(3): 231-241.

Xu, X., Cai, G., Li, J. and Zhao, C. 2018. The strength and dilatancy characteristic of unsaturated soil at low and tensile stresses. Chinese Journal of Rock Mechanics and Engineering, 37(8): 16-25. [in Chinese]

Yin, P. and Vanapalli, S.K. 2018. Model for predicting tensile strength of unsaturated cohesionless soils. Canadian Geotechnical Journal, 55(9): 1313-1333.

Zhang, X.J. and Chen, W.F. 1987. Stability analysis of slopes with general nonlinear failure criterion. International Journal for Numerical and Analytical Methods in Geomechanics, 11(1): 33–50.

Zhang, B., Li, Q., Yuan, H. and Sun, X. 2015. Tensile fracture characteristics of compacted soils under uniaxial tension. Journal of Materials in Civil Engineering, 27(10): 04014274.

Zhang, Y., Zhang, B., Li, G. and Sun, X. 2010a. Combined tension-compression triaxial tests and extended Duncan-Chang model of compacted clay. Chinese Journal of Geotechnical Engineering, 32(7): 999-1004. [in Chinese]

Zhang, Y., Zhang, B., Sun, X. and Li, G. 2010b. Experimental study on triaxial tensile property of compacted clay. Journal of Hydroelectric Engineering, 29(6): 172-177. [in Chinese]

Zhou, H. 1984. The mechanism of fracture of soil samples in triaxial tensile test. Chinese Journal of Geotechnical Engineering, 6(3): 11-23. [in Chinese]

Chapter 7. Conclusions and Recommendations for Further Work

7.1 Major conclusions

7.1.1 State-of-art review on desiccation cracking in cohesive soils and tensile strength of unsaturated soils

(1) Desiccation cracking in cohesive soils is a multiphysical (i.e. thermo-hydro-mechanical) coupled and a multiscale phenomenon. By analyzing the crack water contents of different soils reported in the literature, it is concluded that the crack water content is not the intrinsic soil property but is dependent on the soil properties, initial soil states, and the environmental conditions. Therefore, the crack initiation criterion (i.e. maximum tensile stress criterion) should be investigated extending the framework of unsaturated soil mechanics and fracture mechanics. Based on the earlier observations and interpretations, the soil crack formation (i.e. initiation and propagation) is found to be controlled by both the deterministic factor (i.e. the generated stress field) and the stochastic factor (i.e. randomly distributed heterogeneities).

(2) The crack patterns induced by desiccation are presented and interpreted based on extensive field and laboratory investigation studies. The mixture of two typical patterns (i.e. the simultaneous hexagonal pattern, and the sequential orthogonal pattern) in cracked cohesive soils is a combined result of the strain energy release and the interaction between the generated stress field and the existing or induced heterogeneities. From the fracture mechanics standpoint of view, the effects of soil layer thickness, base friction, and environmental conditions on the crack block size (or crack spacing) can be better understood.

(3) For the various methods for experimental determination, the direct method is recommended as reliable and reproducible tensile failure conditions can be assured from tests, such as the uniaxial tensile test. However, the direct method has relatively stringent testing requirements for the specimen preparation and test equipment, such as the triaxial tensile tests. In contrast, the indirect method is commonly used due to the simple procedure of specimen preparation and the availability of test equipment, such as the Brazilian split test. Indirect methods are widely used in practice, in spite of limitations associated with determining the tensile strength of soils.

(4) The various prediction models of tensile strength of unsaturated soils available in the literature can be summarized in two main categories; (i) empirical models, and (ii) mechanics-based models. Mechanics-based models are preferred due to their reliability and rationality. The core motivation of mechanics-based models is to formulate the tensile resistance as the macroscopic response of unsaturated soils which reflects the stress transmission at the microscale. For example, the concept of suction stress reflects the contribution of suction in unsaturated cohesionless soils to the internal stress state at the level of representative elementary volume (REV). The effect of microstructure on the internal stress transmission in unsaturated cohesive soils remains not well addressed, even though some research work by theoretical and numerical investigation has been published recently.

(5) Investigations related to the effect of confining pressure on the tensile strength of unsaturated soils is limited in the literature. Some researchers have proposed the unified failure criterion considering the various failure modes (i.e. shear failure, tensile failure, combined tensile-shear failure) under different stress conditions; however, these failure modes are not extensively verified.

7.1.2 Model for predicting tensile strength of unsaturated cohesionless soils

(1) From a microscopic point of view, capillary force induced by matric suction from the voids filled with bulk water and surface tension along the air-water interface can be exerted on soil particles, resulting in the bonding effect and developing tensile strength between adjacent soil particles. The effects of both matric suction and surface tension on the tensile strength of unsaturated cohesionless soils are included in the proposed semi-empirical model. The contribution arises independently towards the total tensile strength from the first component (σ_{tun}) and the second component (σ_{tus}). The required information to estimate the tensile strength of unsaturated cohesionless soils includes: the matric suction corresponding to a specific degree of saturation, the capillary degree of saturation (S_c), and residual degree of saturation (S_r) which can be derived from the SWCC; the mean particle size (d_{50}), and coefficient of uniformity (C_u) which can be obtained from the grain size distribution curve; the void ratio (e); and the friction angle (ϕ_t) at low normal stress level.

(2) The proposed model is validated by providing comparisons with the measured data for ten soils (five sandy soils, and five silty soils). This model is capable of reliably predicting the variation of

tensile strength, σ_{tu}, with the degree of saturation, S, using two model parameters (i.e. k and η_s) which can be related to the coefficient of uniformity, C_u. The prediction is more accurately represented by plotting the results on an arithmetic scale and providing comparisons with the measured tensile strength values. The tensile strength values of certain cohesionless soils are rather small (for example, soils 2, 3, and 4 have values less than 2 kPa). Such measurements are difficult to predict in comparison to relatively large values (i.e. tens of kilopascals for soils 7, 8, 9, and 10) due to the sensitive response of instrumentation used in tests and possible experimental errors to measure low values of stresses.

7.1.3 Model for predicting evolution of microstructural void ratio in compacted clayey soils

(1) A more reasonable criterion for identifying different pore populations of compacted clayey soils by interpreting the MIP results is suggested. Compared with the different criteria used in the literature, the suggested criterion in the present study requires the least information (i.e. the PSD or, cumulative intrusion curve) of clayey soil at a given state. The suggested criterion considers not only the PSD shape but also the influence of hydromechanical loading paths on the soil microstructure. Based on the assumption that compaction does not induce irreversible volumetric deformation of clay aggregates, the as-compacted state line (ACSL) of microstructural void ratio is proposed by interpreting the MIP results for seven of the examined soils. Good agreements between the predicted and measured values demonstrate that the proposed ACSL can reproduce the variation of microstructural void ratio with the compaction water ratio of both high-plasticity clays and low-plasticity clays.

(2) The constitutive stress that controls the volumetric deformation of a clay aggregate in an unsaturated condition is derived. The simplified expression of the constitutive stress stems from the force equilibrium of interparticle force acting on the wavy surface through the interparticle contacts in an unsaturated clay aggregate. Thereafter, the linear elastic constitutive model is examined for predicting the change in microstructural void ratio upon monotonic wetting and drying paths of eight of the examined compacted soils. The capability of the proposed approach, i.e. the predictive models together with the estimated model parameters is confirmed by the high

correlation (R^2 = 0.88) between the predicted and measured microstructural void ratios for all the examined soils using total 150 data points.

7.1.4 Experimental studies on the tensile strength of compacted clayey soils

(1) The tensile strength increases as the matric suction of the as-compacted clay specimens increases within the investigated range. This phenomenon could be explained by the variation of inter-aggregate capillary bonding force as the compaction water content decreases from the capillary boundary effect zone (zone III) to the transition zone (zone II). The change in microstructure from the dispersed structure in zone III to the flocculated structure in zone II influences the stress transmission among clay aggregates or clay particles.

(2) The tensile strength decreases as the confining pressure increases for as-compacted clay specimens with the given compaction water content. The initial increase followed with a decreasing trend for the specimens IHT-15 and IHT-14 (see Chapter 6) might be attributed to the remarkable increase in the dry density. As the confining pressure increases, the failure mode transit from pure tensile failure to combined tensile-shear failure in which shear failure occurs first at the weak section and then the tensile failure takes place at the central part of the weak section. The shear failure under tensile normal stress on the shear plane is not fully developed prior to the complete failure of the specimen. The reduction of the section area which provides the tensile resistance results in the reduction in tensile strength which is calculated for the entire test section area.

(3) The Brazilian split test is commonly used in spite of limitations in the testing technique to determine the tensile strength because of the simple procedure of specimen preparation and the wide availability of the test equipment. The theoretical solution of the Brazilian disk specimen is suitable for the compacted clayey specimen with water content less than the plastic limit. In contrast, the calculated Brazilian tensile strength based on the theoretical solution might significantly overestimate the true tensile strength for those compacted specimens with water content higher than the plastic limit. Ductile failure instead of brittle failure occurs for those specimens with high water contents subjected to the diametral compressive load. The considerable

plastic deformation accomplished with the ductile failure leads to the discrepancy between the theoretical solution and actual tensile strength.

7.2 Recommendations for future research

Due to the limitations of the theoretical interpretation and the experimental investigation undertaken in this study, the following recommendations are provided for future research.

(1) The model for predicting the evolution in microstructural void ratio of compacted clayey soils subjected to drying and wetting is only valid for monotonic drying or wetting path. This is mainly due to the oversimplified derivation of the "microstructural average skeleton stress", in which the mechanical isolated clay aggregate is considered. This model might be extended considering the effect of drying-wetting cycles.

(2) The Consolidated-Drained (CD) or Consolidated-Undrained (CD) triaxial tensile test on unsaturated soil specimens could be performed. The conditions of suction-control or suction-monitor would give a more accurate estimation of the matric suction of the specimen at failure. It is recommended to measure the volumetric deformation during the triaxial tensile test as well. In addition, the tensile stress-strain relationship prior to failure as well as the tensile strength could be included in the existing constitutive models for unsaturated soils.

(3) The investigations in this study provide clear evidence of the nonlinearity of the failure criterion. Although several nonlinear failure criteria have been proposed in the literature, the test results corresponding to the failure associated with tensile stress in unsaturated soils remain limited in comparison to the results corresponding to shear induced failure. Therefore, more experimental studies are recommended to investigate the dependency of failure mechanism on the matric suction as well as the confining pressure in various unsaturated soils.